Entorhinal cortex dysfunction in rodent models of dementia

Submitted by Thomas Ridler to the University of Exeter

as a thesis for the degree of

Doctor of Philosophy in Medical Studies

In September 2017

I certify that all material in this thesis which is not my own work has been identified and that no material has previously been submitted and approved for the award of a degree by this or any other University.

Signature: …….

Word Count: 41,767

Abstract

As both the major input and output of the hippocampal formation, the entorhinal cortex (EC) occupies a pivotal position in the medial temporal lobe. The discovery of grid cells in the medial entorhinal cortex (mEC) has led to this region being widely implicated in spatial information processing. Importantly, the EC is also the first area affected by dementia pathology, with neurons appearing particularly susceptible to degeneration. Despite this, little is known about how pathology affects the functional output of mEC neurons, either in their ability to coordinate firing to produce network oscillations, or to represent information regarding the external environment. This thesis will use electrophysiological techniques to examine how dementia pathology contributes to the breakdown of mEC neuronal networks using the rTg4510 mouse model of tauopathy.

The first 2 results chapters will show how the anatomical organisation along the dorso-ventral axis of the mEC has profound influence on the network activity that can be observed both in brain slices and awake-behaving mice. It will further show how deficits in network activity in rTg4510 mice occur differentially across this axis, with dorsal mEC appearing more vulnerable to changes in oscillatory function than ventral.

The third results chapter will begin to explore the relationship between global network activity and the external environment, showing that rTg4510 mice display clear deficits in the relationship between oscillation properties and locomotor activity. Finally, the underlying basis for these changes will be examined, through the recording of single-unit activity in these mice. It will show a decreased tendency for mEC neurons to display firing rates modulated by running speed, as well as an almost complete breakdown of grid cell periodicity after periods of tau overexpression.

Understanding how dementia pathology produces changes to neuronal function and ultimately cognition is key for understanding and treating the disease. This thesis will therefore provide novel insights into the dysfunction of the EC during dementia pathology.

Acknowledgements

To my supervisors, Dr Jon Brown, Prof Andrew Randall and Dr Keith Phillips, thank you for your support, your guidance and your open door. None of this would have been possible without you.

To my co-workers, past and present (Lucy, Holly, Talitha, Ben, Soraya, Maria, Lydia(s) and Francesco to name a few), thank you for making the past 4 years an incredible experience, especially to Darren Walsh and Hannah Smithers, for being there every step of the way.

To my family, and to Jade most of all, thank you for your love and support, and your occasional memorisation of stock science phrases to keep me on my toes. I simply couldn't have done it without you.

To my grandmother, who no longer remembers my name, this is for you.

Table of Contents

Figures

Abbreviations

4-AP	4-aminopyridine
Aβ	Amyloid beta
AChE	Acetylcholinesterase
aCSF	Artificial cerebrospinal fluid
AD	Alzheimer's disease
AHP	After-spike hyperpolarisation potential
AMPA	α-amino-3-hydroxy-5-methyl-4-isoxazolepropionic acid
ANOVA	analysis of variance
ApoE	Apolipoprotein E
APP	Amyloid precursor protein
ATN	Anterodorsal thalamic nucleus
BVC	Boundary vector cell
CA1	Cornu ammonis 1
CA2	Cornu ammonis 2
CA3	Cornu ammonis 3
CAN	Continuous attractor network
CSD	Current source density
DG	Dentate gyrus
DTN	Dorsal tegmental nucleus
EC	Entorhinal cortex
EEG	Electroencephalogram
EM	Expectation maximization
FFT	Fast Fourier transform
fMRI	Functional magnetic resonance imaging
FTD	Frontotemporal dementia
GABA	γ-aminobutyric acid
HCN	Hyperpolarisation-activated cyclic nucleotide-gated (channels)
HD	Head direction
Ih	h-current
IP	Intraperitoneal

LEC	Lateral entorhinal cortex
LED	Light emitting diode
LFP	Local field potential
LMN	Lateral mammillary nuclei
MAPT	Microtubule associated protein tau
mAHP	Medium after-spike hyperpolarisation potential
mEC	Medial entorhinal cortex
mEC-SC	Medial entorhinal cortex stellate cell
MI	Modulation index
mPFC	Medial prefrontal cortex
MS-DBB	Medial septum diagonal band of Broca
MTL	Medial temporal lobe
NFT	Neurofibrillary tangle
NMDA	N-Methyl-D-aspartate
PAC	Phase-amplitude coupling
PaS	Parasubiculum
PBS	Phosphate buffered saline
PP	Perforant path
PrS	Presubiculum
PS1	Presenillin 1
PS1	Presenillin 2
PTX	Picrotoxin
PV+	Parvalbumin positive
S	Subiculum
SEM	Standard error of the mean
SC	Subcutaneous
TA	Temporoammonic
TLE	Temporal lobe epilepsy
TMI	Theta Modulation Index
VCO	Velocity controlled oscillator
VTS	Video tracking software
WT	Wild type

1. Introduction

The entorhinal cortex (EC) occupies a pivotal position in the medial temporal lobe (MTL), representing both the major input and output structure of the hippocampal formation (Amaral & Witter, 1989; Canto *et al.*, 2008). For this reason, the EC is ideally placed to control the flow of information across brain areas and contribute to memory processes.

This thesis will focus on the entorhinal cortex, specifically the medial entorhinal cortex (mEC) and the physiological changes that take place during dementia pathology. During this introduction, it would not be possible to discuss solely the role of the EC, without the giving due attention to rest of the hippocampal formation. However, where possible the emphasis will be given to the effect of, or influence on, the EC.

1.1 The Entorhinal cortex

1.1.1 Anatomy

The entorhinal cortex (EC), corresponding in humans to Brodmann area 28, is located partially enclosed within the rhinal sulcus, within the medial temporal lobe (MTL) and surrounded by a number of important cortical regions. The EC merges medially with structures of the hippocampal, or parahippocampal regions such as the parasubiculum, laterally with perirhinal cortex and posteriorly with the parahippocampal cortex (Canto *et al.*, 2008). It can be broadly divided into two distinct regions: the medial (mEC) and lateral (LEC) entorhinal cortices (see fig 1.1). These are separated not only by their anatomy but also by their neuronal firing patterns, with mEC cells most likely to show spatially modulated activity (Fyhn *et al.*, 2004) and lateral regions encoding non-spatial information such as objects (Deshmukh & Knierim, 2011; Wilson *et al.*, 2013) or olfactory stimuli (Igarashi *et al.*, 2014).

The EC forms a key part of the hippocampal formation, which in addition, contains the dentate gyrus (DG), the hippocampus proper (containing cornu ammonis 1 (CA1), CA2 and CA3 subregions), subiculum, presubiculum and parasubiculum

(Andersen, 2007). The EC is widely considered to provide both the major input and output to the hippocampus, making it a key interface in the hippocampal-cortical circuit (Canto *et al.*, 2008). The flow of information within the hippocampus is predominately unidirectional (fig 1.1) with clearly defined synapses between EC and DG (performant pathway); DG and CA3 (mossy fibre pathway); CA3 and CA1 (Schaffer collateral pathway); and CA1 and EC (temporoammonic pathway). This said, a large number of reciprocal connections exist, either intrinsically, for example within the CA3 region, or extrinsically with other cortical areas (Andersen, 2007).

As with other cortical regions, the EC, can be divided into 6 anatomical layers (I-VI). Layer I generally displays a sparsely populated neuronal population with a dense band of transversely orientated fibres. Layer II represents the outermost cell layer which predominantly project to dentate gyrus (DG) and CA3 region of the hippocampus (Witter, 2007). Layer III is a comparatively wide and loosely arranged area, consisting largely of pyramidal cells which project to the CA1 and subiculum (Witter *et al.*, 1988). Layer IV consists of small, cell-sparse layer below, often referred to as the lamina dissecans. Since layers II and III receive the majority of cortical inputs from a variety of areas (fig 1.1), they are therefore in the ideal place to control the flow of information into the hippocampus. In contrast, layers V and VI receives the majority of hippocampal output, arriving primarily from the CA1/subicular pathway. These deeper cortical layers also in turn form reciprocal connections with a variety of subcortical regions such as the thalamus, basal forebrain and striatum (Canto *et al.*, 2008).

Principle EC cells mainly utilise glutamate as their excitatory neurotransmitter and usually come in the form of pyramidal, or modified versions called stellate cells (in the mEC) or fan cells (in LEC). However, a large population of GABAergic interneurons can be seen in layers II and III EC that provide local inhibitory control. While principle stellate cells in layer II form projections to distinct brain areas, they show little or no connectivity with each other (Dhillon & Jones, 2000; Pastoll *et al.*, 2012; Couey *et al.*, 2013). Layer II stellate cells therefore rely on recurrent inhibition, specifically from parvalbumin-expressing (PV+) interneurons to provide local connectivity (Buetfering *et al.*, 2014). In contrast, intra-laminar projections between principle cells can be seen most extensively between layers III and V (Canto *et al.*, 2008).

1.1.2 Entorhinal cortex connectivity

All regions of the EC project, to some degree, to all regions of the hippocampal formation, terminating on both excitatory and inhibitory cells (Witter *et al.*, 1989). Projections to the DG and CA3, forming the perforant pathway (PP) generally arrive from layer II EC, however some have been shown to originate in deeper layers (Deller *et al.*, 1996). In the mEC, layer II contains two populations of principle excitatory neurons, which have recently also been shown to display different patterns of projection to the hippocampus. These consist of 'oceans' of Reelin-positive stellate cells that project into the dentate gyrus (DG) and CA3, surrounding hexagonally arranged clusters, or 'islands', of CalbindinD28K (Calbindin) positive pyramidal cells that project directly onto CA1 inhibitory neurons and weakly onto CA1 pyramidal cells (Kitamura *et al.*, 2014; Ray *et al.*, 2014). These populations are split, with approximately 60% stellate 'ocean' cells and 40% pyramidal 'islands'. Pyramidal islands are significantly more theta modulated than ocean cells, however although both are modulated by spatial location, islands are more tuned to locomotor activity (Sun *et al.*, 2015). In contrast, layer III cells, in both mEC and LEC, form projections into the distal dendrites of CA1 and subicular pyramidal neurons, traditionally referred to as the temporoammonic (TA) pathway (Witter *et al.*, 1988; Naber *et al.*, 2001; Aksoy-Aksel & Manahan-Vaughan, 2013). The predominant output of the hippocampus also occurs through this pathway, projecting back from CA1/subiculum, this time into layer V and VI of the EC (Canto *et al.*, 2008).

In addition to its hippocampal connectivity, the EC displays a wide array of reciprocal connections with other cortical and sub-cortical regions that generally show fairly diffuse patterns of innervation. For example, a large number of projections arrive into the mEC from the medial septum diagonal band of Broca (MS-DBB). These include long-range GABAergic neurons that synapse directly onto layer II interneurons (Melzer *et al.*, 2012; Gonzalez-Sulser *et al.*, 2014; Unal *et al.*, 2015) as well as cholinergic (Mitchell *et al.*, 1982; Vandecasteele *et al.*, 2014) and glutamatergic connections (Justus *et al.*, 2016). Ultimately, these provide only a small proportion of EC extrinsic connections and an exhaustive list

is not possible here (for a complete review of entorhinal connectivity see Kerr *et al.*, (2007)).

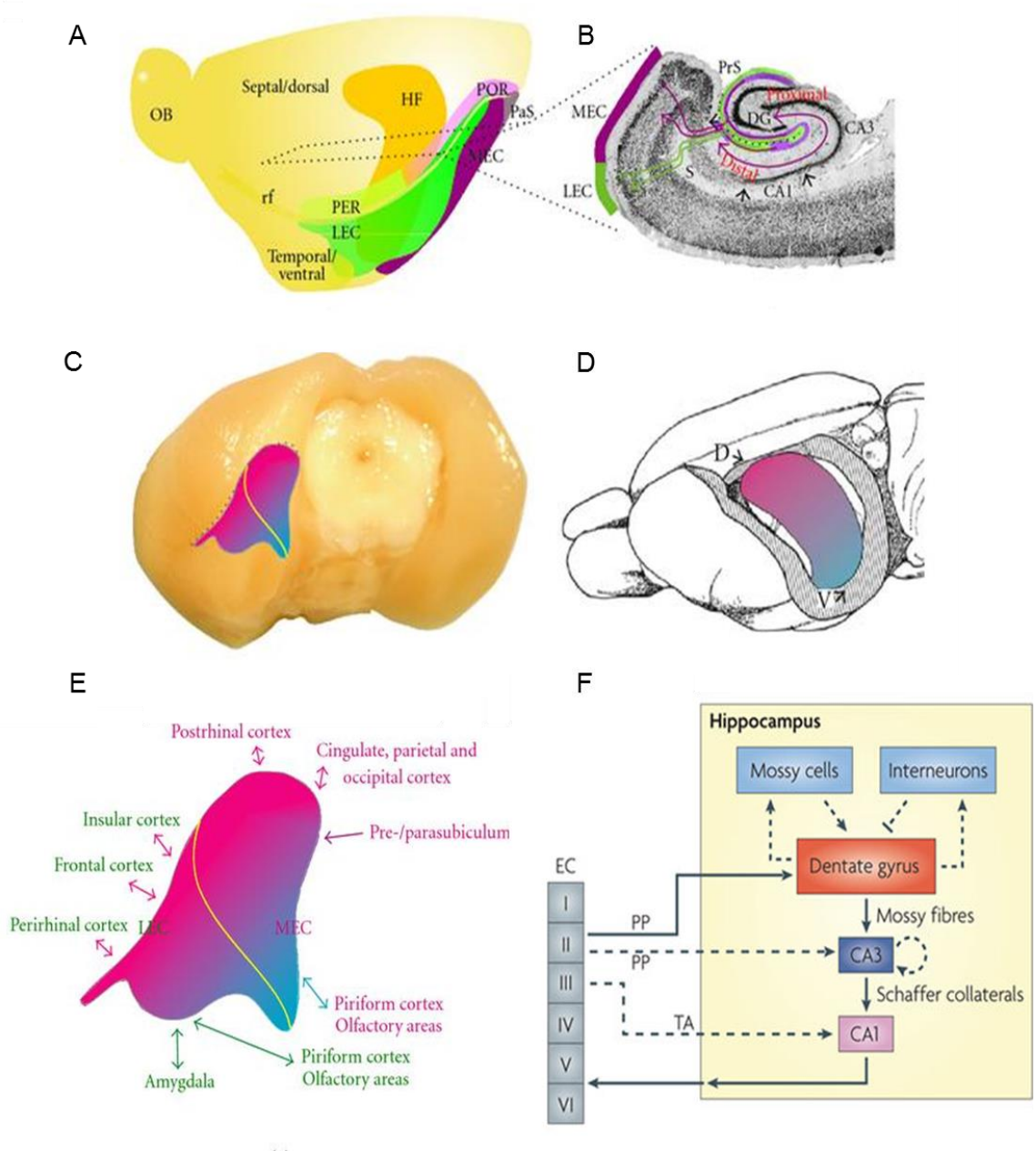

Figure 1.1: Anatomical organisation of the rodent entorhinal cortex. A) Position of entorhinal cortex (MEC: medial entorhinal cortex, LEC: lateral entorhinal cortex) in the sagittal and horizontal plane **(B)** relative to hippocampal sub regions (DG: dentate gyrus, CA1, CA3, s: subiculum). **C)** Topographical organisation of EC, showing dorso-ventral extent **(D),** with colours representing reciprocal connections from dorsal (magenta) and ventral (blue) hippocampal areas. **E)** Schematic of major EC connectivity, specified by area (LEC: green, to MEC: blue). Figure reproduced from (Canto et al., 2008). **F)** Schematic showing major connectivity in hippocampal formation. PP perforant pathway, TA: temporoammonic pathway (Obtained from Deng et al., 2010).

1.1.3 Role of the entorhinal cortex in memory

The hippocampus has long been implicated in the formation and storage of long-term memories for several key reasons. The first of these relies on the seminal studies on patient HM, showing that lesions of the hippocampus and surrounding cortex produce complete impairments in the formation of declarative memory (Scoville & Milner, 1957). The second major finding that has broadly influenced the understanding of the hippocampal formation has been the discovery of spatial encoding by cells in these areas (O'Keefe & Dostrovsky, 1971; Hafting *et al.*, 2005).

Lesions to the EC have been shown to produce memory impairments in both spatial and non-spatial tasks in rodents (Levisohn & Isacson, 1991; Steffenach *et al.*, 2005), non-human primates (Leonard *et al.*, 1995; Buckmaster *et al.*, 2004) and humans (Scoville & Milner, 1957; Abrahams *et al.*, 1997; Schwarcz & Witter, 2002; Jacobs *et al.*, 2016). The encoding of spatial information, specifically relating to mEC function, will be discussed at length below; however, it is likely that the same mechanisms involved in declarative memory are those used for the formation of spatial memories in the hippocampal formation (Buzsáki & Moser, 2013).

1.2 Neuronal oscillations

The process of performing complex tasks, such as memory, requires the coordination of large numbers of individual neurons. The integration of such important information streams requires activity to arrive during a precise temporal window. Hence, neuronal oscillations are an emergent property of neuronal networks (Buzsáki & Draguhn, 2004). This synchrony of neuronal firing ultimately allows for the temporal binding of cell assemblies, potentially allowing for the processing, transfer and storage of information across distributed networks of neurons (Varela *et al.*, 2001; Engel *et al.*, 2001; Buzsáki, 2006). Oscillatory activity in neuronal networks is therefore likely to act as a bridge between the firing of individual neurons and behavioural output (Engel *et al.*, 2001; Buzsáki & Draguhn, 2004; Hasselmo, 2005).

1.2.1 Oscillatory frequency bands

Oscillatory activity can be observed using a number of recording techniques, most notable through either the human electroencephalogram (EEG), first described by Berger, (1929), or the local field potential (LFP) that can be observed from depth electrodes inserted directly into brain tissue (Buzsáki *et al.*, 2012). Neuronal oscillations can cover a wide range of potential frequencies which have been commonly characterised into several frequency bands associated with differing cognitive states, however these classifications can be somewhat arbitrary (Engel *et al.*, 2001; Buzsáki & Draguhn, 2004). Generally however, increases across frequency bands show a linear progression on a logarithmic scale. Neighbouring frequencies are associated with independent cognitive states, whilst those further apart may interact, or at least coexist, with each other (Buzsáki & Draguhn, 2004; Canolty *et al.*, 2006; Colgin *et al.*, 2009; Oke *et al.*, 2010).

The first of such frequency bands to be described in the human was termed alpha activity (7.5-12.5 Hz), found predominantly above the occipital cortex during periods of eyes-closed, but representing the dominant frequency across the EEG (Klimesch, 1999). This was subsequently followed by beta (13–30 Hz), delta (1–4 Hz), theta (4–8 Hz), and gamma (30–70 Hz) frequency bands (Niedermeyer & Lopes da Silva, 2005). Precise frequencies can vary according to factors such as age, cognitive state and importantly for this thesis, species. From here, particular focus will concern neuronal oscillations in the rodent, specifically hippocampal formation, and for this reason the majority of studies will concern the LFP, recorded using depth electrodes.

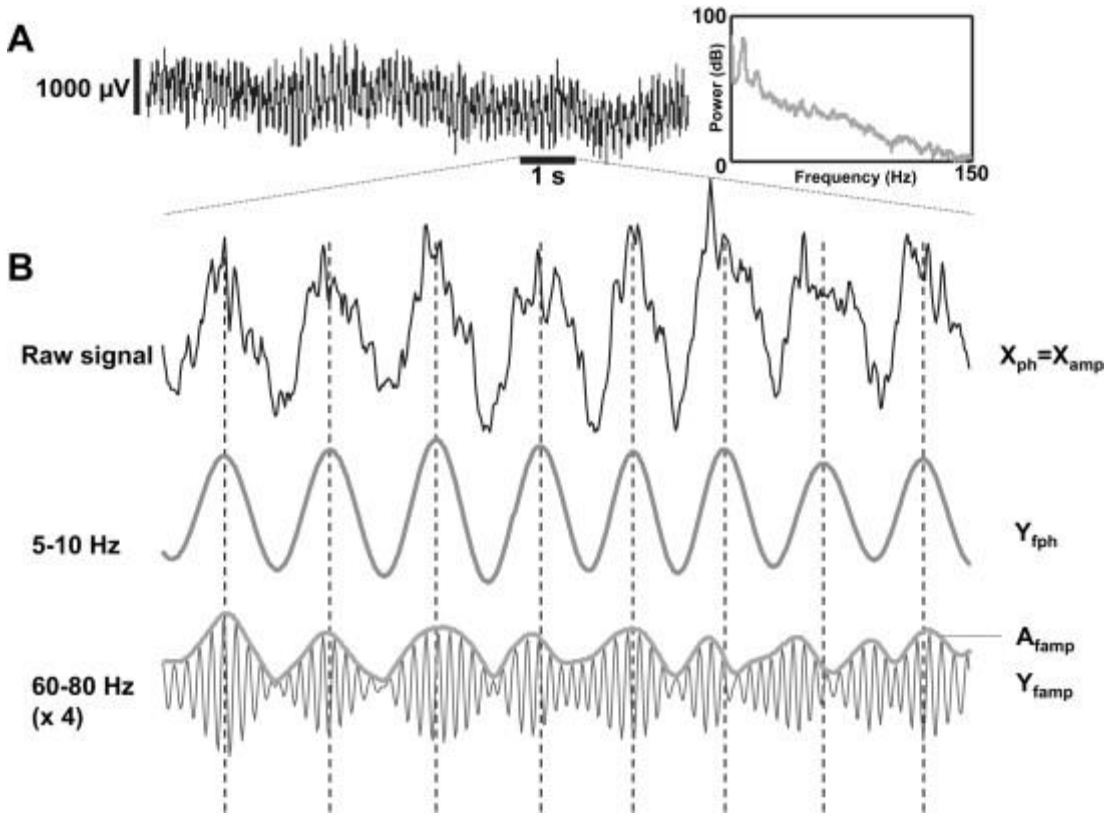

Figure 1.2: Local field potential activity in rodent hippocampus. A) Raw trace recorded from CA1 region of hippocampus, with associated power spectrum. B) Raw signal from 1 second epoch, filtered in the theta and gamma frequency bands below. Note relationship between gamma oscillation amplitude and theta phase, whereby gamma activity is largest on theta peaks. Reproduced from Onslow et al., (2011).

1.2.2 Theta oscillations in the hippocampal formation

In rodents, theta oscillations (8-12 Hz) represent the dominant frequency in the LFP and signify the 'on-line' state of the hippocampal formation (Buzsáki, 2002). Theta oscillations depend heavily on the animal's behavioural state and are predominately observed during periods of voluntary locomotor activity, such as exploration or goal-directed movement (Vanderwolf, 1969), or during REM sleep (Sullivan *et al.*, 2014).

Theta oscillations are likely to be involved in binding anatomically distinct cell networks, since their slow wavelength (100-200 ms wide) can accommodate relatively long conduction delays (Colgin & Moser, 2010). For example, coherence in the theta frequency range can be observed between the hippocampus and medial prefrontal cortex (mPFC) during working memory tasks,

with the phase-locking of principle cells in the mPFC to hippocampal theta rhythm strongly predictive of behavioural output (Hyman *et al.*, 2005; Jones *et al.*, 2005).

Principle neurons in the hippocampal formation show theta frequency resonance (Leung & Yu, 1998; Pastoll *et al.*, 2012) and intrinsic subthreshold oscillations (Hasselmo *et al.*, 2007; Giocomo *et al.*, 2007), with isolated, but intact, hippocampi able to generate theta oscillations independently *in vitro* (Forsyth *et al.*, 2012). However, global theta oscillations are most likely generated by pacemaker cells in basal forebrain areas, specifically the medial septum diagonal band of broca (MS-DBB). Long range glutamatergic, cholinergic and GABAergic projections arrive from septal areas directly into both hippocampus and entorhinal cortex (Melzer *et al.*, 2012; Gonzalez-Sulser *et al.*, 2014; Vandecasteele *et al.*, 2014; Fuhrmann *et al.*, 2015; Fuchs *et al.*, 2015; Kondo & Zaborszky, 2016; Justus *et al.*, 2016). Fast spiking GABAergic projections in particular are most likely to entrain networks to theta frequencies (Hangya *et al.*, 2009; Melzer *et al.*, 2012). Impairments to the medial septum have been shown to abolish theta activity across the hippocampal formation (Mitchell *et al.*, 1982; Lee *et al.*, 1994) and lead to impairments in spatial memory (Winson, 1978; Mitchell & Ranck, 1980; Brioni *et al.*, 1990).

1.2.3 Gamma oscillations in cognition

Gamma oscillations consist of fast network activity in the range of 30-120 Hz and represent the second major class of synchronised activity in the hippocampal formation (Colgin & Moser, 2010). Gamma activity is largest when nested within the theta rhythm and although generated independently, these oscillatory frequencies are highly concurrent (Jensen & Colgin, 2007). This activity has been widely linked to cognitive events, with a number of studies supporting the idea that gamma oscillations may facilitate effective memory encoding and retrieval. For example, in humans, hippocampal gamma oscillation amplitude predicts the encoding of new verbal memories, with only successful trials associated with increased gamma power and synchronisation (Fell *et al.*, 2001; Sederberg *et al.*, 2006). Similar increases in gamma amplitude and coherence can be seen in the rodent hippocampal formation, with peak increases visible around decision points on T-maze tasks (Montgomery & Buzsáki, 2007; Tort *et al.*, 2008).

Gamma oscillations span a relatively wide frequency range, however, they can be further divided into slow (30-50 Hz) and fast (60-120 Hz) components which can be observed independently in the CA1 hippocampus on different phases of the theta rhythm (Colgin *et al.*, 2009). These differing frequency bands are likely to represent the routing of information across the hippocampal formation. Fast gamma oscillations are thought to arise from projections from the EC (Chrobak & Buzsaki, 1998; Colgin et al., 2009). This is consistent with the current source density (CSD) profiles of hippocampal gamma oscillations that resemble those evoked by medial perforant path stimulation (Bragin et al., 1995). In contrast, slow gamma frequencies are more likely generated in the CA3 region (Colgin et al., 2009) and projected through the Schaffer collateral pathway to CA1.

1.2.4 Coupling of oscillatory frequency bands

The relationship between theta oscillation phase and gamma oscillation amplitude is perhaps the most explored example of phase amplitude coupling (PAC). This inter-locking of oscillatory frequencies may allow for assemblies of neurons that are co-active on short timescales, such as over gamma frequencies, to be temporally 'bound' across longer timescales and anatomical distances (Jensen & Colgin, 2007). While theta oscillations may act to bind neuronal ensembles, the fast timing of gamma oscillations makes them an ideal candidate for encoding information. The precise firing of pre- and post-synaptic cells on consecutive gamma cycles is therefore likely to be sufficient for spike-timing-dependent plasticity (Bi & Poo, 1998).

The extent of theta-gamma coupling has been shown to be a strong correlative of cognitive output in both humans and rodent models (Fell *et al.*, 2001; Montgomery & Buzsáki, 2007; Tort *et al.*, 2008; Shirvalkar *et al.*, 2010). The co-modulation of these frequencies may even allow for the representation of several cognitive events in sequential manner (fig 1.3), with ensembles of neurons encoding for individual memories and firing consistently on the same gamma cycle (Jensen & Lisman, 1998). The limited number of gamma cycles found locked to theta rhythms (suggested to be 7±2 oscillatory cycles) has been proposed to reflect that of the limited capacity of humans to retain short term memories (Lisman & Idiart, 1995).

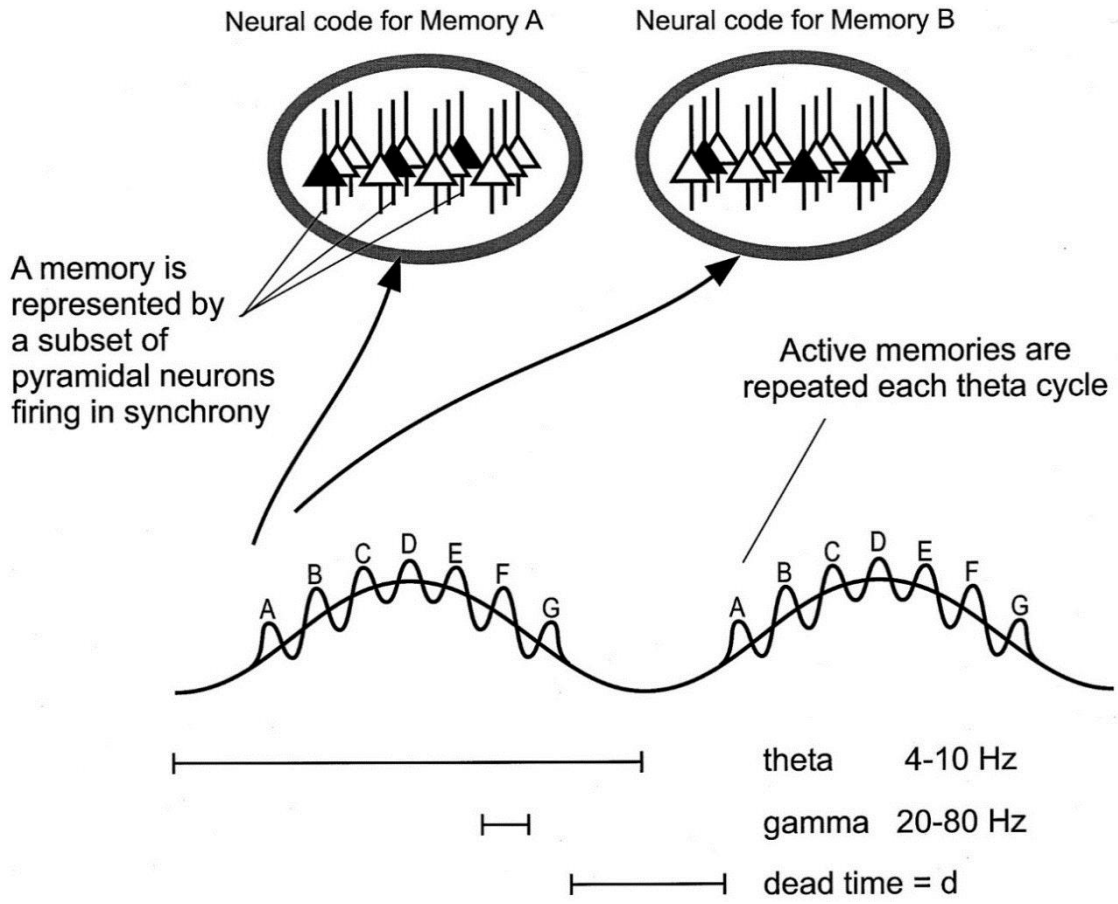

Figure 1.3 Theta-gamma interactions for encoding information temporal sequences. Reproduced from Jensen & Lisman, (1998)**.**

1.2.5 Recording neuronal ensembles

Over the previous decades, significant advances have been made in the ability to record neuronal ensembles in both human and animal models. Such extracellular recording techniques vary in their ability to distinguish sizes of neuronal population ranging from low impedance EEG electrodes placed directly onto scalp, to those designed for LFP and single-unit identification (Buzsáki, 2004).

Most notably, the ability of researchers to distinguish single neurons simultaneously has increased exponentially. Initially these recordings would have been achieved with single metal electrodes (Hubel, 1957). However, in regions with high neuronal density, there are many neurons in close enough proximity for extracellular 'spikes' to be observed at one time. In this situation, single units can

therefore only be isolated by moving the electrode tip extremely close to the cell body. The use of multi-electrode recording arrays, through the use of sterotrode (McNaughton *et al.*, 1983*b*) or tetrode (O'Keefe & Recce, 1993; Gray *et al.*, 1995; Jog *et al.*, 2002) recording subsequently allowed for the simultaneous isolation of several units, based on the principle that the relative amplitude of the recorded spike is proportional to the relative distance between neuron and electrode. This allows for the triangulation of signals, since anatomically separate cells will produce easily distinguishable spike patterns across recording electrode arrays (Gray *et al.*, 1995; Jog *et al.*, 2002; Buzsáki, 2004).

Recently, there have been significant innovations concerning the development of high density silicon probe electrode arrays that can allow for the recording of many hundreds of channels through commercially available acquisition systems (Berényi *et al.*, 2014; Buzsáki *et al.*, 2015). With these advances, the automated clustering of recorded spikes has become ever more important due to the difficultly in scaling-up traditional low-throughput recording and sorting methods (Kadir *et al.*, 2014; Rossant *et al.*, 2016). Silicon probe technology has also allowed for the precise arrangement of recording electrodes over small spatial scales, making it possible to record simultaneous activity across well-defined regions. Additionally, electrode shanks occupy a much smaller anatomical volume than wire electrodes, allowing for decreased tissue damage and hence more stable, long term recordings (Buzsáki *et al.*, 2015; Okun *et al.*, 2016).

Ultimately, while recording neuronal activity in its entirety, whilst not affecting normal brain activity, is unreasonable expectation, recording electrophysiological data from a statistically representative populations in a given brain area is an achievable goal (Buzsáki, 2004).

1.3 Encoding spatial information

1.3.1 Path integration

It is clear that one of the primary roles of the hippocampal formation is to facilitate spatial information processing. By integrating linear and angular motion cues, it can encode relative spatial information, without reference to the environment, meaning that it is in a prime position to perform path integration (McNaughton *et al.*, 2006). Path integration can be defined as the ability to keep a continuous updated record of an animal's current location using only an initial reference and self-motion information. The idea of an inertial-based navigational system, or "dead reckoning", dates back to Charles Darwin (Darwin, 1873), who noticed that most animals can use cues based only on their self-motion to keep track of their current location. This has been shown to appear in a wide variety of species across the animal kingdom (Etienne & Jeffery, 2004); however was not shown experimentally in mammals for many years (Barlow, 1964; Mittelstaedt & Mittelstaedt, 1980).

In recent years, a number of spatially selective cell types have been discovered in the network of neuronal structures thought to be important for path integration in mammals. These cells, many of which were proposed theoretically before their eventual discovery, are thought to provide the neuronal basis for path integration and spatial navigation in general, combining to form a 'cognitive map' of space (O'Keefe & Nadel, 1978; McNaughton *et al.*, 2006).

1.3.2 Place cells in the hippocampus

For many years, the hippocampus has been widely regarded as the centre for the encoding of memories, particularly those of a spatial nature. Since their discovery by O'Keefe & Dostrovsky, (1971), 'place cells' have generally been considered to be a key element for spatial information processing (O'Keefe & Nadel, 1978; McNaughton *et al.*, 1996; Leutgeb *et al.*, 2005*b*). Inspired by the work of Tolman, (1948), they were suggested to be the basic component of the 'cognitive map' of space (O'Keefe & Nadel, 1978). Place cells represent a large fraction of principle cells in the hippocampus that are activate only when the animal occupies a specific location or 'place field', with neighbouring cells firing

at different locations and therefore covering the entire local environment (fig 1.4B) (O'Keefe, 1976; Wilson & McNaughton, 1993). All hippocampal regions display place field firing patterns, but field are most distinct in the CA1 region (Barnes *et al.*, 1990). In novel environments, the same place cells are active, however they 'remap' between setting, giving distinct firing fields for each new environment (Muller & Kubie, 1987).

The precise position of place fields has been shown to be highly dependent on environmental cues (O'Keefe & Conway, 1978). However, hippocampal neurons may also be triggered by other, non-spatial, stimuli (Young *et al.*, 1994) or related to behavioural or cognitive events (Wood *et al.*, 1999). There is also evidence to suggest that place cells can simultaneously represent information relating to space and non-spatial, episodic memory-like information, by maintaining firing field locations, but encoding context with changes in firing rate (Leutgeb *et al.*, 2005*a*).

Ultimately, the firing of place cells in the hippocampus allows for temporal coding, with cell assemblies activated in sequences across environments (Harris *et al.*, 2003; Huxter *et al.*, 2003). One of the most well characterised examples of temporal coding can be seen through the expression of theta phase precession, the tendency for place cells to fire progressively earlier in the theta cycle with each traversal of the their place fields (O'Keefe & Recce, 1993; Harris *et al.*, 2003; Huxter *et al.*, 2003). The implication of this would be that when an animal runs through multiple firing fields in sequence, the firing of neighbouring place cells will be replicated over an accelerated time-frame (Skaggs *et al.*, 1996; Dragoi *et al.*, 2006), potentially allowing for Hebbian plasticity (Hebb, 1949). The re-activation of place cell ensembles can also be seen in the re-play of hippocampal firing patterns, which presumably allow for the off-line consolidation of hippocampal memory during sleep (Wilson & McNaughton, 1994; Lee *et al.*, 2002) and quiet wakefulness (Karlsson & Frank, 2009). Inhibiting such interactions will therefore have profound implications for spatial memory processes (Ego-Stengel & Wilson, 2009; Girardeau *et al.*, 2009; Jadhav *et al.*, 2012).

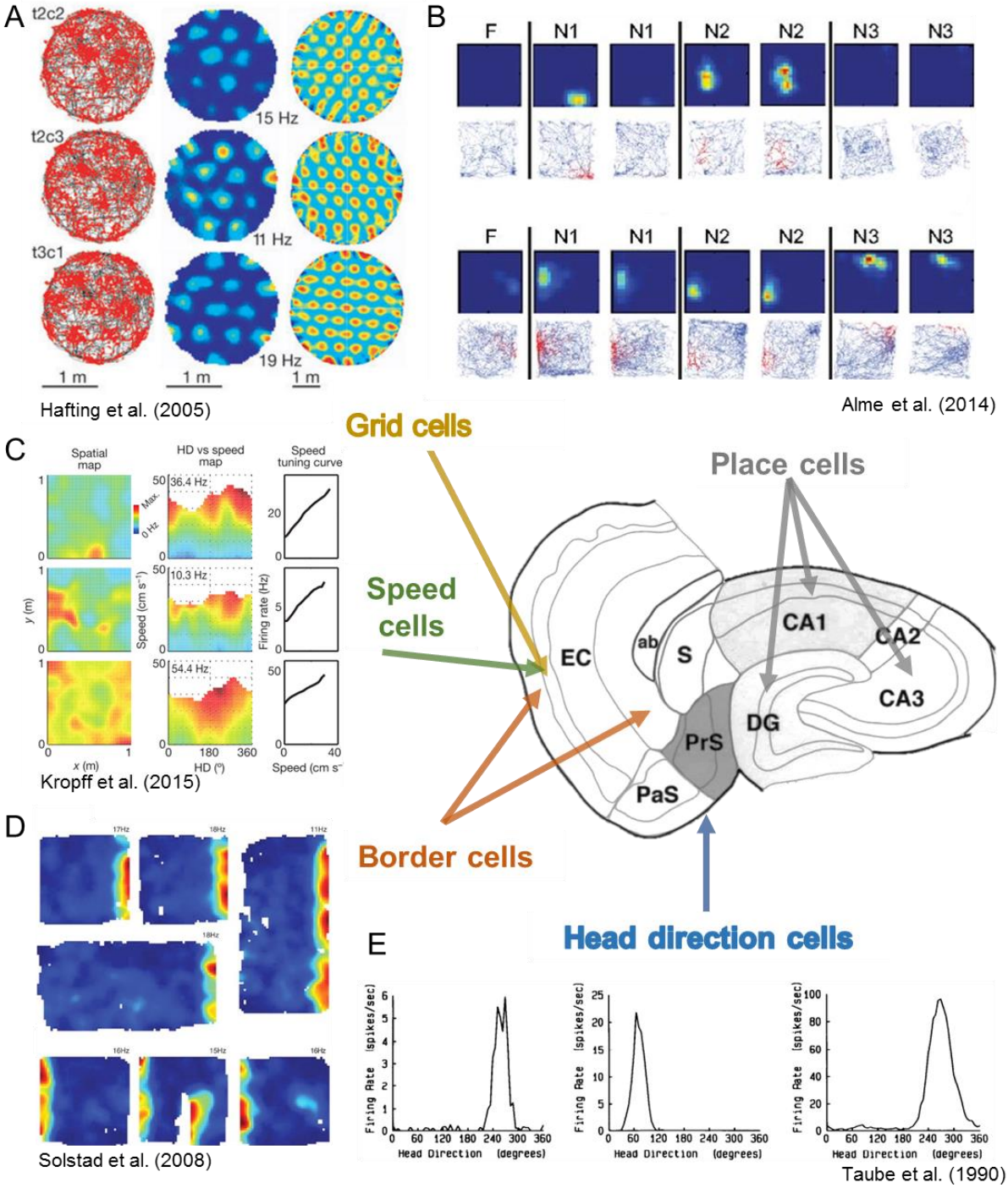

Figure 1.4 Spatially selective cell types in the hippocampal formation. Schematic of hippocampal formation showing hippocampus (CA1, CA3, DG: dentate gyrus), entorhinal cortex (EC) and subiculum (S: subiculum, PrS: presubiculum, PaS: parasubiculum. **A)** Grid cells fire in hexagonal lattice pattern across environment. Black line represents running path and red dots action potentials of single mEC unit. Firing rate maps (middle), with peak firing rate and 2D spatial autocorrelation (right) (adapted from Hafting et al., (2005). **B)** Pace cells in the hippocampus across familiar (F) and 3 novel environments (N) showing consistent spatial remapping (adapted from Alme et al., (2014). **C)** Speed cells, whose firing is entirely dependent on animals running speed (adapter from Kropff et al., (2015). **D)** Head–direction cells, with firing rate dependent on animals direction (adapted from (Taube et al., 1990a).

1.3.3 Grid cells in the mEC

Initial recordings from parahippocampal structures, including the mEC, showed firing patterns that were only weakly modulated by spatial location (Barnes *et al.*, 1990; Quirk *et al.*, 1992; Burwell *et al.*, 1998; Frank *et al.*, 2000; Burwell & Hafeman, 2003; Cohen *et al.*, 2013). The disparity between weak spatial signals from hippocampal projections and strongly spatially modulated hippocampal output suggested, at the time, that the hippocampal circuitry was responsible for the computation of allocentric location (Barnes *et al.*, 1990; Quirk *et al.*, 1992). Importantly however, these original recordings took place in the intermediate or ventral portions of the mEC and when re-examined by Fyhn *et al.*, (2004), neurons in the dorsal mEC showed clear spatial firing, with multiple fields across space. The expansion of previously small recording environments finally revealed a striking tessellating triangular grid extending across the entire arena, named 'grid cells' (Hafting *et al.*, 2005) (fig 1.4A). This hexagonal lattice pattern was shown to be tied to, but not dependent on, spatial cues and persistent during periods of darkness. Grid cell firing has subsequently been described in a variety of other species, including mice (Fyhn *et al.*, 2008; Giocomo *et al.*, 2011*a*; Buetfering *et al.*, 2014), bats (Yartsev *et al.*, 2011; Yartsev & Ulanovsky, 2013) and humans (Doeller *et al.*, 2010; Jacobs *et al.*, 2013).

Grid cells recorded from close anatomical areas show a remarkable similarity in both their field spacing and orientation, however neighbouring cells are offset relative to each other, meaning that all aspects of the environment are covered by the local grid network (fig 1.5) (Hafting *et al.*, 2005; Sargolini *et al.*, 2006; Stensola *et al.*, 2012). While local modules of grid cells display high levels of similarity, a clear topographical organisation of grid cell firing can be seen along the dorso-ventral axis of the mEC, with grid fields becoming progressively larger and more spaced from dorsal to ventral (Hafting *et al.*, 2005; Brun *et al.*, 2008*b*; Stensola *et al.*, 2012). Grid cell patterns are expressed instantly in novel environments and their properties stable across multiple recordings (Hafting *et al.*, 2005). Unlike hippocampal place cells, which remap upon new environmental exposure, grid cells remain consistent and universal, retaining their scale, orientation and phase relationships in all environments. This suggests that grid cells act as a metric for space that can be used in path-integration based processing (Moser *et al.*, 2008).

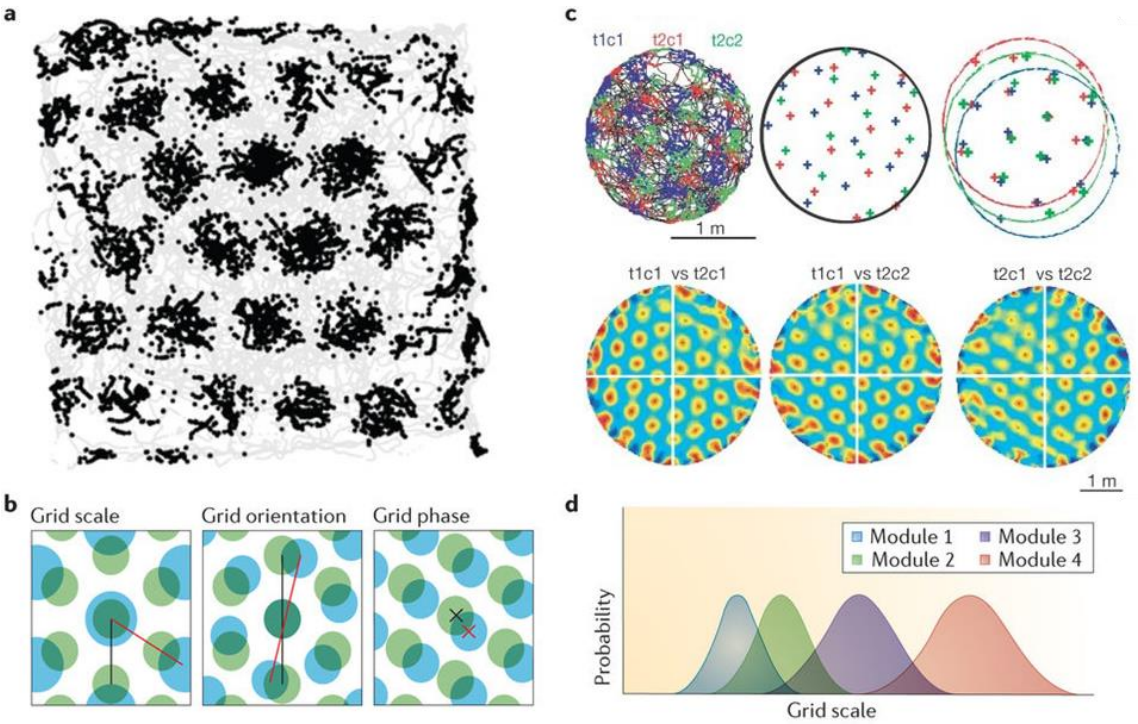

Figure 1.5: Basic grid cell properties. A) Example grid cell firing pattern, grey line: running path of animal, black dots: firing locations for individual mEC neuron. **B)** Schematic to show grid cell properties, grid scale: size of firing field, grid orientation: alignment of grid fields, relative to local environment, grid phase: x-y location of firing fields. **C)** Overlapping firing fields from 3 grid cells recorded from same location, grid scale and orientation remain constant, but all have different grid phase (adapted from Hafting et al., (2005). **D)** Schematic showing overlapping grid cell modules from one animal with increasing grid scale. **A,B** and **D** adapted from Moser et al., (2014).

1.3.4 Border cells

A further spatial cell type was subsequently found to be present in the mEC, namely the border, or boundary vector cell (BVC) (Solstad *et al.*, 2008), which was shown to fire only directly adjacent to, or a set distance from, environmental boundaries (fig 1.4D). These cells, also discovered in parallel in the subliculum (Lever *et al.*, 2009), had previously been predicted by computational models of place cell formation, since stretching familiar environments produced elongation of firing fields along the same axis (O'Keefe & Burgess, 1996). BVCs, that give information regarding the relative distance from each wall, could therefore be sufficient to allow for specific place fields (O'Keefe & Burgess, 1996; Barry *et al.*, 2006; Lever *et al.*, 2009). In the mEC, border cells form only a small population of spatially modulated units, with reports varying between 3-10% (Solstad *et al.*,

2008; Zhang *et al.*, 2013; Kropff *et al.*, 2015); however, this proportion appears to be larger in subicular regions (~25%) (Lever *et al.*, 2009). This suggests, along with some underlying anatomical evidence (Kloosterman *et al.*, 2004; Witter, 2006), a directionality in boundary vector signalling, from subiculum to hippocampus via mEC, in contrast to the more classical view of the subiculum providing hippocampal output.

1.3.5 Encoding head direction

Head direction cells are defined as neurons that show firing rates highly dependent on an animal's direction heading within the environment. First discovered in the rat pre- and postsubiculum (Ranck, 1984; Taube *et al.*, 1990*a*), firing patterns are generally characterised by extremely low baseline firing rates, with peak firing reach as high as 100 Hz in a preferred directional range consisting on average of around 90° (Taube *et al.*, 1990*a*). Each head direction cell is tuned to a single direction, with all orientations equally represented across the population. The preferred firing direction of head direction cells can depend on a variety of allothetic cues, usually consisting of prominent visual landmarks (Taube *et al.*, 1990*b*). The rotation of such cues usually results in a corresponding rotation of preferred firing (Taube *et al.*, 1990*b*; Taube, 1995). However, once established, turning off lights or removing visual cues will not change a cells directional tuning, although the firing maps may drift over time (Taube *et al.*, 1990*b*; Goodridge *et al.*, 1998).

A wealth of electrophysiological and lesion studies have ultimately led to the proposal of an almost complete anatomical pathway carrying head direction information from vestibular centres to thalamic nuclei and into the hippocampal formation (fig 1.6, for comprehensive review see Taube, (2007)). Head direction cells have subsequently described in a number of other regions including the mEC (Sargolini *et al.*, 2006; Giocomo *et al.*, 2014), hippocampus (Leutgeb *et al.*, 2000) and retrosplenial cortex (Chen *et al.*, 1994; Cho & Sharp, 2001), as well as several thalamic nuclei, most notably the anterodorsal thalamic nuclei (ATN) (Taube, 1995; Shinder & Taube, 2011; Jankowski *et al.*, 2014). They have been suggested to originate from deep, subcortical structures, with dorsal tegmental nucleus (DTN) (Sharp *et al.*, 2001) and lateral mammillary nuclei (LMN)

(Stackman & Taube, 1998; Blair *et al.*, 2007) integrating vestibular information (Taube, 2007).

A significant proportion of cells tuned to head direction can be found in the mEC, both as a distinct population and in cells with conjunctive grid-head direction properties (Sargolini *et al.*, 2006). Conjunctive cells are more commonly found in deeper mEC layers, specifically layer V, where the mEC receives cortical inputs, rather than in the output from layer II, where grid cells are rarely conjunctive (Sargolini *et al.*, 2006).

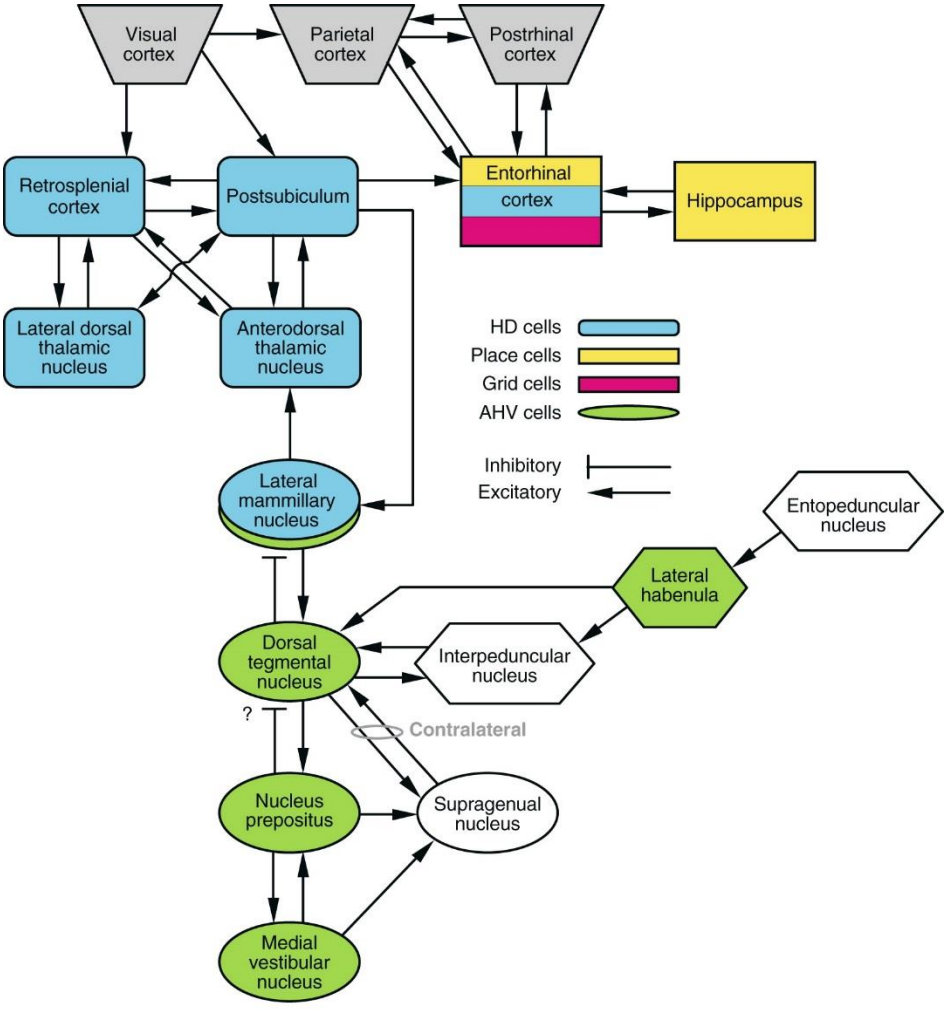

Figure 1.6: Proposed head direction cell circuit. HD: head direction, AHV: angular head velocity. Reproduced from Taube, (2007)

1.3.6 Encoding running speed

Since some of the earliest reports of hippocampal activity, it has been known that the properties of theta oscillations (8-12 Hz), the dominant frequency band, are highly dependent on locomotor activity, with faster running speeds associated with faster and larger amplitude oscillations (Vanderwolf, 1969; Whishaw & Vanderwolf, 1973; McFarland *et al.*, 1975; Sławińska & Kasicki, 1998). Subsequently, a comparable relationship was found for gamma oscillation properties, which similarly increase their magnitude linearly with increases in running speed (Chen *et al.*, 2011) and also modulate their frequency in both slow (30-50 Hz) and fast (60-129 Hz) gamma frequency bands (Zheng *et al.*, 2015).

However, it was not until very recently that a specific population of speed-encoding cells were found to be present in the mEC (Kropff *et al.*, 2015). The existence of such cells were long since postulated, since continuous updating of movement is thought to be necessary for the path integration based representation of space (Fuhs & Touretzky, 2006; McNaughton *et al.*, 2006; Burgess *et al.*, 2007; Burak *et al.*, 2009; Bush & Burgess, 2014). mEC speed cells form an independent population of neurons whose activity is entirely dependent on an animals current speed, rather than acceleration, and are independent of grid, border or head direction firing. There is still however a general tendency of all mEC neurons, specifically grid cells, to be modulated by running speed (Sargolini *et al.*, 2006), with reports of as many as 80% of mEC cells dependant to some degree of locomotive activity (Hinman *et al.*, 2016). There is further evidence to suggest that in layer II mEC, while grid cells occur equally in entorhinal islands (pyramidal cells) and oceans (stellate cells), speed modulated cells are more likely to be from the pyramidal island population (Sun *et al.*, 2015), therefore projecting primarily onto CA1 interneurons, rather than to the dentate gyrus (Kitamura *et al.*, 2014; Ray *et al.*, 2014).

Speed correlated input into the mEC has been postulated to arrive from glutamatergic projections from the medial septum and diagonal band of Broca (MSDB) (Justus *et al.*, 2016). In the hippocampus, these VGluT2^{+} neurons are likely to mediate the transition between locomotive states, controlling the initiation and speed of movement as well as its entrainment to theta (Fuhrmann *et al.*, 2015). Long range GABAergic and cholinergic projections also enter mEC and hippocampus from basal forebrain areas (Colom, 2006; Gonzalez-Sulser *et al.*,

2014; Vandecasteele *et al.*, 2014), which may also be relevant for modulating speed-correlated outputs.

One of the most interesting features of running speed representation is that its precise relationship with locomotion appears not to be fixed. Features such as slope and intercept can be modulated by external factors such as environmental novelty (Jeewajee *et al.*, 2008*b*) or pharmacological manipulations (Jacobson *et al.*, 2013; Wells *et al.*, 2013; Newman *et al.*, 2013). Cholinergic inputs in particular are also likely to play a modulatory role in representing locomotor information. Modulating cholinergic transmission alters slope of running speed-theta oscillation relationships in the hippocampal formation (Newman *et al.*, 2013, 2014). These fibres also potentially underlie context-specific changes to theta frequency-running speed slope, for example during periods of environmental novelty (Jeewajee *et al.*, 2008*a*, 2008*b*), which may have implications on the grid field expansion observed under these conditions (Barry *et al.*, 2012*a*, 2012*b*).

1.3.7 Theoretical models of grid cell firing patterns

The origin of grid cell firing patterns is a topic that has been widely debated and explored through mathematical modelling. Grid cell models can be broadly split into two classifications, those produced by oscillatory interference (O'Keefe & Burgess, 2005; Burgess *et al.*, 2007; Hasselmo *et al.*, 2007; Jeewajee *et al.*, 2008*a*), and those produced by continuous attractor networks (CANs) (Fuhs & Touretzky, 2006; Burak *et al.*, 2009; Navratilova *et al.*, 2012; Yoon *et al.*, 2013; Shipston-Sharman *et al.*, 2016), although the precise physiological mechanism may involve both strategies (Bush & Burgess, 2014). Oscillatory interference models use the interference pattern generated by several oscillators, with frequencies either relatively constant, or dependent on the speed and direction of motion. In contrast, attractor networks are produced by patterns of activity that are moved, also in a speed/direction dependant manner, across a network of neurons that are recurrently connected and periodically active (Giocomo *et al.*, 2011*b*).

The majority of models therefore work on the basis of the mEC as a path-integrator, combining both speed and directional inputs from specialized cells; however their mechanisms are significantly different (Moser *et al.*, 2008). A

detailed commentary on the benefits and weakness of each grid model is beyond the scope of this introduction and will not be present here, for reviews see (McNaughton *et al.*, 2006; Giocomo *et al.*, 2011*b*; Zilli, 2012).

1.3.8 Relationship between place and grid cell firing

Since their discovery, grid cells have been suggested to have implications for the formation of hippocampal place fields (O'Keefe & Burgess, 2005). This hypothesis can be easily formed, based on the anatomical connectivity between the two regions (Canto *et al.*, 2008) and the ability of CA1 place cells to maintain their spatial selectivity in the absence of CA3 inputs (McNaughton *et al.*, 1989; Brun *et al.*, 2002). Perhaps the most obvious explanation for producing place fields from grids is that of simple summation, with the idea that relatively small numbers of grid fields can form single place fields based on the linear summation of appropriately weighted synaptic inputs (Solstad *et al.*, 2006).

More recently however, there has been a growing body of evidence to suggest that this may not be the case. Firstly, place cell firing can be observed in the hippocampus in the absence of mEC inputs (Brun *et al.*, 2008*a*; Van Cauter *et al.*, 2008; Hales *et al.*, 2014), albeit with larger and more dispersed firing fields. In contrast, grid cell periodicity is completely degraded after the removal of hippocampal projections to the mEC (Bonnevie *et al.*, 2013). While inactivating the medial septum is capable of abolishing grid cell firing patterns, this has only minor effects on the spatial properties of place cells (Koenig *et al.*, 2011).

In development, place cell firing can be seen before the emergence of grid patterns (Langston *et al.*, 2010; Wills *et al.*, 2010). While place cells appear earlier in development and mature over time, grid cells develop abruptly, immediately showing adult-like firing properties (Wills *et al.*, 2012; Muessig *et al.*, 2015). In contrast, boundary vector cells (Bjerknes *et al.*, 2014) and head direction cells (Langston *et al.*, 2010; Wills *et al.*, 2010; Bjerknes *et al.*, 2014) are present in the mEC from the earliest time periods able to be recorded. Furthermore, in adult rats, while cells that display grid patterns have been shown to project directly to the hippocampus, other cell types, such as border and head direction cells also make these direct projections (Zhang *et al.*, 2013). This suggests evidence for the BVC model of place cell generation, based on cortical inputs that signal

environmental boundaries (O'Keefe & Burgess, 1996; Barry *et al.*, 2006; Hartley & Lever, 2014).

Ultimately, both the mEC and hippocampus are likely to rely on reciprocal connections (Naber *et al.*, 2001; Zhang *et al.*, 2013), whether direct or indirect, to produce functional spatial firing. While place cells are present in the absence of the mEC, their spatial firing is undoubtably impaired (Brun *et al.*, 2008*a*; Van Cauter *et al.*, 2008; Hales *et al.*, 2014), suggesting that the mEC is essential for place cell stability and fine tuning of place fields.

1.3.9 Dependencies for grid cell periodicity

In support of much of the mathematical modelling of grid cell formation there are several studies that clearly show factors necessary for grid cell firing. Antagonising projections from the medial septum, the region responsible for both speed and theta modulation of mEC activity, produces a complete breakdown of grid cell periodicity (Koenig et al., 2011; Brandon et al., 2011). The same effect can be seen though inhibition of the anterior thalamic nuclei, a key component of the head-direction pathway (Winter et al., 2015) and through blocking reciprocal connections from the CA1 region of the hippocampus (Hafting *et al.*, 2008; Bonnevie *et al.*, 2013). Interestingly, this is not necessarily the case for other forms of spatial firing. For example, the absence of septal or hippocampal inputs has no effect on head-direction tuning (Koenig *et al.*, 2011; Brandon *et al.*, 2011; Bonnevie *et al.*, 2013), which in some cases may show an increased representation under these conditions (Bonnevie *et al.*, 2013).

Taken together these data suggest that grid cells are dependent on a fully functional spatial information system to effectively integrate information and produce precise hexagonal firing patterns. This further suggests that grid cells in particular may be especially vulnerable to degeneration, for example, during dementia pathology.

1.3.10 Non-spatial encoding in the lateral entorhinal cortex

Unlike mEC neurons, that display spatially modulated firing patterns (Fyhn *et al.*, 2004), LEC cells show very little spatial selectivity (Hargreaves *et al.*, 2005;

Yoganarasimha *et al.*, 2011). LEC regions are generally regarded to be concerned with non-spatial information such as objects (Deshmukh & Knierim, 2011; Wilson *et al.*, 2013) or olfactory stimuli (Young *et al.*, 1997; Igarashi *et al.*, 2014). For example, LEC neurons have been shown to fire in the vicinity of discrete objects (Deshmukh & Knierim, 2011) and in locations where objects have been located previously (Tsao *et al.*, 2013). This activity reflects the strong projections arriving from perirhinal cortex, which is strongly involved in performing object recognition memory (Brown & Aggleton, 2001). These data suggest that the mEC primarily concerns information relating to 'where' and the LEC to 'what', with the hippocampus able to combine these processing streams to form conjunctive representations of items and their spatial location.

1.4 Dorso-ventral gradients in mEC physiology

1.4.1 Gradients in grid cell spacing

One of the earliest findings regarding grid cell firing was the topographical organisation of grid spacing (Hafting *et al.*, 2005), with cells in the most dorsal mEC regions displaying tightly packed firing fields and those in ventral mEC showing much larger and more spaced grid patterns (Brun *et al.*, 2008*b*). Interestingly, this relationship does not occur in a linear fashion, with mEC neurons clustering into a small number of discrete modules that overlap anatomically and are independent of cortical layers (Stensola *et al.*, 2012). Individual grid modules display identical grid spacing and orientation, with each able to respond independently to changes in the external environment (Stensola *et al.*, 2012). Variation in grid scale in the mEC are mirrored by place cell properties, which also show increases in field size across the dorso-ventral axis (Jung *et al.*, 1994; Maurer *et al.*, 2005). This is consistent with the anatomical projections between these two regions, with dorsal mEC projecting primarily to dorsal hippocampus and ventral mEC to ventral hippocampus (Fanselow & Dong, 2010).

Head direction cells also show a degree of topography in the mEC, with those in the dorsal regions displaying tuning curves with smaller directional firing ranges.

Conversely, ventral mEC cells more weakly convey head direction information and do so across a much large range of directions (Giocomo *et al.*, 2014).

1.4.2 Gradients in cellular properties of mEC neurons

Gradients in the spatial firing of mEC neurons are mirrored by the intrinsic properties of stellate cells (SCs) in this region. *In vitro* patch clamp studies have identified many gradients that may explain the differential integration of external information in dorsal and ventral mEC. For example, input resistance is higher and membrane time constant is slower in ventral compared to dorsal mEC-SCs (Garden *et al.*, 2008; Boehlen *et al.*, 2010; Pastoll *et al.*, 2012; Yoshida *et al.*, 2013; Booth *et al.*, 2016*a*). Spike after-hyperpolarization (mAHP) duration also increases along the dorso-ventral axis of the mEC (Boehlen *et al.*, 2010; Pastoll *et al.*, 2012; Navratilova *et al.*, 2012; Yoshida *et al.*, 2013; Booth *et al.*, 2016*a*).

A number of studies have identified dorso-ventral gradients in resonant properties, such as intrinsic membrane theta resonance (Giocomo *et al.*, 2007; Giocomo & Hasselmo, 2008, 2009; Boehlen *et al.*, 2010; Pastoll *et al.*, 2012; Heys & Hasselmo, 2012) and subthreshold membrane oscillations (Giocomo *et al.*, 2007; Giocomo & Hasselmo, 2008, 2009; Boehlen *et al.*, 2010; Dodson *et al.*, 2011; Pastoll *et al.*, 2012), with higher frequencies observed in dorsal mEC regions. These findings suggest a mechanism for the graded transformation of mEC inputs to produce differing grid firing patterns across the dorso-ventral axis of the mEC.

Both of these properties are dependent on the hyperpolarization-activated cation current (Ih), with I_h-mediated sag potentials showing decreasing relative amplitude along the dorso-ventral axis (Garden *et al.*, 2008; Giocomo & Hasselmo, 2009), although this may be somewhat dependent on age (Boehlen *et al.*, 2010; Booth *et al.*, 2016*a*). Several studies have observed the effect of hyperpolarization-activated cyclic nucleotide-gated 1 subunit (HCN1) (which conducts Ih) inhibition, showing a slowing of resonance and temporal summation in layer II mEC-SCs (Giocomo & Hasselmo, 2008, 2009; Garden *et al.*, 2008). HCN1 knockout mice show flattened dorso-ventral relationships in mEC resonant properties (Giocomo & Hasselmo, 2009), which corresponds to an increased grid scale (Giocomo *et al.*, 2011*a*), suggesting that grid cells require HCN1 for spatial

scaling. Increases in hippocampal place field size are have also been seen in these mice (Hussaini *et al.*, 2011) suggesting a common mechanism across the hippocampal formation.

Finally, a gradient has also been shown in the expression of inhibitory interneurons along the dorso-ventral axis of the mEC (Beed *et al.*, 2013). Dorsal mEC stellate cells were shown to have stronger inhibitory drive, specifically from parvalbumin (PV) positive interneurons. This gradient of inhibition may also have profound effects on the oscillatory output of the mEC (Beed *et al.*, 2013).

1.5 Understanding dementia

In the UK, over 800,000 people are thought to be suffering from dementia; globally this figure is estimated at 46.8 million (Prince, 2015). In the coming years, with an increasingly ageing population, these figures will undoubtedly rise. Across the globe in 2018, dementia will cost the global economy over $1 trillion and this is projected to double by 2030 (Prince, 2015). There are currently only a handful of symptomatic treatments for patients, with no success in finding disease modifying drugs (Doody, 2003; Ringman & Cummings, 2006; Prince *et al.*, 2014).

Alzheimer's disease (AD) represents the most common form of dementia in the elderly population, followed by Lewy body dementias, frontotemporal dementias and vascular dementias (Ferri *et al.*, 2005; Bang *et al.*, 2015; O'Brien & Thomas, 2015; Walker *et al.*, 2015). However, this thesis will primarily concern the effects of tau pathology, which is common amongst several categories of dementia.

1.5.1 Alzheimer's disease

AD, originally described by Alois Alzheimer in 1907 (Stelzmann *et al.*, 1995), can be defined by the presence of two pathological hallmarks, extracellular senile plaques consisting of beta-amyloid peptide (Aβ) and intracellular neurofibrillary tangles (NFTs) formed from hyperphyosphorylated tau protein. With these come neurodegeneration, neuroinflammation and ultimately cognitive decline, starting with declarative memory and ending with impairments in motor and autonomic functions (Buckner, 2004; Walsh & Selkoe, 2004). There appears to be a long

asymptomatic phase in AD, with significant accumulation of Aβ occurring years before the onset of cognitive symptoms (Ashe & Zahs, 2010). A stereotyped progression of degeneration can be seen in AD patients, with earliest pathology visible in the entorhinal cortex and hippocampus and spreading progressively toward frontal cortical areas (Braak *et al.*, 1991; Braak & Braak, 1995).

While the majority of AD cases are sporadic in origin, there are a small proportion of familial cases caused by genetic mutations which primarily occur clinically at younger age points (Randall *et al.*, 2010). The study of these familial AD patients has identified the amyloid precursor protein (APP) cleaving pathway as a key mediator of disease pathology. However, of these cases, only ~10% involve direct modifications to the APP gene, with the remainder made up of mutations in the presenilin (PS1 and PS2) encoding genes (O'Brien & Wong, 2011; Masters *et al.*, 2015).

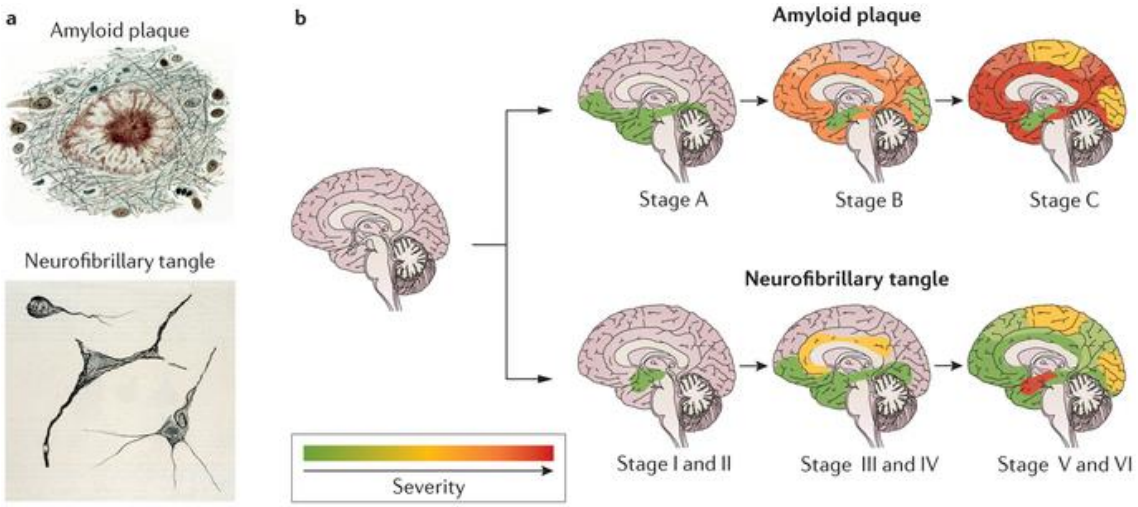

Figure 1.7: Progression of Alzheimer's disease pathology. A) Schematic of pathological hallmarks of AD: amyloid plaque and neurofibrillary tangle. **B)** Progression of amyloid and tau deposition across Braak stages I-VI. Reproduced from Masters et al., (2015).

1.5.2 Tauopathy

Tau is a microtubule-associated protein, in adult neurons it can be found predominantly in axons and interacts with microtubules to provide stabilization, promote their assembly and allow the dynamic reorganisation of the cytoskeleton (Wang & Mandelkow, 2016). There may be as many as 85 phosphorylation sites

on across the unfolded tau protein, which have a physiological role in controlling its function; however, dementia pathology is associated with the aberrant hyperphosphorylation of tau, causing it to dissociate from microtubules and promoting aggregation (Hanger *et al.*, 2009).

Neurofibrillary tangles, made up of aggregated hyperphosphorylated tau, are one of the pathological hallmarks of AD. However, other dementias can also express tau pathology in the absence of Aβ. Frontotemporal dementia (FTD), for example, is characterised by neuronal loss, gliosis and vascular changes in frontal and temporal lobe, with tau protein solely accounting for this pathology (Bang *et al.*, 2015). FTD displays a strong genetic component, with a familial history reported in up to 40% of cases and mutations involving microtubule-associated protein tau (MAPT), chromosome 9 open reading frame 72 (C9orf72), and progranulin (GRN) genes accounting for autosomal dominant forms (Hutton *et al.*, 1998; Bird *et al.*, 1999; Mirra *et al.*, 1999; van Swieten & Heutink, 2008; Sha *et al.*, 2012; Le Ber, 2013; Devenney *et al.*, 2014).

The spread of tau protein across the brain has also been proposed to occur in a prion-like manner, moving trans-synaptically across key synapses in the hippocampal formation (Liu *et al.*, 2012; de Calignon *et al.*, 2012; Holmes & Diamond, 2014). The expression of hyperphosphorylated tau, and subsequent NFT formation, is highly associated with neurodegeneration (Spires *et al.*, 2006); however, the precise role of NFTs in this is unclear. Both structural and functional alterations observed in mouse models of tauopathy appear relatively independent of neurofibrillary tangle (NFT) formation (Hoover *et al.*, 2010; Rocher *et al.*, 2010). Indeed, some neurons bearing NFTs are initially capable of integrating functionally into neuronal networks in cortical areas (Kuchibhotla *et al.*, 2014), suggesting that individual cells may show decline across long time periods, rather than rapid cell loss after tau accumulation.

1.5.3 Disease treatments and development of therapies

There are currently only a handful of therapies licenced for the treatment of AD and other forms of dementia, all of which provide only symptomatic relief with only moderate success (Trinh *et al.*, 2003; Ringman & Cummings, 2006; Masters *et al.*, 2015). Current pharmacological strategies for dementia treatments focus

almost entirely on the use acetylcholinesterase (AChE) inhibitors (Birks, 2006). Such drugs have consistently shown effectiveness in reducing cognitive symptoms associated with Alzheimer's disease pathology; however, the marginal nature of these cognitive improvements is equally consistent (Trinh *et al.*, 2003; Raina *et al.*, 2008).

The idea of the cholinergic system being an important avenue for therapy has been around for many years, since studies emerged showing correlations between the loss of cholinergic innervation and the severity of dementia (Perry *et al.*, 1977). Specifically, the loss of cholinergic neurons in the basal forebrain, which send major projections into the cortex, was shown to be a feature of Alzheimer's disease pathology (Davies & Maloney, 1976; Whitehouse *et al.*, 1982; Coyle *et al.*, 1983). This cholinergic hypothesis of AD is, however, largely outdated, with current avenues focussing on producing disease modification (Terry & Buccafusco, 2003).

The majority of these targets have focussed on the APP processing pathway to reduce Aβ aggregation. In recent years however, there has been a clear failure to produce such disease modifying interventions that can slow or halt dementia pathology, despite a number of promising compounds progressing into phase 3 clinical trials (Cummings *et al.*, 2014). Much of this failure has stemmed from the inability of targets to translate from *in vitro* preparations and animal models into improvements in cognitive function in the clinic (Giacobini & Gold, 2013). They also show that the removal of amyloid, does not by itself, necessarily lead to the improvements for AD patients. For this reason, targeting tau may be a more suitable avenue for investigation (Götz *et al.*, 2012; Wischik *et al.*, 2014; Bakota & Brandt, 2016).

1.5.4 Rodent models of dementia

Much of the current understanding regarding the effects of dementia pathology on neuronal activity has been discovered through the use of animal models of the disease. For over 20 years, mouse models of AD have been produced through genetic mutations associated with either amyloid or tau proteins (Ashe & Zahs, 2010). The majority of mouse models rely on the manipulation of these pathological proteins individually and they therefore broadly fall into two

categories; those displaying amyloid and those displaying tau pathology (Elder *et al.*, 2010; Randall *et al.*, 2010; Hall & Roberson, 2012). Most rely on well characterised familial forms of AD and FTD to produce either plaques of NFTs, caused through mutations of APP, presenilin 1 (PS1) or presenilin 2 (PS2) (Radde *et al.*, 2006; Ozmen *et al.*, 2009) (AD) or MAPT (FTD) genes (Götz & Ittner, 2008).

The first AD mice were produced by the overexpression of mutated human APP (Games *et al.*, 1995; Hsiao *et al.*, 1996), or PS1 genes , or combinations resulting in double transgenic mice showing more aggressive pathologies (Holcomb *et al.*, 1998). While these mouse strains show amyloid plaques similar to those seen in AD patients, as well as some cognitive deficits, the major limitation of these models is the absence of NFT development (Elder *et al.*, 2010; Ashe & Zahs, 2010). More recently however, long term expression amyloid mutations have been shown, in a transgenic rat model, to produce spontaneous tauopathy (Cohen *et al.*, 2013), which may reflect the limitations of mice as a model system. This has led to the production of distinct tau overexpressing mouse lines, mostly from mutation in the MAPT genes involved in familial FTD, rather than AD specifically (Santacruz *et al.*, 2005; Ramsden *et al.*, 2005; Spires *et al.*, 2006; de Calignon *et al.*, 2012). Unlike amyloid overexpressing mice, mouse models of tauopathy show profound levels of cell loss, across hippocampal and cortical regions, reminiscent of those observed in dementia patients (Ramsden *et al.*, 2005; Spires *et al.*, 2006; Rocher *et al.*, 2010).

1.6 Entorhinal cortex in dementia

1.6.1 Entorhinal degeneration in dementia

The entorhinal cortex is one of, if not the, first area to be affected in AD and other forms of dementia (Braak *et al.*, 1991). Neurons in layer II of the EC appear to be particularly susceptible to degeneration, with significant cell loss evident even in very mild cases of AD (Gomez-Isla *et al.*, 1996; Stranahan & Mattson, 2010; Khan *et al.*, 2014). This is also the case in mouse models, which show structural and functional changes in the mEC and LEC at early stages of pathological progression and preceding those in the hippocampus (Baglietto-Vargas *et al.*, 2010; Khan *et al.*, 2014; Duffy *et al.*, 2015; Klein *et al.*, 2016).

It unclear which properties of EC neurons make them particularly vulnerable to degeneration. However, for the rest of the hippocampal formation, the trans-synaptic propagation of tau may have a profound influence on the pattern of degeneration (Holmes & Diamond, 2014). With neurons in layer II EC giving rise to the perforant pathway, this 'seeding' of tau may be responsible for the progression of dementia pathology across key areas for cognition (de Calignon *et al.*, 2012).

1.6.2 Spatial memory deficits in dementia patients

Patients with AD commonly present with difficulties in spatial orientation. Early in dementia, this may mean a failure to navigate unfamiliar environments; however, in later stages patients may be disorientated even in familiar settings (Monacelli *et al.*, 2003). There have been several examples of studies showing spatial navigation or path integration impairments in AD or mild cognitive impairments (MCI) patients (Hort *et al.*, 2007; Laczó *et al.*, 2011; Lithfous *et al.*, 2013; Mokrisova *et al.*, 2016). These deficits are particularly relevant, since they can be readily observed in mouse models of the disease, allowing direct comparisons to be made with human patients.

1.6.3 Neurophysiological alterations in dementia

Since early time periods in AD research, the recording of EEG activity in patients has been used to attempt to find neurophysiological signatures of the disease (Dascalov, 1969; Jeong, 2004). There are several good reasons for EEG to provide a useful tool for assessing disease pathology. EEG is a completely non-invasive technique, which may potentially allow for some insights into the synaptic dysfunction in AD patients. AD is also primarily a cortical, rather than sub-cortical, disorder, meaning that changes can be observed from scalp electrodes (Jeong, 2004). Dementia patients show stereotyped changes to cortical EEG, consisting, in general, of a slowing of dominant rhythms, with decreases in alpha and beta oscillation frequency and increased power in the theta and delta bands (Coben *et al.*, 1985; Brenner *et al.*, 1986; Abásolo *et al.*, 2006; Czigler *et al.*, 2008). These are paralleled with decreases in coherence in both alpha and beta frequencies (Dunkin *et al.*, 1994). Furthermore, changes to EEG are fairly well correlated to the degree of cognitive impairments seen in patients (Hughes *et al.*, 1989; Kowalski *et al.*, 2001). Despite these findings, only limited knowledge can be gained from non-invasive recordings in dementia patients. Rodent models are therefore needed for a more thorough understanding of the changes to neuronal physiology in specific brain areas, such as the mEC.

Since the mEC degeneration occurs at the earliest stages of disease pathology, it is likely that the neurophysiology of this region will be substantially altered. This appears to be the case in the hippocampal CA1 region, with altered intrinsic properties of pyramidal neurons underlying aberrant network oscillations (Booth *et al.*, 2016*b*) and a reduction in sharp-wave ripple activity (Witton *et al.*, 2014). Ultimately, such changes affect the output of the hippocampus, altering the spatial properties of place-field firing sequences (Cheng & Ji, 2013; Booth *et al.*, 2016*b*). However, it is unclear whether these changes are comparable to those in the mEC, since to date, no studies have observed mEC network function in mouse models of dementia.

Recent evidence has suggested that dorso-ventral gradients in certain intrinsic membrane properties, such as membrane capacitance and afterhyperpolarizations, are lost in rTg4510 mice (Booth *et al.*, 2016*a*). Specifically, deficits in mEC properties in these mice were limited to dorsal mEC regions, with ventral mEC stellate cells largely unchanged by tau pathology. This

is also likely to have significant effects of the network activity in the mEC and the effective formation of grid cell patterns.

1.6.4 Grid patterns in dementia

To date, there have been few examinations of grid cell firing patterns after periods of dementia pathology. However, recent studies have provided some evidence of grid cell malfunction in an entorhinal specific model of tauopathy (Fu *et al.*, 2017), which correlate well with spatial memory impairments. In humans, grid-like representations using fMRI recordings have also been shown to be reduced in adults with high genetic risk of Alzheimer's disease (APOE-ε4 carriers), years before the potential onset of disease symptoms (Kunz *et al.*, 2015).

Place cell firing has been examined in both amyloid (Cacucci *et al.*, 2008) and tau (Cheng & Ji, 2013; Booth *et al.*, 2016*b*) overexpression mouse models. While the place fields in these mice are undoubtedly degraded, showing decreased spatial information content and expanded field size, they are however still consistently present. The precise temporal nature of grid and place cell impairment is as yet unknown. Given the pattern of degeneration across the hippocampal formation, weak place fields (Cacucci *et al.*, 2008; Cheng & Ji, 2013; Booth *et al.*, 2016*b*) may be the result of reduced entorhinal inputs (Brun *et al.*, 2008*a*; Van Cauter *et al.*, 2008; Hales *et al.*, 2014). Reductions in grid and place field activity may therefore mirror their appearance in neuronal development, where place cells appear before grid cell and maturing fully only after grid cell development (Wills *et al.*, 2012; Muessig *et al.*, 2015).

1.7 Aims

It is clear that the entorhinal cortex has a significant role in the processing of spatial memory, controlling the flow of information across the hippocampal formation. It is also clear that understanding the EC, and its dysfunction, is a key to understanding the progression of dementia pathology. However, surprisingly little is known about the effect of this degeneration on the neurophysiological properties of the mEC, specifically the effect on neuronal network activity in this region. This thesis will aim to provide novel insights into the electrophysiological changes that occur to mEC physiology after periods of neurodegeneration. For this reason, it will focus of tau pathology, specifically in the rTg4510 mouse model, which produces large cell loss in hippocampal and cortical areas. The key aims of this thesis are outlined below:

1. **Assess the effect of tau pathology on neuronal network activity in the mEC.** Little is known about how degeneration in the mEC, the area first affected by dementia pathology, corresponds to changes in neuronal network activity in this region.

2. **Determine the effect of dorso-ventral mEC gradients on network activity and their alterations in tauopathy**. Since recent evidence has suggested that tau pathology in this mouse may show differential impairments in intrinsic properties of mEC stellate cells across the dorso-ventral axis (Booth *et al.*, 2016*a*), efforts will aim to examine how these changes effect network activity in the mEC. Initially, this will focus on the observing the presence of dorso-ventral gradients in oscillatory activity under normal conditions.

3. **Observe the effect of tau pathology on key spatial information processing systems in the mEC.** The work will aim to understand the impact of degeneration on the ability of the mEC to represent spatial information, which will have a broad relevance to cognitive processing across the hippocampal formation.

2. General Methods

The chapter bellow will describe in detail the methods used in this thesis. However, for clarity, an overview of specific methods used will also be given at the beginning of each results chapter. Where appropriate, computer code, developed in house, for analysing specific parameters will be included in the appendix.

2.1 Ethical Approval

All procedures were carried out in accordance with the UK Animal (Scientific Procedures) Act 1986 and were approved by the University of Exeter Animal Welfare and Ethical Review Body. All steps were taken in order to minimize animals' pain and suffering.

2.2 Animals

2.2.1 rTg4510 mouse

The majority of the experiments described below were performed using the rTg4510 mouse model of tauopathy. This mouse is one of the most commonly used and well characterized models for assessing the functional impacts of progressive tauopathy (Santacruz *et al.*, 2005; Ramsden *et al.*, 2005; Spires *et al.*, 2006; de Calignon *et al.*, 2010). The model is produced through the forebrain-restricted over-expression of human 4 repeat tau expressing the frontotemporal dementia-associated P301L mutation and exhibits progressive deficits in cognitive processing that can be prevented by suppression of transgene expression with dietary doxycycline. These mice display clear spatial memory deficits, neurofibrillary lesions, and pronounced neuronal loss in both hippocampus and entorhinal cortex (Santacruz *et al.*, 2005; Booth *et al.*, 2016*a*) but they lack the severe and ultimately lethal functional consequences that arise when tau is more widely expressed in the CNS.

Specific deficits in neuronal function, both at the single cell and network levels have been widely studied both in our own lab (Witton *et al.*, 2014; Booth *et al.*,

2016*a*, 2016*b*) and others (Kopeikina *et al.*, 2013; Cheng & Ji, 2013; Wells *et al.*, 2015) probably in more detail than any other model of tauopathy.

Male rTg4510 mice were bred at Harlan Laboratories (Hillcrest, UK) and shipped to the University of Exeter before use. Animals were allowed to equilibrate for at least 7 days after transport and housed on a 12:12h light/dark cycle with *ad libitum* access to food and water.

2.2.2 C57/BL6 mice

The remaining experiments, specifically those reported in **chapter 3,** were performed using the C57/BL6 mouse strain.

Whilst this strain is a common experimental model, it is worth noting that these animals differ from the 'Wild-type' controls used in experiments with rTg4510 mice, with this mouse bred from the FVB/N strain. However, it is possible to maintain the rTg4510 line on a C57/BL6 background strain without affecting the fidelity of the phenotype (Bailey *et al.*, 2014). While there is some evidence for subtle differences in electrophysiological properties between experimental mouse strains (Ryan, 1984; Bampton *et al.*, 1999), this is likely to have a little impact on the findings explained below.

C57/BL6 were bred in-house and maintained on a 12:12h light/dark cycle with *ad libitum* access to food and water.

2.3 *In vitro* electrophysiology

2.3.1 Parasagittal slice preparation

Mice were killed by cervical dislocation and the brain rapidly extracted and placed in cold (~4 °C), oxygenated sucrose-based solution, comprising (in mM): sucrose (189), D-glucose (10), $NaHCO_3$ (26), KCl (3), $MgSO_4$ (5), $CaCl_2$ (0.1) and NaH_2PO_4 (1.25). The cerebellum was removed and the remaining brain tissue hemisected. Parasagittal brain slices (400 µm thick), containing the entire dorsal-ventral extent of the mEC, were prepared whilst immersed in the sucrose-based cutting solution, using a vibratome (VT1200, Leica Microsystems). After cutting, the slices were immediately removed to a holding chamber containing

oxygenated (95% O_2/5% CO_2) artificial cerebrospinal fluid (aCSF) comprising (in mM): NaCl (124), KCl (3), $NaHCO_3$ (24), $MgSO_4$ (1), D-glucose (10), $CaCl_2$ (1.2). The slices were gradually warmed to ~37 °C (for 30 minutes) and then maintained at room temperature (~20 °C, for at least another 30 minutes) until ready for use. Whole slices were then transferred to an interface-style recording chamber maintained at 34 ± 1 °C and allowed to equilibrate for a further 30 minutes.

2.3.2 Data acquisition

Continuous extracellular recordings were made using one of two approaches: 1) Pairs of glass micropipettes (filled with aCSF) were positioned in the superficial layers of dorsal and ventral ends of the mEC; or 2) a single 16-channel silicone probe consisting of 16 individual shanks (55 µm wide, 100 µm apart), with a single electrode contact point at the end of each shank (Neuronexus, Ann Arbor, MI; probe catalogue number: A16x1-2mm-100-177), was positioned parallel to the dorso-ventral axis of the mEC (fig 2.1).

For the glass electrode experiments, data were recorded using the two channels of a MultiClamp 700A (in I=0 mode; Molecular Devices, Sunnyvale, CA), band-pass filtered at 1 Hz-1 kHz and digitized at 5 kHz, using Clampex 10.4 software (Molecular Devices).

For the silicone probe recordings, data were recorded using a 32-channel amplifier (RHD2132; Intan, Los Angeles, CA) coupled to an open-source acquisition board (Open Ephys Inc, Cambridge, MA). These data were band-pass filtered (1-500 Hz) and digitized at 2 kHz. All data were stored on the hard drive of a PC for off-line analysis.

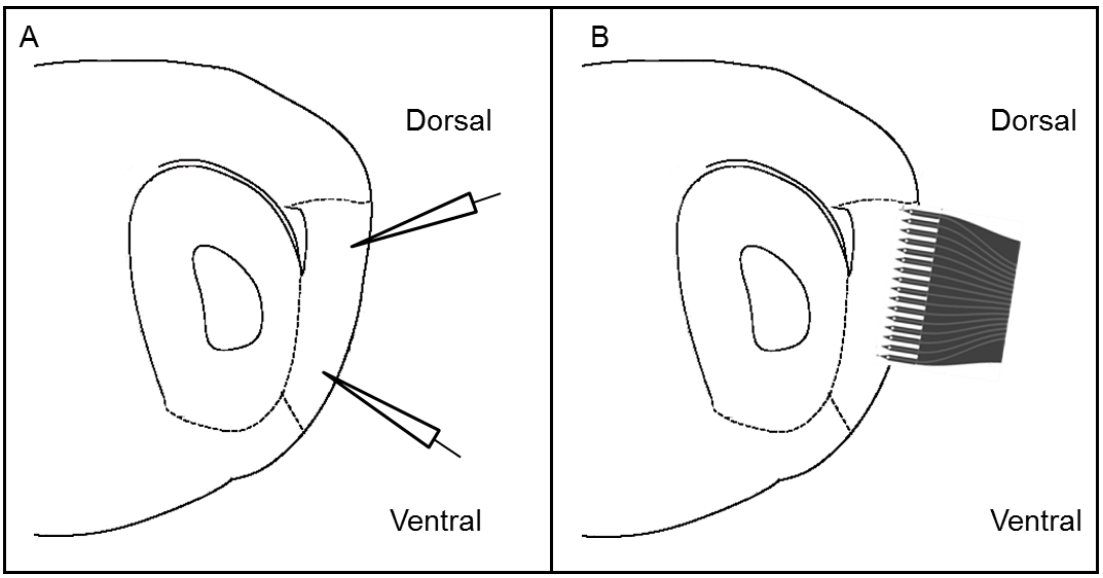

Figure 2.1*:* Recording positions for *in vitro* electrophysiology. A) Indicative recording locations from paired glass electrodes filled with aCSF positioned in dorsal and ventral mEC. B) 16 channel silicone probe with 16 individual positioned parallel to the dorso-ventral axis of the mEC.

2.3.3 *In vitro* gamma oscillations

Pharmacologically induced gamma oscillations (30-80 Hz) were evoked using low concentrations of kainate and recorded simultaneously in dorsal and ventral portions of the mEC. After an initial baseline, network activity was elicited by continuous bath application of either 200 nM or 500 nM kainate ((2S,3S,4S)-3-(Carboxymethyl)-4-prop-1-en-2-ylpyrrolidine-2-carboxylic acid, Tocris Cookson, Bristol, UK) for up to 1 hour. In a proportion of slices, the $GABA_A$ receptor agonist picrotoxin (PTX, Tocris) was subsequently applied in order to eliminate network activity and produce regular bursts of hyperexcitability.

2.3.4 Epileptiform activity

In a subsection of experiments, after the observation of *in vitro* gamma oscillations, picrotoxin (50 μM) was bath applied in addition to kainate (500 nM). This application was firstly, to abolish mEC oscillatory activity and secondly, to induce hyperexcitable discharges, described here as interictal-like activity.

In a further subsection of slices used for kainate/picrotoxin experiments, a scalpel blade was used to make a cut in the intermediate mEC immediately after slice preparation, thus anatomically separating dorsal and ventral portions.

Ictal-like epileptiform activity, defined as long periods of regular seizure-like waveforms, was also induced by bath application of 4-aminopyridine (4-AP; 100 µM, Tocris, UK).

2.3.5 Data analysis – gamma oscillations

All data were analysed using MATLAB, spectral analysis was conducted for 1 min bins of recorded data using the Chronux toolbox (available at http://chronux.org/) (Mitra & Bokil, 2008; Bokil *et al.*, 2010). Spectral power was calculated as the total area under the curve between the limits of relevant frequency band, using the mid-ordinate rule. Peak gamma frequency was defined as the frequency with the highest spectral power (fig 2.2B).

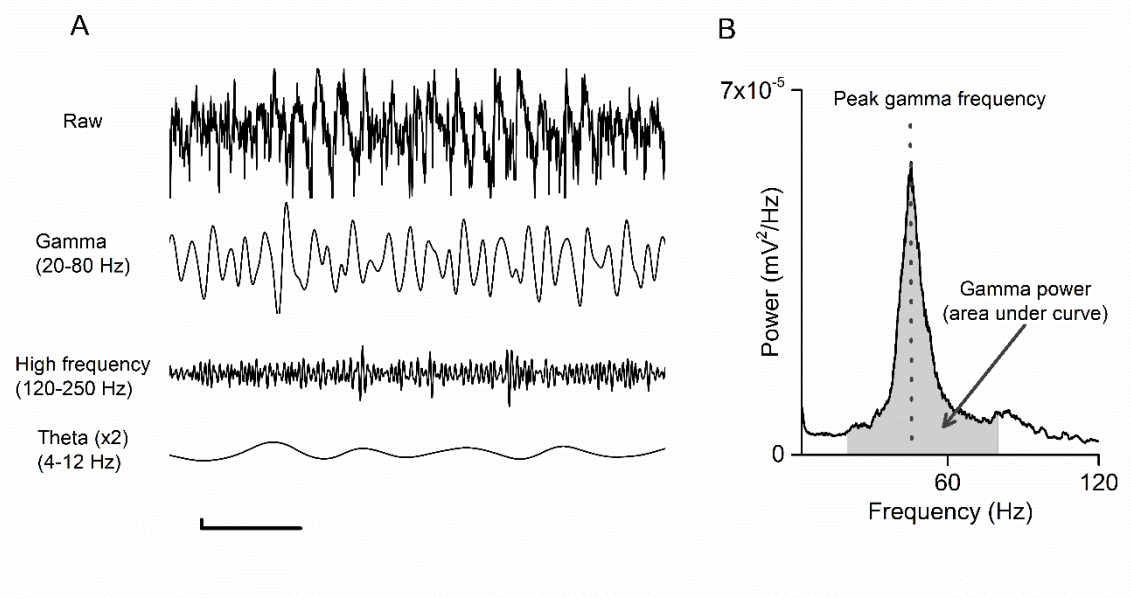

Figure 2.2. Analysis of in vitro gamma oscillations. A) Example of network activity recorded from mEC *in vitro*, filtered in increasing frequency bands. Scale bar: 100 ms, 20 µV. **B)** Power spectrum from 1 min of recorded data, showing measurement of peak gamma frequency and total gamma power.

2.3.6 Data analysis – epileptiform activity

Recordings of mEC hyperexcitability were analysed using built-in and custom-written functions in Matlab (Mathworks). Interictal and ictal bursts were identified using a threshold detection algorithm. Data were filtered (0.5 – 10 Hz and 15-35 Hz for interictal and ictal bursts, respectively) rectified and z-normalised (fig 2.3). Subsequently the envelope in these frequency bands was determined by Hilbert

transform, and burst initiation was determined by the first time point over a threshold of 1.5-3 standard deviations from the mean (fig 2.3).

For interictal activity, individual burst waveforms were extracted (window size = 0.9 s) from each recording probe and the resulting waveforms were grouped using an unsupervised k-means clustering algorithm (from the Matlab 2016a Statistics and Machine Learning Toolbox; distance measure was the sum of absolute differences). The most appropriate number of clusters (k) was the solution (where k>1 and <10) which resulted in the highest mean silhouette value.

Ictal burst start time for each electrode was plotted relative to the first recorded threshold crossing and slope of ictal propagation calculated in µm/s for each burst, assuming linear progression between recording sites. For analysing within-burst properties, cross correlation analysis was performed on 1 s time bins of data between the most ventral recording site and each subsequent dorsal electrode. Dorsal – ventral cross correlations were performed, meaning that positive peaks in the cross correlation correspond to waveforms that occur first in ventral mEC. Interictal bursts were also measured by a variable threshold search and their frequency expressed as number of bursts in each 60 s bin. Cross-correlation analysis was also performed on time windows containing individual bursts.

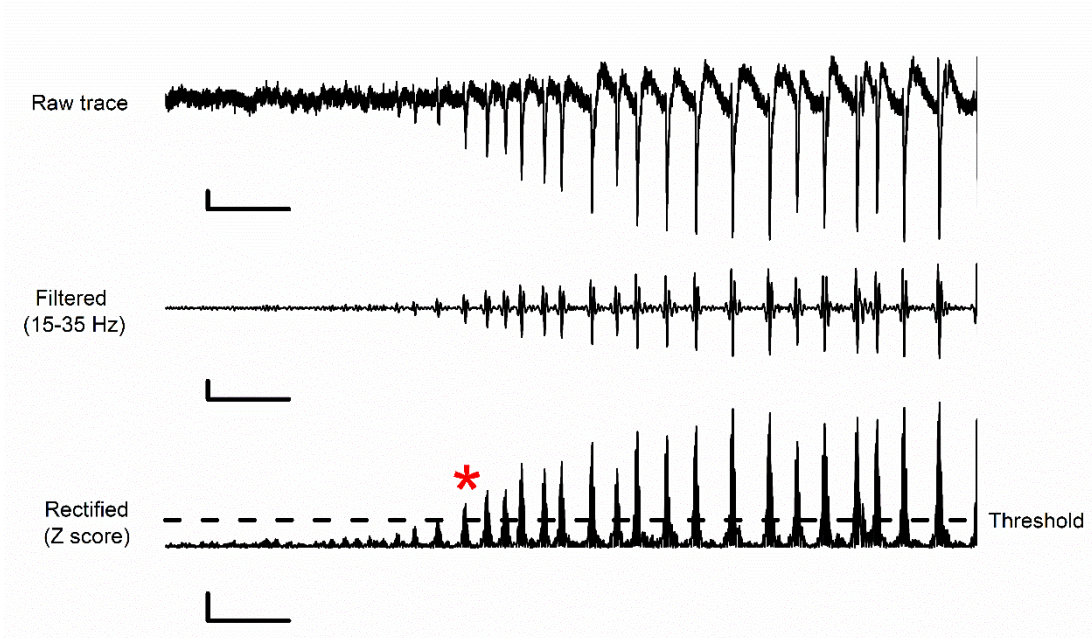

Figure 2.3 Ictal-like burst detection. Top: raw trace recorded after application of 4-AP (scale bar: 1s, 50 µV). Middle: filtered trace between 15 and 35 Hz (scale bar: 1s, 50 µV). Bottom: trace rectified and then Z-normalised, threshold 1 SD above mean, red star: 1st threshold crossing, (scale bar: 1s, 1 z).

2.4 *In vivo* electrophysiology

2.4.1 Silicon probe electrode arrays

Silicon probe electrode arrays were used throughout the experiments described below. This technology allows for highly precise arrangement of recording electrodes over small spatial scales, making it possible to record simultaneous activity across well-defined regions. The specific recording configurations used in the experiments described below would be impossible to achieve using individual wires or handmade electrode configurations. Importantly, the consequence of this is the relatively low numbers of animals needed for each experiment, with electrode arrays showing relatively small levels of variation.

The *in vivo* electrophysiology experiments described in chapters 4-6 use two forms of recording array:

1) Fixed 16-channel linear silicon probes with 150 µm inter-electrode spacing (NeuroNexus Technologies; site impedance 200-400 kΩ, catalogue number: A1x16-5mm-150-703, fig 2.4A). These electrodes are optimised for recording local field potential (LFP) activity, with the large electrode spacing meaning that signals can be recorded along the majority of the dorsal ventral axis of the mEC.

2) Moveable, high density electrode arrays containing 2 shanks of 16 electrodes arranged in 2 parallel columns with 25 µm spacing (Cambridge NeuroTech; ASSY-116 DBC-2-1, shank pitch 250 µm, fig 2.4B) attached to a miniature Microdrive with screw moving 205 µm per turn (Cambridge NeuroTech; Nano-Drive CN-01 V1). This approach is highly optimised for distinguishing singe-unit activity across smaller regions of cortex, with lower impedance measures of 25-40 kΩ producing an enhanced signal-to-noise ratio and long-term stable recordings from a large number of individual cells. This therefore gives many advantages over traditional tetrode recordings, which will be discussed further in chapter 6.

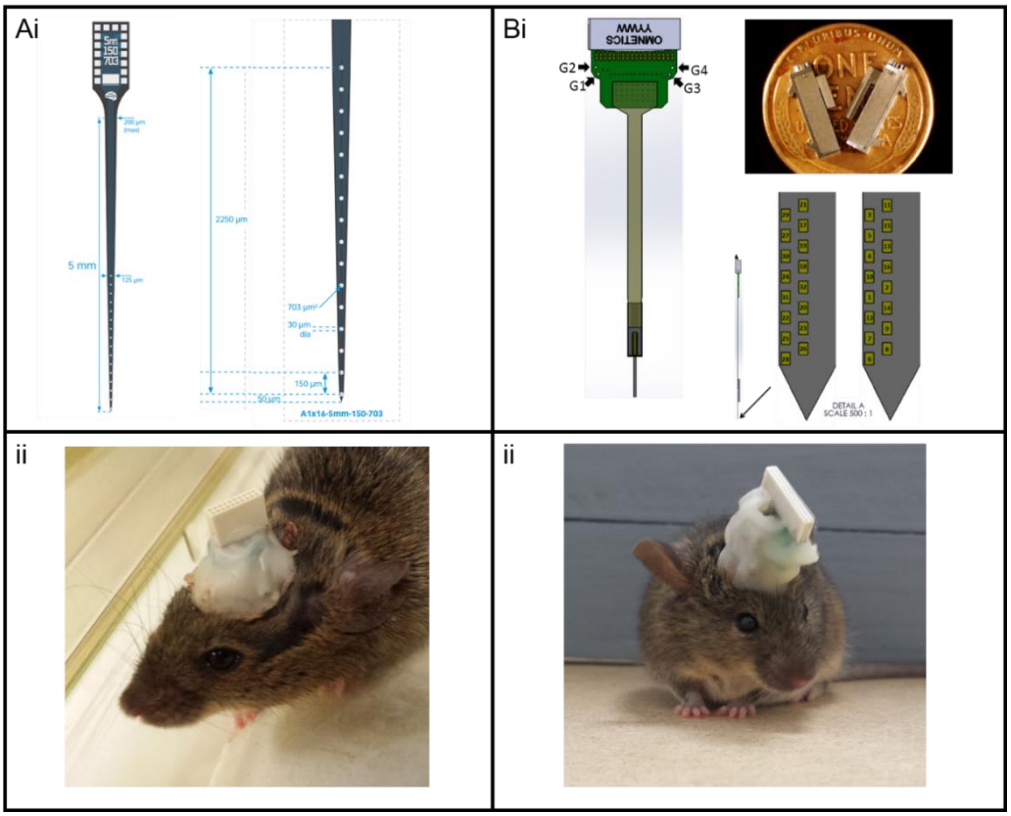

Figure 2.4: Silicon probe electrode configurations. A) Schematic of fixed 16-channel linear silicon probe used in chapter 4/5 (i) (NeuroNexus; catalogue number: A1x16-5mm-150-703, image from http://www.neuronexus.com/) with example of implanted animal. B) Schematic of high density electrode arrays used in chapter 6 (Cambridge NeuroTech; image from http://www.cambridgeneurotech.com/) and example implant (ii) containing miniature microdrive encased in dental cement.

2.4.2 Surgical implantation

All surgical procedures were conducted using standard sterile and aseptic techniques. Animals were anaesthetized using isoflurane (4%) and fixed into a stereotaxic frame (ASI instruments). Anaesthesia was reduced and maintained at 1-2% during surgery. Body temperature was maintained using a homoeothermic blanket (Harvard instruments) and mice compensated for fluid loss with Hartmann's solution given subcutaneously (SC) before and at regular periods throughout surgery. For the purpose of analgesia, animals were administered carprofen (5 mg/kg) intraperitoneally (IP) before first incision and again postoperatively at intervals of 12-24 hours as required.

After careful cleaning of the skull surface, small screws (antrin miniature specialities, ref: PN M.08 x 0.60 SL FLAT FILL MS SS) were inserted into each

bone plate in order to anchor the electrode array. Silver wire (World Precision Instruments) was soldered to a screw overlying the cerebellum to be used as a ground.

Probes were implanted at 0.2-0.3 mm anterior to the transverse sinus and 3-3.25 mm from midline. Linear probes were implanted and fixed 3 mm below the dura mater and angled at 10 degrees in the posterior to anterior direction in the sagittal plane in order to record consistently from layer II/III along the dorsal-ventral axis of the mEC.

High density silicon probes were implanted 0.3-0.5 mm below dura at an angle of 5 degrees, also in the posterior direction and subsequently moved slowly into the cortex using their attached microdrive (Cambridge NeuroTech). The shallower angle used in these experiments was chosen to allow for a greater penetration of mEC cortical layers, whist leaving maximal space in the dorso-ventral direction to advance the electrode array.

Gentamycin impregnated bone cement (DePuy International Ltd) or RelyX Unicem 2 dental cement with blue curing light (Henry Schein) were used to anchor the probe to the skull and anchor screws. After surgery mice were maintained on a heat mat until fully conscious and transferred to a heated recovery tank for ~4 hours before being returned to their home cage. Animals were singly housed and monitored carefully throughout experimental proceedings.

2.4.3 Data acquisition

Animals were given at least 1 week of post-operative recovery before initial recording sessions. Local field potential (LFP) signals were recorded using a Digital lynx 10S recording system (Neuralynx, Bozeman, MT, USA) tethered to a HS-18 or HS-36 unity gain headstage and Cheetah 5 data acquisition software (Neuralynx). The headstage and tether were counterbalanced using a moveable, weighted arm to allow for the maximum flexibility of movement.

Two light-emitting diodes (LEDs) on the headstage and an overhead video camera (sample rate 25 Hz) were used to continuously track the animals' location using Cheetah's built in video tracking software (VTS), allowing estimation of

position and therefore running speed. Once recorded, invalid tracking points, i.e. time-points where no light threshold was reached, were excluded and the animal's position interpolated from the two nearest points. Estimation of running speed was performed on binned position data, with erroneous bins, above 50 cm/s, also removed.

LFP data were recorded while animals explored either a linear track (1.5 m) or square open field (1.25 m x 1.25 m)(fig 2.5). Total recording time for each animal was limited to 1 hour per day.

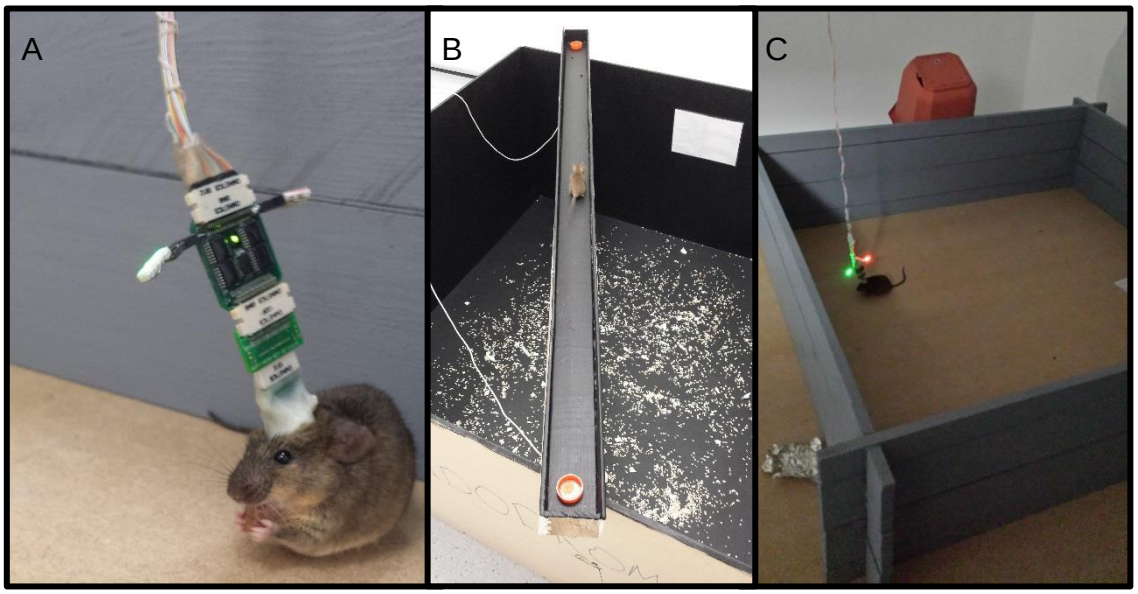

Figure 2.5: Recording environments for in vivo electrophysiology. A) Implant and Neuralynx HS-36 headstage on mouse implanted with 32 channel electrode array (Cambridge Neurotech). **B)** Linear track (1.2m), with reward points at ends to deliver diluted condensed milk. **C)** Mouse in open field environment (1.25m x 1.25m).

2.4.4 Analysis of local field potential (LFP) signal

Data recorded using 16-channel linear silicon probe electrodes were continuously sampled at 2 kHz, band-pass filtered (1 – 500 Hz) and stored on a PC for offline analysis. All LFP signals were analysed in MATLAB, using open-source toolboxes or custom routines utilising built-in functions. Multi-tapered spectral analysis was performed using the Chronux toolbox (available at http://chronux.org/) (Mitra & Bokil, 2008; Bokil *et al.*, 2010) and phase-amplitude coupling (PAC) measured using a toolbox available at

http://www.cs.bris.ac.uk/Research/MachineLearning/pac/ (Onslow *et al.*, 2011). A linear regression analysis between probe position and modulation index (MI) was performed and the slope of this line was determined. Furthermore, the Pearson's R value for each correlation was transformed to a normally distributed Z score for comparison between the two groups.

LFP frequency bands were defined as follows; delta: 1-5 Hz, theta: 6-12 Hz, low gamma: 30-50 Hz, high gamma: 60-120 Hz.

Due to the significant effect of running speed on LFP activity in the hippocampal formation, analysis of oscillatory properties (seen primarily in chapter 4) was performed on 'speed-controlled' data. All sections of data recorded while animals were running between 10-12 cm/s were concatenated and used for subsequent analysis.

Power and peak frequency of LFP frequency bands were also compared to running speed (chapter 5) in a similar manner. In this case however, spectral analysis was conducted on 0.5 s bins of LFP data and compared to running speed calculated from the same time frame. For running speed curves, locomotor activity was divided into 1 cm/s bins (between 1-30 cm/s) and oscillatory power and peak frequency averaged across all relevant sections of data. Theta and gamma oscillation power was normalised to the power in these frequency bands during non-movement, defined as speeds under 1 cm/s.

2.4.5 Single-unit spike detection

For single unit data, recordings referenced to the ground electrode, were continuously sampled at 40 kHz, bandpass filtered between 1-30 kHz and saved unprocessed on a PC for offline analysis.

Individual data files were converted from Neuralynx '.ncs' format to a single flat binary file ('.dat') for each recording session organised by timestamp, in the format:

[Time**1**Channel**1**, Time**1**Channel**2** ... Time**1**Channel**N**, Time**2**Channel**1**, Time**2**Channel**2**… Time**2**Channel**N**...]

Each channel was referenced offline to a common-average of the opposite 16-channel shank (250 µm away) in order to eliminate signals common across the electrode array such as noise and movement artefacts.

Extracellular spike activity was detected and sorted using the klusta open source software package found at: http://klusta.readthedocs.io/en/latest/ (Rossant *et al.*, 2016). Spike detection was performed using the *SpikeDetekt* program. Data was first high-pass filtered and spikes detected using a double-threshold flood filled algorithm, whereby all points must exceed a 'weak threshold' (2 standard deviations away from the filtered mean) and a least one exceed a 'strong threshold' (above 4 standard deviations).

Automated clustering of detected spikes was then conducted using the program *KlustaKwik.* Clusters were determined using a 'masked EM' (expectation–maximization) algorithm (Kadir *et al.*, 2014). Detected waveforms were defined by both a 'feature vector' containing principle component analysis of each channel on the recording electrode and a 'mask vector' using the peak amplitude of channels, but clipped so as to only contain those in spatially adjacent recording sites. This approach allows for temporally overlapping spikes to be clustered easily into separate units, a phenomenon that is increasingly common as channel count increases.

A final manual correction stage using the user interface *KlustaViewa* was then conducted by using auto- and cross-correlograms, and cluster shapes produced from principle components analysis. This typically involved the merging of clusters split by the algorithm (due to electrode drift or bursting activity) or the removal of clusters with irregular waveforms deemed to be noise artefacts (fig 2.6).

2.4.6 Cell classification

Clusters were classified as either putative interneurons or putative excitatory cells (pyramidal or stellate cells) by their spike half-width, taken from the peak to the subsequent trough of the average extracellular waveform. While the majority of cells recorded in the mEC are excitatory, a significant population can be classified as inhibitory interneurons (Miettinen *et al.*, 1996; Beed *et al.*, 2013; Buetfering *et al.*, 2014). Using the average spike waveform, putative interneurons were

classified as displaying spike-width less than 0.4 ms, based on the extracellular properties of PV+ interneurons isolated optogenetically (Buetfering *et al.*, 2014). This approach was taken alone, rather than in combination with average firing rare of neurons, since contra to traditional classifications, since mEC interneurons have been shown to vary widely in their spike frequency (Buetfering *et al.*, 2014).

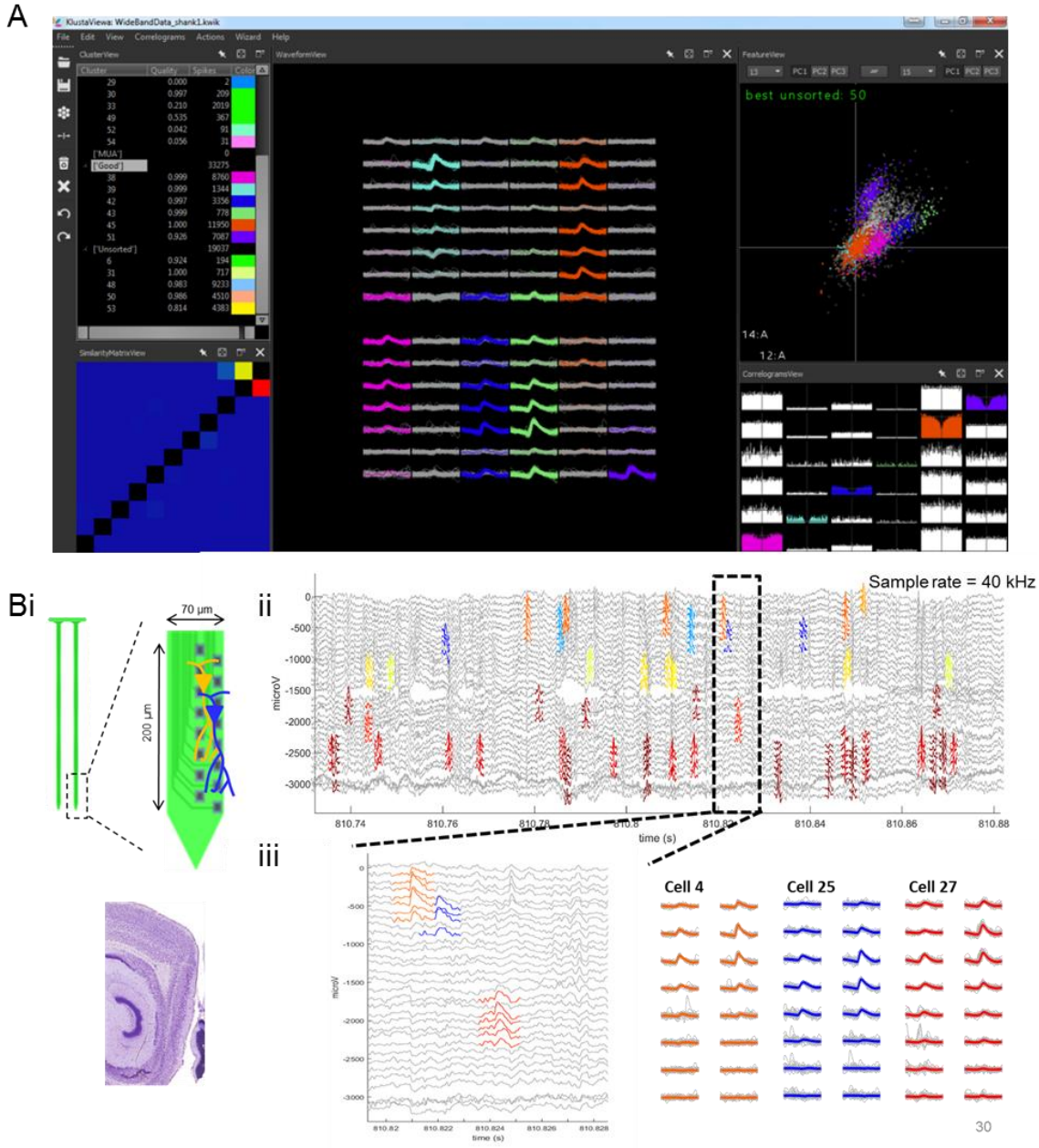

Figure 2.6. Clustering of single unit activity using KlustaKwik. A) KlustaViewa graphical user interface showing clustered mEC single units (middle) with comparison of principle components in 2 electrode channels (top right) and cross- and auto-correlations of clustered units (bottom right). **Bi)** Schematic showing 2 shanks of 16 channel recording electrode array. **ii)** Continuously sampled data showing clustered units in different colours, with zoomed trace and average waveforms bellow (**iii**).

2.4.7 Theta modulation

Neurons were described by a theta modulation index (TMI), based on the fast Fourier transform (FFT) of spike-train autocorrelations, using methods described previously (Langston *et al.*, 2010; Wills *et al.*, 2010; Booth *et al.*, 2016*b*). Autocorrelations were produced with ± 500 ms lags and 2 ms bin size. The peak at 0 lag was reduced to the next maximal value and the entire function mean-normalised by subtracting the mean from all values. The autocorrelation was tapered using a Hamming window to reduce spectral leakage and FFT calculated. The power spectrum was calculated by dividing the square of the FFT by the transform length (2^{16}, scaled to the length of the autocorrelation). TMI was defined as the mean power in the within 1 Hz of each side of the peak in the theta frequency range (5-12 Hz) dived by the mean power between 0 and 125 Hz. Cells were defined as 'theta modulated' if their TMI was greater than 5.

2.4.8 Analysis of speed modulated firing

Speed modulation of single unit activity was calculated based on analysis described in Kropff *et al.*, (2015). Running speed and firing rate of individual clusters were calculated for 40 ms bins of data and smoothed across 500 ms using a Gaussian window function. Running speeds from 2-30 cm/s and containing more than 0.5% of recording duration were used for further analysis. Speed modulation of cells was then defined by the correlation (p) between all running speed and firing rate bins and expressed using the Fisher-z transformation for variance stabilization.

Observed speed correlations were compared to a distribution of randomly sampled correlations of shuffled data. For shuffling, time stamps were forward-shifted by a pseudorandom period between 20 s and the total trial length minus 20 s, with the end of the trial wrapped to the beginning and reanalysed using the method above. Cells were defined as 'speed modulated' if their speed score (z) was greater than the 95th percentile, or less than the 5th percentile, of the global distribution of scores produced from at least 250 shuffled data sets for each unit (fig 2.7).

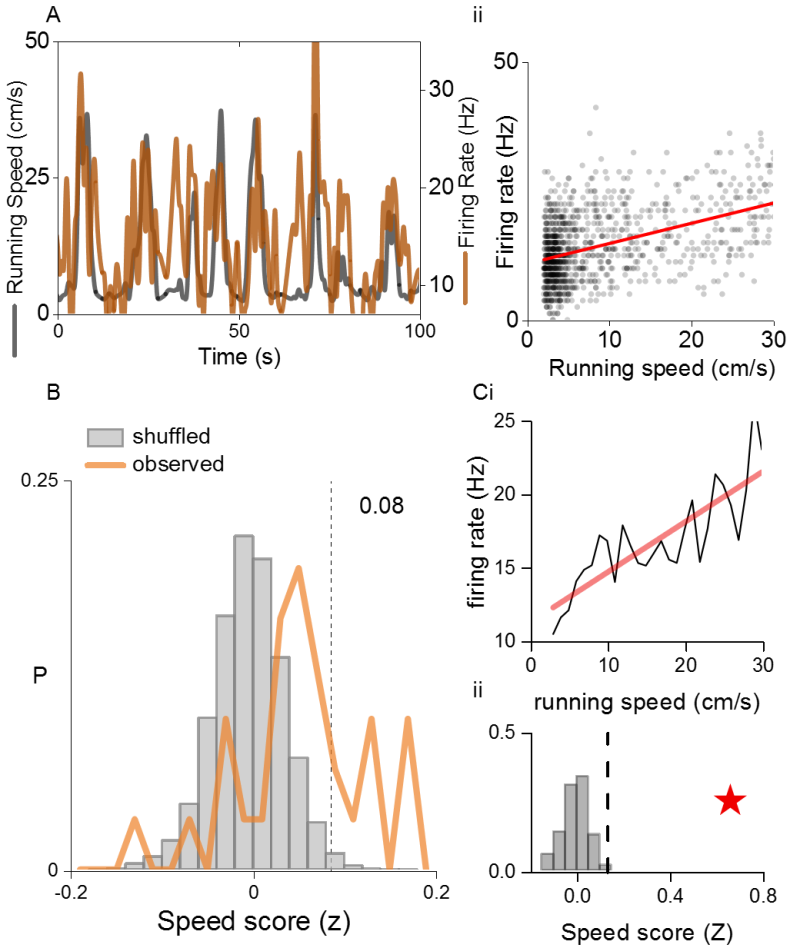

Figure 2.7 Calculation of speed modulated firing. A) Example cell firing rate of single speed modulated cell (orange) and running speed (grey) on linear track, with correlation between both for each 40 ms time bin (**ii**). **B)** Shuffled distribution of speed scores (z) produced from 250 shuffled time-stamps for each isolated cell (grey), with observed distribution (orange) from a single shank in mEC. **C)** Average firing rate of example unit above, across 1 cm/s bins (i), with speed score (star) in relation to shuffled distribution (ii, dotted line = threshold).

2.4.9 Analysis of head direction properties

Head direction was determined by calculating the angle between two LEDs attached to the animal's headstage. Time periods where neither, or only one, of the LEDs were observed above threshold were discarded. Firing rate was calculated for 3º bins of head direction and smoothed, using a Gaussian window over 14º. A 'head direction score' was defined as the resultant mean vector length, calculated from the smoothed firing rate maps. Observed mean vector length was also compared to the 95th percentile of a distribution of shuffled data produced as above.

2.4.10 Analysis of spatial firing properties

Spike locations for each cell were obtained with a 2D histogram count, using the MATLAB function *histcounts2*. Firing rate was calculated for 3 cm^2 bins across recording environments and smoothed using a 2D Gaussian function across 1.5 standard deviations.

'Gridness' was calculated using a 2D autocorrelation of smoothed firing rate maps (Sargolini *et al.*, 2006). Spatial periodicity was determined by rotating autocorrelations in steps of 30°, between the central peak and the 6 closest peaks, and correlating the rotated versions with the original. Grid score was expressed as the difference between rotations at 30°, 90° and 150°, where if firing maps show a hexagonal pattern give low correlations and 60° and 120° where correlations will be high (fig 1.8D).

Grid scale was determined by measuring grid score for multiple circular samples around the central peak, with increasing radius (Langston *et al.*, 2010). Grid scale was identified as the radius producing the highest grid score, corresponding the edge of the first peak (fig 2.8Cii).

The spatial information content (SI) of each cell was defined using the measure described by Skaggs *et al.*, (1993) and expressed in terms of bits/spike. This approach measures the extent to which a cells firing rate can be used to predict the animal's location. By definition, this does not assume spatial periodicity and has been used for quantifying place cell activity (Brun *et al.*, 2008*a*; Cacucci *et al.*, 2008; Hussaini *et al.*, 2011; Booth *et al.*, 2016*b*) as well as spatially selective firing in the lateral EC (Deshmukh & Knierim, 2011).

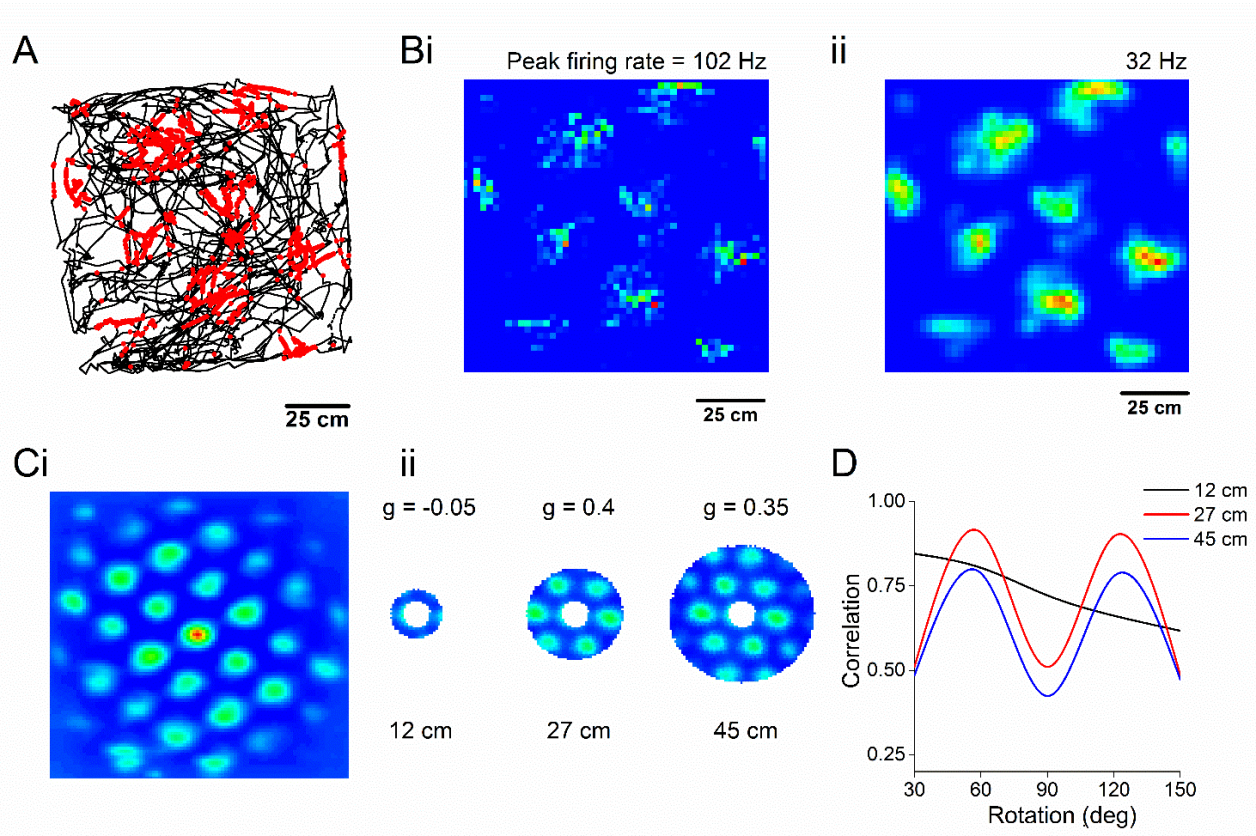

Figure 2.8: Calculation of grid-score and grid-spacing. A) Running path of animal in open field arena (black line) with individual spike locations (red dots). **B**) Rate maps for raw (i) and smoothed (ii) firing in 3 cm^2 bins across environment. **C)** 2D autocorrelation of **Bii** with masked versions with the middle field removed and increasing distances from centre, grid score for each displayed above. **D)** Correlation between original autocorrelation and rotated versions, showing peaks at 60° and 120°, as expected for hexagonal firing pattern. Also shown for increasing radius from central peak, showing highest grid score with distance equalling the edge of first 6 firing fields. For analysis only correlations for 30°, 60°, 90°, 120° and 150° were used, however for illustrative purposes smaller bins were used here.

2.5 Histology

2.5.1 Electrode placement

At the end of *in vivo* electrophysiological experiments, mice received an overdose of sodium pentobarbital (Euthetal) and electrolytic lesions were made at several electrode locations across the recording array.

Mice were then transcardially perfused with 4% v/v formaldehyde in 0.1 M phosphate buffered saline (PBS). Brains were extracted from the skull and stored

in 4% formaldehyde before being cut in sagittal sections (50 µm) using a vibratome (Leica VT1000) and stained with cresyl violet. The position of electrode sites was determined from digital pictures taken with a 2.5X objective on a light microscope using QCapture pro 7 software (Qimaging). Probe electrode location was expressed as distance from the most dorsal electrode site in layer II/III mEC.

2.5.2 Assessment of gross anatomical properties

To assess the gross anatomy of the mEC, additional 6 µm sections were stained with cresyl violet solution (Thermo Scientific, Cheshire, UK). Male rTg4510 mice were bred at Harlan Laboratories (Hillcrest, UK) and sections prepared at Eli Lilly UK, before being shipped to the University of Exeter. After de-paraffinization and rehydration slides were treated with 1% cresyl violet for 8 minutes, followed by differentiation in ethanol and acetic acid and dehydration with increasing concentrations of ethanol. Sections were then treated with xylene and immediately cover-slipped with DPX (Sigma-Aldrich, UK). Images were obtained using a light microscope and quantification of cortical thickness and cell density performed with ImageJ software (Schindelin *et al.*, 2012) using the measure and analyse particles tools respectively. Location of the mEC was determined with reference to the Allen Developing Mouse Brain Atlas (© 2015 Allen Institute for Brain Science. Allen Developing Mouse Brain Atlas. Available from: http://developingmouse.brain-map.org).

2.6 Statistical analysis

All pooled data was tested for normal distribution and the appropriate parametric or nonparametric test used for comparisons. Details of statistical tests will be provided in the main text of each results chapter. However, comparisons between groups were typically implemented with student's t-test (parametric) or Mann-Whitney U test (nonparametric). 2 way analysis of variance (ANOVA) test were used to compare more than two groups, with individual differences between means compared using Bonferroni corrected t-test where appropriate. Unless otherwise stated, data were presented as mean ± standard error of the mean (SEM) in text/figures. Where box plots were used, they consisted of the following: dotted line: median, diamond: mean ± SEM (box), whiskers: $25^{th}/75^{th}$ centile.

3. Consequences of dorso-ventral gradients for mEC network activity

3.1 Introduction

While many have described dorso-ventral relationships in mEC physiology (Giocomo *et al.*, 2007; Garden *et al.*, 2008; Boehlen *et al.*, 2010; Dodson *et al.*, 2011; Pastoll *et al.*, 2012; Navratilova *et al.*, 2012; Yoshida *et al.*, 2013; Booth *et al.*, 2016*a*), the precise impact of these on neuronal network function is less well understood. Before examining the effects of neurodegeneration, the initial aim of this project was therefore to assess the role of these gradients on oscillatory activity in the mEC.

3.1.1 *In vitro* gamma oscillations

*In vitro g*amma oscillations have been widely described, both in the hippocampus (Fisahn *et al.*, 1998; Traub *et al.*, 2000; Brown *et al.*, 2006; Butler *et al.*, 2016) and entorhinal cortex (Cunningham *et al.*, 2003, 2004, 2006; Beed *et al.*, 2013; Klein *et al.*, 2016), as well as several other brain areas (Hájos *et al.*, 2004; Oke *et al.*, 2010; McNally *et al.*, 2011). This activity has been shown to be dependent on $GABA_A$ receptor-mediated synaptic transmission (Cunningham *et al.*, 2003). Since there appears to be a dorso-ventral gradient in inhibitory inputs in the mEC (Beed *et al.*, 2013), it is therefore likely that this will have profound implications on the emergence of synchronous network activity.

3.1.2 mEC hyperexcitability

This chapter will also examine the role that anatomical gradients may play in hyperexcitable states across the mEC. While not the primary objective of this thesis, the experiments described below will have implications for temporal lobe epilepsy (TLE). Through this additional pathological condition, there is much to gain in understanding the organisation of the mEC. There are also strong links between dementia and epilepsy, with hyperexcitibility a common phenotype in

mouse models of Alzheimer's disease (Palop *et al.*, 2007; Minkeviciene *et al.*, 2009; Brown *et al.*, 2011; Verret *et al.*, 2012; García-Cabrero *et al.*, 2013).

Temporal lobe epilepsy (TLE) is one of the most common forms of epilepsy in adulthood (French *et al.*, 1993; Spencer & Spencer, 1994; Bartolomei *et al.*, 2005). While studies of TLE have typically concentrated on the hippocampus as an epileptic focus, the EC is of particular importance due to its pivotal role as a gateway between hippocampus and other cortical regions (Amaral & Witter, 1989; Canto *et al.*, 2008). In this regard, a number of clinical (Du *et al.*, 1993; Spencer & Spencer, 1994; Bartolomei *et al.*, 2005) and preclinical (Du *et al.*, 1995; Kohling *et al.*, 2000; Kobayashi *et al.*, 2003; Berretta *et al.*, 2012) studies point to the EC as an important epileptogenic zone. A variety of epileptogenic pharmacological agents promote seizure-like activity in EC brain slices prepared from rats, mice and guinea-pigs. For example, $GABA_A$ receptor antagonists (e.g. picrotoxin), potassium channel blockers (e.g. 4-aminopyridine, 4-AP) and low Mg^{2+} recording solutions all produce differing patterns of epileptiform activity, either on their own, or as part of combined applications (Collins *et al.*, 1983; Jones & Heinemann, 1988; Nagao *et al.*, 1996; Gulyás-Kovács *et al.*, 2002; Avoli *et al.*, 2002, 2013; Gnatkovsky *et al.*, 2008; Losi *et al.*, 2010; Gonzalez-Sulser *et al.*, 2011). The neurophysiological processes underpinning each of these models vary widely; however, each in some way disrupts the balance between excitation and inhibition.

3.2 Methods

Male C57/BL6 mice (aged 6-12 weeks) were bred at the University of Exeter and housed on a 12:12 h light cycle with ad libitum access to food and water. Parasagittal slices containing mEC were cut using the methods described in **section 2.3.** Gamma oscillations, recorded from dorsal and ventral portions of mEC, were elicited by bath application of either 200 or 500 nM kainate and spectral power and frequency analysed for each 1 min section of data after kainate application. Maximum power and frequency were defined as the highest values irrespective of time.

Hyperexcitable, interictal-like bursts were subsequently initiated by the addition of picrotoxin (PTX, 50 μM) to the bath containing kainate (500 nM). A distinct section of slices were also used, with a scalpel cut performed in the intermediate mEC, in order to anatomically separate the dorsal and ventral poles. Prolonged ictal-like activity was elicited using 4-AP (100 μM) and recorded at 100 μm intervals across the dorso-ventral axis of the mEC using a 16-shank silicon probe array (NeuroNexus). In additional slices, 4-AP was followed by co-application of $GABA_A$ receptor modulators acting at the benzodiazepine binding site, either diazepam (positive) or Ro19-4603 (negative) (Wong & Skolnick, 1992).

3.3 Results

3.3.1 Dorso-ventral gradients mEC network activity

In vitro gamma oscillations were elicited using two concentrations of kainate and recording simultaneously in dorsal and ventral portions of the mEC. Previous reports have shown that concentrations above 200 nM kainate are capable of reliably inducing network activity in the mEC (Cunningham *et al.*, 2003, 2004, 2006; Beed *et al.*, 2013; Klein *et al.*, 2016). However, since the majority of studies were conducted using horizontal brain sections, the implications for a parasagittal preparation were unclear. Therefore, a higher concentration (500 nM) was also used for comparison.

In this slice preparation, application of 200 nM kainate was capable of producing gamma oscillation activity within mEC (fig 3.1). As reported previously (Beed *et al.*, 2013; Klein *et al.*, 2016), this activity was also shown to be of larger amplitude in dorsally located recording electrodes than those in ventral aspects of mEC (fig 3.2A), with little variation in gamma oscillation frequency (fig 3.2B). Network activity was shown to be abolished by addition of picrotoxin (50 μM) into the extracellular solution, consistent with the critical dependence of $GABA_A$ receptor activity for the occurrence of in vitro gamma oscillations (Cunningham *et al.*, 2003).

While these recordings produced synchronous activity, gamma oscillation power was found to be low in both recording sites. In order to further push the system into oscillatory activity a higher concentration of kainate was used. Application of

500 nM kainate produced significantly larger oscillations in both dorsal and ventral mEC (2-way ANOVA, main effect – concentration: $F = 13.8$, $p = 0.006$, location: $F = 4.4$, $P = 0.04$, fig 3.2C). Under these conditions of more robust oscillatory activity, it was also evident that the frequency of stimulated gamma oscillations was dependent on dorso-ventral mEC location (2-way ANOVA, main effect -location: $F = 5.0$, $P = 0.03$, fig 3.2D). During treatment with 500 nM kainate, the maximum observed oscillatory frequency was greater in dorsal recording sites when compared to ventral (dorsal: 81.8 ± 2.3 Hz, ventral: 53.0 ± 2.6 Hz, $p = 0.008$, $n=13$; post-hoc Bonferroni corrected comparison). Interestingly, the time-course of gamma oscillation frequency appeared to vary across the mEC (fig 3.3), with activity in the dorsal regions producing peak frequency earlier in the recording session (dorsal: 21.8 ± 1.8 min, ventral: 34.5 ± 4.7 min; Paired T-test; $p = 0.008$, $n=13$) and decreasing over time to become coherent with ventral mEC recording electrodes.

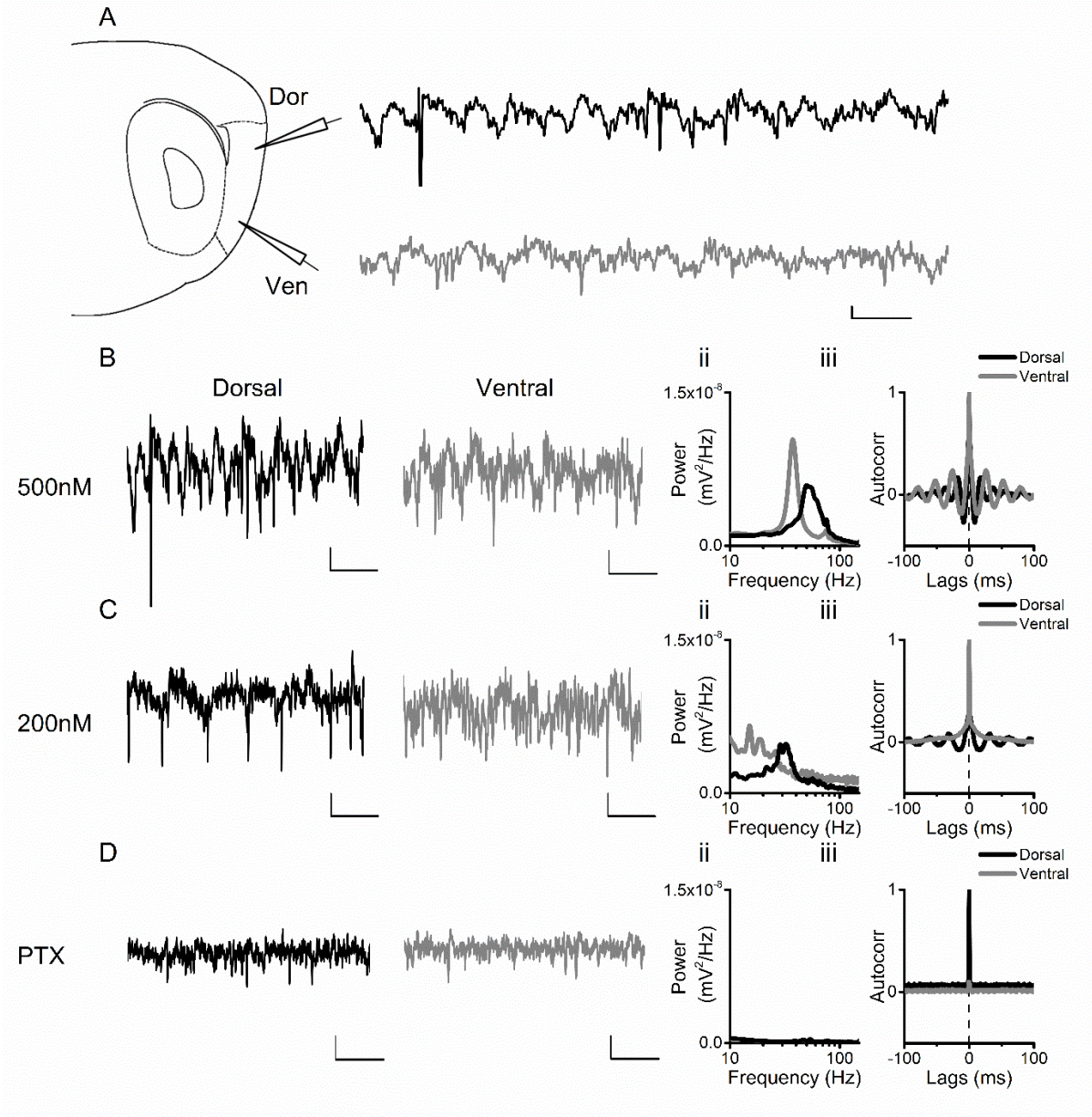

Figure 3.1: Kainate application produces gamma oscillations (30-100 Hz) at both dorsal and ventral ends of mEC. A) Relative position of dorsal (top) and ventral (bottom) recording electrodes with example traces (scale bar: 50 uV, 20 ms). Example traces shown of gamma oscillations recorded after 500 nM (B) and 200 nM (C) kainate application with corresponding power spectrum (ii) and autocorrelation (iii). D) Gamma oscillations induced by 500 nM kainate were abolished after addition of picrotoxin (PTX) (50 uM). Scale bars 50 uV, 40 ms.

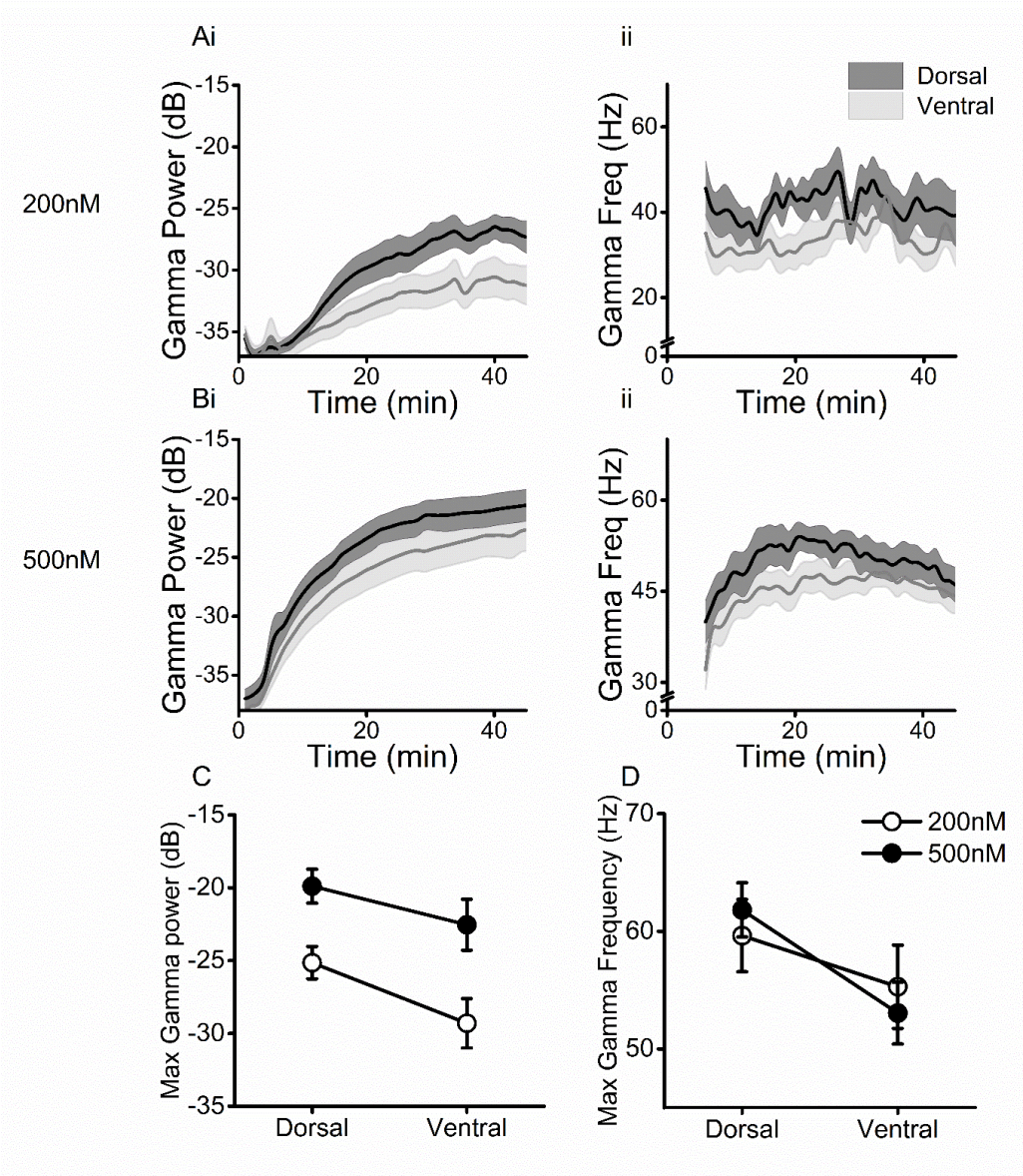

Figure 3.2: Gradient in gamma oscillations along the dorsal-ventral axis of the mEC. A) Pooled time-course data showing development of gamma oscillation amplitude (i) and frequency (ii) in dorsal (black) and ventral (grey) recording sites following bath application of kainate (200 nM). Solid line represents mean (±SEM in shaded areas) in 60s bins, n = 7. B) Time-course after 500 nM application of kainate, n = 13. C) Summary data showing mean (±SEM) maximum gamma power (and frequency (D) in dorsal and ventral mEC. 2-way ANOVA shows significant main effect of recording location ($F = 4.33$, $P = 0.044$) and Concentration ($F = 14.07$, $p<0.001$) on maximum gamma power. D) Significant main effect of recording location ($F = 6.53$, $p=0.015$) but not concentration ($F=0.0019$, $p = 0.97$) (2-way ANOVA).

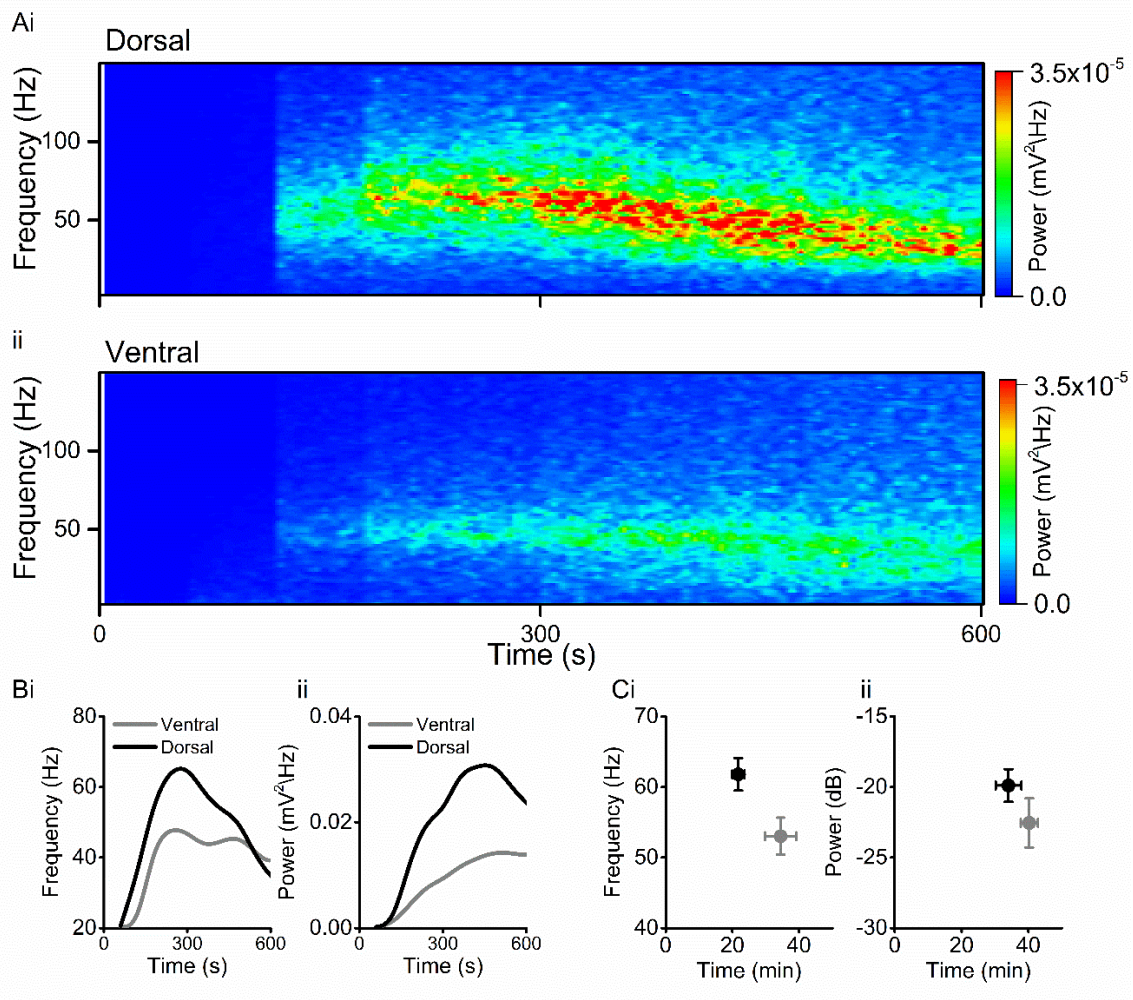

Figure 3.3: Time-course of gamma oscillation onset. A) Example spectrograms for dorsal (i) and ventral (ii) mEC recording electrodes, showing emergence of gamma oscillation activity after application of 500 nM kainate at time 0 s. B) Corresponding plots showing peak frequency (i) and total power (ii) in the gamma frequency band for 1 min bins across recordings. C) Pooled data showing peak frequency (i) and peak power (ii) recorded across sessions and the mean time at which they were recorded.

3.3.2 Disinhibition of mEC produces hyperexcitatory bursting activity originating the ventral mEC regions

As described above, application of pictroxin (50 uM) was sufficient to eliminate gamma oscillation activity in mEC slices (fig 3.4). However by completely eliminating GABAergic transmission, whilst maintaining enhanced levels of excitation it is likely that the network will produce periods of hyperexcitability.

Indeed, co-application of kainate and picrotoxin resulted in interictal-like events at both dorsal and ventral recording sites (fig 3.4A,B). Interestingly, under these conditions, bursting activity was led by ventral mEC, such that individual bursts were almost always initiated at the ventral end of the mEC (fig 3.4B,E). Furthermore, the onset of bursting activity was also seen to appear first at ventral recording sites (434 ± 56 s after kainate/picrotoxin application) compared to those in the dorsal aspect of mEC (635 ± 98 s) (fig 3.4D, Paired T-test, P = 0.01, n= 8 slices from 5 animals), though upon reaching equilibrium bursting occurred uniformly across the mEC (fig 3.4C).

To further test the hypothesis that the ventral mEC is more excitable than the dorsal, the two ends of the mEC were anatomically separated with a scalpel cut (fig 3.5A). This allowed examination of whether the dorsal mEC would produce interictal-like bursting independently, rather than as a result of ventral mEC hyper-excitability. Slices cut in this manner produced interictal bursting in both ventral and dorsal recording sites. Similar to control (uncut) slices, the initiation of bursting activity was first recorded in the ventral mEC after kainate/picrotoxin application (fig 3.5D, Paired T-test, P = 0.025, n= 4, from 4 animals). However, in contrast to observations in intact control mEC slices, it was evident that events in cut dorsal mEC slices occurred at a slower rate when compared to ventral (fig 3.5B, C). At ventral mEC recording sites, burst frequency was similar between cut and control slices (fig 3.5D). Conversely, bursts in the cut dorsal mEC occurred at a slower frequency than those in intact mEC slices (fig 3.5E; frequency at 30 mins: cut- dorsal: 8.1 ± 4.2, ventral: 20.3 ± 3.3; control - dorsal: 16.1 ± 2.9, ventral: 19.25 ± 3.0, main effect: dorso-ventral: p = 0.006 F = 4.1; interaction: p = 0.06, F = 4.2; 2-way repeated measures ANOVA). As expected, the cross-correlation between dorsal and ventral electrodes was largely absent following anatomical separation of the dorsal and ventral mEC, illustrating that the two regions had become desynchronised (fig 3.5G,H; max correlation: control: 0.6 ± 0.1, cut: 0.22 ± 0.1; Unpaired T-test, p = 0.03, n = 4/8 slices from 4/5 animals). Taken together these findings suggest that the dorsal mEC is less likely to produce epileptiform activity in the absence of the ventral mEC.

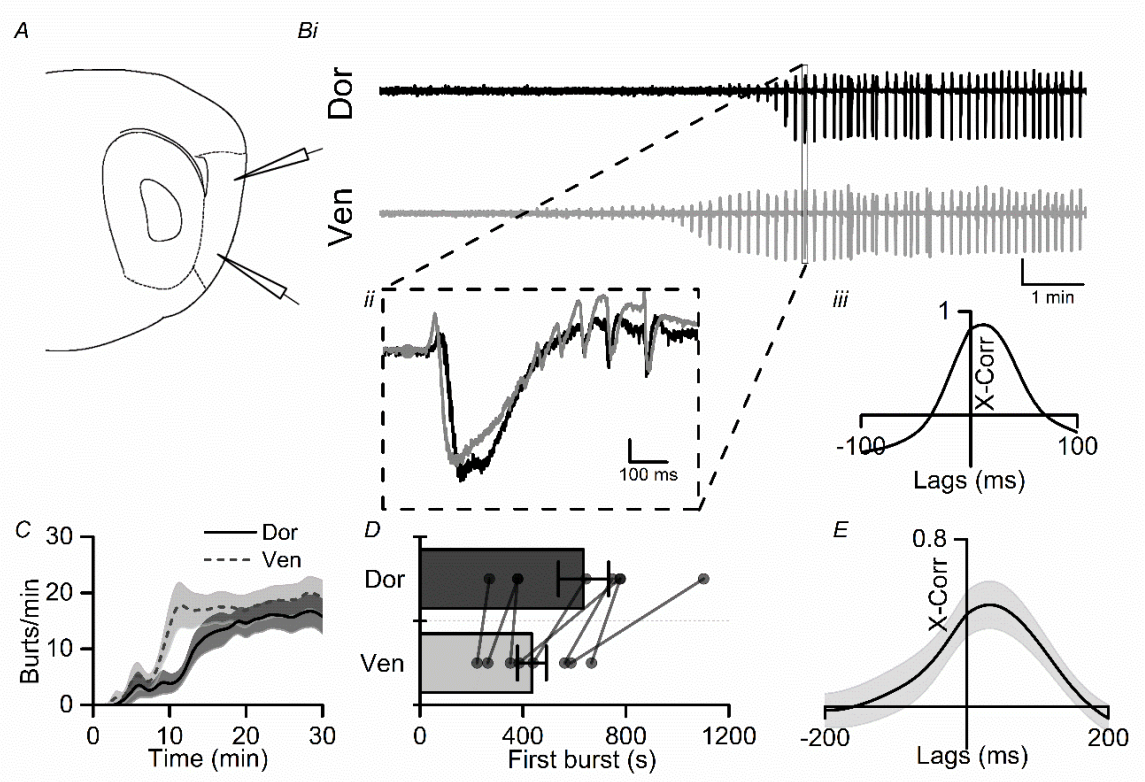

Figure 3.4: Application of 500 nM kainate and 50 µM picrotoxin produces interictal-like events which originate in ventral mEC. A) Relative position of glass recording electrodes in dorsal (top) and ventral (bottom) mEC. B) Example trace after application of picrotoxin (50 µM), box represents one interictal event (ii) with cross correlation (iii) showing peak occurring in ventral mEC before dorsal (scale bar: 0.1 mV). C) Average time-pooled data showing the development of burst frequency (/min) in dorsal (black) and ventral (blue) mEC (n=8 slices from 5 animals). Solid line represents mean (± SEM in shaded areas) D) Mean (±SEM) time in seconds until first recorded epileptic event is shorter in ventral than dorsal mEC (Paired T-test p = 0.013) (n=8 slices from 5 animals). D) Average cross correlation between dorsal and ventral events (n=8 slices from 5 animals) showing peak lag time >0 s.

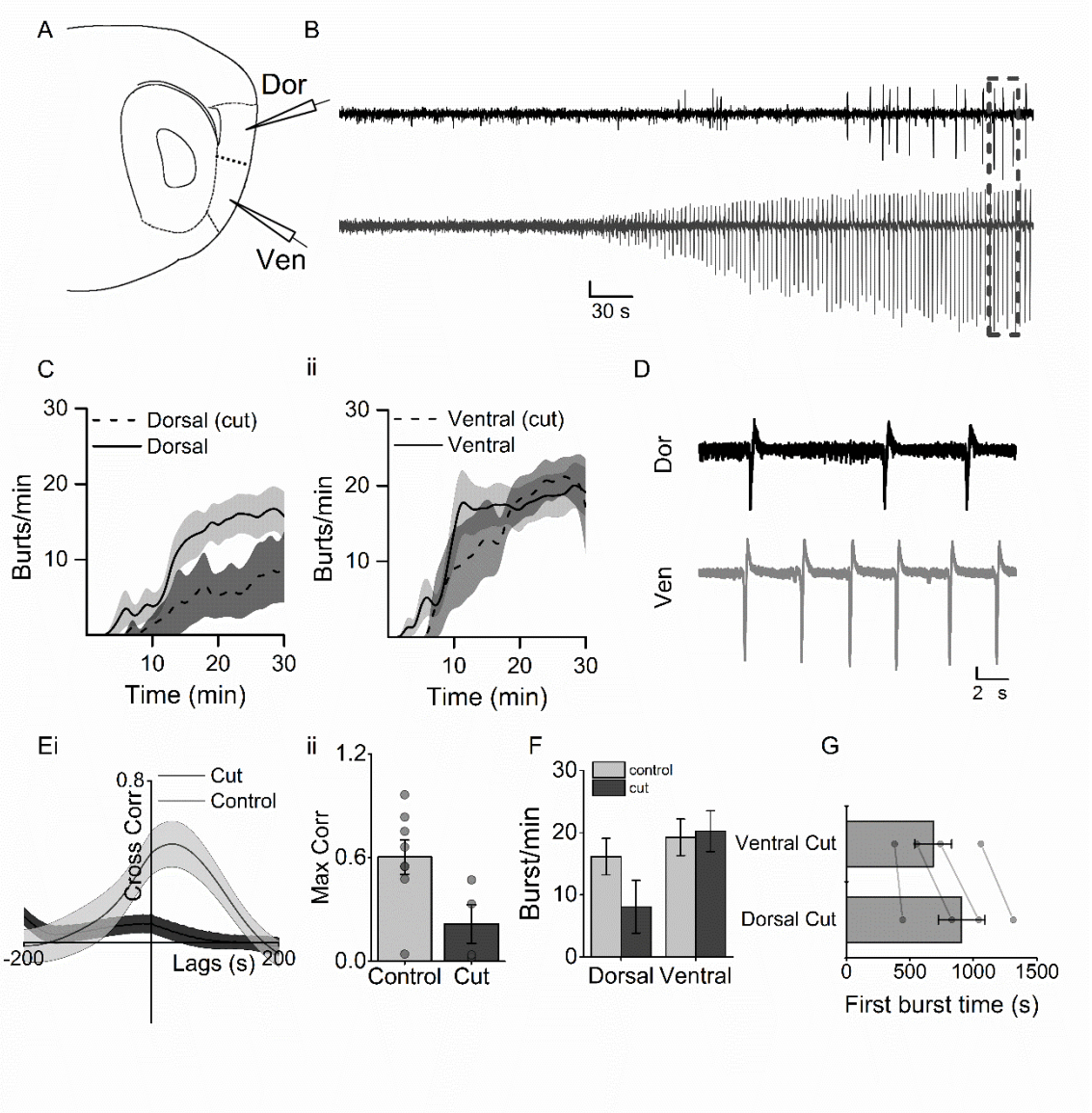

Figure 3.5. Separation of dorsal and ventral mEC produces preferential decrease in epileptic events in the dorsal mEC. A) Relative position of dorsal (top) and ventral (bottom) recording electrodes with scalpel cut (dotted line) between electrodes and example trace (B) (scale bar 0.2 mV, 30 s). C) Averaged time-pooled data showing the development of burst frequency in dorsal (i) and ventral (ii) cut slices compared to control (n=4). D) zoomed plot of data shown in box (dotted line) showing incoherent burst activity (scale bar 0.2 mV, 2 s). E) Average cross correlation of cut slices (n=4 slices from 4 animals) compared to controls (n=8 slices from 5 animals), shows significant decrease in correlation of epileptic bursts (ii) (unpaired T-test P = 0.031). F) Decreased average burst frequency in dorsal mEC in cut slices compared to control. G) Bar graph showing mean (±SEM) time in seconds until first recording epileptic event is also shorter in ventral than dorsal mEC when ends are separated (Paired T-test p = 0.026) (n=4 slices from 4 animals).

3.3.3 Role of dorso-ventral gradients in mEC hyperexcitability

By removing inhibitory drive in the mEC, these data suggest that the intrinsic properties of ventral mEC excitatory cells play a key role stereotyped patterns of hyperexcitability in this region. To further understand the emergence of epileptiform activity in this region, compounds were used to elicit activity that more closely resembles generalized, ictal-like seizures.

While several studies have observed the effect of convulsant compounds on the mEC (Barbarosie & Avoli, 1997; Gnatkovsky *et al.*, 2008; Berretta *et al.*, 2012; Lévesque *et al.*, 2016), differences in hyperexcitability across the anatomical extent of this cortical area are less well understood. Electrical activity was therefore recorded from 16 sites across the dorso-ventral axis of the mEC, perfusing compounds commonly used to induce epileptiform activity.

As reported previously (Nagao *et al.*, 1996; Gulyás-Kovács *et al.*, 2002; Gonzalez-Sulser *et al.*, 2011), bath application of 4-AP (100 µM) was shown to reliably induce both ictal- and interictal-like bursting activity in mEC (fig 3.6). A wavelet transform-based time-frequency analysis of individual bursts revealed that interictal-like discharges consisted of waveforms which were readily apparent in the 1- 10 Hz range. In contrast, ictal-like activity comprised repetitive, large amplitude events which were apparent in the 1-10 Hz range on the wavelet scaleogram, but in addition these longer discharges were also associated with higher frequency activity (10-30 Hz) (fig 3.7).

Interictal-like activity comprised brief (<1 s) paroxysmal discharges which appeared to be relatively synchronous along the dorso-ventral axis of the mEC. Individual interictal-like event traces were detected using a threshold detection approach. Using an unsupervised *k*-means clustering approach (see Methods) waveforms were grouped based on the time of the peak of the waveforms. This approach usually resulted in 2-3 clusters of waveforms, which corresponded to bursts which were initiated at different sites. In the example in Figure 3.8B, there was an approximately even split between interictal waveforms travelling in a ventral-to-dorsal and a dorsal-to-ventral direction, suggesting that these bursts were initiated at multiple sites along the dorso-ventral axis of the mEC. The maximum time between interictal peaks across the 16 recording sites averaged 356 ± 30 ms (n=10 slices from 8 animals).

Ictal-like discharges occurred in all the slices tested, appearing first after 1166 ± 148 s and continuing with an average interval of (259 ± 14 s). Interestingly, ictal activity was substantially more likely to be first detected in the most ventral mEC recording sites than those located in more dorsal aspects of mEC. In total (37/43) ictal bursts were first detected in ventral mEC compared to (6/43) in dorsal (fig 3.6D). The propagation of activity from ventral to dorsal recording sites was shown to occur over a prolonged time frame (linear regression: R^2 = 0.98, p <0.001, slope = 128.2 ± 4 µm/s), meaning that ictal activity in the most dorsal electrode occurred 15.5 ± 3.4 s (n=10 slices from 8 animals) after the initiation of the event in the most ventral electrode (fig 3.6E).

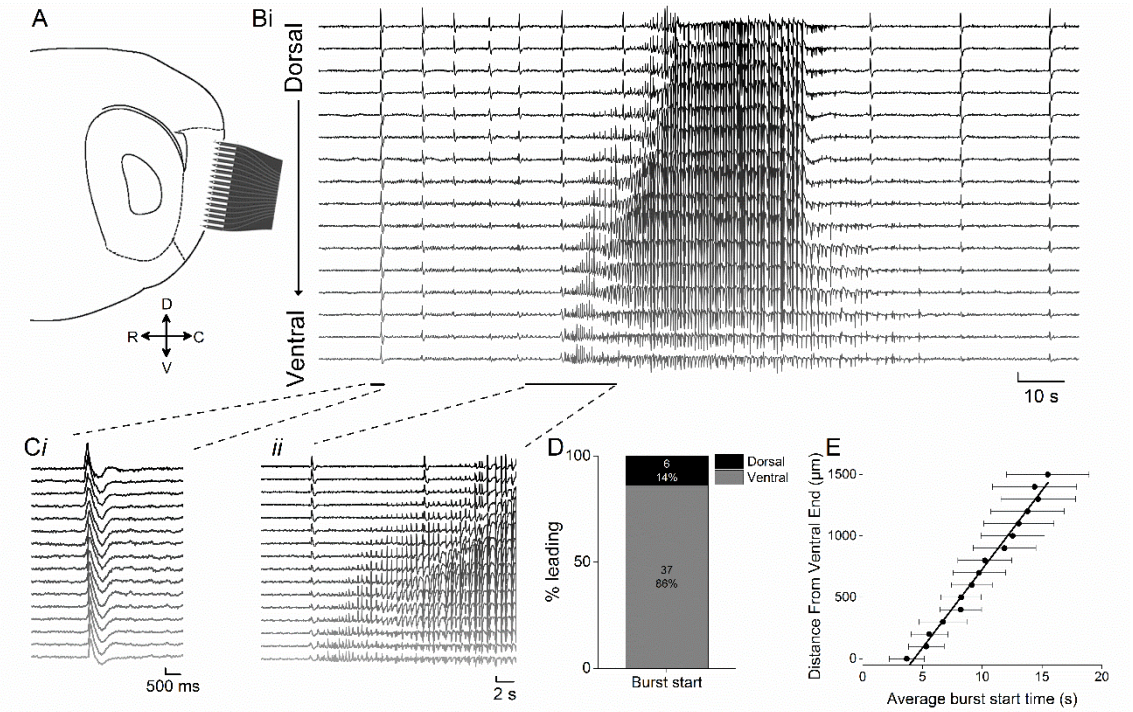

Figure 3.6: 4-AP induced ictal-like activity in mEC is initiated in ventral recording sites. A) Recording position of 16-shank electrode array on parasagittal mEC slice, with scale depicting dorsal (D), ventral (V), rostral (R) and caudal (C) directions. B) Example ictal-like bursting activity from dorsal (top) to ventral (bottom) mEC showing bursting recorded first in most ventral electrode site, (scale bar: 200 µV, 10 s). C) Zoomed examples of (i) interictal- and (ii) ictal-like events (scale bars: 100 µV, 0.5 s and 200 µV, 2 s respectively). D) Proportion of bursts starting at dorsal and ventral recording sites (n = 123 bursts from 10 slices slices from 8 animals). E) Average start time of burst relative to first channel to meet threshold for ictal activity increases linearly with distance from ventral pole, linear regression: R^2 = 0.98, p <0.001, slope = 128.2 ± 4 µm/s In dorsal mEC recording sites, bursts start 15.5 ± 3.4 s after initiation of event.

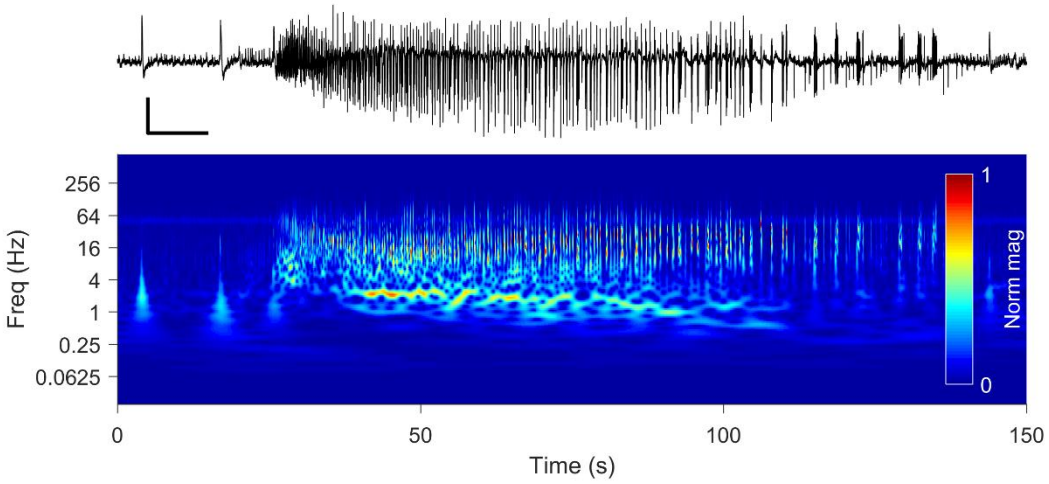

Figure 3.7: Time-frequency analysis of ictal- and inter-ictal like bursts. Top panel is an example recording from a ventrally positioned electrode, illustrating 2 interictal like waveforms (first two vertical deflections) followed by an ictal-like burst (scale bar: 0.2 mV, 10 s). The bottom graph is a continuous wavelet transform scalogram, illustrating the frequency components of the above recording. Note that the interictal-like bursts consist mainly of lower frequency (1-10 Hz) components, whilst the ictal burst is associated with both lower frequency and higher frequency (10-30 Hz) events.

Closer examination of the burst waveforms within an ictal event indicated that the individual spike-wave discharges were initiated in the ventral regions of the mEC. To quantify this, cross-correlations were performed on data binned across time between the most ventral recording site and each of the subsequent dorsal electrodes. Figure 3.9A/B shows recordings taken from dorsal and ventral poles of the electrode array, with dorsal-ventral cross-correlation values for each time bin displayed in the colour "heatmap" axis (fig 3.9Aii). During the ictal bursting, activity across the dorsal and ventral electrodes became highly synchronous with largely positive lag time values, indicating that activity was largely led by the ventral mEC. The proportion of 1s time bins with correlation peaks in the positive (ventral leading) was shown to be significantly greater during ictal events when compared to non-ictal bins (fig 3.9D, paired T-test, P= 0.002, n = 10 slices from 8 animals). The lag time associated with the maximum correlation values were also observed to linearly increase with distance from the most ventral recording site. This indicates within-burst activity is spreading in the ventral to dorsal direction (fig 3.9C, linear regression: R^2 = 0.93, p <0.001, slope =55.9 x10^3 ± 5 x10^3 µm/s).

The relatively slow spread of ictal-like waveforms from ventral to dorsal recording sites, suggests that some process regulates and dampens spike-wave propagation from the ventral to dorsal poles of the mEC. Since there is a gradient in GABAerigc inhibition along the dorso-ventral axis of the mEC (Beed *et al.*, 2013; Booth *et al.*, 2016*a*), it is reasonable to suggest that a greater inhibitory drive onto principal cells in the dorsal mEC may be responsible for the slow spread of ictal-like discharge activity (fig 3.6). To examine this hypothesis, we pharmacologically modulated postsynaptic GABAergic receptors during pre-established 4-AP-induced ictal-like activity. Application of diazepam, a positive allosteric modulator of $GABA_A$ receptors, significantly decreased the speed of ictal propagation by ~2 fold (fig. 3.10Ai, B), from 147.5 ± 23 µm/s to 64 ± 14 µm/s (fig 3.10Cii, Paired T-test, $P<0.001$, n= 6 slices from 6 animals). Conversely, the application of $GABA_A$ receptor inverse agonist, Ro19-4603, significantly increased propagation speed by ~7.5 fold (170.3 ± 45 µm/s to 1272.7 ± 117 µm/s) when compared to paired baseline, such that burst initiation was almost instantaneous along from ventral to dorsal mEC (fig 3.10Dii, Paired T-test, $P<0.001$, n= 6 slices from 6 animals).

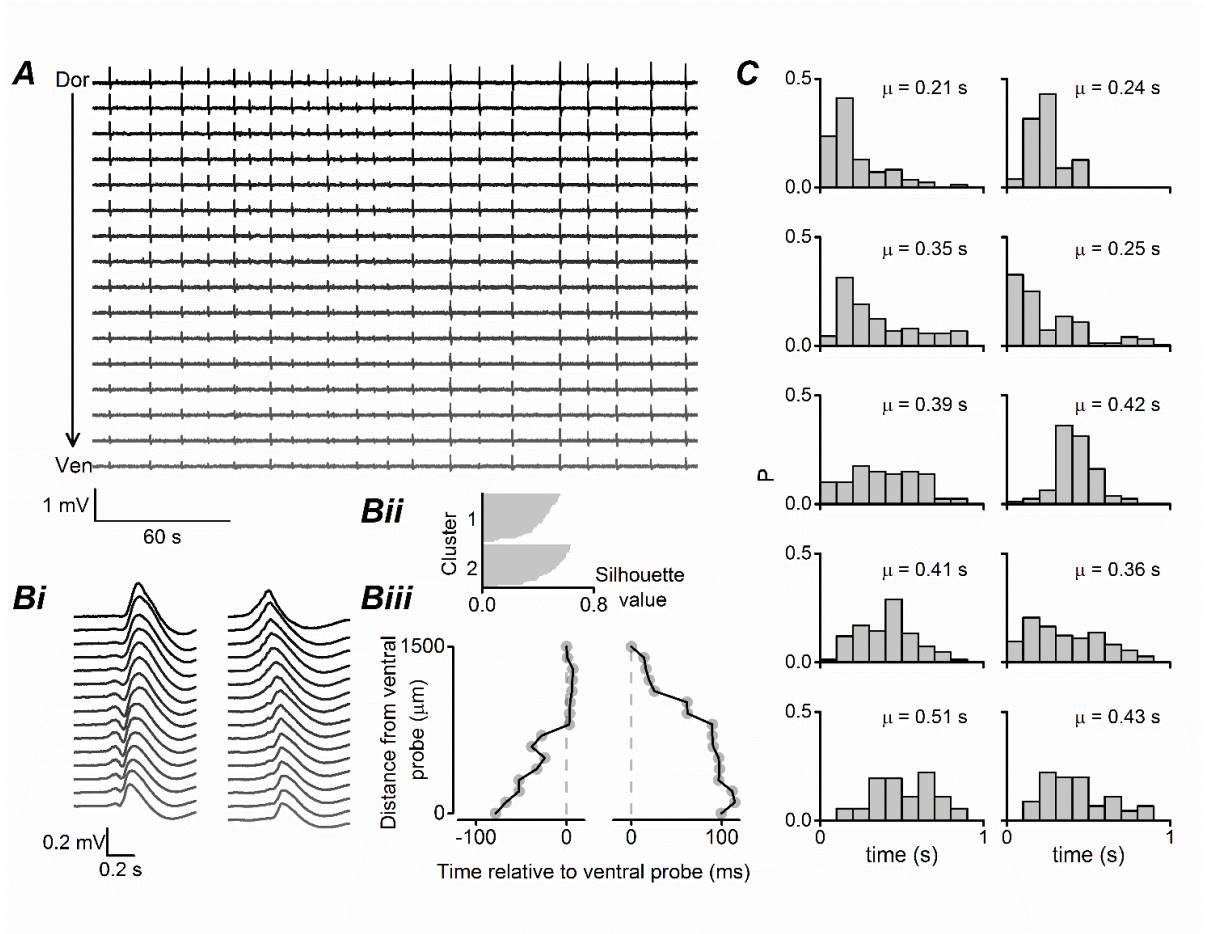

Figure 3.8: Interictal-like bursts are generated in both dorsal and ventral portions of the mEC. A) An example recording of interictal-like bursts recorded using a 16-shank electrode array on parasagittal mEC slice. This 4.5 minute segment of data was recorded between 2 ictal like bursts (not shown). Numerous interictal-like bursts were observed, visible on this time scale as brief vertical deflections on the recording. B) Individual bursts were detected and clustered into groups according to the time of the waveform peak. In this recording, two groups were identified, the average waveforms of which are depicted in (i). (ii) Silhouette plot of the resulting k-means clustering algorithm. The time of the average waveform peak (plotted relative to the time on the most ventral probe) for the two clusters in shown in (iii). These data illustrate that interictal bursts are initiated at different points along the dorso-ventral axis of the mEC. C) Probability histograms showing the maximum difference in interictal peak times across all 16 probes for 10 different slices. The mean (μ) maximum difference in peak times is shown for each distribution. These data illustrate that, on average, interictal bursts take 0.2-0.5 s to spread along the dorso-ventral axis of the mEC.

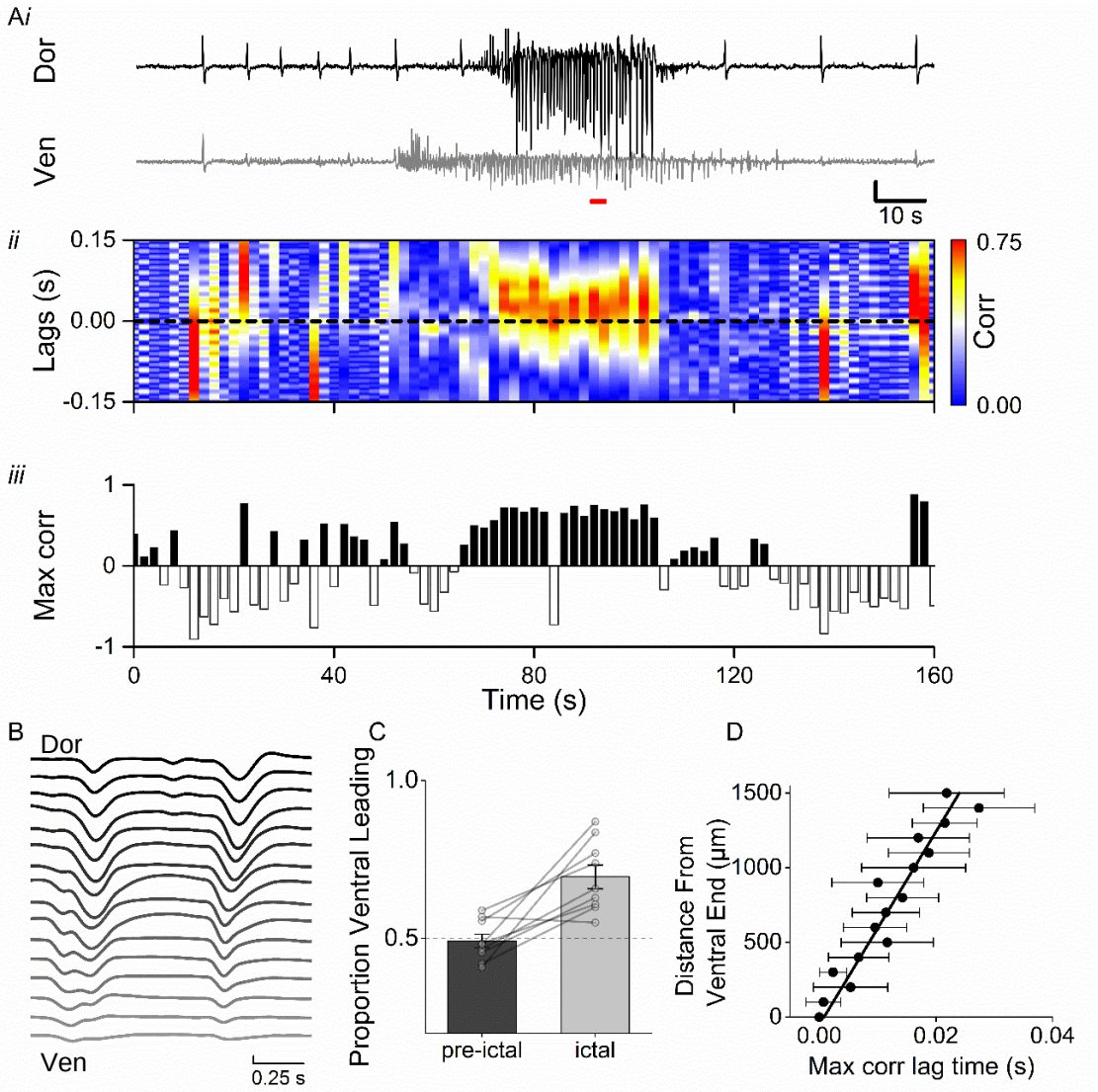

Figure 3.9: Intra-ictal burst waveforms initiated in ventral mEC regions. Ai) Example traces from most dorsal (top) and ventral (bottom) recording sites of electrode array (scale bar: 100 µV, 10 s): with (ii) binned cross correlations for every 1 second of data. Correlation values are shown in the colour axis, with positive peaks indicating ventral-leading activity and negative peaks dorsal-leading (iii). B) Example of intra-burst activity across 16-shank electrode array initiating in ventral mEC during red bar in A (scale bar: 200 µV, 250 ms). C) Lag time associated with peak cross correlation between most ventral site and each dorsal recording electrode, shows linear increase with distance from ventral pole (linear regression: R2 = 0.93, p <0.001, slope =55.9 ± 5 mm/s). D) Proportion of 1s time bins with correlation peaks in the positive (ventral leading) greater during ictal events when compared to non-ictal bins (paired T-test, P= 0.002, n = 10 slices from 8 animals).

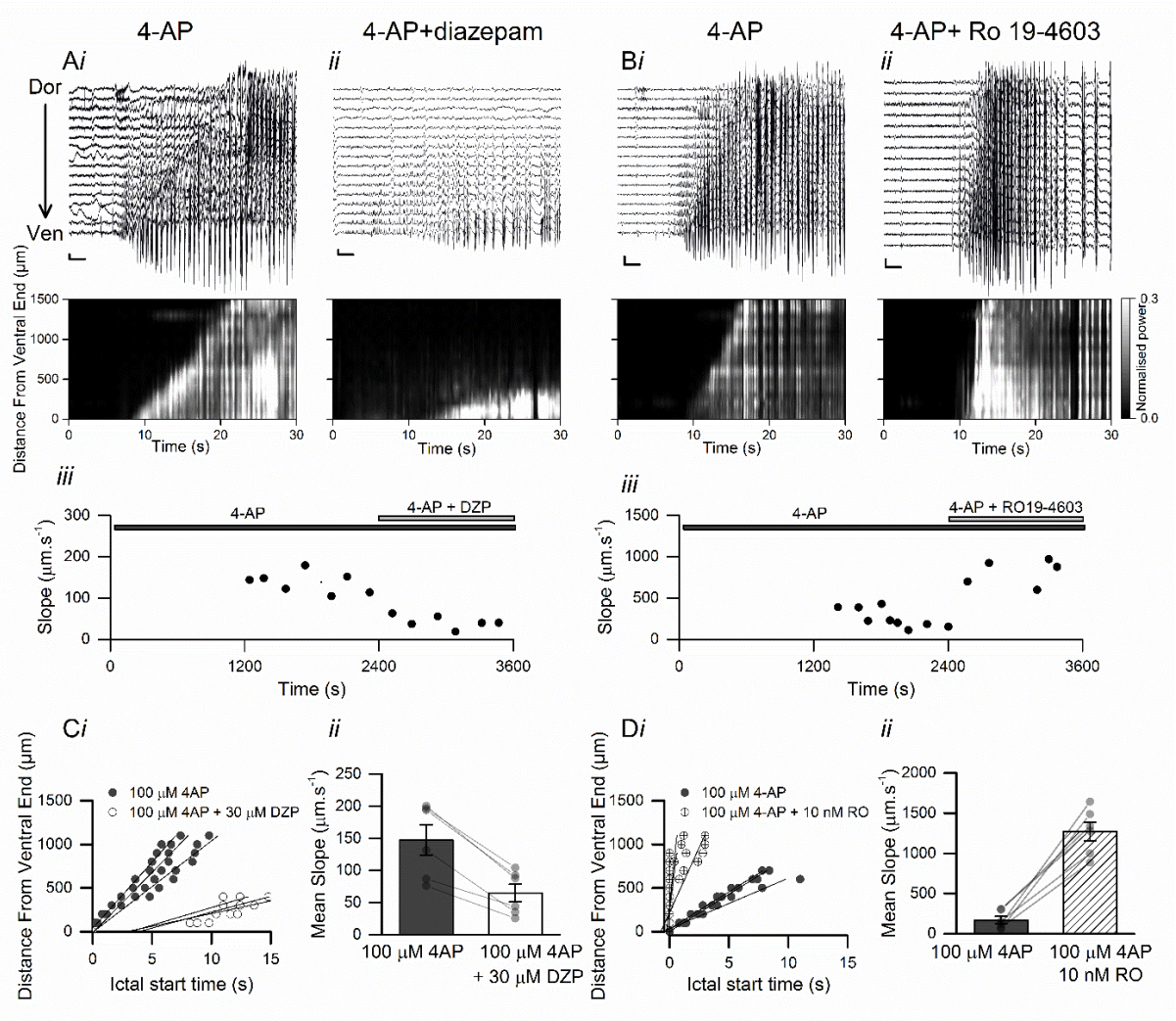

Figure 3.10: Modulation of GABAergic transmission changes slope of ictal-like propagation in mEC slices. A) Example traces of ictal-like events (top) with normalised power (bottom) on 16-shank recording array after application of 4-AP (scale bar: 500 µV, 5 s) (Ai/Bi) and subsequent application of diazepam (DZP) (30 µM) (Aii) or Ro19-4603 (RO) (10 nM)(Bii). Aiii/Biii show time-course of ictal burst slope before and after manipulation of GABAergic transmission C) Decreased ictal slope in example slice after diazepam application (white) compared to 4-AP alone (grey), 3 ictal bursts shown pre- (1800-2400 s) and post (3000-3600 s) –drug, with mean slope decreasing ~2 fold (ii) (Paired T-test, P<0.001, n= 6 slices from 6 animals). D) Ictal propagation is faster after application of Ro19-4603 (i) (Paired T-test, P<0.001, n= 6 slices from 6 animals), (ii). Data was collected in collaboration with P. Mathews.

3.4 Discussion

3.4.1 Summary

The data presented above clearly show that the dorso-ventral organisation of the mEC can have pronounced effects on neuronal network activity *in vitro*, both in the production of gamma frequency oscillations and in network activity associated with periods of hyperexitability.

By pharmacologically inducing gamma oscillation activity using low concentrations of kainate and recording simultaneously from dorsal and ventral mEC, these data show that dorsal regions are capable of producing both larger and faster network activity. Additionally, after removing inhibition in mEC slices, it was also evident that ventral regions were more prone to the onset of hyperexcitable discharges, which propagated to the dorsal end within several milliseconds. When inhibition remains intact, ictal-like epileptiform activity was also initiated in ventral mEC. However, the propagation of this large-scale seizure activity along the dorso-ventral axis occurred in a surprisingly slow time-frame, taking ~15 s to reach the most dorsal regions of the recording array (approximately 1.5 mm). Furthermore, by pharmacologically modulated GABAergic tone, it was shown the speed of ictal propagation depends heavily on dorso-ventral organisation of inhibition in the mEC.

3.4.2 Dorso-ventral gradient in mEC gamma oscillation properties *in vivo*

The data presented in this chapter support the findings of Beed et al., (2013), that kainate-induced gamma oscillations are larger in dorsal mEC than ventral (fig 3.2). However, they are the first to show differences gamma oscillation frequency across these regions. These discrepancies are likely due to the concentrations of kainate used in each experiment, with only higher concentrations capable of producing increased gamma oscillation frequency (fig 3.2D). Furthermore, maximal gamma frequencies were reserved for early time periods after kainate application, returning to those more similar to ventral over the course of the experiment. This shows, at least in principle, that dorsal mEC networks are capable of maintaining oscillations that are not coherent with ventral oscillations.

Whether these results are a result of multiple gamma generators in the mEC is unclear. However, since gamma oscillations are suggested to provide a rigid temporal framework for communication, in which only coherent neuronal ensembles can interact successfully (Fries, 2005), independent frequencies across the mEC may represent independent information flow to downstream areas. For example, dorsal mEC neurons project more prominently to the dorsal hippocampus, and ventral mEC neurons project mainly to ventral hippocampus, with these areas potentially having differing role in cognitive processing (Fanselow & Dong, 2010).

Parvalbumin (PV) positive interneurons are critical for the generation of gamma oscillations, both *in vivo* and *in vitro* (Cunningham *et al.*, 2003; Cardin *et al.*, 2009; Sohal *et al.*, 2009). The increased inhibitory drive in dorsal mEC (Beed *et al.*, 2013) is most likely to contribute to the larger gamma oscillations observed. However, the gradients seen in intrinsic properties of mEC stellate cells (Giocomo *et al.*, 2007; Garden *et al.*, 2008; Boehlen *et al.*, 2010; Dodson *et al.*, 2011; Pastoll *et al.*, 2012; Navratilova *et al.*, 2012; Yoshida *et al.*, 2013; Booth *et al.*, 2016*a*) may also have implications for network properties, since excitatory cells are also necessary for gamma generation (Cunningham *et al.*, 2003).

3.4.3 Ventral mEC regions drive network activity during periods of hyperexcitability

This study is the first to highlight the differential role of dorsal and ventral mEC in the generation of hyperexcitable events *in vitro*. In essence, it is likely that previously reported gradients in inhibitory networks (Beed *et al.*, 2013) and intrinsic membrane properties (Garden *et al.*, 2008; Giocomo & Hasselmo, 2009; Boehlen *et al.*, 2010; Booth *et al.*, 2016*a*) combine to make the ventral mEC more prone than the dorsal mEC to the generation of epileptiform discharges.

Bath application of 4-AP resulted in complex neuronal network behaviours in parasagittal slices of the mEC, consisting of both ictal- and interictal-like spike-wave discharges (fig 3.6). This combination of brief and prolonged epileptiform activity has been extensively studied previously, both in the entorhinal cortex (D'Antuono *et al.*, 2010; Avoli *et al.*, 2013; Lévesque *et al.*, 2016) and other brain regions such as the hippocampus (Nagao *et al.*, 1996; Gonzalez-Sulser *et al.*,

2011; Berretta *et al.*, 2012). Nevertheless, the propagation of this activity within the entorhinal cortex has not previously been observed. Indeed, many of these previous studies have often considered the entorhinal cortex as a homogenous structure. Using multi-site extracellular recording techniques interictal-like events were observed which generally propagated along the full extent of the dorso-ventral axis of the mEC. By detecting individual bursts and statistically grouping them on the basis of the relative time of the waveform peak, it was established that interictal-like discharges could be generated at multiple points along the dorso-ventral axis (fig 3.8). Furthermore, bursts propagated from the site of origin to the furthest extent of recording probes (maximum distance 1.5 mm) within a few tenths of a second.

In contrast, the slow time-frame of the spread of the ictal-like activity was surprising. On average ictal-like events initiated in the ventral mEC spread dorsally with a velocity of ~ 130 μm/s, taking ~15 s to propagate to the most dorsal aspects of mEC. However, once ictal-like behaviour was apparent in both dorsal and ventral poles of the mEC, the spike-wave discharges became tightly synchronised, albeit with the ventral burst generally preceding the dorsal bursts by a few milliseconds. Given that axonal action potential conduction velocity and synaptic transmission is several orders of magnitude faster than the ictal propagation speed, it is likely that ictal propagation is constrained by differential levels of GABAergic control along the dorso-ventral axis of the mEC (Beed *et al.*, 2013; Booth *et al.*, 2016*a*). In support of this, application of pharmacological agents that increased (diazepam) or decreased (Ro19-4603) postsynaptic $GABA_A$ receptor activation respectively reduced or increase the slope of ictal initiation (fig 1.10).

In this context, it is pertinent to note that mEC stellate cells are unlikely to form large numbers of recurrent excitatory connections, with less than 1 in 500 pairs of stellate cells being synaptically coupled (Pastoll *et al.*, 2013*b*; Couey *et al.*, 2013). Fast spiking GABAergic interneurons, in contrast, form a powerful recurrent inhibition circuit, with stellate cells connecting primarily to interneurons which in turn project back predominantly onto other stellate cells (Couey *et al.*, 2013; Buetfering *et al.*, 2014). In this situation, the anatomical arrangement of such inhibitory connections will have strong implications for the generation of epileptiform events. Dorsal mEC stellate cells receive a greater number of

inhibitory inputs than those in ventral mEC, however, perhaps more significantly, they receive a greater proportion of their inputs from more distal inhibitory neurons (Beed *et al.*, 2013). This would therefore suggest that ictal events would need to overcome an increasing level of feed-forward inhibition as they travel from ventral to dorsal mEC.

Several reports suggest the activity of GABAergic interneurons regulates seizure initiation. The period immediately before ictal events can be characterized by an increased interneuron firing that reaches its peak at ictal onset, while the activity of principal cells does not change until after initiation (Ziburkus *et al.*, 2006; Lévesque *et al.*, 2016). Additionally, optogenetic activation of GABAergic interneurons was shown to be capable of suppressing ictal seizure activity in mEC *in vivo* (Lu *et al.*, 2016). Taken together, one interpretation of these findings is that GABAergic systems act to control the initiation of seizure-like events. Coupled with the high density of PV-positive staining in the dorsal mEC, this would suggest that the dorsal mEC would be less likely to initiate an ictal bursts than the ventral mEC.

The intrinsic properties of mEC stellate cells are also likely to play a role in the organisation of epileptiform activity. In this regard, it has been widely reported that ventral mEC stellate cells exhibit a higher input resistance, a slower membrane time constant and a lower action potential threshold compared to dorsal mEC stellate cells (Garden *et al.*, 2008; Giocomo & Hasselmo, 2009; Boehlen *et al.*, 2010; Booth *et al.*, 2016*a*). Combined, these cell intrinsic properties will produce higher levels of excitability in the ventral mEC, with less current required to produce action potential firing and greater levels of synaptic integration (Garden *et al.*, 2008). Consequently, even in the absence of GABAergic inhibition, one might expect to observe an increased propensity for epileptiform bursting in the ventral mEC when compared to the dorsal mEC. This hypothesis was tested by incubating mEC slices in a blocker of $GABA_A$ receptors (picrotoxin) along with a glutamate receptor agonist (kainate) (fig 3.4). The treatment resulted in interictal-like, but not ictal-like, epileptiform discharges. We found that, not only did the disinhibition-mediated interictal-like discharges develop first in the ventral mEC, but that once bursts were established in both dorsal and ventral ends of the mEC, a cross-correlation analysis of individual bursts revealed that the ventral bursts almost always preceded the dorsal bursts.

Furthermore, when the dorsal and ventral poles of the mEC were physically separated with a scalpel cut, bursts recorded from the ventral mEC were of a similar frequency to those in uncut slices, whilst bursts in the dorsal mEC were significantly less frequent than those in the uncut dorsal mEC (fig 3.5). Presumably, in the uncut slices, the dorsal mEC is entrained to the more frequent disinhibition-mediated epileptiform bursts in the ventral mEC. Taken together, these data suggest that the intrinsic properties and/or excitatory synaptic transmission properties (which are intimately linked;(Garden *et al.*, 2008) of ventral mEC neurons predispose this region to seizure like activity, when compared to the dorsal mEC.

In any case, blocking or slowing the propagation of ictal activity is likely an essential characteristic for pharmacological agents designed to treat TLE (Marson *et al.*, 1997; Takeda *et al.*, 1998). It remains to be seen whether results seen here in parasagittal slices are also relevant in the temporal lobe *in vivo*, either in rodent models or human patients. At the very least, this preparation presents a reliable model for testing antiepileptic compounds and their ability to slow down the propagation of ictal events *in vitro*. However, this study suggests that the ventral portion of the mEC is a major site of seizure initiation within the entorhinal cortex, and consequently therapies that target this region may be a more effective strategy in TLE treatment. This is pertinent when differences in gene expression of potential targets along the dorsal ventral axis are factored in and may also be important with approaches that may not readily be able to access all areas of mEC, such as in vivo optogenetics. Furthermore, investigating means to perturb communication between ventral and dorsal regions might disrupt seizure propagation *in vivo,* although this may also generate consequences for spatial navigation.

3.4.4 Relevance of pharmacologically induced network activity

While pharmacologically induced gamma oscillations are undoubtedly a useful tool to study interactions within neuronal networks, it is also clear that they do not necessarily represent physiologically relevant brain activity. The same can be said for the pathological relevance of pharmacologically-induced hyperexcitability. This is particularly evident when assuming similar responses from diseased tissue and tissue that is otherwise healthy, but pharmacologically

challenged. It is therefore important to be wary of drawing conclusions relating to the hyperexcitability presented here and pathological patterns of activity in epileptic patients.

In any case, the experiments in this chapter can be thought of as pharmacological challenges to the system and are able to show how the mEC can respond to acute changes to excitatory or inhibitory tone. It is clear that the specific anatomical and physiological organisation of the mEC infers tight control over its output. This will likely have implications for the function of the mEC as a whole, for example, in spatial navigation and the variety of grid cell activity across the dorso-ventral axis.

3.4.5 Conclusions

The data in this chapter clearly show that previously described dorso-ventral gradients in mEC physiology have pronounced implications for local neuronal networks. Both gradients in the intrinsic properties of mEC stellate cells (Booth *et al.*, 2016*a*) and inhibitory function (Beed *et al.*, 2013) give rise to stereotyped network behaviours which may have implications for both cognitive processing (and therefore its breakdown in dementia) and epileptiform activity.

These data pave the way for further experiments described below, both to confirm these findings *in vivo* and to understand the implications that disease pathology may have on this system.

4. Deficits in mEC network activity in rTg4510 mice

The results shown in the previous chapter establish a clear effect of dorso-ventral location on neuronal network activity in the mEC. The chapters below will discuss how this network activity is influenced by tau pathology. Work presented in this chapter has been published in Booth, Ridler, et al. (2016).

4.1 Introduction

The medial entorhinal cortex (mEC) occupies a pivotal position in the temporal lobe, controlling the flow of information across the hippocampal formation (Amaral & Witter, 1989; Canto *et al.*, 2008). However, the mEC is highly vulnerable to degeneration in Alzheimer's disease (AD) and other forms of dementia (Braak *et al.*, 1991) where tau pathology is a defining feature. This area is most likely to be the first to suffer degeneration, with profound loss of layer II neurons seen in very mild cases of AD (Gomez-Isla *et al.*, 1996). Despite this, relatively little is known about the consequences of tau pathology on mEC function.

4.1.1 rTg4510 model of tauopathy

The rTg4510 mouse is one of the most commonly used models of tauopathy. It was produced by overexpression of the human mutant (P301L) form of tau protein and develops age-dependant neurodegeneration, neurofibrillary tangles and cognitive deficits (Santacruz *et al.*, 2005; Spires *et al.*, 2006; Crimins *et al.*, 2012; Kopeikina *et al.*, 2013; Ramsden *et al.*, 2015). Several studies have now described intrinsic and morphological changes to neurons in these mice, both in the hippocampus (Booth *et al.*, 2016*b*) and cortex (Rocher *et al.*, 2010; Crimins *et al.*, 2012; Kopeikina *et al.*, 2013; Jackson *et al.*, 2017). Many of these point to a dissociation between structural and functional changes, with electrophysiological deficits preceding morphological ones (Crimins *et al.*, 2012) and both alterations being relatively independent of neurofibrillary tangle (NFT) formation (Hoover *et al.*, 2010; Rocher *et al.*, 2010). Indeed, some neurons bearing NFTs are initially capable of integrating functionally into neuronal

networks in cortical areas (Kuchibhotla *et al.*, 2014), suggesting that there may be periods of decline for individual cells across large time frames, rather than rapid cell loss after tau accumulation.

In any case, even small changes of function at the level of the individual neuron can have pronounced effects on the ability of neuronal networks to function effectively. This appears to be the case in the hippocampal CA1 region, with altered intrinsic properties of pyramidal neurons underlying aberrant network oscillations (Booth *et al.*, 2016*b*) and a reduction in sharp-wave ripple activity (Witton *et al.*, 2014). Ultimately, such changes affect the output of the hippocampus, altering the spatial properties of place-field firing sequences (Cheng & Ji, 2013; Booth *et al.*, 2016*b*). It is unclear whether these changes are comparable to those in the mEC, since to date, no studies have observed mEC network function in mouse models of dementia.

4.1.2 Dorso-ventral mEC gradients in rTg4510 mice

The existence of dorso-ventral gradients, ranging from the spacing of grid cells to the intrinsic properties of stellate cells, have already been discussed at length in the previous chapters. However, recent evidence has suggested that dorso-ventral gradients in certain intrinsic membrane properties, such as membrane capacitance and afterhyperpolarizations, are lost in rTg4510 mice (Booth *et al.*, 2016*a*). Specifically, deficits in mEC properties in these mice were limited to dorsal mEC regions, with ventral mEC stellate cells largely unchanged by tau pathology.

Given that, as shown in the previous chapter, mEC network activity is also defined by anatomical location, it was therefore important to determine if such tauopathy-associated deficits occur in the oscillatory activity of dorsal mEC regions. The results shown below aim to answer this question, using a combination of both *in vitro* and *in vivo* electrophysiology.

4.2 Methods

4.2.1 *In vitro* electrophysiology

Male rTg4510 mice (aged 7-8 months) and wild-type (WT) litter mate controls were bred at Harlan Laboratories (Hillcrest, UK) and shipped to the University of Exeter before use. Animals were allowed to equilibrate for at least 7 days after transport and housed on a 12:12h light/dark cycle with *ad libitum* access to food and water. Parasagittal slices containing mEC were cut using the methods described in **section 2.3.** Gamma oscillations, recorded from dorsal and ventral portions of mEC, were elicited by bath application of 500 nM kainate and spectral power and frequency analysed for each 1 min section of data after kainate application. Maximum power and frequency were defined as the highest values irrespective of time.

4.2.2 *In vivo* electrophysiology

Mice were implanted with 16-channel linear silicon probes with 150 µm inter-electrode spacing (fig 2.4A) (NeuroNexus). After at least 1 week post-operative recovery, mice were placed on a novel linear track (1.5 m long) and allowed to explore for 15-20 min. Local field potential (LFP) signals were band-pass filtered (1-500 Hz) and continuously sampled at 2 kHz. Two light-emitting diodes on the headstage and an overhead video camera (sample rate 25 Hz) were used to continuously track the animals' location, allowing estimation of position and running speed.

All data analysis was performed in Matlab (Mathworks). Epochs of LFP were selected where the animal's speed was constant (10-15 cm/s). Spectral analysis of the resulting epochs of LFP was performed using the Chronux toolbox (http://chronux.org/). Modulation index (MI) (Canolty *et al.*, 2006) was calculated to measure phase-amplitude coupling between theta and gamma frequency oscillations using a toolbox available at: http://www.cs.bris.ac.uk/Research/MachineLearning/pac/ (Onslow *et al.*, 2011). A linear regression analysis between probe position and MI was performed and the slope of this line was determined. Furthermore, the Pearson's R value for

each correlation was transformed to a normally distributed Z score for comparison between the two groups.

4.3 Results

4.3.1 *In vitro* gamma oscillation are preferentially impaired in dorsal mEC

Gamma frequency oscillations (induced by continuous bath application of 500 nM kainate) were simultaneously recorded in dorsal and ventral ends of mEC slices as described in the previous chapter (fig 4.1). In WT slices, the maximum spectral frequency (peak after approximately 15 minutes of kainate application) of gamma oscillations was significantly faster in the dorsal (59.0 ± 1.4 Hz) than ventral (55.6 ± 1.5 Hz, n=12; P<0.05, paired t-test) regions of the mEC (fig 4.1D). Furthermore, as described previously (Beed *et al.*, 2013), the maximal power of gamma oscillations was significantly higher in the dorsal (-20.7 ± 1.6 dB) versus ventral (-25.8±1.4 dB, n=12; P<0.05, paired t-test) mEC (fig 4.1D). In contrast, in rTg4510 slices, there was no difference in maximal gamma frequency in the dorsal (53.0 ± 1.4 Hz) and ventral (53.2 ± 1.1 Hz, n=18; P=0.7, paired t-test) mEC. With regard to gamma power, a dorso-ventral gradient was detected in rTg4510 slices, but the direction was reversed such that gamma oscillations in the dorsal mEC were smaller in magnitude that those in the ventral mEC: dorsal power, -32.4 ± 1.0 dB; ventral power, -29.0 ± 0.8 dB (n=18; P<0.05, paired t-test; fig 4.1D)

4.3.2 Broad-band oscillatory activity is impaired in mEC of rTg4510 mice

Brain slice pharmacological models are useful approaches to explore the cellular and pharmacological basis of neuronal network oscillations, however, they do not entirely recapitulate oscillatory activity observed *in vivo*. For instance, pharmacologically induced gamma oscillations, such as those presented above are often observed continuously, whereas *in vivo*, gamma frequency oscillation power in the hippocampus and entorhinal cortex is coupled to a specific phase of an ongoing theta oscillation (Chrobak & Buzsaki, 1998; Colgin *et al.*, 2009). To examine whether the alterations in gamma frequency network oscillations observed in mEC slices translate to equivalent network disruptions *in vivo*,

multielectrode linear arrays were implanted into layer II/III of the mEC of WT and rTg4510 mice. These probes contained 16 recording sites (150 µm apart, linearly arranged on a single shank) which were implanted such that at least 10 recording sites ventral to the postrhinal border were positioned along the dorsal-ventral axis of the mEC (as determined by post-hoc histological analysis; fig 4.2A). Following post-surgery recovery, mice were tethered to a multichannel recording system and allowed to explore a novel linear track and local field potential (LFP) data were analysed from epochs where mice were running at speeds between 10 and 15 cm/s.

Broadband spectral power was significantly reduced in rTg4510 mice along the entire dorsal-ventral axis of the mEC compared to WT (WT, total power 45.9 ± 1.8 dB, n=3; rTg4510 total power 34.0 ± 1.5 dB, n=5; $P<0.01$, unpaired t-test; fig 4.2A,B), similar to previous observations in the CA1 region of the hippocampus (Cheng & Ji, 2013; Booth *et al.*, 2016*b*). Absolute power was decreased in both the theta (4-12 Hz) and gamma (30-120 Hz) frequency bands (theta: WT, 43.9 ± 1.9 dB, rTg4510, 29.4 ± 1.8 dB, $P<0.01$ unpaired t-test; gamma: WT, 37.6 ± 1.4 dB, rTg4510, 28.0 ± 2.0 dB, $P<0.05$ unpaired t-test; fig 4.2C). However, as a proportion of total power, decreases in oscillatory activity appeared to be specific to theta frequency bands (WT: 62.3 ± 1.5 %, rTg4510, 37.4 ± 4.1 %, $P<0.01$ unpaired t-test; fig 4.2D), with gamma oscillations comprising a larger proportion of total power (WT: 14.7 ± 1.4 %, rTg4510, 23.8 ± 0.8 %, $P<0.05$ unpaired t-test; fig 4.2D).

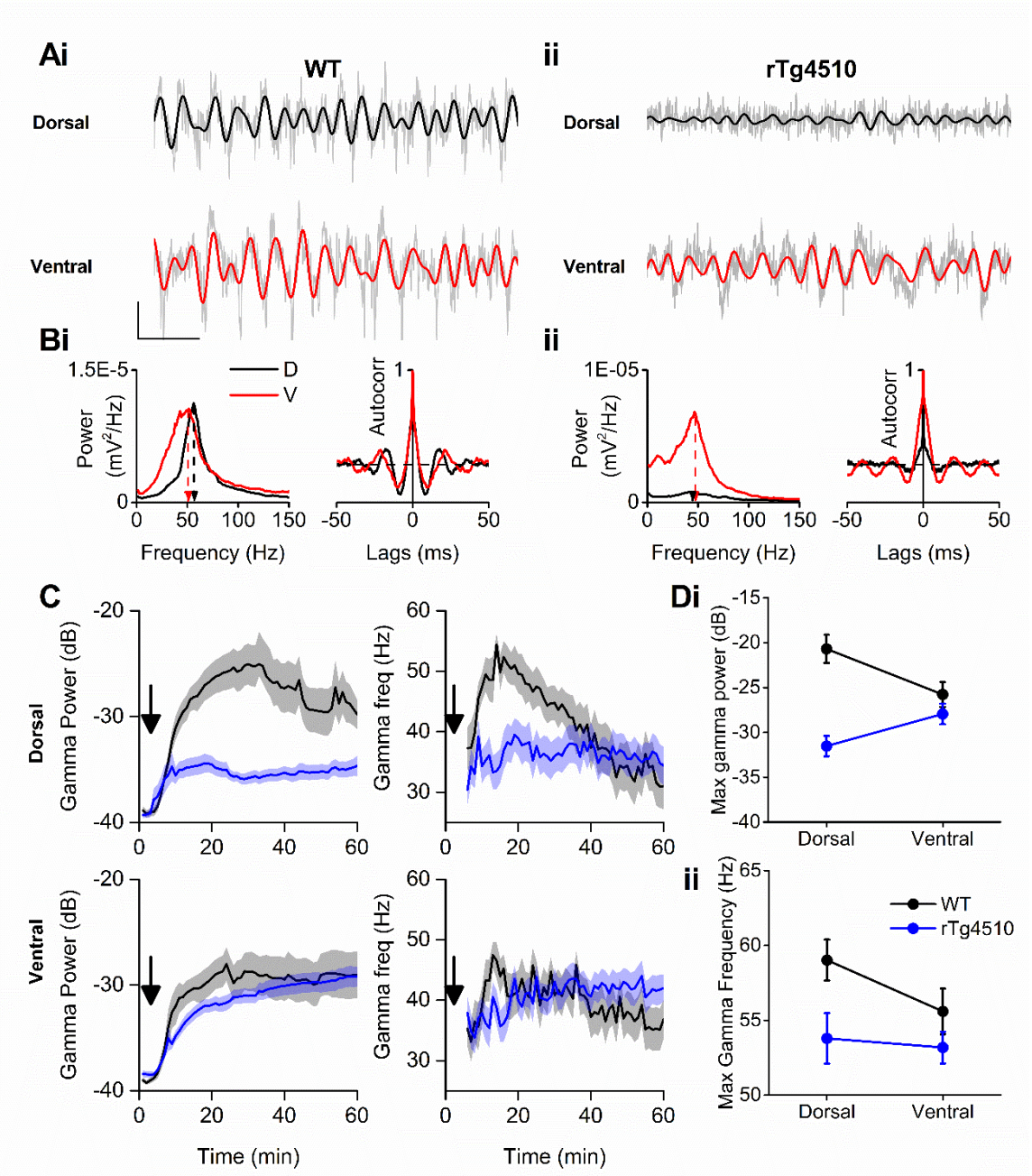

Figure 4.1: In vitro gamma (30-80 Hz) oscillations in layer II of dorsal, but not ventral, entorhinal cortex are preferentially disrupted in rTg4510 mice. **A)** Simultaneously recorded extracellular gamma oscillations evoked by bath application of 500 nM kainate in WT **(i)** and rTg4510 **(ii)** slices made approximately 15 minutes after the start of drug application. Grey traces are raw data; black (dorsal) and red (ventral) traces are bandpass filtered (30-80 Hz). Scale bar: 50 μV, 50 ms. **B)** Power spectra and autocorrelograms of recordings shown in **A**. In WT slices **(i),** gamma oscillations were faster in dorsal (black) versus ventral (red) regions, both in terms of peak spectral frequency and the primary non-zero peak in the autocorrelogram. In rTg4510 slices **(ii)** gamma oscillations in the dorsal mEC had significantly reduced power compared to WT slices. **C)** Pooled time-course data showing development of gamma oscillations following bath application of kainate (start point indicated by arrow). Solid lines show the mean (±SEM; shaded areas) gamma power (dB) and frequency of oscillations in 60 s bins. **D)** Summary data showing the maximum gamma power **(i)** and frequency (**ii**) in WT and rTg4510 slices. Note the selective effects of transgene expression on dorsal gamma oscillations.

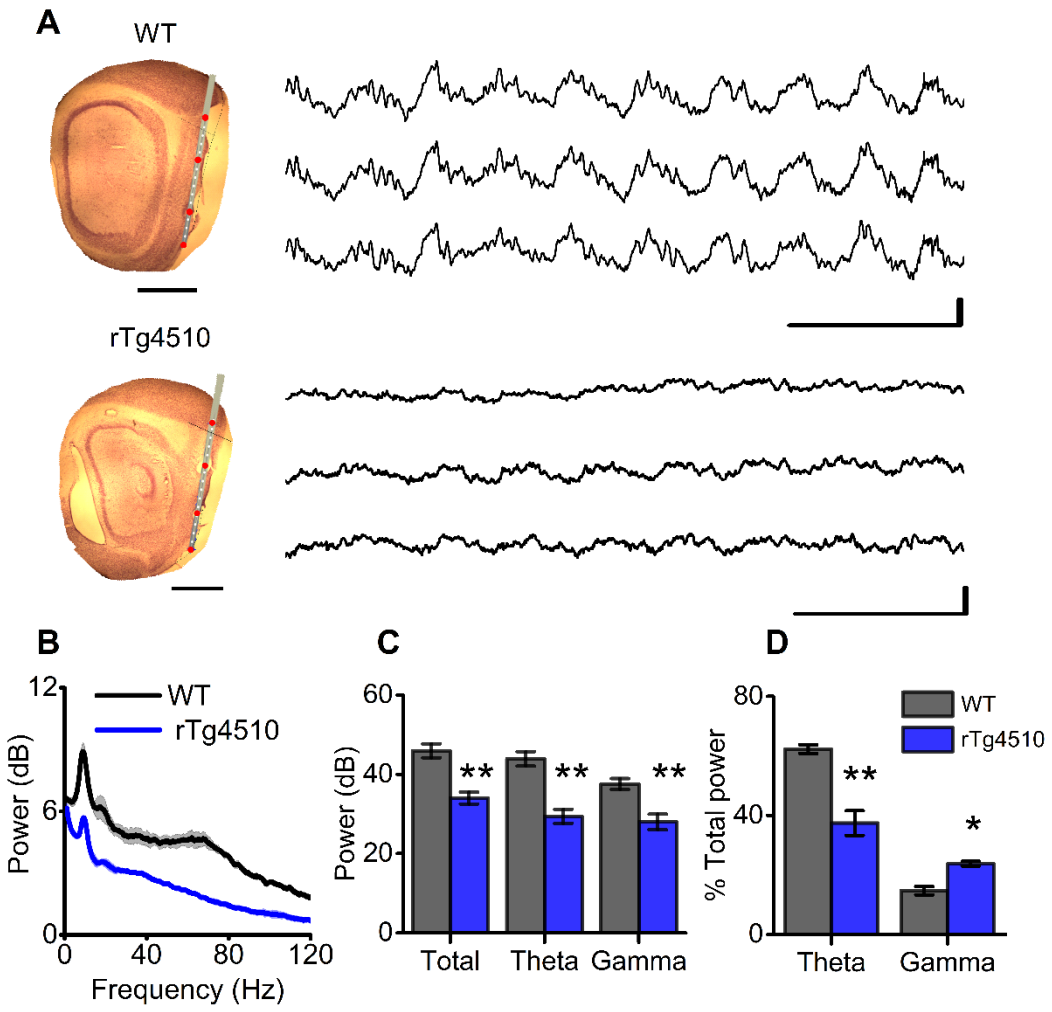

Figure 4.2: Broad-band impairment of oscillatory activity in rTg4510 mice in vivo. A) Light microscopy images of parasagittal sections through the mEC of a WT and rTg4510 mouse which were implanted with 16 channel linear silicone probes. The position of the probe, as determined by post-hoc analysis of lesion marks (red dots), is shown on each image (scale bar: 1 mm). Three example local field potential (LFP) recordings are shown to the right of each image with the location of the recording site illustrated by the arrows. Note the prominent theta oscillation with superimposed gamma frequency oscillations occurring towards the peak of each theta cycle (scale bar: 250 ms, 500 µV). **B)** Pooled power spectra (mean across all sites within the mEC and then averaged across animals) from epochs of LFP recorded whilst mice were running at 10-15 cm/s. **C)** Pooled data showing the significant reduction in broadband power (Total) in rTg4510 mice (n=5) compared to WT (n=3), as well as specific reductions in the theta and gamma bands (*P<0.05, **P<0.01). **D)** Relative percentages of oscillatory activity comprising of theta and gamma frequency bands. Showing relative reduction of theta oscillations and increased gamma oscillation expression in rTg4510 mice compared to WT.

4.3.3 Absence of dorso-ventral gradients in oscillatory activity in mEC of rTg4510 mice *in vivo.*

Since gamma oscillation power has been shown to decrease along the dorso-ventral axis both *in vitro* and in an acute anaesthetised *in vivo* preparation (Beed *et al.*, 2013), it was therefore important to determine whether the was also the case in an awake-behaving animal, where connectivity remains fully intact. Since this experimental paradigm allowed for simultaneous recordings across a large portion of the mEC (~1.5 mm) in the same cortical layer, it was possible to accurately determine this relationship across precise anatomical areas. In WT mice, a gradient in both gamma (fig 4.3) and theta (fig 4.4) oscillation amplitude was detected across the linear electrode array, whereby oscillatory activity was larger in dorsal mEC areas. This relationship was not present for either frequency bands in rTg4510 mice (fig 4.3/4/B). However, as described above, the broad-band spectral activity across the entire mEC was significantly reduced.

In order directly compare anatomical relationships in network activity between genotypes, data were Z-normalised and expressed as standard deviations from the mean for each experimental subject. Normalised theta and gamma oscillation power showed a clear relationship across the mEC in WT animals (linear regression, theta: R^2= 0.8, Slope: -1.7 z/mm; gamma: R^2= 0.8, Slope: -1.7 z/mm, n=3) but not in rTg4510 (linear regression, theta: R^2=0.06, Slope: 0.29 z/mm, gamma: R^2=0.06, Slope: 0.29 z/mm, n=5). The average slope for each animal was closer to zero in rTg450 mice when comparing both theta (WT: -1.73 ± 0.3 z/mm, rTg4510: 0.03 ± 0.79, Unpaired T-test: p=0.04, n=3/5) and gamma (WT: -1.82 ± 0.34 z/mm, rTg4510: 0.017 ± 0.048, Unpaired T-test: p=0.03, n=3/5) and significantly less correlated (Unpaired T-test: p = 0.04, n=3/5). For gamma oscillations, the quality of fit was significantly less in rTg4510 mice (WT: R^2=0.7 ± 0.2, rTg4510: R^2=0.2 ± 0.08, Unpaired T-test: p = 0.03, n = 3/5), but not for theta oscillations (WT: R^2=0.6 ± 0.2, rTg4510: R^2=0.5 ± 0.2, Unpaired T-test: p = 0.5, n = 3/5).

4.3.4 Gradient in theta-gamma phase-amplitude coupling is impaired in mEC of rTg4510 mice

In WT mEC *in vivo*, theta and gamma frequency oscillations do not work independently of each other. As has been previously reported (Chrobak & Buzsaki, 1998), gamma frequency oscillations were nested within the theta rhythm (fig 4.5). This process is proposed to be important for memory processes, since it allows for the coordination of neuronal ensembles over accelerated timescales (Lisman & Idiart, 1995; Lisman, 2005; Belluscio *et al.*, 2012). Interestingly, in oscillatory activity observed from WT mice, this interaction was also dependant on mEC recording location, with dorsal mEC showing greater modulation of gamma amplitude across theta phase (linear regression: R^2=0.98, Slope: - 2.1 z/mm, n=3; fig 4.5D). Since large scale deficits are seen in the magnitude of oscillatory activity in rTg4510 mice, it is difficult to directly compare between experimental groups. The extent of cross frequency coupling for rTg4510 mice was therefore calculated and the resulting comodulograms plotted.

In WT mice, analysis of these data revealed a peak in the theta modulation of gamma power that was evident in the pooled comodulograms (peak modulating frequency, 9.1 ± 0.2 Hz; peak modulated frequency, 66.3 ± 0.2 Hz, mean across all recording locations in the mEC; fig 4.6D). There was also a clear gradient in the magnitude of theta-gamma cross-frequency coupling along the dorsal-ventral axis of the mEC, such that higher levels of theta-gamma coupling were observed at dorsal compared to ventral electrodes (fig 4.6A). Regression analysis revealed a linear correlation between probe location (relative to the most dorsal probe) and modulation index (MI) in WT mice (slope, -68.3 ± 16.3 M/µm; $Z^{'}$= 2.2 ± 0.2; n=3; fig 4.6E).

In rTg4510 mice, the absolute magnitude of theta-gamma coupling was significantly reduced across all electrodes when compared to WT (fig 6A; WT mean MI, 25 ± 0.1x10^4; rTg4510 mean MI, 2.0 ± 0.3x10^4; P<0.001, unpaired t-test), which likely reflects the overall reduction in broadband LFP power. rTg4510 mice also showed reduced frequencies in both peak modulating frequency (8.0 ± 0.2 Hz) and peak modulated frequency (48.1 ± 1.9 Hz), (Main effect – genotype: p = 0.004, F = 50.8; interaction: p = 0.02, F = 2.26; 2 way repeated measured ANOVA; fig 4.6D). Furthermore, the gradient in cross-frequency coupling was

significantly reduced in rTg4510 mice (slope, 18.2 ± 11.6 M/µm; Z=0.9 ± 0.2; n=5, P<0.05, unpaired t-test) compared to WT (fig 4.6C,E), suggesting that theta-coupled gamma oscillations in rTg4510 mice were similar across different locations along the dorso-ventral axis of the mEC.

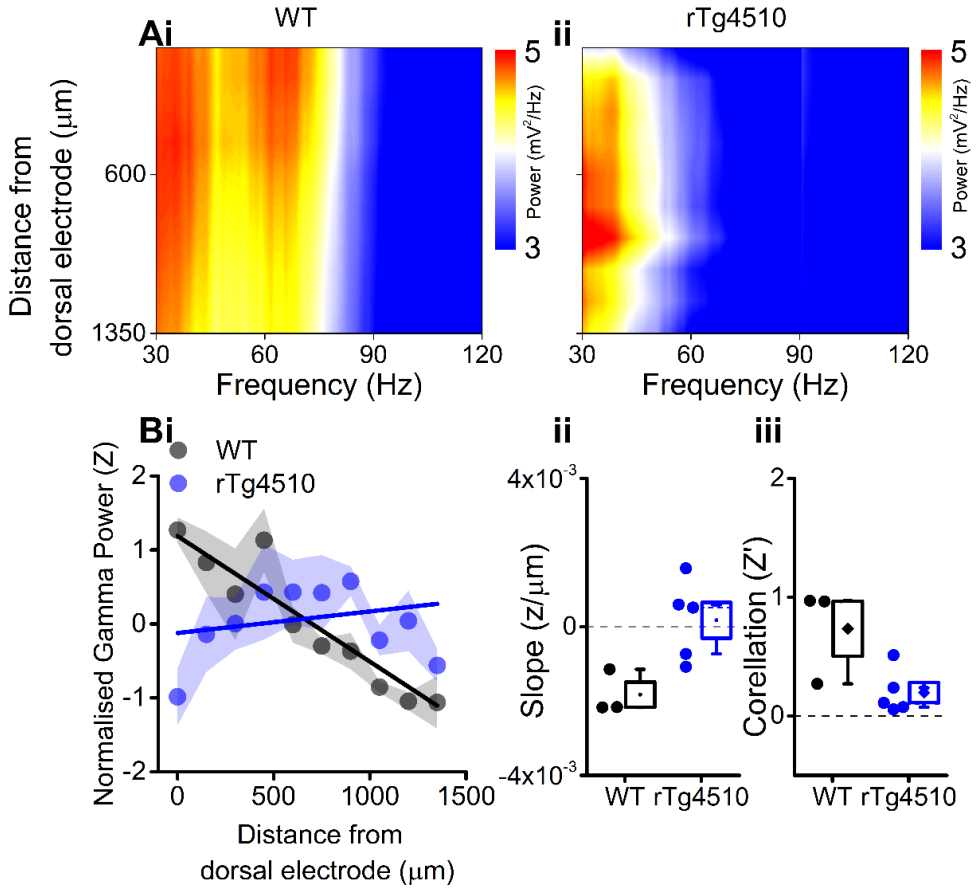

Figure 4.3 Impaired dorso-ventral gradients in gamma oscillations in mEC of rTg4510 mice *in vivo*. A) Average power spectra from 10 electrodes across layer II/III mEC, with colour axis oscillatory representing oscillatory power (dB) at each anatomical level. In WT mice (i) gamma power is greater in dorsal mEC recording sites, whereas there is no relationship in rTg4510 mice. **Bi**) Z-normalised gamma oscillation power across mEC, showing clear relationship in WT (linear regression: R^2=0.8, Slope: -1.7 z/mm, n=3) and not in rTg4510 (linear regression: R^2=0.06, Slope: 0.29 z/mm, n=5). Average slope (**ii**) for each animal was greater (closer to zero) for rTg450 mice (Unpaired T-test: p = 0.03, n = 3/5) and significantly less correlated (**iii**,Unpaired T-test: p = 0.04, n = 3/5) Box plots: dotted line: median, diamond: mean ± SEM, whiskers: 25th/75th centile).

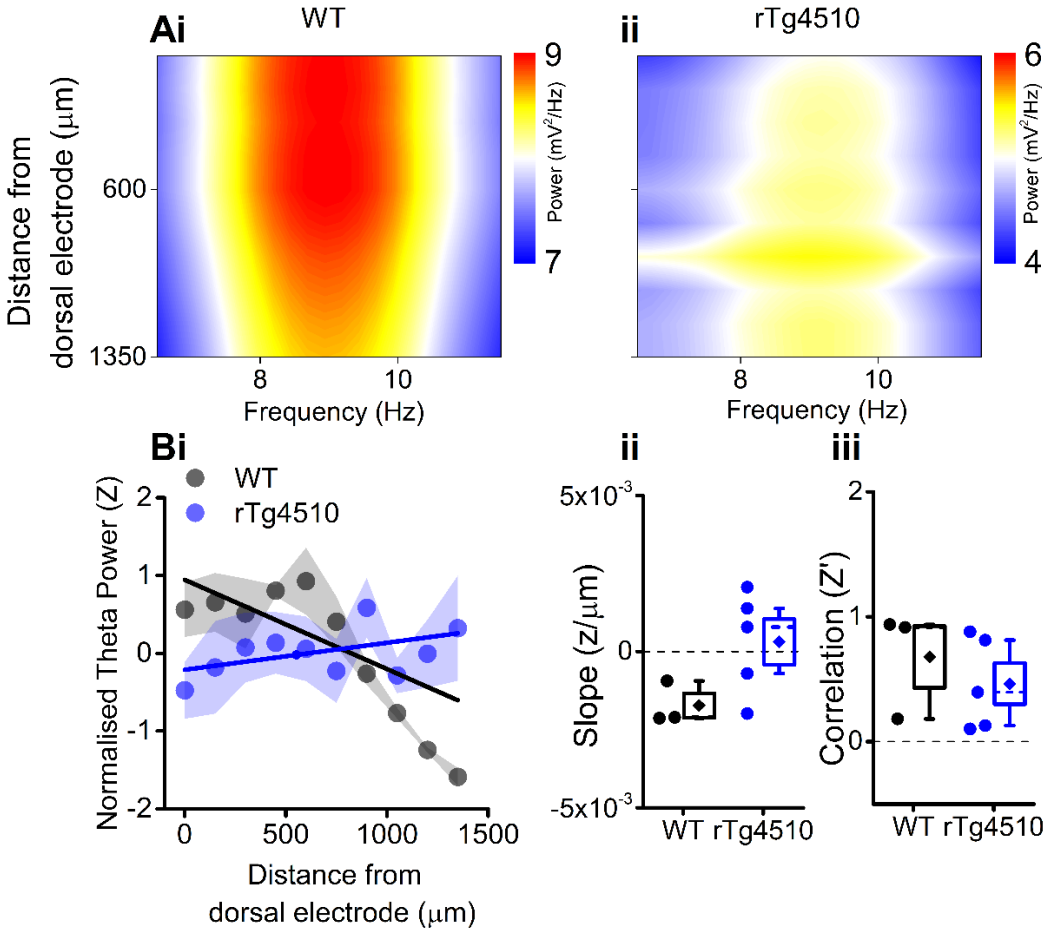

Figure 4.4: Dorso-ventral gradients in theta oscillations in mEC of rTg4510 mice *in vivo*. A) Average power spectra from 10 electrodes across layer II/III mEC, with colour axis oscillatory representing oscillatory power (dB) at each anatomical level. In WT mice (i) theta power is greater in dorsal mEC recording sites, whereas there is no relationship in rTg4510 mice. **Bi**) Z-normalised theta oscillation power across mEC, showing relationship in WT (linear regression: R^2=0.42, Slope: -1.15 z/mm, n=3) and not in rTg4510 (linear regression: R^2=0.22, Slope: 0.35 z/mm, n=5). Average slope (**ii**) for each animal was greater (closer to zero) for rTg450 mice (Unpaired T-test: p = 0.05, n = 3/5) but not significantly less correlated (**iii**, Unpaired T-test: p = 0.48, n = 3/5) Box plots: dotted line: median, diamond: mean ± SEM, whiskers: 25th/75th centile).

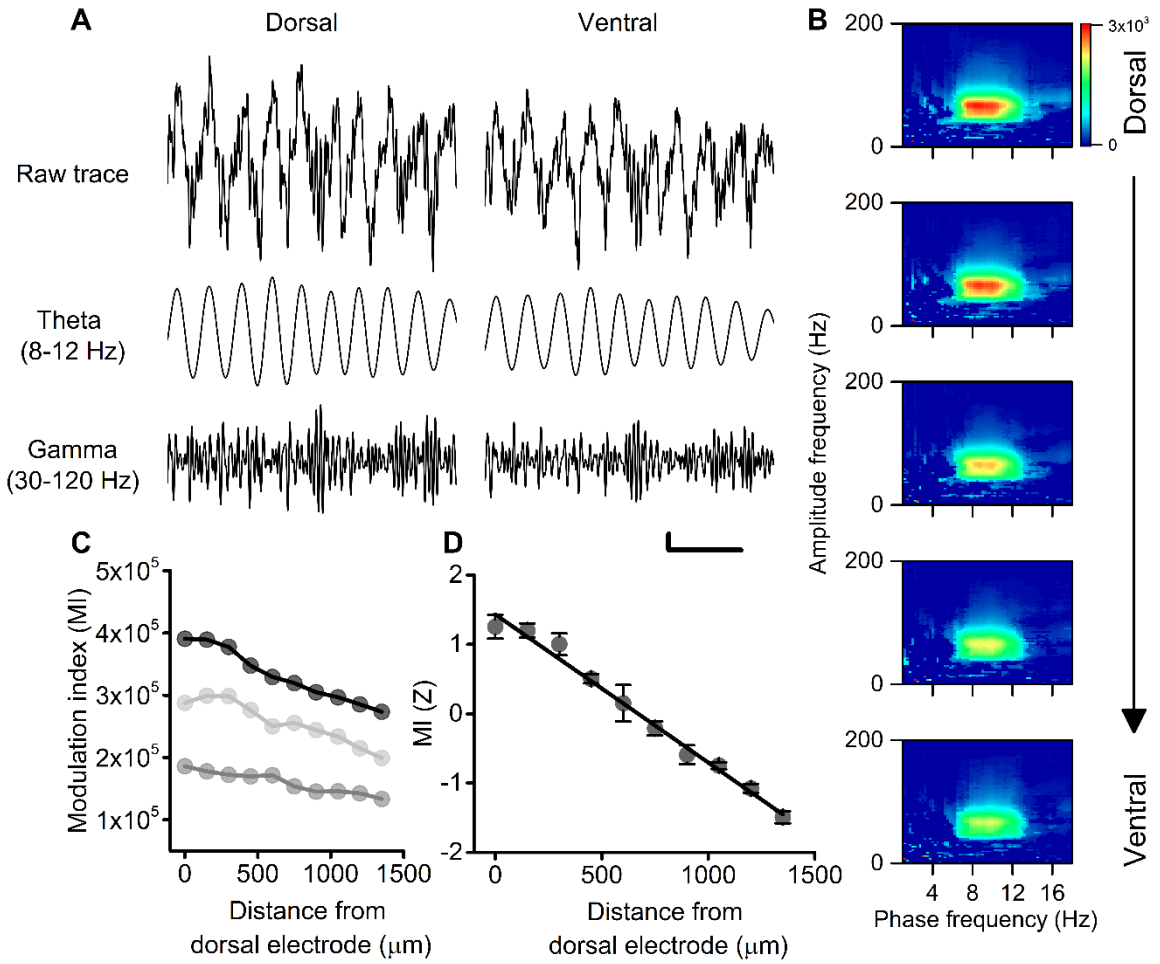

Figure 4.5: Dorso-ventral gradient in phase-amplitude coupling (PAC) interactions in WT mice. A) Example traces showing simultaneous recordings of most dorsal and ventral recording electrodes with theta (8-12Hz) and gamma (30-120Hz) filtered traces underneath (scale bar: 200µV, 250 ms). **B**) Averaged comodulograms showing theta-gamma cross-frequency coupling along the dorsal (top) to ventral (bottom) axis. **C)** MI index plotted against dorso-ventral location for 3 individual WT mice. **D)** Pooled data showing tight linear correlation of Z-normalised MI across mEC (linear regression: R^2=0.98, Slope: - 2.1 z/mm, n=3).

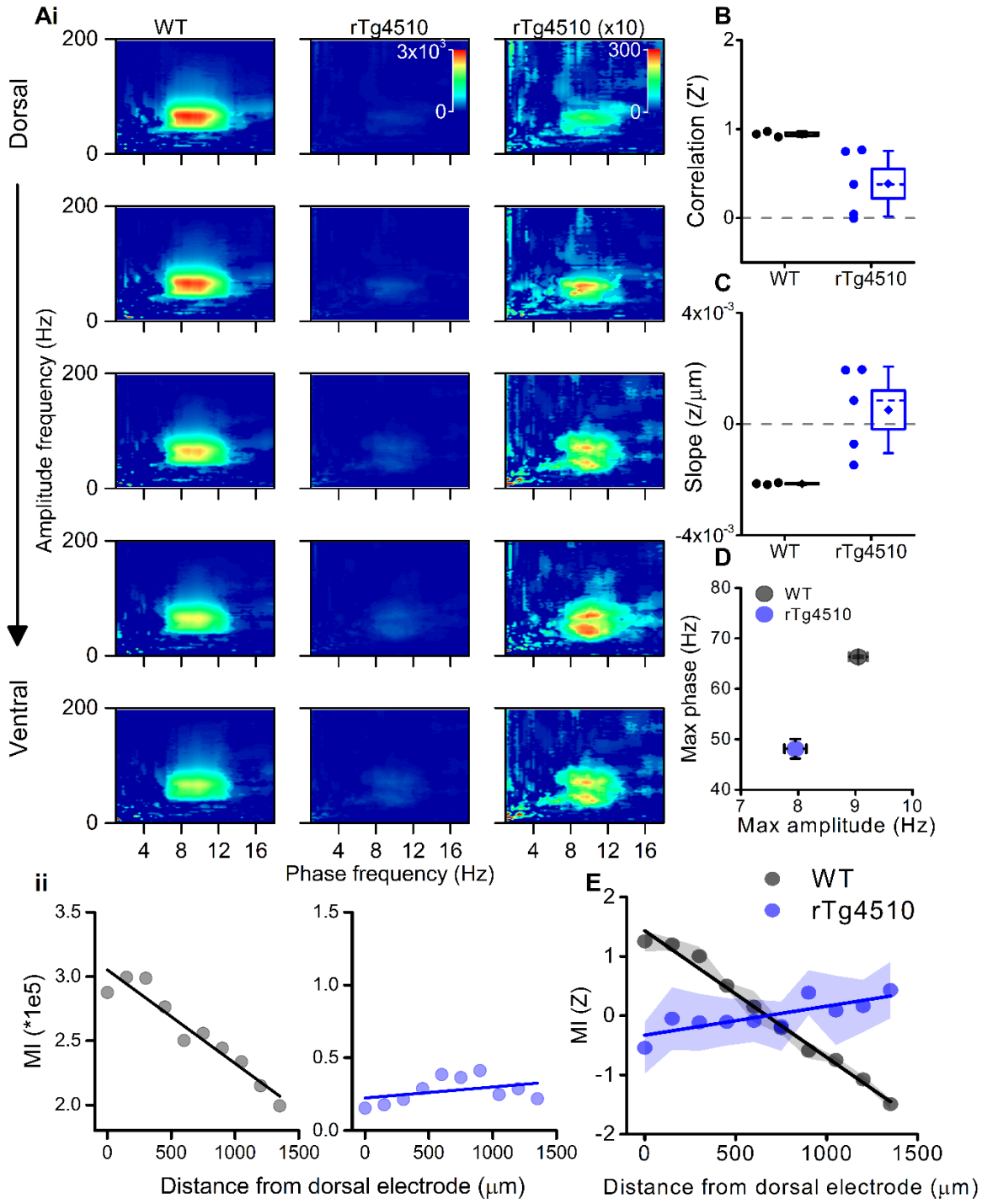

Figure 4.6: Flattened dorso-ventral gradient in PAC in rTg4510 mice. Ai: Averaged comodulograms showing theta-gamma cross-frequency coupling along the dorsal (top) to ventral (bottom) axis, right column shows rTg4510 with scale increased by 10 fold so coupling is discernible. Shown below (**ii**) is modulation index (MI) plotted as a function of distance from the most dorsal electrode from an example WT (left) and rTg4510 (right) mouse. Pooled regression analysis reveals a significantly ($P<0.01$) lower Z-normalized correlation coefficient (**B**) and slope **(C**) in rTg4510 mice compared to WT. Filled circles represent data from each individual animal, the horizontal line is the mean ± SEM. **D**: Reduction in peak frequency phase-ampltude coupling in both theta (amplitude) and gamma (phase) oscillations. **E**: Pooled Z-normalized MI as a function of dorso-ventral location shows loss of gradient in rTg4510 mice. Box plots: dotted line: median, diamond: mean ± SEM, whiskers: 25th/75th centile).

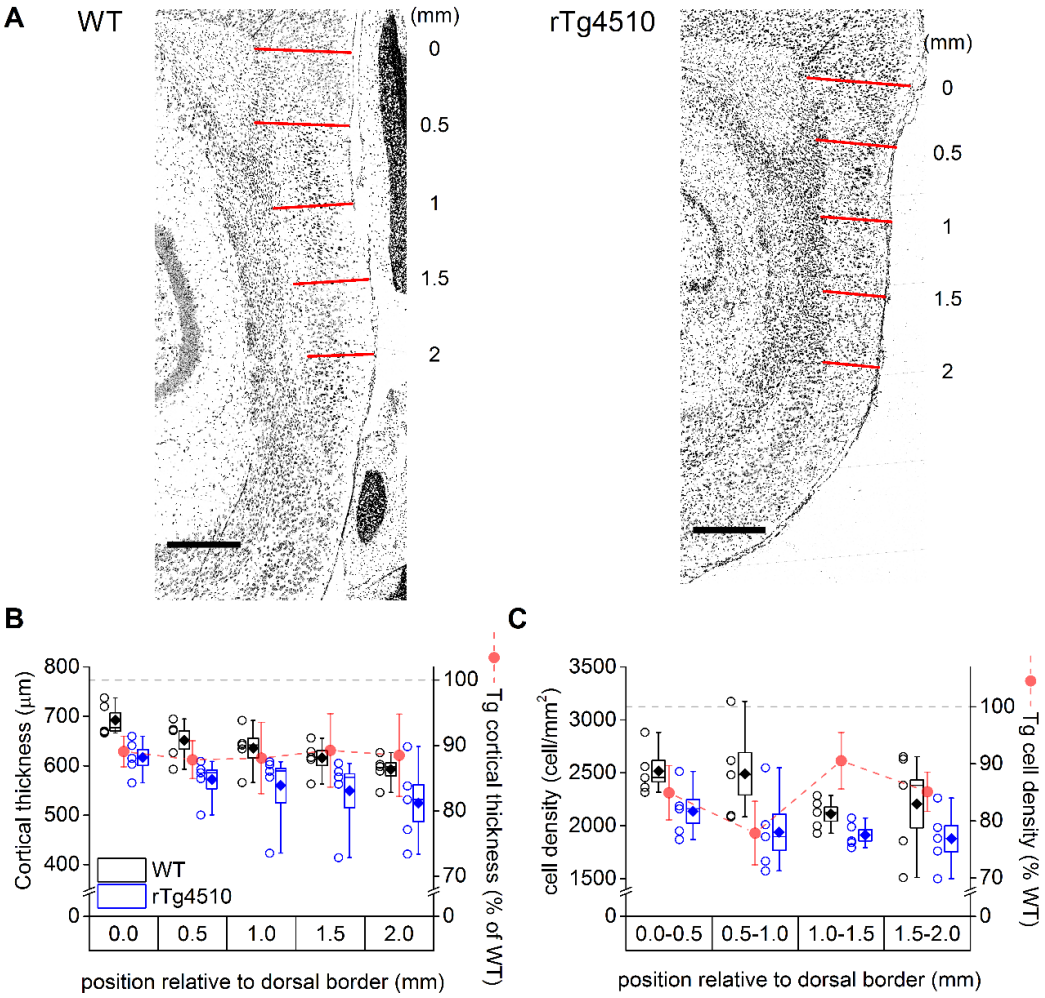

Figure 4.7: Cortical degeneration occurs evenly along the dorso-ventral axis of the mEC. A) Example photomicrographs of cresyl violet-stained sections from a WT (left) and rTg4510 (right) mouse. Lines representing the measurement locations (0-2 mm in 0.5 mm increments) are shown in red. Scale bar: 0.5 mm. B&C: Box plots illustrating cortical thickness (**B**) and cell density in layer II (**C**) in WT (n=5) and rTg4510 (n=5) at the points/regions marked in A. The open symbols represent the data from sections from individual animals, the filled diamond is the mean, the central line is the median, the box is the SEM and the whiskers are the interquartile range.

4.3.5 mEC degeneration is not dependant on dorso-ventral location in rTg4510 mice

Changes to the power and phase amplitude coupling of gamma frequency oscillations may be the result of the substantial levels of gross neurodegeneration that are known to occur in these mice (Santacruz *et al.*, 2005; Ramsden *et al.*, 2005; Spires *et al.*, 2006). Indeed, this is the likely explanation for the overall decrease in broadband power along the dorso-ventral axis (fig 4.6B). This raises the possibility that dorsal mEC regions degenerate in a preferential manner, leading to a flattening of the dorso-ventral gradient in network oscillations. To address this, a quantitative assessment of cortical thickness and cell density was performed in cresyl violet-stained parasagittal sections (6 µm thick; fig 4.7A). The dorsal-ventral extent of the mEC in WT sections was 2.8 ± 0.03 mm in length (range: 2.68-2.86 mm) whereas in rTg4510 sections the mEC was significantly shorter (2.5 ± 0.04 mm, range: 2.40-2.65 mm; $P<0.01$, unpaired t-test). Therefore, mEC thickness was measured in 0.5 mm increments between 0 and 2 mm ventral to the postrhinal cortex border (see fig 4.7A for illustration). In WT sections, the mEC became progressively thinner down the dorso-ventral axis, such that at the most dorsal point it was 693±15 µm from the edge of layer I to the edge of the white matter separating the mEC from the hippocampus, whilst at the most ventral aspect (2 mm from dorsal edge) it was 575±28 µm thick (fig 4.7B). In rTg4510 sections, the mEC also decreased in thickness along the dorso-ventral axis; at the dorsal end it was 617 ± 16 µm thick, whilst at the most ventral end (2 mm from dorsal edge) it was 540±36 µm thick. The rTg4510 mEC was significantly thinner than in WT littermates; thus, there was a significant main effect of genotype on cortical thickness ($F=6.2$, $P<0.05$, repeated measures ANOVA; n=5 for both genotypes). There was also a significant main effect of dorso-ventral position on cortical thickness ($F=13.8$, $P<0.001$). Importantly, there was no significant interaction between genotype and position ($F=0.8$, $P=0.9$), suggesting that, whilst there were significant levels of cortical degeneration at this age point in rTg4510 mice, this occurred evenly along the dorso-ventral axis of the mEC (fig 4.7B). Consistent with this, when we plotted the thickness of the rTg4510 mEC as a percentage of the mean WT thickness at different positions along the dorso-ventral axis, no significant relationship was observed (fig 4.7B).

Equivalent findings were observed when cell density was examined along the dorso-ventral axis of layer II of the mEC (fig 4.7C) with lower overall cell density in rTg4510 sections compared to WT sections ($F=8.5$, $P<0.05$, repeated measures ANOVA, main effect of genotype; n=5 both groups). There was a non-significant trend of dorso-ventral position on cell density in layer II ($F=2.6$, $P=0.08$) and, importantly, there was no significant interaction between genotype and position ($F=0.6$, $P=0.6$). Finally, in layer III, there was no significant main effect of genotype ($F=1.6$, $P=0.2$; repeated measures ANOVA, main effect of genotype; n=5 both groups) although in this layer there was a main effect of dorso-ventral position ($F=3.9$, $P<0.05$) on cell density. However, once again there was no significant interaction between these two factors ($F=1.1$, $P=0.4$; data not shown). Taken together, these findings suggest that, whilst there is significant loss of neural tissue in the mEC (particularly in layer II) of rTg4510 mice, the dorsal regions of the mEC were not selectively vulnerable.

4.4 Discussion

4.4.1 Summary

These data are the first to describe changes to mEC dorso-ventral gradients in network activity in transgenic models of disease. They show clear changes to the network organisation in the mEC in the rTg4510 mouse model of tauopathy. Recordings both from mEC slices and in freely moving mice show deficits in gamma oscillation activity, both in terms of raw oscillatory power and in the phase-amplitude coupling interaction between theta and gamma oscillations. Importantly, this deficit is not due to selective degeneration of the dorsal mEC, with the cell loss and cortical shrinkage described previously (Santacruz *et al.*, 2005; Ramsden *et al.*, 2005) occurring uniformly across the mEC.

4.4.2 Effect of neurodegeneration on mEC gamma oscillations

In freely behaving rTg4510 mice, broadband LFP power was substantially reduced across all recording sites along the dorsal-ventral axis of the mEC compared to WT mice, in a manner consistent with reports in the CA1 region of the hippocampus (Cheng & Ji, 2013; Booth *et al.*, 2016*b*), which may reflect the generalized neurodegeneration observed in this model of tauopathy (Santacruz *et al.*, 2005; Ramsden *et al.*, 2005).

Histological analysis revealed that there were significant levels of neurodegeneration (both in terms of cortical thickness and cell density) in rTg4510 mEC, but that this degeneration was not specific to the dorsal mEC (fig 4.7). In addition, further analysis from the same mice showed that tau expression was also not preferentially high in dorsal mEC regions (Booth *et al.*, 2016*a*). Consequently, the observed alterations in oscillatory activity cannot be specifically attributed to selective degeneration of the dorsal mEC.

4.4.3 Differences between *In vitro* and *in vivo* mEC recordings

Experiments conducted on *in vitro* slice preparations in this chapter clearly show selective reduction to dorsal mEC network activity (fig 4.1). This reflects similar

findings from the intrinsic properties of mEC stellate cells, which are largely unchanged in ventral mEC regions (Booth *et al.*, 2016*a*). Interestingly, network activity *in vivo* was significantly reduced across all frequency bands (fig 4.2). Given the degree of degeneration in these animals, this is not particularly surprising, however, it does highlight differences between experimental setups. It is likely that gamma oscillations evoked *in vitro* are recruiting smaller numbers of neurons, since this model system does not receive coordinated activity from anatomically separate structures. *In vivo,* the mEC receives long range in GABAergic inputs from areas such as the hippocampus and medial septum, capable of influencing rhythmic activity (Jinno *et al.*, 2007; Melzer *et al.*, 2012; Gonzalez-Sulser *et al.*, 2014; Fuchs *et al.*, 2015).

PV-positive interneurons provide recurrent inhibition within the mEC (Buetfering *et al.*, 2014) in a manner proposed to contribute to grid cell formation (Couey *et al.*, 2013). Beed et al (2013) reported graded PV expression along the dorso-ventral axis, corresponding with the extent of inhibitory connectivity and gamma power. Importantly, Booth et al. (2016) also identified a prominent dorso-ventral gradient in PV expression in both WT and rTg4510 mice suggesting that deficits in dorsal mEC gamma oscillations were not caused by changes in dorsal mEC PV expression. Since excitatory synaptic transmission is required for gamma oscillations in the mEC (Cunningham *et al.*, 2003), it is likely that disturbances to excitatory stellate neuron firing patterns in the dorsal mEC contribute to the deficits in gamma band oscillations in this cortical subregion. Nevertheless, since inhibitory circuits in these regions were not directly studied, it is possible that, whilst immunohistochemically normal, GABAergic transmission is altered in rTg4510 entorhinal cortex.

4.4.4 Phase-amplitude coupling deficits in rTg4510 mice

While rTg4510 mice show deficits in oscillatory power in both the theta (8-12 Hz) and gamma (30-120 Hz) frequency bands, the interaction between these oscillations is perhaps more important as a marker for cognitive processing. During awake-behaving recordings in WT mice, this relationship was perhaps the most pronounced along the dorso-ventral axis of the mEC, showing a decreased variability compared to oscillatory amplitude alone.

In WT mice a dorsal-ventral gradient was identified in theta-gamma cross-frequency modulation. Importantly, this gradient was absent in rTg4510 mice (fig 4.7), suggesting that the circuitry responsible for coordinating theta-modulated gamma oscillations was differentially disrupted across the mEC. Evidence from optogenetically-driven gamma oscillations in mEC slices suggests that the disruption in theta-gamma cross-frequency coupling might arise from impairment in excitatory drive onto fast spiking interneurons (Pastoll *et al.*, 2013*a*). Indeed, it has recently been hypothesised that glutamatergic drive on to CA1 hippocampal interneurons is defective in rTg4510 mice (Witton *et al.*, 2014). These data contribute to an emerging picture of disruption of GABAergic circuits in mouse models of dementia (Driver *et al.*, 2007; Palop *et al.*, 2007; Baglietto-Vargas *et al.*, 2010; Verret *et al.*, 2012).

4.4.5 Consequences for spatial firing

These findings, and those from Booth et al. (2016), suggest that the neurons in dorsal mEC may be preferentially impaired in rTg4510 mice. Since degeneration occurred evenly across the mEC, this therefore suggests that dorsal mEC stellate cells are more vulnerable to tau pathology than ventral. The mechanism(s) for such deficits is(are) as yet unclear, as is how this deficit translates into changes in spatial firing patterns of mEC neurons. Both the *in vitro* and *in vivo* data presented here give rise to the hypothesis that grid cells in rTg4510 mice will not display the variations in spacing across the dorso-ventral axis reported in normal rodents (Fyhn *et al.*, 2008; Stensola *et al.*, 2012).

The data collected *in vivo* also suggest a loss of function across the entire mEC, despite deficits being greater in the dorsal areas. This has the potential to explain some of the changes to hippocampal place cells observed in rTg4510 mice (Cheng & Ji, 2013; Booth *et al.*, 2016*b*). Inactivation of the entorhinal cortex is capable of altering spatial representation in the hippocampus, producing increased firing field size, reduced spatial information content (Brun *et al.*, 2008*a*; Hales *et al.*, 2014; Ormond & McNaughton, 2015) and reduced stability (Van Cauter et al., 2008) of CA1 place cells. The entorhinal cortex also receives reciprocal connections from the hippocampus, alternatively, this may affect grid cell firing regardless of specific mEC reorganisation (Bonnevie *et al.*, 2013).

There are few examples of changes to dorso-ventral gradients in grid cell spacing. However, mice with HCN1 channels knockout show flattened mEC dorso-ventral gradients in some intrinsic neuronal properties, such as subthreshold membrane resonance and theta frequency oscillations (Giocomo & Hasselmo, 2009). This is turn alters the size and spacing of grid cell firing fields (Giocomo et al., 2011) and significantly reduces spatial information content of CA1 place cells (Hussaini *et al.*, 2011). However, these changes do not ultimately alter the overall gradient in grid cell spacing and it therefore remains to be seen whether changes to dorso-ventral gradients in rTg4510 correspond directly to alterations in grid spacing.

4.4.6 Conclusions

These data indicate preferential modulation of dorsal mEC in rTg4510 mice, resulting in a flattening of entorhinal dorso-ventral gradients. It is likely that this will contribute to disturbances in spatial learning and memory observed in this model of tauopathy (Ramsden *et al.*, 2005), as indeed will the overall levels of neurodegeneration observed within the mEC and throughout the cortex.

5. Dysfunctional mEC processing of speed information in rTg4510 mice

5.1 Introduction

The data in the previous chapter establish the presence of a pronounced deficit in neuronal network activity in the mEC of rTg4510 mice. Since one of the primary roles of the mEC concerns spatial navigation, the subsequent chapters will aim to relate this activity to the external environment. Perhaps one of the simplest way to do this is to examine the relationship between running speed and theta/gamma oscillations, which have long been known to be positively correlated (McFarland *et al.*, 1975; Sławińska & Kasicki, 1998; Chen *et al.*, 2011; Ahmed & Mehta, 2012; Zheng *et al.*, 2015).

5.1.1 Running speed representation in path integration

Specific speed-encoding cells in the mEC have long been postulated, since continuous access to information regarding running speed has been proposed to be a theoretical requirement for a path integration-based representation of space (Fuhs & Touretzky, 2006; McNaughton *et al.*, 2006; Burgess *et al.*, 2007; Burak *et al.*, 2009; Bush & Burgess, 2014). This process, by which an animal's location can be maintained relative to a set point using only external cues, is widely thought to be dependent on mEC activity (Etienne & Jeffery, 2004; Parron & Save, 2004; Fuhs & Touretzky, 2006; Allen *et al.*, 2014). Grid cells in particular display important characteristics for path integration systems, since their activity is constant across environments (Fyhn *et al.*, 2004; Hafting *et al.*, 2005; McNaughton *et al.*, 2006) and mice without functional grid cells are unable to perform behavioural tasks dependent on path integration (Allen *et al.*, 2014). However, the mEC also contains many other spatially selective cell types proposed to be important for path integration, most notably speed and head-direction tuned cells (Sargolini *et al.*, 2006; Valerio & Taube, 2012; Kropff *et al.*, 2015). Inactivation of projections to the mEC containing either of these information types is capable of impairing grid periodicity and presumably path integration (Koenig *et al.*, 2011; Brandon *et al.*, 2011; Winter *et al.*, 2015).

These data highlight the important principle, that any changes to path integration mechanisms may have profound effects for an animal's ability to effectively navigate its environment. Therefore changes to these systems in rTg4510 mice may directly correspond to those seen in the human condition. Indeed, impaired spatial memory and specific deficits to path integration have been shown to be present in dementia patients (Hort *et al.*, 2007; Lithfous *et al.*, 2013; Mokrisova *et al.*, 2016).

5.1.2 Running speed - oscillatory activity interactions

Since early descriptions of hippocampal theta activity it has been observed that both oscillatory power and frequency are highly dependent on an animal's movement (Vanderwolf, 1969; Whishaw & Vanderwolf, 1973; McFarland *et al.*, 1975; Sławińska & Kasicki, 1998), with faster running speeds associated with larger amplitude and higher frequency theta. A similar relationship exists for gamma oscillation properties, which similarly increase their magnitude linearly with increases in running speed (Chen *et al.*, 2011) and also modulate their frequency in both slow and fast gamma frequency bands (Zheng *et al.*, 2015). Changes to large scale local field potential (LFP) activity in response to locomotion are presumably underpinned by both the general tendency of mEC neurons to increase their firing rate at faster running speeds (Sargolini *et al.*, 2006; Sun *et al.*, 2015; Hinman *et al.*, 2016) and an independent population of mEC neurons that only respond to changes in speed (Kropff *et al.*, 2015).

Interestingly, the precise relationship between the oscillation properties and running speed appears not to be fixed. Features such as slope and intercept can be modulated by external factors such as environmental novelty (Jeewajee *et al.*, 2008*b*) or pharmacological manipulations (Jacobson *et al.*, 2013; Wells *et al.*, 2013; Newman *et al.*, 2013). For this reason, running speed relationships, which can be easily observed in the LFP, have the potential to act as a sensitive biomarker for changes to neuronal network activity that may ultimately affect cognition. To test this hypothesis, we employed the implanted linear electrode arrays described in chapter 4 to investigate interactions between theta/gamma oscillations and running speed while animals ran for relatively short periods of time on a linear track.

5.2 Methods

5.2.1 Data acquisition and analysis

Data used in this chapter were obtained from the same experimental subjects as the previous chapter. Mice were placed on a linear track (1.5 m long) and allowed to explore for 15-20 min. Local field potential (LFP) signals were continuously sampled at 2 kHz, while two light-emitting diodes on the headstage and an overhead video camera (sample rate 25 Hz) were used to continuously track the animals' location, allowing estimation of position and running speed.

All data analysis was performed in Matlab (Mathworks). Spectral analysis was performed on 0.5 s epochs of LFP data using the Chronux toolbox (http://chronux.org/). Power and peak frequency of LFP frequency bands were compared to running speed calculated from the same time windows. Running speed was divided into 1 cm/s bins (between 1-30 cm/s) and spectral properties averaged across all time bins at each speed. Theta/gamma oscillation power was normalised to non-movement, defined as running speeds under 1 cm/s.

5.2.2 Grid cell modelling

Simulated grid cell firing patterns were generated using a hybrid-oscillatory interference/continuous attractor model produced by Bush and Burgess (2014), whose source code is freely available in ModelDB (McDougal *et al.*, 2017) at http://modeldb.yale.edu/3454. This model contains a parameter (β) representing the VCO velocity/oscillation frequency gradient which was substituted for experimental values of theta vs theta frequency slope. 25 simulated grid cells were produced using the average slope of theta frequency running speed relationship from both WT and rTg4510.

5.3 Results

5.3.1 Theta oscillation – running speed relationship is impaired in rTg4510 mice

It has long been known that there is a positive relationship between running speed and theta oscillation amplitude and frequency in both the hippocampus and mEC (McFarland *et al.*, 1975; Chen *et al.*, 2011). Since rTg4510 mice display broad deficits in neuronal network activity (Booth *et al.*, 2016*a*), and also show pronounced impairments in spatial information processing (Ramsden *et al.*, 2005) it is possible that these are accompanied by changes to the representation of running speed in the mEC. The interaction between running speed and theta oscillations was therefore measured for rTg4510 and WT control mice shown in chapter 4. As expected, in WT mice, theta oscillation properties clearly follow changes to locomotor activity (fig 5.1A), with pooled data showing a clear relationship observed between running speed and theta oscillation power (linear regression: R^2=0.75, p<0.001, n=3) and frequency (linear regression: R^2=0.55, p<0.001, n=3) (fig 5.2Ci). In contrast, in rTg4510 mice, running speed had little influence on theta oscillation amplitude (fig 5.2B) which was shown to be poorly correlated with locomotor activity and remained at consistent levels throughout recording sessions (linear regression: R^2=0.15, p=0.03, n=5, fig 5.2Ci). Although less pronounced than in WT animals, theta frequency did show correlation with running speed in rTg4510 mice (linear regression: R^2=0.46, p<0.01, n=5, fig 5.2Cii) which across the population was not significantly different from WT (Correlation (Z'); WT: 1.0 ± 0.16, rTg4510: 0.58 ± 0.26, unpaired T-test, p=0.1, n=3/5, fig 5.2E).

5.3.2 Gamma oscillation – running speed impairment is specific to fast (60-120 Hz) rather than slow (30-50 Hz) gamma frequencies

More recently, similar relationships have been observed with regards to gamma oscillation properties, both in the fast (60-120 Hz) and slow (30-50 Hz) gamma frequency bands (Chen *et al.*, 2011; Zheng *et al.*, 2015). In WT mice, both fast and slow gamma oscillation amplitude was positively correlated with running

speed (linear regression; fast gamma: R^2=0.88, p<0.001, n=3, fig 5.3Ai; slow gamma: R^2=0.36, p<0.01, n=3, fig 5.3Bi), although there was a trend for the slope of this association to be greater for fast gamma frequencies (slow gamma: 27.1 ± 8.4 $mV^2/Hz.cm^{-1}$, fast gamma: 80.6 ± 19.2 $mV^2/Hz.cm^{-1}$, p = 0.07, paired T-test, n= 3). rTg4510 mice did not show significant correlations for either gamma frequency band (linear regression; fast gamma: R^2=0.03, p=0.52, n=5, fig 5.3Ai; slow gamma: R^2=0.15, p=0.27, n=5, fig 5.3Bi), however, compared to the WT population, on average this correlation was significantly lower only in the higher gamma frequency range (2-way repeated measures ANOVA, main effect – genotype: P= 0.001 F = 32.3, interaction: p = 0.003, F = 23.7; Bonferroni multiple comparisons; fast gamma: p<0.001, slow gamma: p=0.2, n=3/5).

Since gamma oscillations produce a broad peak in the mEC power spectrum, accurate determination of peak gamma frequencies can prove difficult. However, applying these techniques to small sections of data (0.5 s) allowed for more defined peaks in the gamma frequency range. Across running speeds, on average WT mice showed a positive relationship with fast gamma oscillations (linear regression: R^2=0.58, p<0.001, n=3, fig 5.3Ai). However, rTg4510 mice showed a reversed relationship with running speed, with periods associated with low locomotion producing much faster oscillatory activity than WT controls, which decreased as animals ran at faster speeds (Correlation (Z'); WT: 0.6 ± 0.06, rTg4510: -0.43 ± 0.22 Unpaired T-test, P=0.01, n=3/5, fig 5.3C).

Contrary to previous reports (Chen *et al.*, 2011; Kemere *et al.*, 2013), for slow gamma frequencies, WT mice showed a non-significant negative correlation with running speed (linear regression: R^2=0.1, p=0.08, n=3, fig 5.3Bii). However, similar to high gamma, this relationship was also reversed in rTg4510 mice (linear regression: R^2=0.52, p<0.001, n=5, fig 5.2Bii), with these mice displaying positive relationships with running speed (Correlation (Z'); WT: -0.06 ± 0.01, rTg4510: 0.06 ± 0.03, Unpaired T-test, P=0.02, n=3/5).

5.3.3 Oscillation – running speed relationships are dependent mEC dorso-ventral location

The examination of running speed – theta/gamma interactions in the mEC has previously been limited to recordings in dorsal mEC regions (Chen *et al.*, 2011;

Kemere *et al.*, 2013; Newman *et al.*, 2014; Zheng *et al.*, 2015). In our experiments, LFP activity was recorded at multiple sites along the dorso-ventral axis of the mEC. It was therefore possible to measure whether this relationship changed according to anatomical location, in a similar manner to basic oscillatory properties determined from speed controlled data (chapter 4).

Surprisingly, in WT mice the relationship between theta oscillation power and running speed was also shown to vary along the dorso-ventral axis of the mEC (fig 5.4Ai), such that increases in locomotion were associated with larger increases in amplitude in dorsal mEC regions than ventral. This was not the case for rTg4510 mice that showed running speed-oscillation relationships which were independent of anatomical location (fig 5.4Aii). Regression analysis showed that z-normalised theta power decreased across probe, varying from the mean by ~2 standard deviations/mm, which was not the case in rTg4510 mice (slope; WT = -2.0 ± 0.09 z/mm, rTg4510 = -0.046 ± 0.056 z/mm; p=0.05, Unpaired T-test, n = 3/5, fig 5.4B/Ei). The same relationship was not observed for theta oscillation frequency, which did not vary across the dorso-ventral axis for either genotype (slope; WT = -0.002 ± $9x10^{-5}$ Hz/mm, rTg4510 = $-4.6x10^{-4}$ ± $5.6x10^{-4}$ Hz/mm; p=0.05, Unpaired T-test, n = 3/5 fig 5.4Eii).

Fast gamma oscillation relationships with running speed were also observed to be dependent on dorso-ventral mEC location, in an almost identical manner to theta (fig 5.4Cii). Regression analysis showed that z-normalised fast gamma power decreased across the electrode array, also varying from the mean by ~2 standard deviations/mm, which was also not the case in rTg4510 mice (slope; WT = -2.12 ± 0.036 z/mm, rTg4510 = -0.47 ± 0.35 z/mm; p=0.01, Unpaired T-test, n = 3/5 fig 5.4D/Fi). The same relationship was not observed for gamma oscillation frequency, which did not vary across the dorso-ventral axis for either genotype (slope; WT = -0.008 ± 0.006 Hz/mm, rTg4510 = 0.04 ± 0.02 Hz/mm; p=0.1, Unpaired T-test, n = 3/5, fig 5.4Fii). Slow gamma oscillation amplitude – running speed relationships were shown to be less prominent than fast gamma frequencies (fig 5.3B). Despite this, the slope of the association was also dependent on anatomical location (linear regression: R^2=0.82, p=0.001, n=3). However, there was no significant difference observed between WT and rTg4510 mice (slope; WT = -0.31 ± 0.01 Hz/mm, rTg4510 = 0.11 ± 0.14 Hz/mm; p=0.07, Unpaired T-test, n = 3/5) and no dorso-ventral relationship for either genotype in

slow gamma frequency (slope; WT = -0.002 ± 0.002 Hz/mm, rTg4510 = -0.004 ± 0.003 Hz/mm; p=0.26, Unpaired T-test, n = 3/5).

5.3.4 rTg4510 mice display hyperactive phenotype

rTg4510 mice have been shown to display a hyperactive phenotype under various conditions, which becomes more pronounced with developing tau pathology (Selenica *et al.*, 2014; Cook *et al.*, 2014; Jul *et al.*, 2015). Since the experiments shown here display data that is heavily influenced by running speed, it was therefore important to observe this effect in the current experimental subjects. Under these recording conditions, rTg4510 mice also displayed a hyperactive phenotype (fig 5.5). rTg4510 mice were shown to spend more time at faster running speed, with average speeds across recording sessions greater than WT control mice (P = 0.04, Unpaired T-test, n=3/5, fig 5.5B).

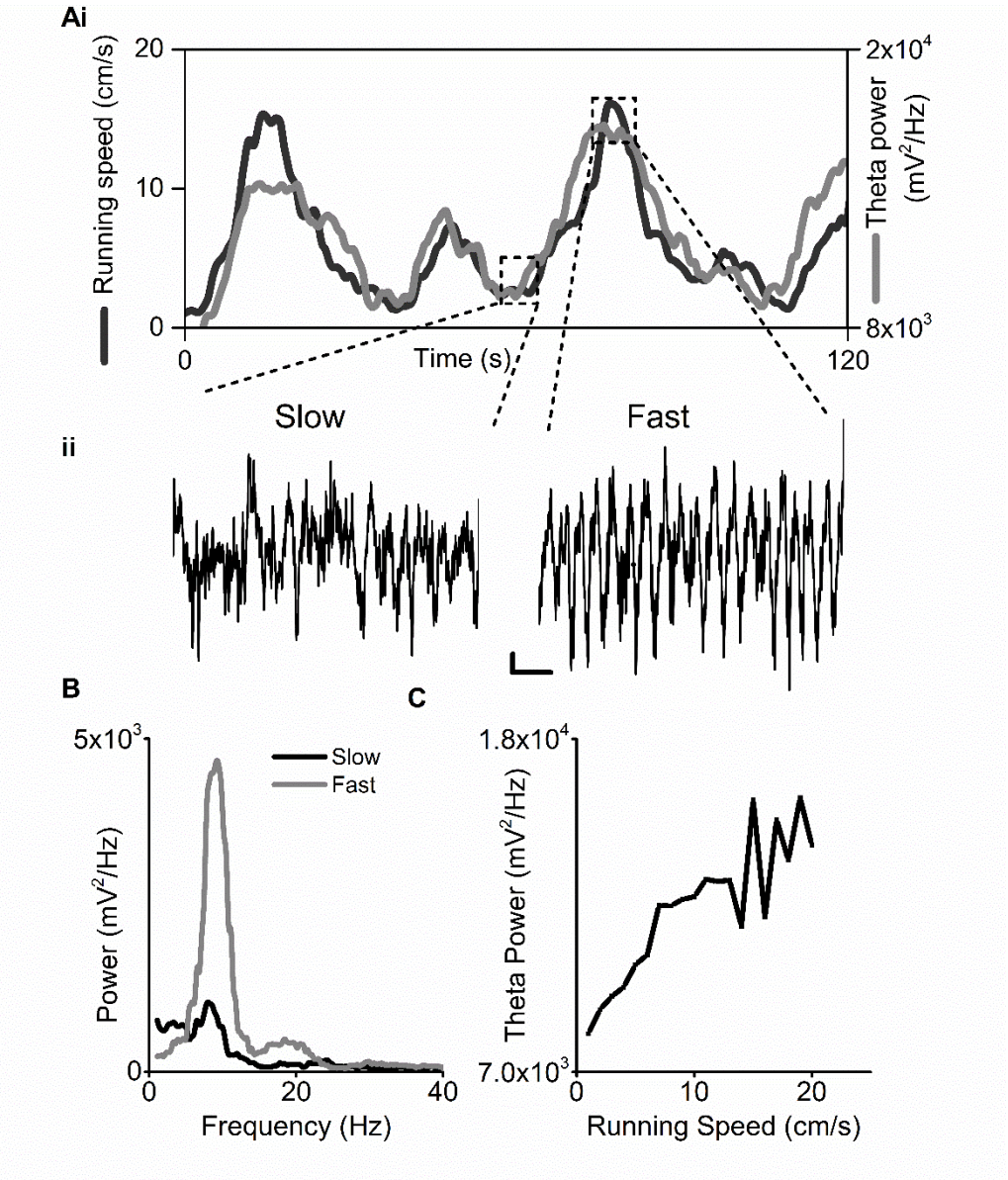

Figure 5.1 Theta oscillation are positively correlated with running speed. **Ai)** Example plots showing animals running speed on linear track (black, left Y axis) showing high correlation with theta oscillation amplitude (grey, right Y axis) (top) over several minutes of recording. **ii)** Local field potential from periods of slow and fast running speed (boxes) showing faster and larger theta oscillations during locomotor activity. **B)** Power spectra for data shown in **ii** for slow (black) and fast (grey) running periods. **C)** Example relationship between running speed and average theta oscillation power across recording session.

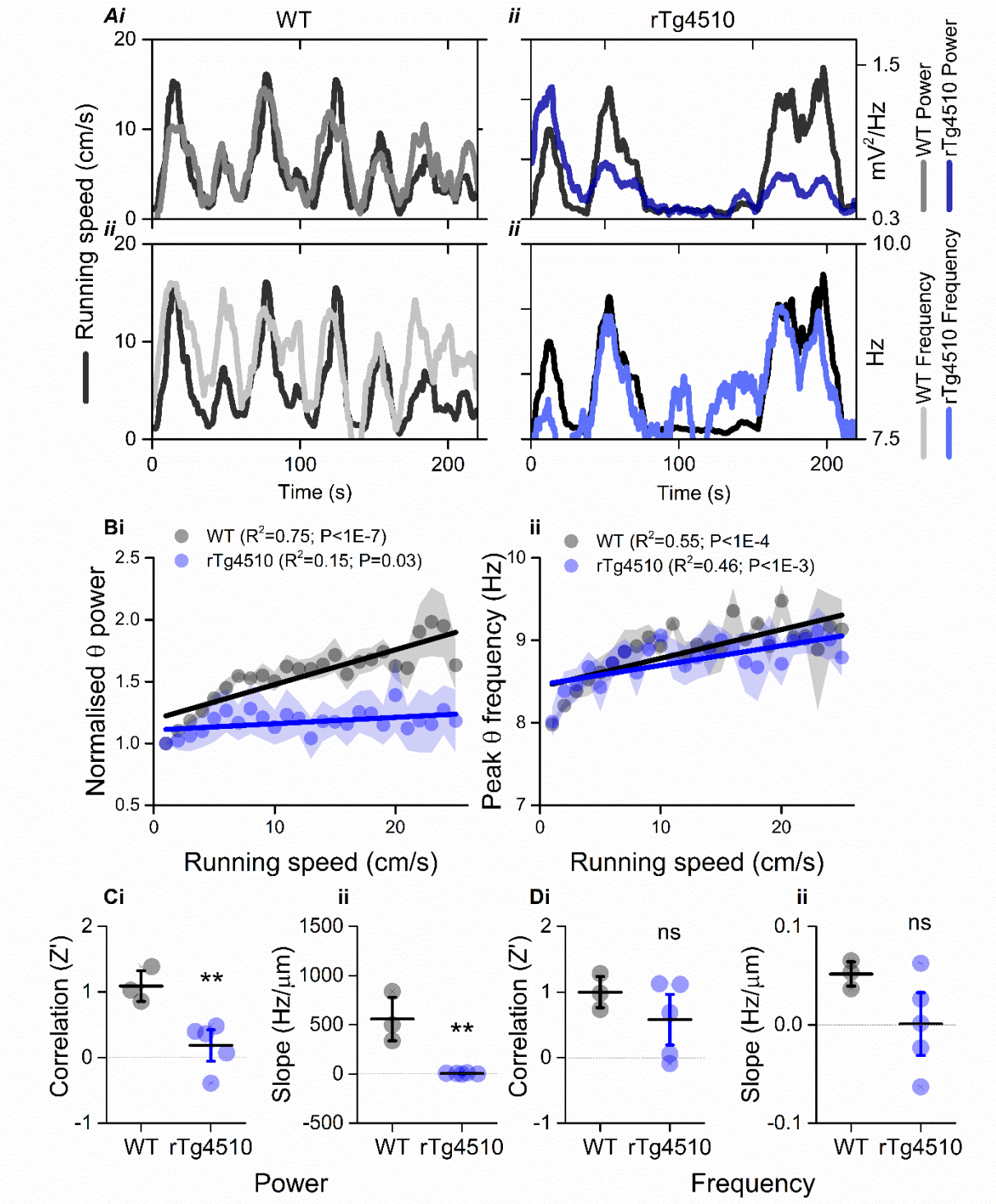

Figure 5.2: Theta oscillation- running speed relationship is impaired in rTg4510 mice. A) Example plots showing animals running speed on linear track (black, left Y axis) showing high correlation with theta oscillation (grey, right Y axis) amplitude (i) and frequency (iii) over several minutes of recording. **B)** Corresponding example from rTg4510 mouse showing with theta oscillation amplitude (ii) and frequency (iv) with decreased association with running speed. **B)** Running speed – theta oscillation slopes for power (**i,** normalised to >1cm/s) and frequency (**ii**) WT and rTg4510 mice, line shows linear regression fit. **C)** Pooled data for each animal showing positive correlation (**i**) and slope (**ii**) associated with increased running speeds in WT but not transgenic mice. **D)** Pooled data showing correlation and slope of running speed - theta oscillation frequency relationship. (* p<0.05, ** p <0.01, ns = not significant, unpaired T-test)

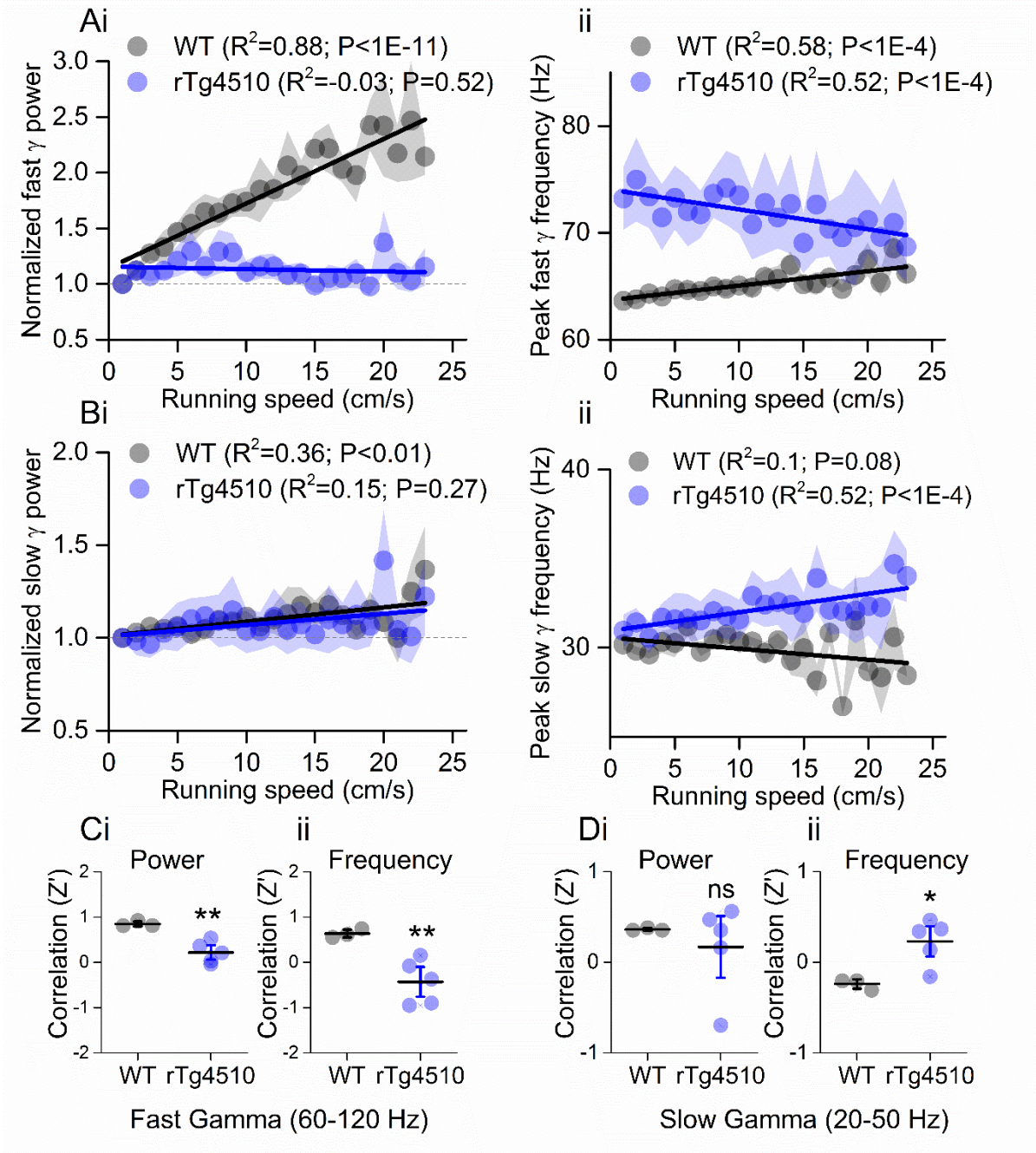

Figure 5.3 Deficits in gamma oscillation – running speed relationships are specific to fast gamma (60-120 Hz) frequencies. A) Average running speed relationships for fast gamma amplitude (i) and power (ii) with linear regression lines, showing strong positive relationship in WT mice, but not rTg4510. **Bi**) Weak correlation between running speed and slow gamma (20-50 Hz) oscillation power in WT mice, which is unchanged in rTg4510. **ii)** Weak negative relationship between running speed and slow gamma frequency, which is reversed in rTg4510 mice. **C)** Pooled data showing correlation for oscillatory power and frequency for slow and fast (**D)** gamma oscillation relationship with running speed. (* p <0.05, ** p<0.01, *** p <0.001, ns = not significant, unpaired T-test).

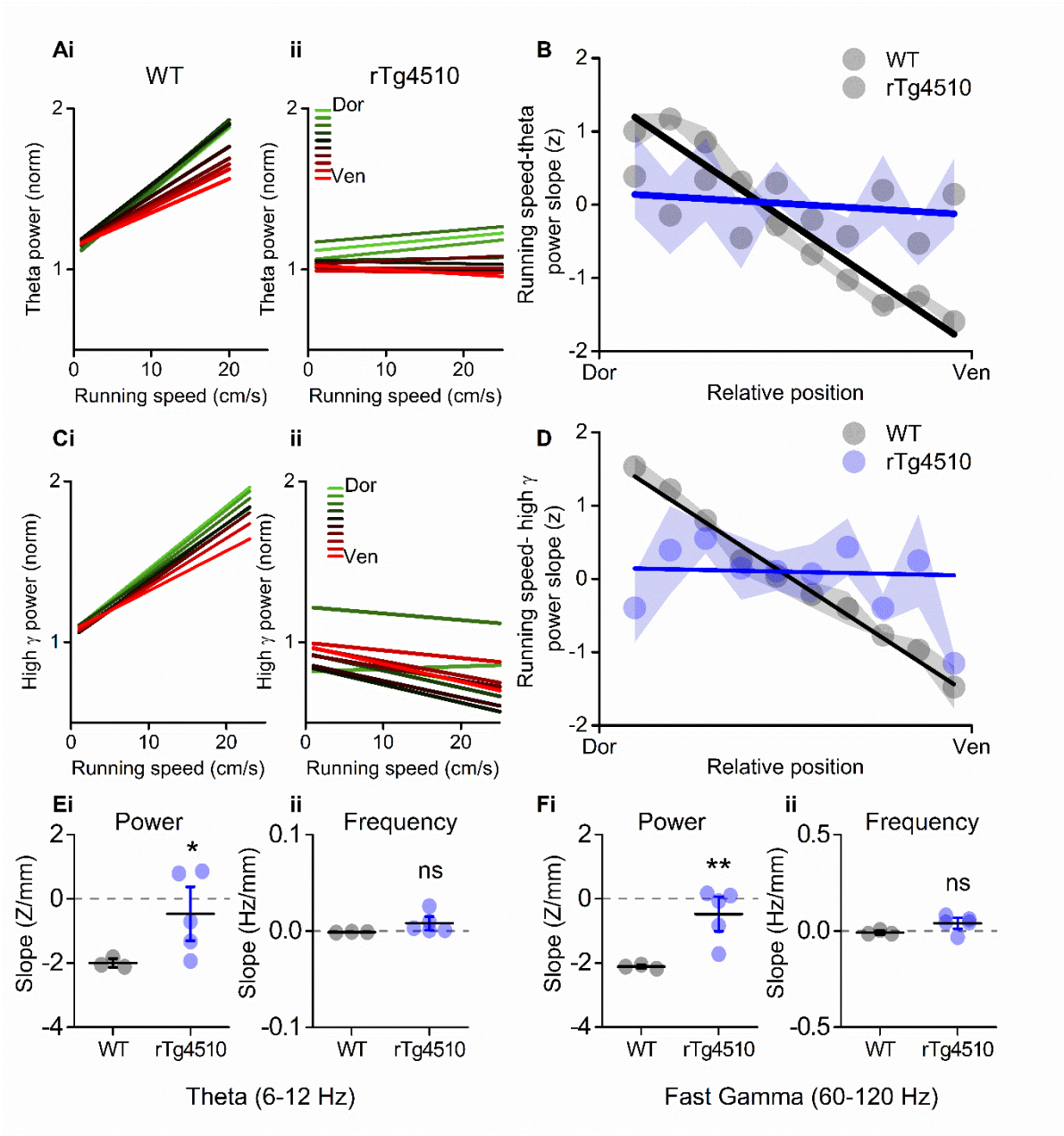

Figure 5.4: Theta/gamma oscillation – running speed relationships are dependent on mEC dorso-ventral location. A) Example running speed – theta oscillation amplitude relationships for WT (i) and rTg4510 (ii) mice, coloured from green (most dorsal electrode) to red (most ventral). **B** Pooled z-normalised data across dorso-ventral axis of the mEC, showing strong relationship between running speed slope and recording location in WT mice, which is not present in rTg4510 mice. **C)** Examples for fast gamma power for WT (i) and rTg4510 (ii) mice, with pooled Z-normalised data showing same relationship as theta. E) Pooled slopes across dorso-ventral axis of each animal theta (E) and fast gamma (F), displayed as standard deviations from the mean (z)/mm for power and Hz/mm for frequency. Decreases in slopes were observed only for oscillatory power across the dorso-ventral axis, while frequencies remained largely unchanged with location. (* $p<0.05$, ** $p<0.01$, ns = not significant, unpaired T-test)

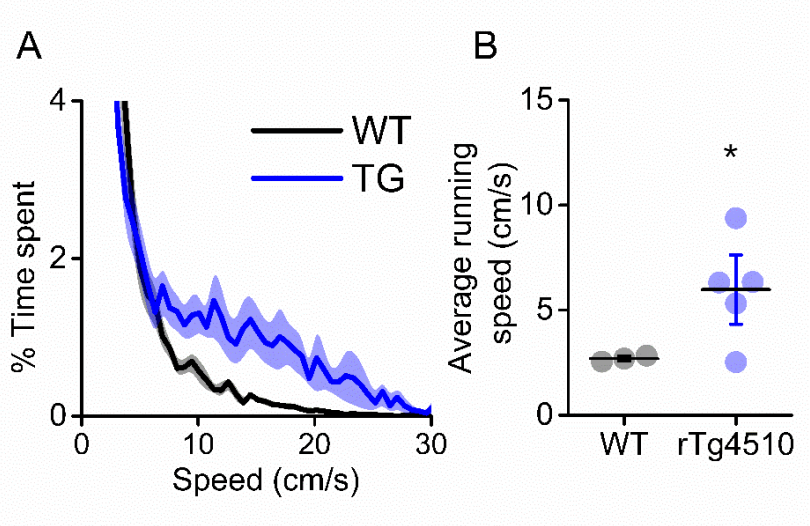

Figure 5.5: rTg4510 display hyperactive phenotype. A) Breakdown of animal's time spent at each running speed, showing rTg4510 mice spend more time moving at higher velocities. **B)** Average running speed across (mean ± SEM) entire recording session is greater in rTg4510 mice (* P < 0.05, Unpaired T-test).

5.3.5 Computational model predicts reduced grid cell periodicity in rTg4510 mice

The relevance of running speed-theta relationships to the spatial firing of grid cells in the mEC is yet to be established. However, velocity controlled oscillators (VCOs) form an integral part of many computational models of grid cell firing (Fuhs & Touretzky, 2006; Burgess *et al.*, 2007; Giocomo *et al.*, 2011*b*; Zilli, 2012; Bush & Burgess, 2014), predominantly in oscillatory interference models that generate grid patterns. In order to illustrate the potential effect of even small changes to running speed versus theta frequency relationships, grid cells were simulated from a hybrid oscillatory interference/continuous attractor model of grid cell firing (Bush and Burgess 2014), with source code obtained from ModelDB (McDougal *et al.*, 2017) at http://modeldb.yale.edu/3454. 25 grid firing patterns were simulated for each using the experimental theta frequency relations (fig 5.6B) as the slope of the VCO (WT: 0.035 Hz/cms^{-1}, rTg4510: 0.014 Hz/cms^{-1}). On average, model grid cells produced using WT VCOs showed grid scores significantly higher than those from rTg4510 mice (median WT: 0.61, rTg4510: 0.22 , p=0.027, U= 198, Mann-Whitney U test, n =25, fig 5.6Cii). However, using this model, high grid score measurements were dependent on the peak firing rate of modelled cells (fig 5.6Ci), with high firing rates showing low grid scores due to periods of hyperexcitability in modelled recordings.

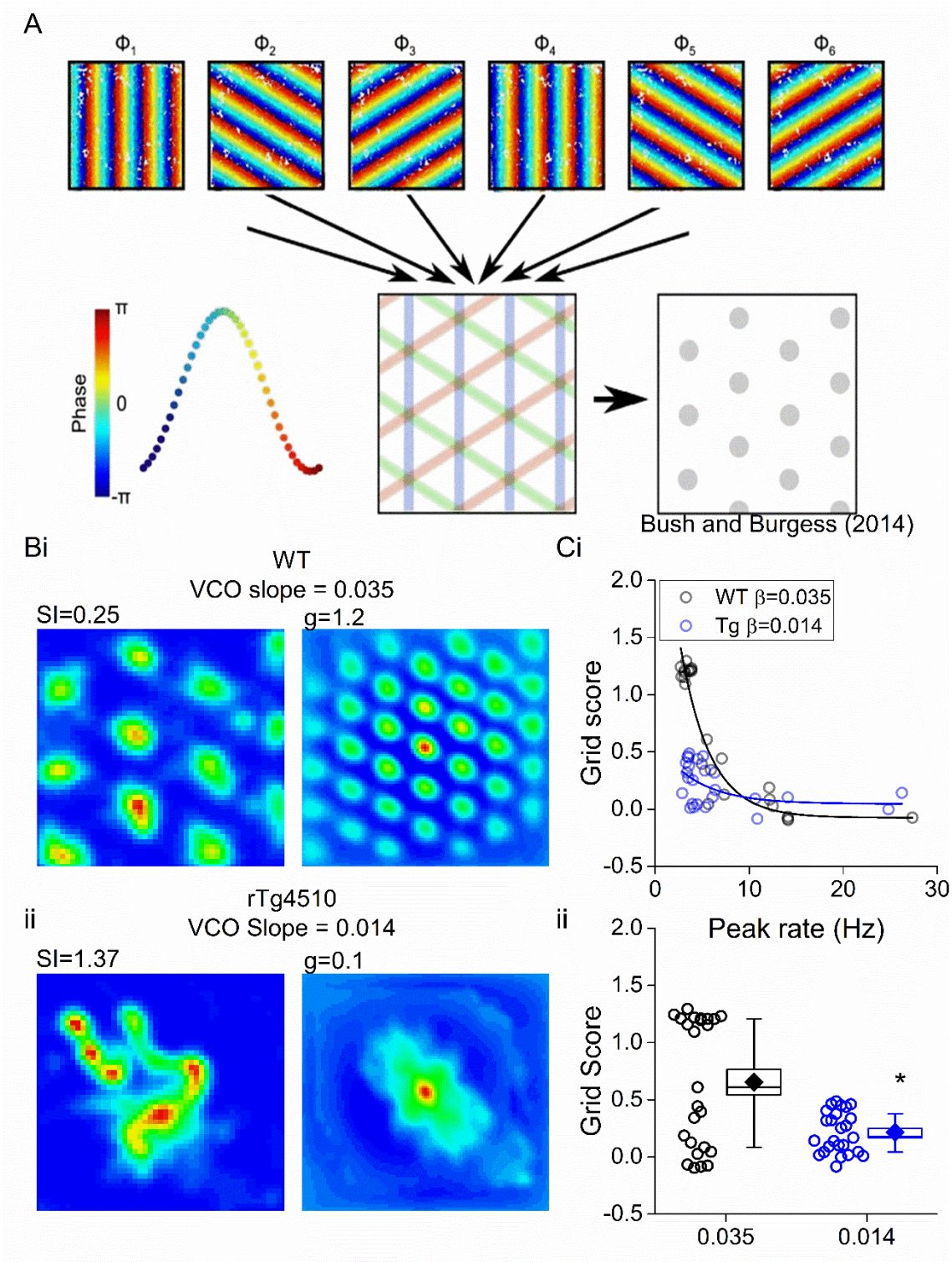

Figure 5.6 Grid cell model predicts large scale changes to grid periodicity from small alterations in running speed theta frequency slope. A) Schematic of hybrid oscillatory interference model, containing multiple VCOs with preferred directional phases, obtained from (Bush & Burgess, 2014). **Bi)** Example simulated grid cells obtained using average slope from running speed-theta frequency relationship in WT and rTg4510 mice with 2D spatial autocorrelations. **C)** Distribution of 25 simulated grid cells for each genotype, showing relationship between grid score and peak firing rate (i) and reduced average grid score in rTg450 simulated grids (ii),* $p<0.05$, Mann-Whitney U test.

5.4 Discussion

5.4.1 Summary

Continuous integration of running speed information in the mEC has been proposed to be critically important for spatial navigation and path integration (Sargolini *et al.*, 2006; McNaughton *et al.*, 2006; Burgess *et al.*, 2007; Kropff *et al.*, 2015). The current experiments clearly show that unlike WT animals, rTg4510 mice do not display adequate representations of locomotor activity in the mEC LFP, since theta and gamma oscillations properties display blunted, or absent, relationships with running speed. They further show, for the first time, that in WT mice, this relationship varies along the dorso-ventral axis of the mEC. However, this is also clearly not the case in rTg4510 mice, where no association is seen between running speed interactions and anatomical location.

5.4.2 Impaired running speed representations in rTg4510 mice

Theta oscillations show increases in both amplitude and frequency depending on running speed (fig 5.1). Spatially modulated mEC neurons are required to integrate large quantities of multimodal sensory information from their environment. At fast running speeds, the time window for this integration is smaller and it may therefore be necessary to increase the sensitivity of such neurons during locomotion to accurately retrieve spatial associations from memory. In rTg4510 mice, theta oscillation power appears to be independent of running speed meaning that these animals are unable to integrate this information effectively.

Interestingly, effects on the fast gamma power relationship with running speed were more pronounced than those relating to theta. This is similar to results displayed in the previous chapter, where dorso-ventral organisation of gamma oscillations is more prominent than theta. It is likely that gamma oscillations are a phenomenon requiring the entrainment of smaller groups of mEC neurons and therefore better directly represent local neuronal networks. Unlike oscillatory power, fast gamma frequency showed a reversed relationship with locomotor activity, with slow movement speeds associated with the fastest gamma activity

(fig 5.3Aii). Increased gamma frequency is inconsistent with the phase-amplitude coupling plots shown in the previous chapter, which show peaks at lower frequencies in rTg4510 mice (fig 4.6D). Since these are arguably not physiologically relevant frequencies for cognitive processing, it could be suggested that they are pathological and perhaps interfering with normal function seen in WT mice. This is reminiscent of similar aberrant changes to fast oscillatory activity that can be seen with NMDA receptor hypofunction and may have potential relevance to other neurological disorders such as schizophrenia (Pinault, 2008; Hakami *et al.*, 2009; Phillips *et al.*, 2012; Kocsis, 2012).

In WT mice, the gamma oscillation relationship with running speed shows a strong predominance for fast gamma frequencies (fig 5.3). This is consistent with the proposed information flow across the hippocampal formation, in which the mEC provides the input responsible for fast gamma frequencies in CA1 region of the hippocampus (Colgin *et al.*, 2009). While the CA1 area has been shown to display two distinct peaks in power spectra, mEC LFP predominantly contains faster frequencies only (Chrobak & Buzsaki, 1998; Colgin *et al.*, 2009) and this is consistent with the spectral analysis from these animals and the phase-amplitude coupling plots shown in chapter 4. It is perhaps not surprising then that changes between genotypes (fig 5.3) are seen only at these faster frequencies. For this reason also, conclusions regarding the slow gamma oscillation frequency should be made with caution. While slow gamma frequency has previously be shown to display a negative speed relationship in the hippocampus, mEC correlations are generally thought to be positive (Kemere *et al.*, 2013; Zheng *et al.*, 2015). These data show a negative frequency relationship with running speed which is reversed in rTg451 mice (fig 5.3Bii), however this association is weak. It is possible that without consistent peaks in low gamma activity, these values are modulated by the power in the surrounding frequency bands. For example, in rTg4510 mice, increases in slow gamma frequencies mirror decreases in fast gamma, the peaks of which may bleed increasingly into the slow gamma range.

It is also worth noting that rTg4510 mice exhibit a hyperactive phenotype (fig 5.5), and hence altered patterns of locomotor activity. An interpretation of this is that these mice are displaying compensatory mechanisms in which to increase network activity. It is unclear whether or not this is the case under these conditions and there is currently no evidence to suggest this. Potentially, this

could be observed using a head-fixed virtual reality preparation. However, at the very least it should be noted that rTg4510 mice are experiencing their environment at a generally higher state of arousal, at least in terms of locomotor activity.

5.4.3 Implications for grid cell firing

The theta frequency-running speed relationship has been proposed to be critical for the generation in grid field firing patterns, with oscillatory interference models, for example, relying on the interaction between baseline and velocity-controlled oscillators (VCOs) (Burgess *et al.*, 2007; Bush & Burgess, 2014). For this reason, it is possible that small changes to the slope of this relationship may have profound implications grid cell periodicity. Grid spacing is also thought to be dependent on this, with the slope in models such as Bush and Burgess (2014) consisting of the reciprocal of field size. This is based on experimental findings that show, for example, when theta frequency slope decreases during environmental novelty, grid fields expand (Jeewajee *et al.*, 2008*b*; Barry *et al.*, 2012*a*). The intrinsic resonance of mEC stellate cells is also slower in ventral mEC areas than dorsal, suggesting that such frequency changes across the mEC may play a role in the gradient of grid cell spacing (Giocomo *et al.*, 2007; Giocomo & Hasselmo, 2009; Pastoll *et al.*, 2012). In these experiments, rTg4510 mice showed a trend towards a decreased theta frequency slope (fig 5.2Dii). However, if the slope of the averaged running speed relationship for each genotype were to be used to scale VCO slopes from models such as (Bush & Burgess, 2014), rTg4510 mice would show a vast expansion of grid fields compared to WT, leading to the reduction in grid score seen in figure 5.6.

5.4.4 Dorso-ventral organisation of running speed representation

Interestingly, these data also highlight the novel finding that WT mice display a dorso-ventral gradient in running speed- theta/gamma oscillation interactions (fig 5.4). Oscillatory power was observed to show greater increases in dorsal mEC for given increases in locomotion activity when compared to ventral, meaning that as WT mice run faster, the distinction between dorsal and ventral mEC becomes more pronounced. The functional consequences of this are as yet unclear,

however these data strongly suggest the hypothesis that, like grid (Brun *et al.*, 2008*b*; Stensola *et al.*, 2012) and head direction (Giocomo *et al.*, 2014) firing, speed cells may also display dorso-ventral gradients in their activity. As stated above, fast running speeds require an increased sensitivity to locomotive activity, since the time window for integration of spatial information is smaller. It is possible that this required compensation is uneven across the dorso-ventral axis of the mEC, with tightly spaced grid cells in dorsal regions, for example, needing to shift activity states more frequently than ventral.

Speed correlated input into the mEC has been postulated to arrive from glutamatergic projections from the medial septum and diagonal band of Broca (MSDB) (Justus *et al.*, 2016). Intriguingly, this appears to arrive preferentially into ventral mEC areas, however, how this input is integrated and ultimately forms mEC output is unclear. Further modelling by Justus et al. (2016) suggested that while pyramidal cells may most efficiently transform speed inputs to outputs (backed up experimentlally by Sun et al. 2015), theta modulated output could be most effectively generated by fast spiking interneurons, which as previously discussed display a strong preference for dorsal mEC expression (Beed *et al.*, 2013). This potentially suggests a dissociation between running speed-associated changes in firing rate and theta rhythmicity. Indeed, inactivation of the medial septum has been shown to impair increases in the oscillatory frequency of theta rhythmic cells in the mEC, but not the relationship between running speed and firing rate (Hinman *et al.*, 2016). It is unclear whether a second speed signal is projecting to the mEC, however it is possible that these signals are anatomically disparate within basal forebrain areas, which were not equally impaired by the muscimol infusion employed in these experiments.

Long range GABAergic and cholinergic projections also enter mEC from basal forebrain areas (Colom, 2006; Gonzalez-Sulser *et al.*, 2014; Vandecasteele *et al.*, 2014), which may also be relevant under these conditions. Cholinergic inputs in particular are also likely to play a modulatory role in representing locomotor information. Modulating cholinergic transmission alters slope of running speed-theta oscillation relationships in the hippocampal formation (Newman *et al.*, 2013, 2014). These fibres also potentially underlie context-specific changes to theta frequency-running speed slope, for example during periods of environmental

novelty (Jeewajee *et al.*, 2008*a*, 2008*b*), which may have implications on grid field expansion (Barry *et al.*, 2012*a*, 2012*b*).

In contrast to WT, rTg4510 mice displayed no gradients in the relationship between running speed and oscillatory activity. Considering the pronounced deficit seen across all electrodes, this was perhaps not surprising. However, it further highlights the findings seen in the previous chapter, suggesting a reorganisation of mEC physiology. It remains to be seen whether the specific deficits in locomotor information processing in rTg4510 mice arise from reduced, or impaired, inputs from basal forebrain areas. The hypothesis of basal forebrain degeneration is by no means novel, and dates back to early reports of Alzheimer's pathology (Davies & Maloney, 1976; Coyle *et al.*, 1983; Francis *et al.*, 1999; Terry & Buccafusco, 2003). Specifically, these focused on dysfunction of cholinergic projections, however, the complexity of mEC inputs from this region highlight further avenues for exploration.

5.4.5 Theta/gamma oscillation - running speed interactions as a biomarker for impaired network activity

Given that the relationship between oscillatory activity and running speed can be observed using relatively simple electrophysiological techniques, and is a phenomenon that has been shown to be adaptive to environmental context, this interaction could be presented as a good functional biomarker with which to measure the effect of disease pathology in rodent models of dementia. As a process, this will undoubtedly require the integration of numerous information streams and coordination of large scale neuronal networks, which are likely to be influenced by tau pathology. Theta oscillation-running speed relationships have previously been shown to be modulated by pharmacology and environmental stimulus. For example, blocking muscarinic acetylcholine receptors with scopolamine, which is widely known to cause memory impairments, has been shown to reduce the slope relating movement speed to theta frequency (Newman *et al.*, 2013). Anxiolytic compounds also effect this relationship, in this case decreasing the intercept of the slope (Wells *et al.*, 2013), suggesting a dissociation of spatial and arousal based cognitive states.

The precise relationship between the progression of rTg4510 pathology and impaired locomotor encoding is yet to be determined. However, it is possible that this impairment could be tightly associated with, or even precede, cognitive deficits. In any case, these findings may prove useful for assessing the effectiveness of potentially cognitive enhancing compounds and may allow for a relatively high throughput screening of new drug targets.

5.4.6 Conclusions

The data presented in this chapter clearly show changes to the representation of locomotor activity in the mEC of rTg4510 mice. The underlying impact of this on the firing of individual mEC neurons remains to be seen. However, it is likely that this will have direct consequences for the spatial firing patterns of grid cells in the mEC, which will be addressed in the next chapter, and for path integration mechanisms in general.

6. Decreased speed modulation of mEC neurons coincides with breakdown of grid cell periodicity in rTg4510 mice

6.1 Introduction

It has been established in the previous chapters that rTg4510 mice display large scale changes to mEC neuronal networks. However, how tau overexpression affects individual cell firing in the mEC is yet to be examined. The final chapter of this thesis will establish how the deficits described above, specifically to speed modulated activity, correspond to changes in spatial firing properties in the mEC.

6.1.1 Spatial information processing in the mEC

Since the discovery of grid cells, the mEC has been generally recognised to have a critical role in spatial representation and navigation. Grid cells fire selectively in regular and stable fields, forming a hexagonal lattice that covers an entire environment (Fyhn *et al.*, 2004; Hafting *et al.*, 2005). Unlike hippocampal place cells, which readily remap in new environments, they provide an invariant spatial metric that can integrate idiothetic cues in order to continuously update self-location, making them a prime candidate for performing path integration based representation of space (Barry & Bush, 2012). In order to provide this, grid cells must continuously integrate information relating to movement and direction. This is achieved through dedicated populations of neurons encoding for running speed (Kropff *et al.*, 2015) and head direction (Ranck, 1984; Sargolini *et al.*, 2006; Valerio & Taube, 2012; Giocomo *et al.*, 2014), as well as large populations of conjunctive cells, found increasingly in deeper mEC layers, that display firing preferences for several, or all, spatial information types (Sargolini *et al.*, 2006).

6.1.2 Spatial navigation in dementia

Spatial disorientation appears as a common symptom in Alzheimer's disease (AD) and it has been proposed that reduced grid cell representation in the mEC may underlie these changes (Kunz *et al.*, 2015). Spatial navigation is known to

be affected early in dementia pathology (Hort *et al.*, 2007; Laczó *et al.*, 2011; Lithfous *et al.*, 2013; Allison *et al.*, 2016), including specific deficits in path integration (Mokrisova *et al.*, 2016). It is therefore important to understand specific changes to mEC spatial navigation systems that may occur in mouse models of dementia.

A handful studies have examined the spatial firing properties of individual neurons in the hippocampus in models of tauopathy (Cheng & Ji, 2013; Booth *et al.*, 2016*b*). However more recently, the activity of grid cells has been observed in an entorhinal cortex specific overexpression model (Fu *et al.*, 2017) showing that after long periods of tau expression, grid cell periodicity and firing rate are reduced. Despite this, little is known about how tau overexpression may affect the projections into the mEC from other pathways processing spatial information. The activity of single units in the mEC was therefore recorded in rTg4510 mice that display widespread tau pathology across all forebrain areas.

6.2 Methods

6.2.1 Single-unit spike detection

Extracellular recordings were carried out using 2x16 channel electrode shanks (section 2.4.1) in male 7-8 month old rTg4510 and WT control mice. Data were referenced to the ground electrode, continuously sampled at 40 kHz, bandpass filtered between 1-30 kHz and saved unprocessed on a PC for offline analysis. Each channel was referenced offline to a common-average of the opposite 16-channel shank (250 µm away). Extracellular spike activity was detected and sorted using the klusta open source software package (Rossant *et al.*, 2016). LFP data were recorded while animals explored either a linear track (1.2 m) or square open field (1.25 m x 1.25 m).

6.2.2 Cell classification

Speed modulation of cells was defined by the correlation (r) between all running speed and firing rate bins and expressed using the Fisher-z transformation (z) for variance stabilization. Head direction was determined by calculating the angle

between two LEDs attached to the animal's headstage. Firing rate was calculated for 3º bins of head direction and smoothed, using a Gaussian window over 14º. A 'head direction score' was defined as the resultant mean vector length, calculated from the smoothed firing rate maps.

Spike locations for each cell were obtained using a 2D histogram count. Firing rate was calculated for 3 cm x 3 cm bins across recording environments and smoothed using a 2D Gaussian function. 'Gridness' was calculated using a 2D autocorrelation of smoothed firing rate maps (Sargolini *et al.*, 2006). Spatial periodicity was determined by rotating autocorrelations in steps of 30° and correlating the rotated versions with the original. Grid score was defined as the minimum difference between rotations at 60° or 120°, where if firing maps show a hexagonal pattern correlations will be high, and 30°, 90° or 150°, where correlations will be low.

The spatial information content of each cell was defined using the measure described by Skaggs *et al.*, (1993) and expressed in terms of bits/spike. This approach measures the extent to which a cells firing rate can be used to predict the animal's location.

All observed speed, head direction and spatial firing scores were compared to a distribution of randomly sampled correlations of shuffled data. 250 shuffles were performed for each cell and combined for each group. Cells were classified as significant if their score was greater than the 95th percentile, or for speed modulation less than the 5th percentile, of the shuffled distribution.

6.2.3 Hippocampal CA1 data

Single unit data recorded from CA1 pyramidal cell layer were obtained by Jon Witton (Booth *et al.*, (2016*b*)). Data were collected using microdrives containing independently moving tetrodes, while animals ran on a linear track. Running speed – firing rate relationships were re-analysed using the pathway described above.

6.3 Results

6.3.1 Decreased theta modulation of mEC single units in rTg4510 mice

In order to determine the underlying cellular basis for impaired network activity in rTg4510 mice, firing patterns were observed from a total of 279 single-units in layer II/II mEC, isolated from 10 mice (WT:145 units from 5 mice, rTg4510: 134 units from 5 mice). Across the entire population, rTg4510 mice showed a small decrease in the average firing rate of mEC single units (fig 6.1A Median: WT: 3.1 Hz, rTg4510: 2.0 Hz, U = 4472, p = 0.01, Mann-Whitney U, n= 145/134). rTg4510 cells also showed a pronounced decrease in theta modulation of firing patterns (fig 6.2C, Median (theta modulation index): WT: 7.4, rTg4510: 2.3, U = 2296, p < 0.001, Mann-Whitney U, n= 145/134). Individual units with theta modulation index (TMI) greater than 5 were defined as 'theta modulated'. While the majority of WT mEC cells (63%) showed significant theta modulation, only a small proportion (16%) passed threshold in rTg4510 mice (χ^2 (1) = 64.1, p = <0.0001, Chi-Square test, fig 6.2D).

A significant population of mEC neurons can be classified as inhibitory interneurons (Miettinen *et al.*, 1996; Beed *et al.*, 2013; Buetfering *et al.*, 2014). Using the average spike waveform, putative interneurons were classified as displaying spike-width less than 0.4 ms, based on the extracellular properties of PV+ interneurons isolated optogenetically (Buetfering *et al.*, 2014), (fig 6.1B). In WT mice, the proportion of putative interneurons was shown to be approximately 8% which was not significantly different to units recorded from rTg4510 mice (WT: 11/145, rTg4510: 13/134, χ^2 (1) =0.4, p = 0.53, Chi-Square test, fig 6.2C).

6.3.2 Speed modulated firing is impaired in rTg4510 mice

Results from the previous chapter suggest that rTg4510 mice are unable to effectively represent running speed information within the mEC. In addition to representation at the LFP level, there is good evidence that running speed is encoded by the firing rates of individual cells (Sun *et al.*, 2015; Kropff *et al.*, 2015; Hinman *et al.*, 2016), therefore, the modulation of mEC single units by running speed was computed. A speed score (z) was produced, based on the correlation between instantaneous firing frequency and running speed while mice ran on an

L-shaped linear track. Units were described as 'speed modulated' if their correlation was higher than the 95th centile of a shuffled distribution of data produced from 250 shuffles for each cell. In WT mice, a large proportion of cells had firing rates significantly modulated by running speed (~52%). However, this proportion was significantly lower (~22%) in rTg4510 mice (WT: 120/145, rTg4510: 41/134, χ^2 (1) =22 p <0.0001, Chi-Square test, fig 6.3E). As an overall population, rTg4510 mEC units also displayed a significantly lower average speed score compared to WT mice (Median: WT: z=0.09, rTg4510: z=0.006, U = 4530 p < 0.001, Mann-Whitney U, n= 145/134, fig 6.3D), with cells recorded from rTg4510 mice, on average displaying a running speed correlation close to zero.

Speed modulated mEC neurons can be broadly split into those that display linear and saturating exponential relationships between running speed and firing rate (Hinman *et al.*, 2016). To account for this, speed scores were performed for log transformed data and further classified as linear or exponential by the best regression fit. In WT animals these cells were slightly more likely to best fit linear running speed relationships (fig 6.4C). However, rTg4510 mEC neurons showed a greater tendency for saturating fits (WT: linear: 76/120, saturating: 44/120, rTg4510: linear: 16/41, saturating: 17/41, χ^2 (1) =6, p = 0.014 Chi-Square test, fig 6.4C).

6.3.3 Over representation of negatively speed modulated cells in rTg410 mice

rTg4510 mice show almost no correlation between oscillatory power and running speed; however although decreased compared to WT, a significant population of speed modulated cells (~22%) was observed in these animals (fig 6.3E). While the majority of speed modulated cells in the mEC of wildtype animals have positive correlations with running speed, a small proportion have been shown to decrease firing frequency during locomotor activity (Kropff *et al.*, 2015; Hinman *et al.*, 2016). On the linear track, in WT mice, this population was observed to be consistent with previous reports (~17%)(Kropff *et al.*, 2015; Hinman *et al.*, 2016). In contrast, in rTg4510 mice the proportion of cells with negative speed relationships was substantially and significantly higher (WT: 20/120, rTg4510:18/36, χ^2 (1) =17, p <0.0001, Chi-Square test, fig 6.5C), meaning that

speed modulated cells were almost split evenly between positive and negative associations with firing rate.

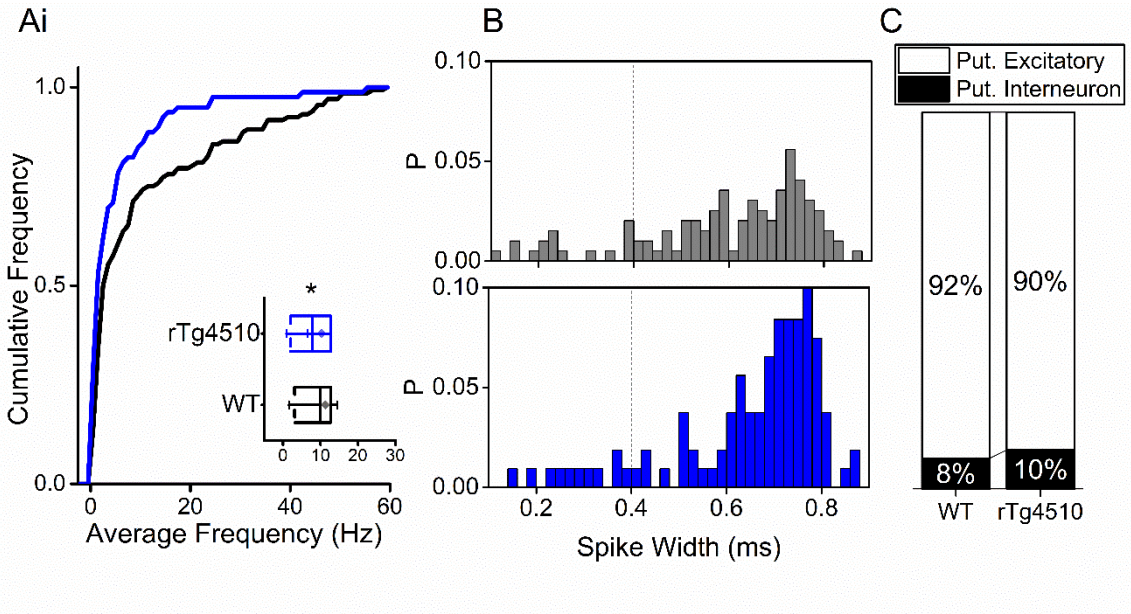

Figure 6.1 Firing properties of mEC single units. A) Average firing frequency across entire recording session of mEC neurons for WT (black) and rTg4510 (blue) mice, average inset. **B)** Spike-width histogram for WT (black) and rTg4510 (blue) units. **C)** Proportion of cells classified as putative interneurons (spike-width <0.4ms, dotted line in E) and putative excitatory. Box plots: dotted line: median, diamond: mean ± SEM, whiskers: 25th/75th centile), * p<0.05, *** p <0.001 Mann-Whitney U test.

6.3.4 Speed modulation in CA1 hippocampus shows similar changes to mEC in rTg4510 mice

Speed modulated firing of single units has also been observed in the hippocampus (McNaughton *et al.*, 1983*a*; Lu & Bilkey, 2009; Kropff *et al.*, 2015). It was therefore important to ascertain whether deficits in speed tuning in rTg4510 mice were specific to the mEC, or also represented downstream in the hippocampus proper. For this purpose, data was taken from previous single unit and local field potential recordings in the hippocampal CA1 region of rTg4510 mice (Booth *et al.*, 2016*b*) at a similar age point and reanalysed to assess the contribution of locomotor activity to firing rate.

In this region, CA1 theta band activity in the local field potential is also correlated with running speed in WT mice (linear regression; theta power; WT: R^2=0.83,

p<0.001, n=6), but not in rTg4510 mice (linear regression: R^2= -0.04, p=0.6, n= 4, fig 6.6B). A significant proportion of CA1 neurons were shown to have firing rates modulated by running speed in both WT and rTg4510 mice (WT: 25 /46, rTg4510: 27/52). Importantly however, as seen in mEC recordings, a much larger proportion of CA1 cells were negatively modulated by locomotor activity than in WT controls (WT: 5/25 rTg4510:13/27, χ^2 (1) =4.5, p = 0.03, Chi-Square test, fig 6.6E).

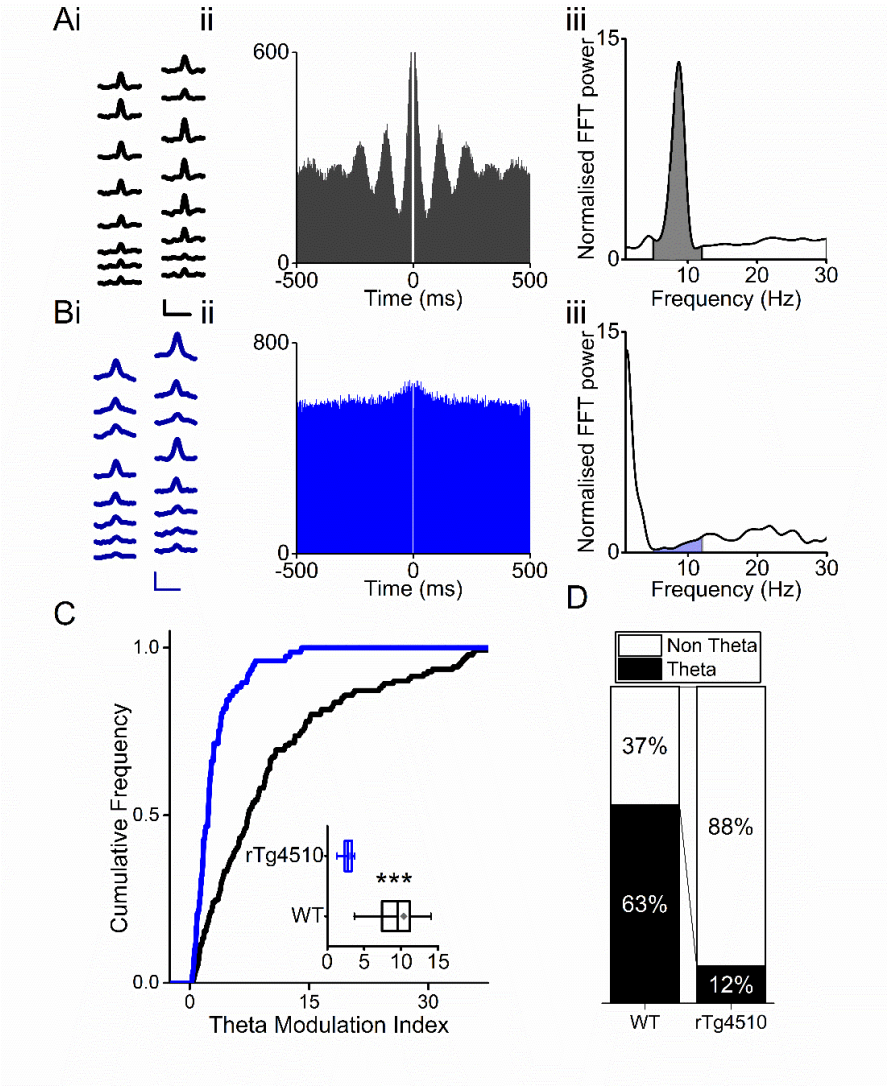

Figure 6.2 Decreased theta modulation of mEC single units in rTg4510 mice **A)** Average waveforms from example cell on 16 channel shank for WT and rTg4510 (**B**) mouse, with firing autocorrelations (ii) and Fourier transform (FFT) of autocorrelation showing theta peak in WT but not rTg4510 example cell. Scale bars: 40 ms, 50 µV. **C)** Theta modulation of all recorded mEC units, cumulative frequency plot, with average modulation for WT (black) and rTg4510 (blue) mice inset. **D)** Proportion of cells displaying theta modulation (threshold: TMI>5).

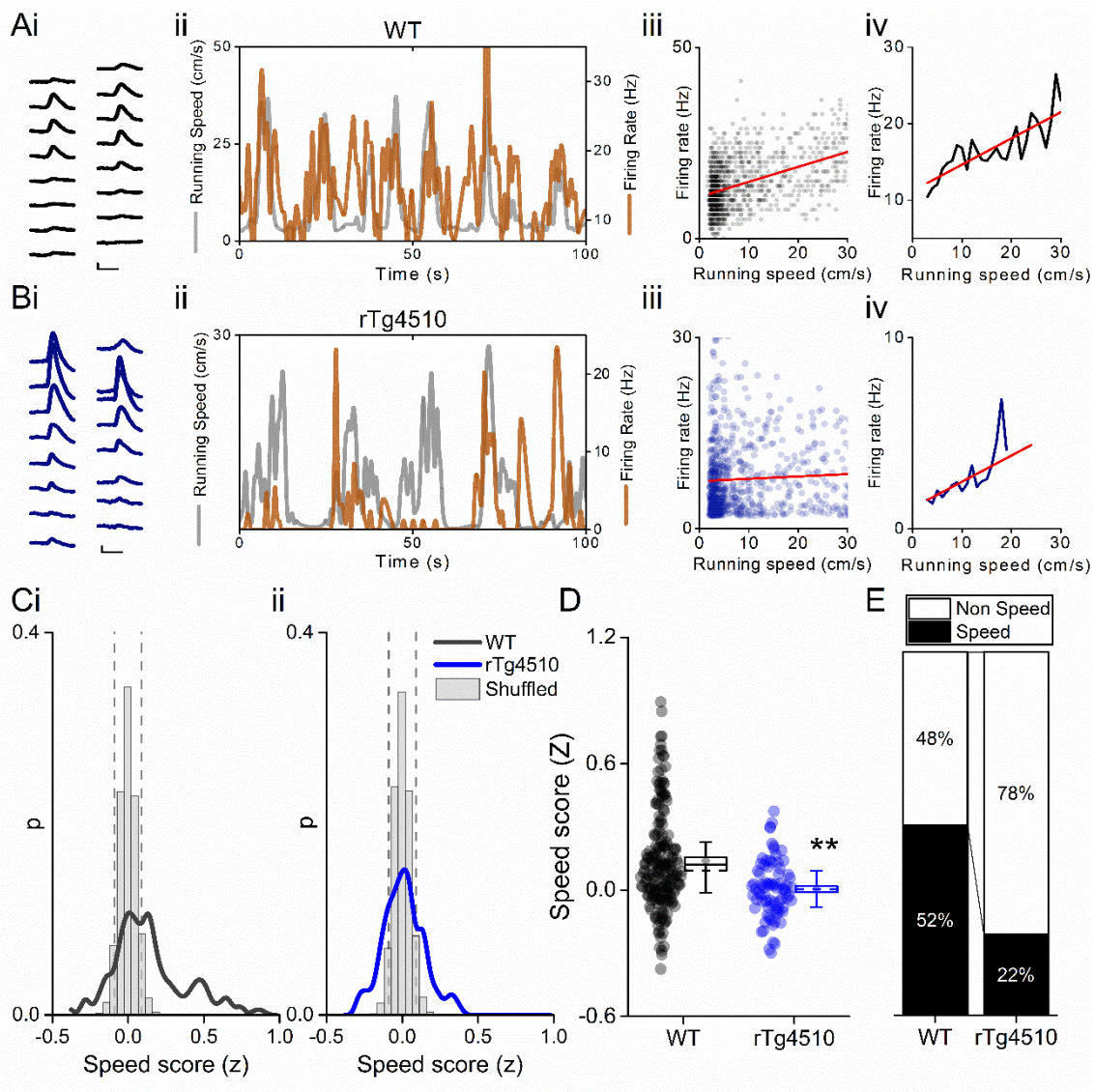

Figure 6.3 Decreased speed modulation of mEC single units in rTg4510 mice. Ai) Average waveforms from 16 channel shank, for WT and rTg4510 (**Bi**) example cells, with running speed (grey) and cell firing rate for WT (orange) and rTg4510 (blue) cells (**ii**), correlation between running speed and firing rate for each time bin (40 ms) and average for each speed bin (1 cm/s) (**iv**). Red line: linear fit for each. Scale bars: 40 ms, 50 µV. **C)** Distribution of speed scores for WT (i) and rTg4510 mice (ii) with shuffled distribution of scores (grey), 5^{th}/95^{th} centile threshold: dotted line. **D)** Average speed score for each recorded mEC unit. Box plots: dotted line: median, diamond: mean ± SEM, whiskers: 25^{th}/75^{th} centile), ** p<0.01, Mann-Whitney U test. **E)** Proportion of cells classified as speed modulated (>95^{th} or <5^{th} centile of shuffled distribution).

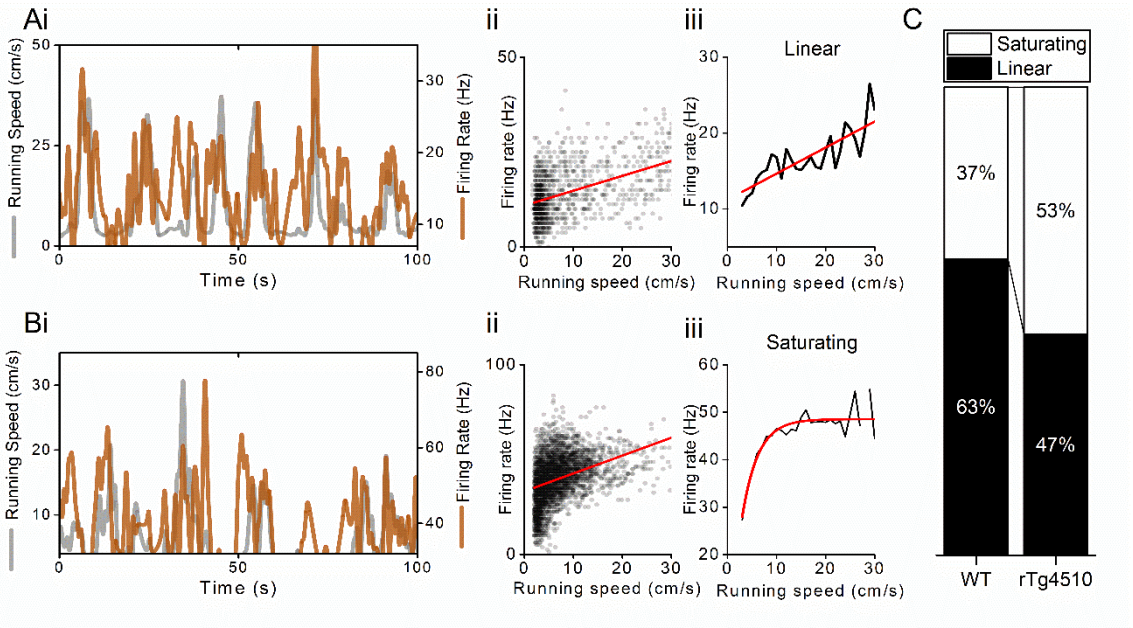

Figure 6.4 rTg4510 mice show decrease in linear speed relationship. A) Example cell, with linear speed relationship. Running speed (grey) and cell firing rate for WT (orange) and rTg4510 (blue) cells (**i**), correlation between running speed and firing rate for each time bin (40 ms) **(ii)** and average for each speed bin (1 cm/s) (**iii**). **B)** Same for cell with saturating speed relationship. **C**) Proportion of speed modulated mEC cells that are best described by linear and saturating fits for WT and rTg4510 mice.

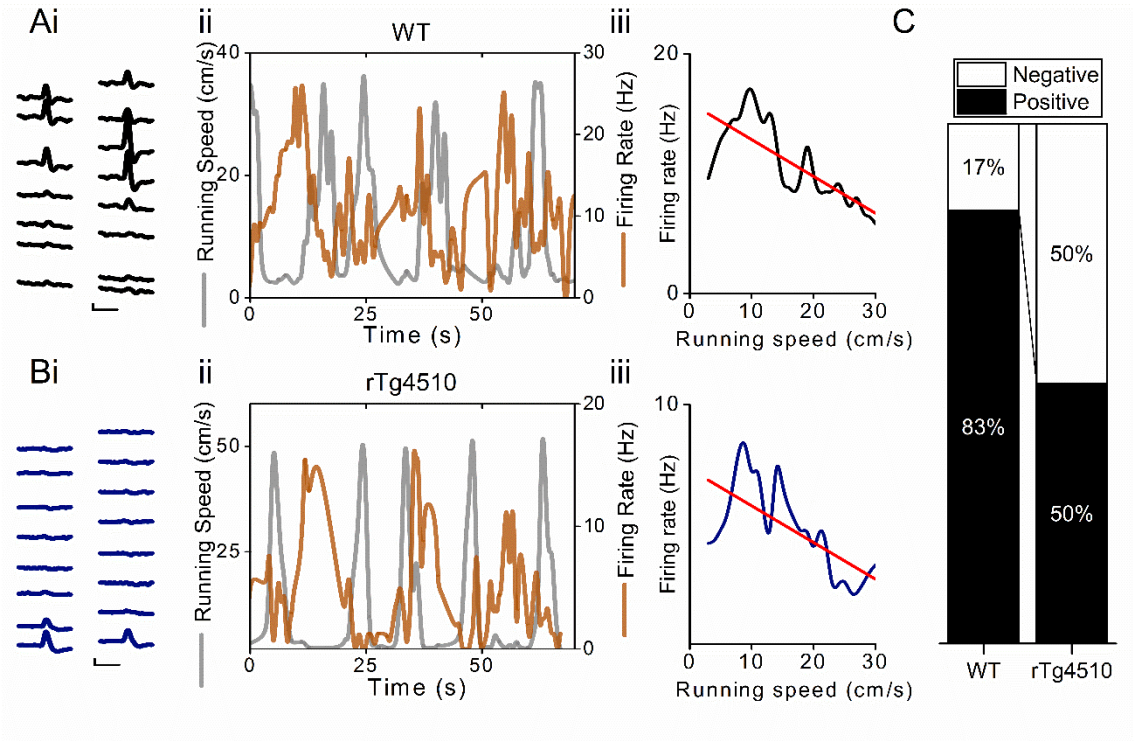

Figure 6.5 Increased representation of negative speed modulation in rTg4510 mice. Ai) Average waveforms from 16 channel shank, for WT and rTg4510 (**Bi**) example cells, with running speed (grey) and cell firing rate for WT (orange) and rTg4510 (blue) cells (**ii**), and average for each speed bin (1 cm/s) (**iii**). Red line: linear fit for each. Scale bars: 40 ms, 50 µV. **C)** Proportion of speed modulated units that show positive (>95th centile of shuffled distribution) and negative (<5th centile of shuffled distribution) speed modulation.

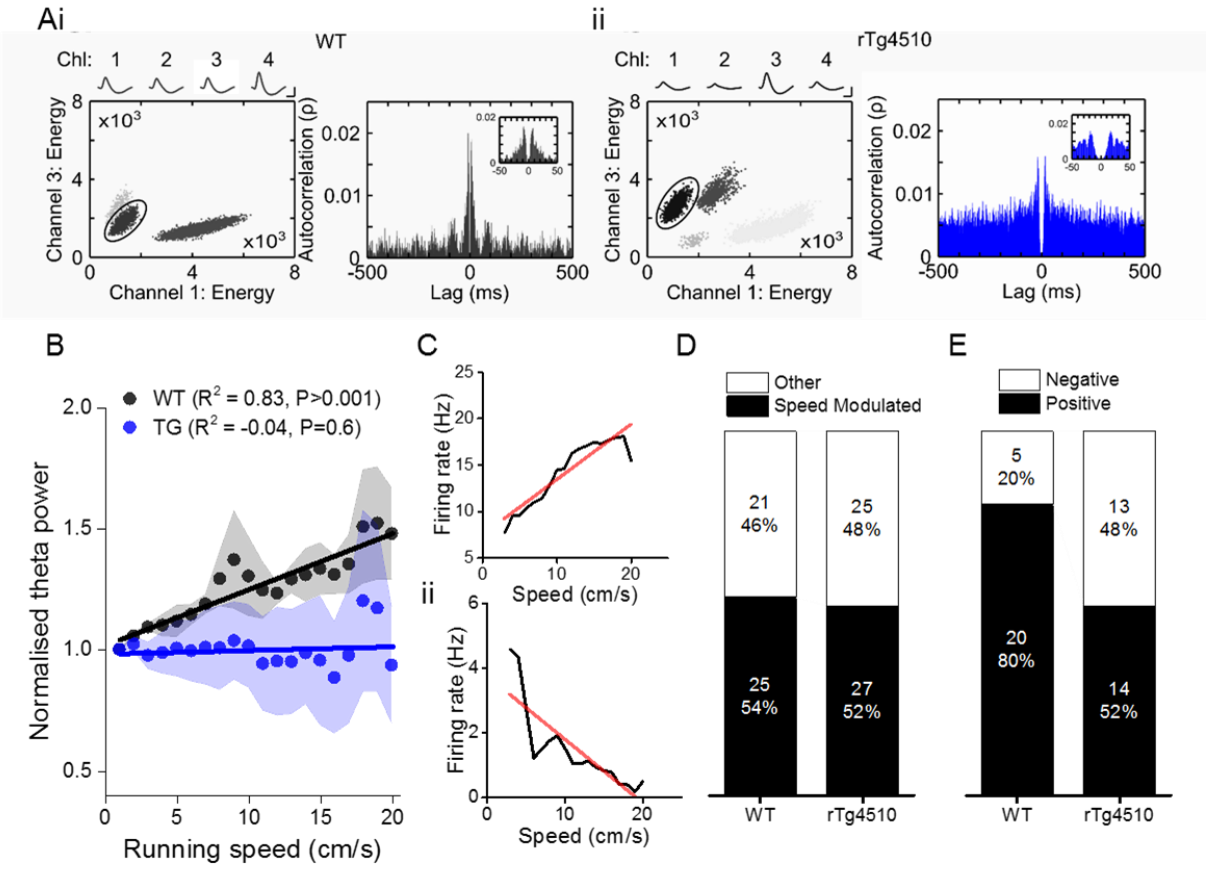

Figure 6.6 Speed modulation of single units in hippocampal CA1 pyramidal cell layer also shows similar increase in negatively speed modulated firing. **A**) Example cells from WT (**i**) and rTg4510 (**ii**) mice, with waveform energies of action potentials from 2 channels of tetrode, mean waveforms and spike-train autocorrelation for clustered unit (circled). **B)** Normalised theta oscillation amplitude from WT and rTg4510 mice with increasing running speed, with average linear regression above. **C)** Example positive and negative (**ii)** speed modulated cells recorded form CA1 pyramidal cell layer. **D)** Proportion of cells passed criteria for speed modulated firing is approximately even between genotypes. **E)** Increased proportion of negatively speed modulated units in CA1 in rTg4510 mice, compared to WT controls. Data recorded by J.Witton and panel A reproduced from (Booth et al., 2016b).

6.3.5 Breakdown of grid cell periodicity in rTg4510 mice

In parallel with the LFP data (chapter 5), rTg4510 mice show a clear reduction in the speed modulation of mEC single units, however the direct effect of this on the spatial firing properties of grid cells is unclear. The firing of mEC cells was therefore recorded in a 2D square recording environment (1.25 m x 1.25 m), while mice foraged for food rewards and grid score calculated for each cell using the 2D autocorrelation of rate-maps across recording environments (see Methods section). These analyses revealed a significant population of grid cells in layer II/III mEC in WT mice (33/145 units, 22.3%), with grid scores higher than the 95th percentile of the distribution produced from shuffled spike timestamps (threshold = 0.21). However, in rTg4510 mice there was an almost complete breakdown of grid cell periodicity (4/136 units, 2.9%, threshold: 0.26), with animals displaying irregular, non-uniform, firing fields across recording environments (χ^2 (1) = 18.63, $p < 0.0001$, Chi-Square test, fig 6.7A/C).

While as a population grid score values were significantly lower in rTg4510 mice (fig 6.7D, Median: WT: 0.03, rTg4510: 0.002, U = 4316, $p < 0.0001$, Mann-Whitney U, n= 145/134), this was not the case for the spatial information content of cells, which across the population was slightly higher compared to WT controls (fig 6.7E, Median (bits/spike): WT: 0.01, rTg4510: 0.12, U = 4316, p = 0.0065, Mann-Whitney U, n= 145/134). There was also no difference in the number of spatial non-grid cells observed across groups (WT: 6/145, rTg4510: 5/136), defined as cells that cross threshold for spatial information content (WT: 0.53, rTg4510: 0.58) but not grid score (χ^2 (1) = 0.2, p = 0.66, Chi-Square test, fig 6.5C).

6.3.6 Head direction tuning is not effected by tau overexpression

Interestingly, while there were profound decreases in both the speed- and spatially modulated firing in rTg4510 mice, this was not the case for the head-direction tuning of mEC cells. As a population, the head direction (HD) score (mean vector length) was slightly, but significantly, higher in rTg4510 mice (fig 6.8D/E, Median (mean vector length): WT: 0.06, rTg4510: 0.1, U = 14258, p = 0.01, Mann-Whitney U, n= 145/134). However, there was no significant effect on the proportion of cells that passed 95th centile threshold set from the shuffled distribution of HD scores (χ^2 (1) = 0.04, p =0.84, Chi-Square test, fig 6.8C).

6.3.7 Conjunctive representation of spatial firing properties in mEC rTg4510 mice

In summary, the analysis of spatial information measures in the mEC revealed that rTg4510 mice displayed a marked reduction in the prevalence of both speed and grid cell activity, with little effect on the proportion of head direction cells (fig 6.10A). In WT mice, the majority of recorded cells reached criteria for either speed modulation, grid periodicity or head direction tuned firing (~62%), with many of these being conjunctively modulated by 2 or more spatial parameters (~16%). In contrast, no neurons recorded from rTg4510 mice that showed conjunctive firing of speed, grid or head direction tuning (WT: 22/145, rTg4510:0/134, fig 6.9/ 6.10B). In addition, compared to WT controls, rTg4510 single units were much more likely be not classified into one of the categories described above (Non-classified, WT: 40/145 rTg4510: 94/134, χ^2 (2) = 58.5, p <0.0001, Chi-Square test).

In these recordings, a large proportion of WT grid cells also showed either speed or directional modulation. Specifically, around half of these cells were also modulated by speed, which was not the case in rTg4510 mice (fig 6.10C). Furthermore, although the proportion of head direction cells was not significantly different between genotypes, the majority of recorded head direction cells (~75%) were also conjunctive grid cells (fig 6.10 D). However, this was also not the case in rTg4510 mice.

6.3.8 Recording location is consistent between genotypes

Recording locations were determined by electrolytic lesions of each recording shank before the perfusion-fixation of tissue. While the recording location of each electrode shank varied along the dorso-ventral axis of the mEC, locations were not significantly different between WT and rTg4510 genotypes (Median (µm): WT: 300, rTg4510: 430, U = 22, p = 0.8, Mann-Whitney U). Since the recording array used in these experiments contained electrodes across 200 µm of tissue, more precise recording locations were estimated using the largest average waveform for each isolated unit. Recording location was also not different between genotypes when using this estimated measure (Median (µm): WT: 350, rTg4510: 385, U = 9660, p = 0.77, Mann-Whitney U test).

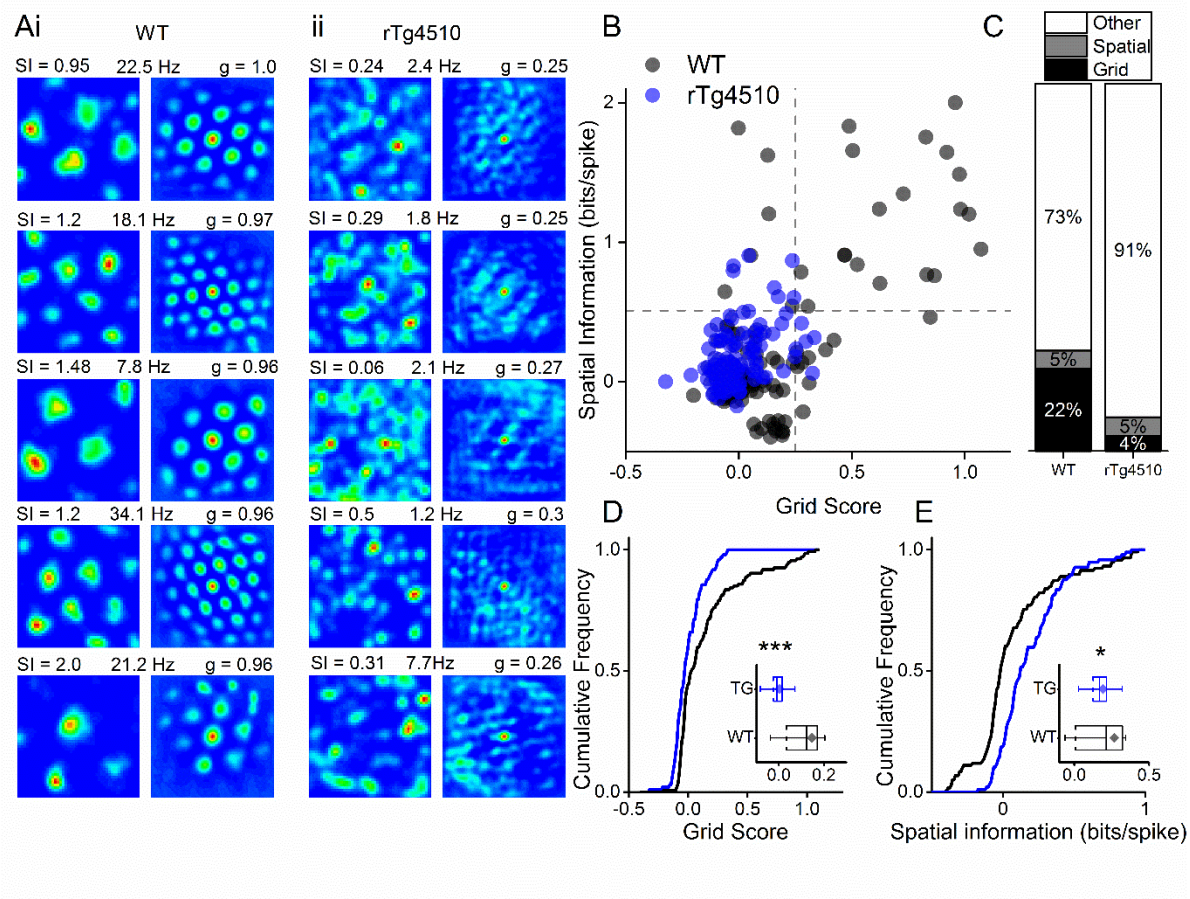

Figure 6.7: Breakdown of grid cell periodicity in rTg4510 mice. A) Example spatial firing patterns of cells from WT (i) and rTg4510 (ii) mice in a 1.25 m square arena, displayed with grid score (g), spatial information content (SI) and peak firing rate across recording environment. 5 cells with the highest grid score displayed for each genotype. **B)** Grid score plotted against spatial information content for each cell in WT and rTg4510 mice, for illustrative purposes dotted lines represent threshold (95th centile of shuffled distribution) for grid/spatial firing in WT mice. **C)** Proportions of grid and spatial non-grid cells greater than threshold in WT and rTg4510 mice. **D)** Cumulative frequency plots for grid score and spatial information content (**E**) with average values for each genotype (dotted line: median, diamond: mean ± SEM, whiskers: 25th/75th centile), * p<0.05, *** p<0.001, Mann-Whitney U test.

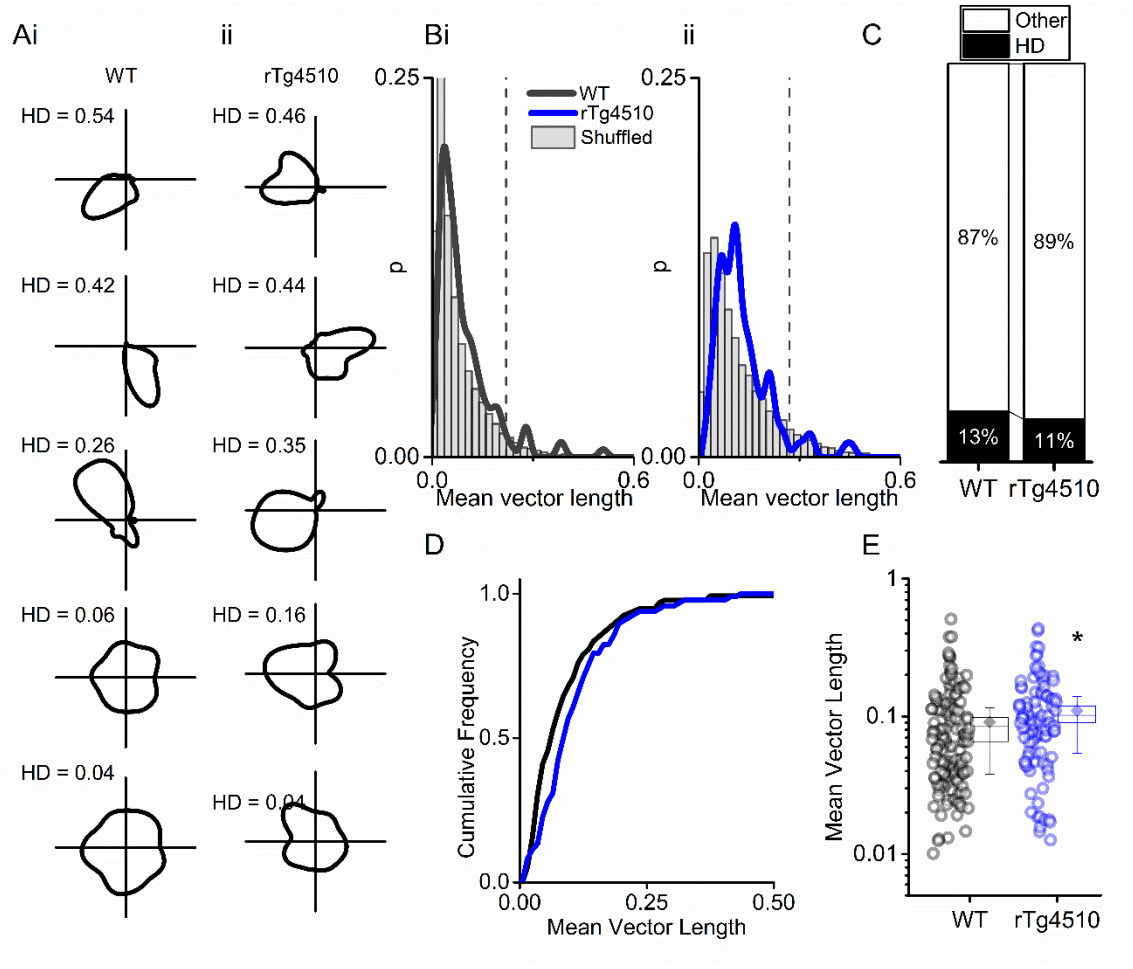

Figure 6.8 rTg4510 mice retain mEC head-direction tuning. A) Example head-direction tuning of WT and rTg450 units, displayed with head direction score (HD) and peak firing rate across head direction bins. **B)** Distribution of HD scores for WT (i) and rTg4510 mice (ii) with shuffled distribution of scores (grey), threshold: dotted line. **C)** Proportions of cells with head direction scores over threshold in WT and rTg4510 mice. **D)** Cumulative frequency distribution of HD scores (mean vector length), dotted line: WT threshold. **E)** Mean vector length for all cells, showing increased head-direction tuning across population in rTg410 mice (dotted line: median, diamond: mean ± SEM, whiskers: 25th/75th centile), * p<0.05 Mann-Whitney U test.

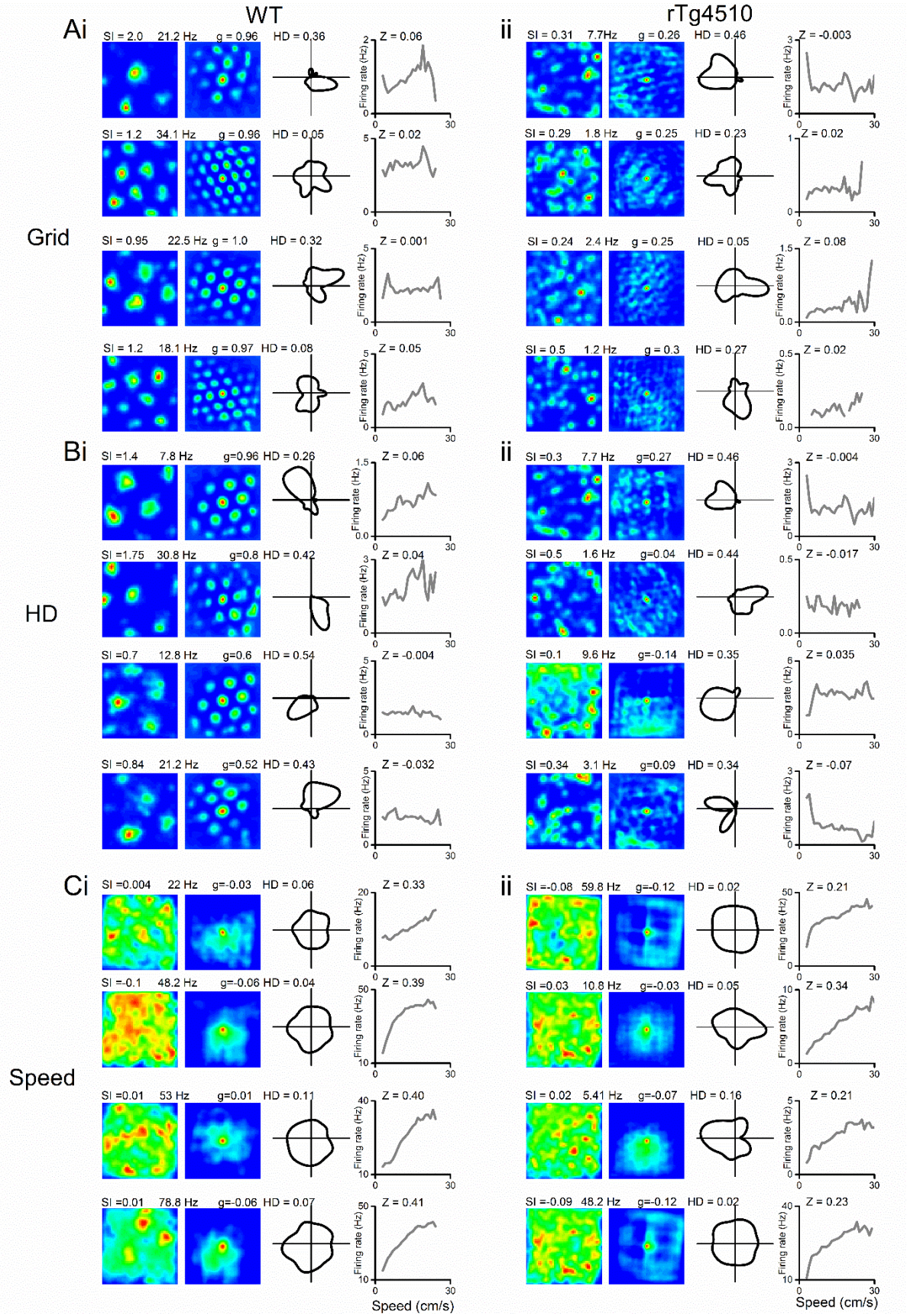

Figure 6.9 Example mEC units. Example grid (A), head direction (B) and speed (C) cells taken from the highest modulation scores from WT (i) and rTg4510 (ii) mice, showing spatial firing patterns with 2D spatial autocorrelation, head direction tuning and running speed-firing rate relationship and corresponding score (SI: spatial information, HD: mean vector length, Z: speed score).

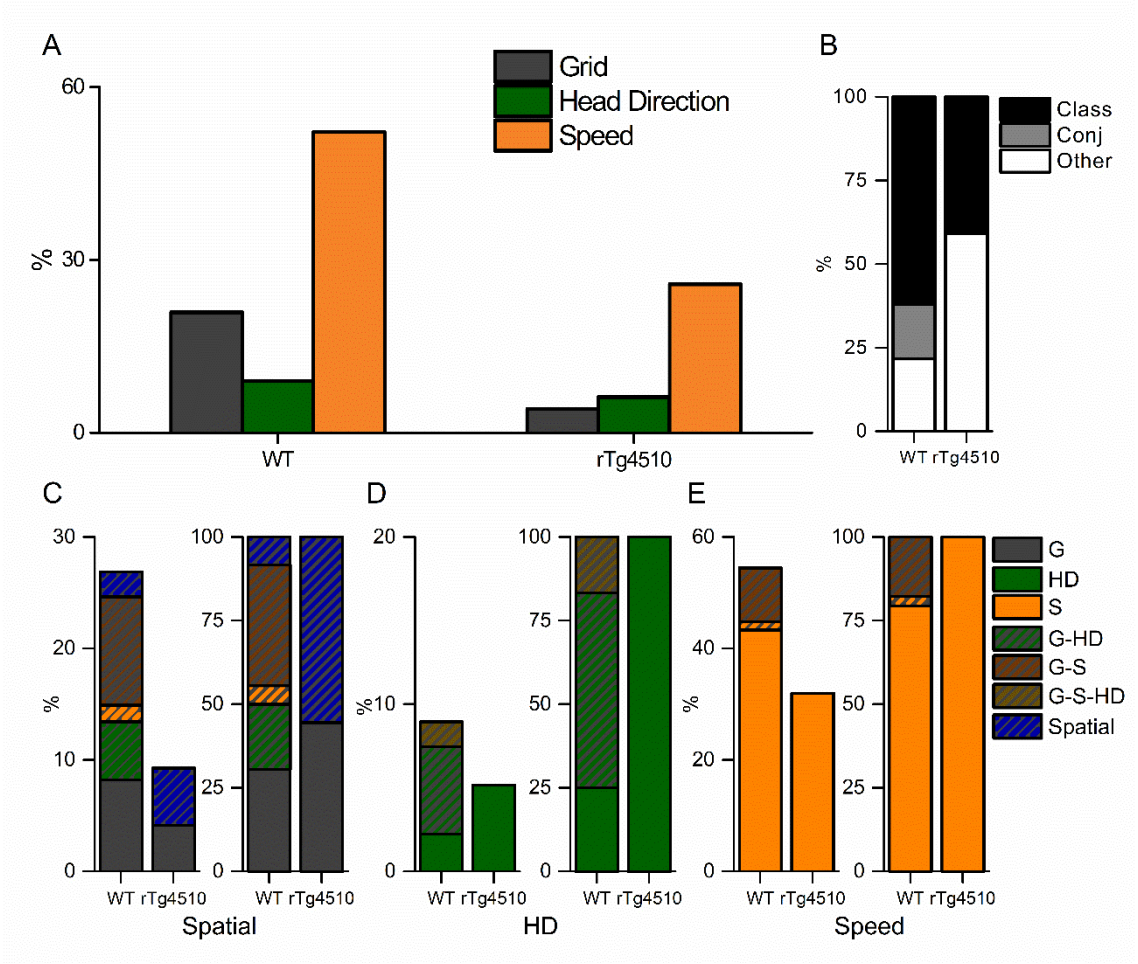

Figure 6.10 Conjunctive representation of grid, head direction and running speed in WT and rTg4510 mice. A) Proportions of grid, head-direction and speed modulated cells recorded in mEC, showing reduced number of grid and speed, but not head-direction, cells passing threshold (95% centile of shuffled distribution). **B)** Breakdown of units from WT and rTg4510 mice that satisfied a single criteria (class), multiple criteria (conj) or no discernible firing pattern (other). **C)** Conjunctive proportions of grid cells, head direction cells **(D)** and speed modulated cells **(E)** recorded from WT and rTg4510 mice with comparison scaled to 100% on right (ii). Key, G: grid, HD: head direction, S: speed, Sneg: negative speed, G-HD: gird-head direction, G-S: grid-speed, G-S-HD: grid-speed-head direction. Class: classed as cell type, Conj: conjunctive representation (more than 1 classification), other: not classified as grid, speed or HD.

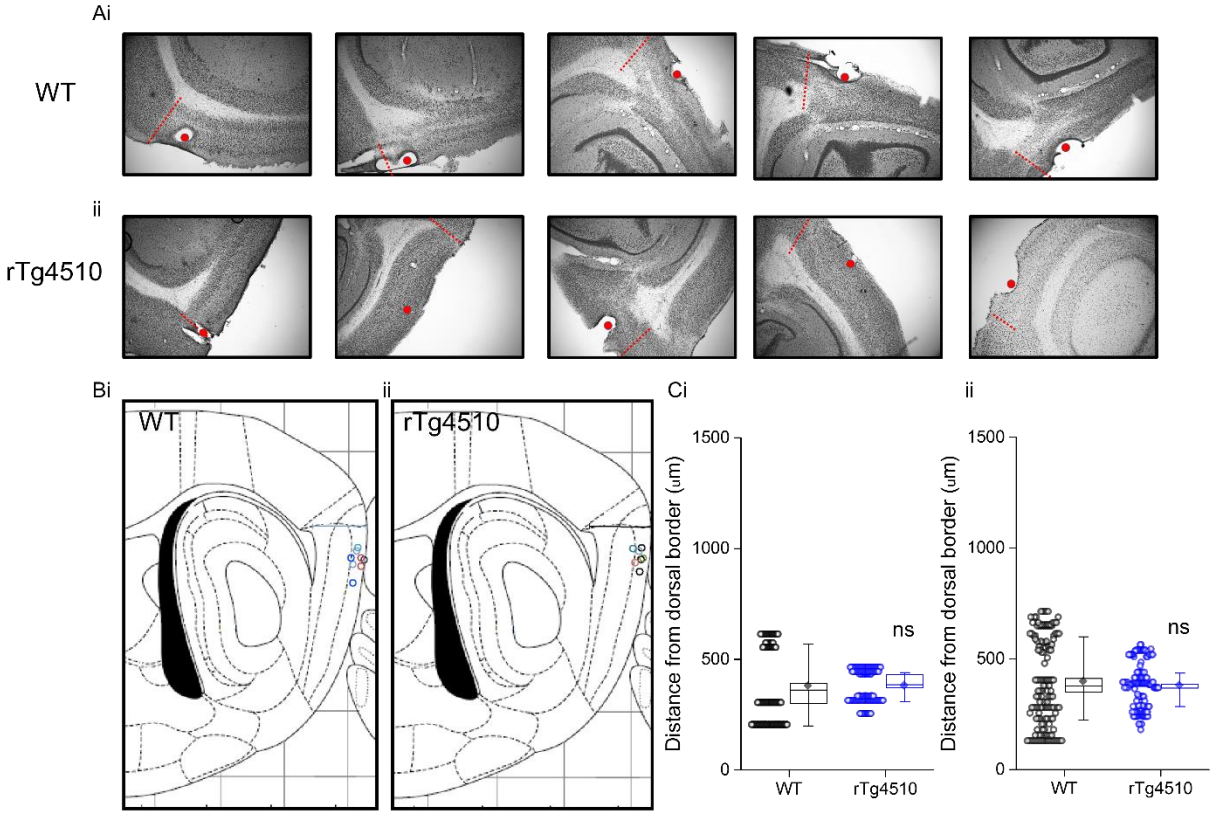

Figure 6.11 Recording locations of mEC single units do not vary between WT and rTg4510 mice. A) Example sections showing electrode lesions (red dot) of final location in mEC of WT (i) and rTg4510 mice (i), dorsal mEC boarder shown in red dotted line. **B)** Reconstructed recording locations used for analysis for WT (i) and rTg4510 (ii), colours represent recordings from the same experimental subjects. Scale bar: 200 µm. Box (below): 1 mm. **Ci)** Recoding locations for each probe used for analysis. **ii)** Estimated location based on relative position of largest waveform for each cell on electrode shanks (line: median, diamond: mean ± SEM, whiskers: 25^{th}/75^{th} centile), ns = non-significant, Mann-Whitney U test.

6.4 Discussion

6.4.1 Summary

The data described in this chapter are the first to show alteration in mEC single unit activity in rTg4510 mice. The finding that mEC neurons show disrupted relationships with locomotor activity support the assertion from the previous chapter, that rTg4510 mice are unable to adequately represent running speed information. Similarly, the occurrence of grid cell firing fields was shown to be absent in rTg4510 mice, although mEC cells retained a similar, or slightly increased, spatial information content compared to WT. Furthermore, the abolition of grid cell periodicity in these mice can be predicted by small changes to running speed oscillation relationships seen in chapter 5.

While, at this relatively late stage of degeneration, speed and grid cell representation appear to be severely influenced by tau pathology, rTg4510 mice do not show decreased tuning to head direction inputs. If anything, as a population these mice are significantly more tuned to head direction than WT controls.

6.4.2 Decreased speed modulation may underlie reduced grid cell periodicity in rTg4510 mice

There has been some suggestion in the literature that dementia pathology affects the firing pattern of grid cells in the mEC both in mice (Fu *et al.*, 2017) and grid-like neural representations in humans (Kunz *et al.*, 2015). However, to date no studies have examined changes to speed modulated firing of mEC single units. Data presented in this and the previous chapter suggest the hypothesis that reduced grid cell periodicity may be the result of the impaired integration of running speed information in the mEC. It is unclear whether the reintroduction of locomotor signals, for example through closed-loop optogenetic stimulation, could restore grid cell activity in these mice. However, unlike artificially inserting grid cell activity, this may be an achievable, if challenging, avenue for investigation.

Given the role of the medial septum in locomotor encoding (Fuhrmann *et al.*, 2015; Justus *et al.*, 2016) and grid cell formation (Koenig *et al.*, 2011; Brandon *et*

al., 2011), this work also further highlights a role for this area in the breakdown of neuronal networks in dementia models.

6.4.3 Global vs entorhinal specific tau overexpression

The findings seen above are largely consistent with those described in mice displaying an entorhinal-specific pathology (EC-tau) (Fu *et al.*, 2017); however, there are several key differences between experiments. Firstly, since EC-tau mice (Harris *et al.*, 2012; Liu *et al.*, 2012; de Calignon *et al.*, 2012) show pathology that is specific to the hippocampal formation, the activity of projections from key path integration systems, such as running speed and head direction, are presumably entirely functional. This suggests that the failure of grid cell formation is due to the inability of individual mEC neurons to integrate incoming information effectively.

EC-tau mice are produced using the same P301L mutant tau gene as rTg4510 mice, it is therefore possible to directly compare differences in global and entorhinal specific tau overexpression across age points. Tau-EC mice, at the ages used in the current experiment (7-8 months) show no cognitive deficits in behavioural tasks (Harris *et al.*, 2012). Indeed, much older mice (14 months) were also capable of effectively processing spatial information and of normal grid cell function (Fu *et al.*, 2017), with deficits not apparent until 30 months of age. Clearly these models will produce differences in mEC pathology, however it could be suggested that in the rTg4510 mice used above, mEC pathology alone would not be sufficient to produce grid cell dysfunction. In this case, impaired grid cell activity could be the product of aberrant mEC inputs and this is consistent with the finding of impaired representation of running speed. It is possible that grid cell deficits seen in this chapter could be entirely explained by dysfunctional processing of locomotor activity, rather than specific changes to mEC neuronal function. Nevertheless, it is most likely that deficits seen in rTg4510 mice are the result of a combination of these factors, since there are also clear changes to intrinsic properties of mEC stellate cells and synaptic deficits in these animals (Booth *et al.*, 2016*a*).

6.4.4 Negative speed modulation of mEC neurons

In WT animals, only a small population of mEC neurons display negative relationships with running speed (Kropff *et al.*, 2015; Hinman *et al.*, 2016). These data show that during recordings on the linear track, rT4510 mice have a larger proportion of cells that decrease their firing rate with increases in running speed. Interestingly, neurons in the medial septum also display a more even split between positive and negative speed modulation (Justus *et al.*, 2016), suggesting that, under normal physiological conditions, the mEC does not simply recapitulate these firing patterns, but integrates this information differently. The precise targets of negatively speed modulated inputs into mEC are unclear; however it is possible that they are more likely to be conjunctive with other spatial information systems, such as grid or head direction. Indeed, negatively speed modulated cells are more likely to be tuned to head direction (Hinman *et al.*, 2016), which is consistent with the increase in mean vector length observed in rTg4510 neurons at a population level.

6.4.5 Vulnerability of grid cell firing to external influences

These results may highlight the importance of an intact path integration system in order to maintain grid cell periodicity. There have been several examples in the literature that show a breakdown of grid cell firing patterns after the inactivation of important spatial information streams. For example, inhibition of the medial septum, which controls theta rhythmicity, but also speed modulated inputs, produces a complete breakdown of grid cell periodicity (Koenig *et al.*, 2011; Brandon *et al.*, 2011). The same is true for disruption of head direction pathways, with inactivation of the anterior thalamic nuclei (ATN) also impairing the grid cell signal (Winter et al., 2015), and for inactivation of reciprocal hippocampal inputs into the mEC (Bonnevie *et al.*, 2013).

The removal of theta oscillation input into the mEC in particular may represent a potential mechanism for the breakdown of grid cell periodicity, independent of speed inputs. However, speed and theta outputs from the medial septum may be difficult to separate in this context. In any case, it is likely that the decrease in theta oscillations (chapter 4) and theta rhythmicity of mEC neurons will have profound effects on grid cell firing, since the majority of these neurons are strongly modulated by theta (Sargolini *et al.*, 2006; Jeewajee *et al.*, 2008*a*; Koenig *et al.*,

2011; Brandon *et al.*, 2011; Domnisoru *et al.*, 2013). It remains to be seen whether the reintroduction of theta signals could restore grid or speed cell firing in rTg4510 mice.

The almost complete breakdown of grid cell firing in rTg4510 mice contrasts with the effect of tau overexpression on the hippocampus of these animals. While several studies have shown a reduction in the spatial information and stability of hippocampal place cells (Cheng & Ji, 2013; Booth *et al.*, 2016*b*), firing fields are still consistently present in these mice. Given the pattern of degeneration across the hippocampal formation, weak place fields (Cacucci *et al.*, 2008; Cheng & Ji, 2013; Booth *et al.*, 2016*b*) may be the result of reduced entorhinal inputs (Brun *et al.*, 2008*a*; Van Cauter *et al.*, 2008; Hales *et al.*, 2014). Reductions in grid and place field activity may therefore mirror their appearance in neuronal development, where place cells appear before grid cell and mature fully only after grid cell development (Wills *et al.*, 2012; Muessig *et al.*, 2015). The precise temporal nature of grid and place cell impairment is as yet unknown. However, taken together, these data suggest further evidence of hippocampal place fields in the absence of effective grid cell firing.

6.4.6 Stability of head direction tuning

A further feature of the inactivation studies described above is the stability of head direction tuning in the mEC. Blocking medial septum activity impairs grid cell firing, but not head direction tuning (Koenig *et al.*, 2011; Brandon *et al.*, 2011). Interestingly, the breakdown of grid periodicity after hippocampal inactivation has also been shown to reveal head direction tuning in grid cells that would previously not have been modulated by head direction (Bonnevie *et al.*, 2013). It is possible that the population increase in head direction firing in rTg4510 mice may reflect this unmasking of head direction inputs from cells that would have previously displayed grid patterns. However, this is a hypothesis that would need to be addressed directly with long term recordings of grid cells as tau pathology increased to critical levels to impair spatial firing patterns. This approach is unlikely to be achieved with current technology. In any case, the arrival of head direction information into the mEC is likely the result of an anatomically distinct pathway (Taube, 2007) that appears to be unaffected by tau pathology in rTg4510 mice at this stage. This is most likely due to a greater dependence on subcortical

structures, that integrate vestibular information (Stackman & Taube, 1998; Sharp et al., 2001; Blair et al., 2007).

6.4.7 Implications for spatial navigation and path integration

Although not examined directly in this chapter, the breakdown of key spatial information streams is likely to have profound implications for the ability of rTg4510 mice to perform spatial navigation. Deficits in spatial memory have been consistently observed in these mice, at several age-points and using multiple behavioural tasks (Santacruz *et al.*, 2005; Ramsden *et al.*, 2005; Bailey *et al.*, 2014; Cook *et al.*, 2014; Booth *et al.*, 2016*b*).

Grid cells are proposed to play a key role in path integration systems (Etienne & Jeffery, 2004; Fuhs & Touretzky, 2006; McNaughton *et al.*, 2006; Burak *et al.*, 2009). For example, mice lacking GluA1-containing AMPA receptors have been shown to display reduced grid cell periodicity, correlating with impairments on path integration-based task (Allen *et al.*, 2014). Path integration has also been suggested to be impaired in populations of dementia and MCI patients (Hort *et al.*, 2007; Mokrisova *et al.*, 2016; Allison *et al.*, 2016). The direct association between these two factors is still unclear; however, it is likely that grid cell deficits, as described above, directly contribute to the deficits in spatial information processing in rTg4510 mice.

6.4.8 Dorso-ventral organisation of single unit properties in rTg4510 mice

One of the major hypotheses constructed from the LFP studies described in chapter 4 was that dorso-ventral gradients in spatial firing are disrupted in rTg4510 mice. In the current study however, no grid patterns were observed in these animals, meaning that it was not possible to adequately determine the effect of dorso-ventral location on spatial firing properties of mEC neurons. Additional experiments are required on mice earlier in disease pathology, which would also most likely require simultaneous single unit recordings from multiple dorso-ventral locations in each animal subject to achieve the required statistical power for comparisons. However, since recording locations in the experiments presented here were similar in rTg4510 and WT mice, the current data are compared directly, independent of dorso-ventral location. It is likely that these

deficits are displayed along the entire dorso-ventral axis of the mEC, however it is also possible that these changes are more (or less) prominent depending on their precise anatomical location at different stages of pathology.

6.4.9 Thresholding spatial modulated firing scores

While studying firing properties from transgenic animals that likely show impairments in spatial representation, it is important to carefully consider the thresholding of mEC cell categories. This research has particular challenges, namely, the classification of poorly performing cells that are likely to not meet strict criteria produced though shuffled distributions of data. For example, it is almost impossible to know, without ultra-long term (i.e. many weeks or months) recordings from rTg4510 single units, that a cell displaying a poor grid score is doing so because it is a dysfunctional grid cell, or because it is one of the many that do not show grid periodicity to begin with.

For this reason, the data presented in this chapter have shown changes to the population dynamics of firing modulated by speed, head direction and spatial information. Wherever possible raw, or minimally processed, data have been displayed, as not to bias with specific thresholds. It is however, impossible not to set arbitrary thresholds for such firing properties and these have been set at 95% of shuffled distribution in order to avoid missing cells whose association is less pronounced. These thresholds are consistent with several reports in the literature (Langston *et al.*, 2010; Sun *et al.*, 2015; Fu *et al.*, 2017); however it should be noted that others have used stricter thresholds (Koenig *et al.*, 2011; Giocomo *et al.*, 2014; Kropff *et al.*, 2015; Hinman *et al.*, 2016) and exact proportions of mEC cell types may differ accordingly.

6.4.10 Conclusions

Overall, these data show a clear breakdown in grid cell periodicity in rTg4510 mice compared to WT controls. In addition, they suggest a role for the dysfunctional processing of locomotor activity in this process, since the representation of running speed information in mEC single units is severely disrupted in these mice, while head direction tuning remains constant, or slightly increased. The changes to mEC single unit firing are likely to have profound implications for the impairments in spatial memory observed in these mice and suggest observable parameters to assess in dementia patient populations, for example through speed modulated fMRI signals in virtual environments.

7. General discussion

7.1 Key findings

The experiments detailed above have used a variety of experimental approaches to produce numerous novel findings that have relevance both to basic mEC physiology and to the breakdown of mEC neuronal networks as a result of tau pathology. The principle findings will be summarized here:

7.1.1 Novel mEC dorso-ventral gradients

While dorso-ventral gradients have been well described at a single cell level, both in terms of intrinsic neuronal properties (Giocomo *et al.*, 2007; Garden *et al.*, 2008; Boehlen *et al.*, 2010; Dodson *et al.*, 2011; Pastoll *et al.*, 2012; Navratilova *et al.*, 2012; Yoshida *et al.*, 2013; Booth *et al.*, 2016*a*) and in the firing of individual grid cells (Brun *et al.*, 2008*b*; Giocomo *et al.*, 2011*a*; Stensola *et al.*, 2012), much less is known about how this precise organisation of the mEC corresponds to activity at the level of the neuronal network. Throughout this thesis novel dorso-ventral gradients have been observed in various aspects of mEC network activity that should be highlighted in their own right and are therefore outlined below:

- **Gradient in gamma oscillations along the dorso-ventral axis of the mEC**. Chapters 3 and 4 clearly show clear gradients in gamma oscillation activity in the mEC, both using pharmacologically induced oscillations *in vitro* and *in vivo* recordings from freely moving mice. Specifically, gamma oscillations in dorsal mEC are larger than corresponding oscillation in ventral regions. Gamma oscillation amplitude also shows stronger coupling to theta phase in dorsal mEC and under periods of high arousal local networks may be able to produce rhythmic activity at higher frequencies. Since gamma oscillations are heavily linked with cognition, this may have functional implications for the processing of spatial information in the mEC.

- **Dorso-ventral gradient in mEC running speed-oscillation relationships.** In addition to gradients in basic network properties, chapter 5 shows that this

organisation of the mEC may have implications for the integration of spatial information. The relationship between oscillation size and running speed has been known for many years; however, by recording simultaneously from regularly spaced sites across the dorso-ventral axis of the mEC, results from this thesis demonstrate that oscillatory power shows greater increases in dorsal mEC for given increases in locomotion than ventral. This suggests that as mice run faster, the distinction between dorsal and ventral mEC becomes more pronounced. This will also likely impact the processing of incoming spatial information and may be relevant to the formation of grid cell patterns across the mEC, with increased sensitivity to locomotive activity allowing dorsal mEC neurons to shift activity states more frequently than ventral, producing smaller, tightly packed firing fields.

- **Gradient in hyperexcitability along the dorsal-ventral axis of the mEC.** Results shown in chapter 3 also highlight the aberrant consequences of the stereotyped anatomical organisation of the mEC. With ventral mEC stellate cells exhibiting a higher input resistance, a slower membrane time constant and a lower action potential threshold than dorsal (Garden *et al.*, 2008; Giocomo & Hasselmo, 2009; Boehlen *et al.*, 2010; Booth *et al.*, 2016*a*), this region presents itself as a potential epileptogenic zone within the medial temporal lobe. The increased intrinsic excitability in ventral mEC, coupled with the relative decrease inhibitory connectivity (Beed *et al.*, 2013) give rise to an increased likelihood for producing epileptiform-like bursting activity. After initiation, the inhibitory organisation of the mEC also allows for an unexpectedly slow spread of ictal-like activity, which may also highlight the complex connectivity in this area.

7.1.2 mEC network activity in rTg4510 mice

To date, no other studies have examined changes to neuronal network activity in the mEC in rodent models of disease. This thesis describes further novel findings that show clear changes to oscillatory activity, both in terms of dorso-ventral gradients and in global network properties across the mEC during tau pathology. They are listed below:

- **Broad-band reduction in mEC network activity in rTg4510 mice.**
  Firstly, results in chapter 4 show wide-scale reduction of neuronal network oscillations in the mEC of rTg4510 mice. Decreases in oscillatory power were consistent across all frequency bands, however, as a proportion of the LFP, theta oscillations were specifically impaired.

- **Disruption in running speed-oscillation relationship in rTg4510 mice.**
  Chapter 5 described the novel finding that rTg4510 display a blunted ability to modulate neuronal network activity in relation to changes in locomotion. Specifically, while clear running speed relationships exist in WT animals for both theta and gamma oscillations, changes to locomotion have almost no effect on the oscillatory amplitude in rTg4510 mice. This may have a profound influence on the formation of grid cell firing patterns which almost certainly rely on the effective integration of movement speed to continuously update the representation of an animal in space.

- **Flattened dorso-ventral gradients in oscillatory activity in rTg4510 mice.**
  Significantly, the results described in chapter 4 show clear changes to dorso-ventral relationships in oscillatory activity. Experiments with pharmacologically induced gamma oscillations *in vitro* clearly show preferential disruption of network activity in dorsal mEC regions, with ventral mEC activity remaining similar to WT controls. *In vivo*, despite broad-band changes to oscillatory power, the relationship between anatomical location and network activity was abolished in rTg4510 mice and this may have profound implications for the spacing of grid fields along the dorso-ventral axis. Perhaps the most striking example of this can be seen with some of the novel mEC network gradients described above, specifically the gradient in theta-gamma phase amplitude coupling (PAC) and running speed – theta/gamma relationship that are not present in rTg4510 mice.

7.1.3 Reorganisation of mEC spatial firing in rTg4510 mice

The final chapter of this thesis explores how the individual firing of mEC single units is effected by tau overexpression. These data show the following:

- **Reduced representation of running speeds from single unit firing rate in rTg4510 mice.**
  The relationship between running speed and oscillatory activity was shown clearly in chapter 5. Data presented in chapter 6 further shows a decreased speed modulation of mEC single units in rTg4510 mice. In addition, this is accompanied by an increased likelihood of mEC neurons to have firing rates negatively modulated by running speed.

- **Breakdown of grid cell periodicity in rTg4510 mice.**
  Changes in speed modulation of mEC single units are accompanied by an almost complete breakdown of grid cell periodicity in rTg4510 mice. However, mEC neurons do retain spatial information content in these mice.

- **No change in head-direction tuning of rTg4510 mEC single units.**
  Unlike grid and speed modulated neurons, rTg4510 mice showed no changes in the number of head direction cells recorded in mEC. Furthermore, as a population, mEC units were more tuned to head direction than WT controls.

7.2 Relevance of rodent models of disease

7.2.1 Limitations of mouse models

There are many reasons for which rodents are an excellent model system for studying both basic and disease physiology. The mouse and human genomes are widely overlapping (~99%) and combined with relatively small space requirements, short lifespans, fast breeding cycles and a wide array of genetic and molecular tools, this makes mice an ideal model organism for animal studies (Vandamme, 2014). However, while rodent models of dementia are one of the most useful tools for the discovery of new treatments for AD, it is still the case that many of the potentially disease modifying treatments that show preclinical success have failed to provide positive results in the clinic (Mangialasche *et al.*, 2010; Hall & Roberson, 2012).

One of the major limitations for mouse models of dementia is that, for an overwhelmingly sporadic, rather than familial, condition the majority of rodent models rely on the overexpression of proteins produced through genetic mutations. For example, the MAPT P301L mutation, that forms the basis of the rTg4510 mouse (Santacruz *et al.*, 2005; Ramsden *et al.*, 2005) has been observed in only a small number of families around the world (Hutton *et al.*, 1998; Dumanchin *et al.*, 1998; Bird *et al.*, 1999; Mirra *et al.*, 1999). While these animals successfully recapitulate large amounts of disease progression, they do not necessarily represent the patient population as a whole. Furthermore, the transgenic overexpression of mutant transgenes itself is not necessarily an ideal model, since these animals may express unphysiological levels of aberrant proteins.

Another potential factor to consider when producing mouse models of dementia is the speed of pathological progression. An ideal disease model to replicate the human condition would develop disease pathology over a prolonged timescale, such as the entire lifespan of a mouse, however this is not experimentally viable. It is important to note that, while in laboratory terms 8 month old mice could be regarded to be considerably 'aged', WT mice may comfortably have another year of life. The animals used in this thesis may not faithfully replicate changes seen through the combination of both disease pathology and normal ageing, which in itself produces cognitive deficits (Buckner, 2004; Jacobson *et al.*, 2013; Lithfous *et al.*, 2013; Harada *et al.*, 2013). In any case, replicating a disease produced through decades of slow development is likely to prove difficult in a species with a lifespan of only 2 years (McGowan *et al.*, 2006).

7.2.2 Technical challenges of *in vivo* electrophysiology in rodent models of degeneration

One of the most significant experimental challenges with the *in vivo* electrophysiological recordings described in this thesis is the stereotaxic placement of electrode arrays in tissue that shows pronounced neurodegeneration. This is most notable for experiments utilizing fixed silicon probe arrays (chapter 4), where coordinates needed to be substantially adapted. At this age point, a decrease in cortical thickness of over 10% was observed in the mEC (fig. 4.7) and extrapolating this over the entire brain means that standard

stereotaxic coordinates (Paxinos & Franklin, 2001) used to reach mEC areas are not viable. Fortunately, many studies implanting electrodes into the mouse mEC use coordinates relative to the transverse sinus (Fyhn *et al.*, 2008; Giocomo *et al.*, 2011*a*; Booth *et al.*, 2016*a*), which at least anecdotally in this case does not show relative changes in position with the mEC.

The recording of single unit activity also presents logistical challenges and especially so in aged, transgenic animals. These animals may need longer recovery times after surgical procedures, as well as larger periods for habituation and training to cover open field environments effectively. Electrode arrays also need to be lowered slowly into position over a period of weeks, meaning that there can be a variable amount of time before stable single units are detected in the mEC. These techniques are therefore relatively low throughput, with experimenters only able to use small batches of animals for optimal recordings and analysis techniques requiring many hours of computation for each recording session. This presents difficulties when observations of disease models are best achieved across precise time-windows corresponding to specific stages of disease progression. For this reason, the current studies (chapter 6) show recordings from 7-8 month old animals where pathology is well established. However, further refinement may be needed to adequately describe early changes to mEC single unit activity relating to tau pathology.

7.2.3 Effective biomarkers for the assessment of disease progression

One of the most important motives for studying network activity in rodent models of disease is to identify relevant and translatable biomarkers to assess disease pathology. Ultimately, such findings could provide assistance for the clinical assessment of dementia patients (Yamasaki *et al.*, 2012). These studies show clear changes to network activity in the mEC; however, it remains to be seen whether such changes could easily or reliably be seen in human patients, although reductions to grid-like representations in the mEC have been observed APOE-ε4 carriers even before disease onset (Kunz *et al.*, 2015).

Once established as relevant to the human condition, changes to neuronal network activity could easily be used assess the neurophysiological effects of potential therapeutic compounds developed for the treatment of neurological

disorders. As discussed in chapter 5, the relationship between oscillatory activity and running speed could provide an ideal candidate for this, since it can be observed using relatively simple electrophysiological techniques, and is a phenomenon that has been shown to be adaptive environmental context, meaning that as a process, it will likely require the integration of numerous information streams and coordination of large scale neuronal networks.

7.3 Lessons for spatial information processing from rodent models of dementia

7.3.1 Vulnerability of grid cell periodicity to cognitive decline

The results presented in chapter 6 add to a growing body of literature that highlights the vulnerability of grid cell firing to external influences. Since the entorhinal cortex is the first area to see degeneration in AD it is reasonable to suggest that the make-up of grid cells in particular is such that they are sensitive to degeneration. Indeed, the inhibition of inputs into the mEC that are presumed to provide grid cells with important spatial representations all impair grid cell periodicity. Antagonising projections from the medial septum (speed/theta) (Koenig *et al.*, 2011; Brandon *et al.*, 2011), anterior thalamic nuclei (head-direction) (Winter et al., 2015) and hippocampus (place cells) (Bonnevie *et al.*, 2013) all produce a complete breakdown of grid cell periodicity. This is not necessarily the case for other spatial information streams, for example, the absence of septal or hippocampal inputs has no effect on head-direction tuning (Koenig *et al.*, 2011; Brandon *et al.*, 2011; Bonnevie *et al.*, 2013), which in some cases may show an increased representation under these conditions (Bonnevie *et al.*, 2013).

It is therefore important to highlight that this work not only has relevance to tauopathy, but also that by understanding the reorganisation of information processing systems during disease there is much to learnt about underlying physiology.

7.3.2 Relevance of spatial information processing to other forms of memory

Using rodents to assess episodic or declarative memory is a difficult task, the majority of animal studies therefore primarily rely on a well-established battery of spatial memory task, such as the Morris water maze or T-maze to assess memory function (Dudchenko, 2004). This is predominantly the result of necessity and while areas such as the mEC are undoubtedly important for spatial memory, 'cognitive map' theory does not solely be applied to spatial planes. Perhaps the most notable examples of this can be seen through human hippocampal cells that have the capacity to code for not just individual location, as would be expected from rodent place cells, but also individuals, landmarks or objects (Fried *et al.*, 1997; Quiroga *et al.*, 2005).

Grid cells can also be found in the human memory network, using both direct recordings from neurosurgical patients (Jacobs *et al.*, 2013) and grid-like representations in fMRI signals (Doeller *et al.*, 2010; Kunz *et al.*, 2015; Horner *et al.*, 2016). Importantly, these signals are present when participants navigate virtual environments (Doeller *et al.*, 2010), but also imagined ones (Horner *et al.*, 2016), highlighting further the role for the entorhinal cortex in goal-directed behaviour (Chadwick *et al.*, 2015). There is also evidence to suggest that, in humans, grid-like signals are not unique to the mEC, but can be measured during spatial navigation in parts of the medial frontal and parietal cortices (Doeller *et al.*, 2010; Jacobs *et al.*, 2013). Importantly, they are also not confined to spatial 'cognitive maps', with several of these regions displaying grid-like neural representation of conceptual space (Constantinescu *et al.*, 2016). These studies suggests grid patterns as a common neural coding mechanism for storing both spatial and conceptual information.

7.4 Future directions

The work presented in this thesis highlights a number of questions for providing greater understanding the neurophysiological changes to the mEC in mouse models of dementia. Although not exhaustive, some of the potential future directions are listed below:

7.4.1 Key experiments

- Ascertain the time-course of tauopathy induced impairment of neuronal network activity in the mEC, specifically in order to observe whether such changes can be seen prior to the onset of behavioural deficits.

- Provide detailed analysis of dorso-ventral organisation of the spatially modulated firing of mEC neurons in younger rTg4510 mice to understand precisely how preferential impairment of dorsal mEC corresponds to the individual firing across the dorso-ventral axis.

- Establish specific relationship between deficits in speed modulated firing and breakdown of grid cell periodicity in rTg4510 mice. If, as hypothesised, a causal relationship is shown to exist between the breakdown of speed information processing and grid cell firing, then a secondary aim would be to determine whether artificially reproducing the speed signal, for example through optogenetic stimulation, could restore function in the mEC and/or behavioural deficits seen in these mice.

- Provide evidence for relationship between grid or speed cell degeneration and spatial memory impairments in rTg4510 mice, with associated behavioural or path integration based tasks.

7.5 Final conclusions

The work presented in this thesis has provided novel insights into changes to mEC physiology that can occur during tau pathology. It shows clear changes to network activity in rTg4510 mice that is likely to correspond with the deficits in the representation of spatial information in the mEC. Understanding how dementia pathology produces changes to neuronal network function and ultimately cognition is key for understanding and testing viable treatment pathways which could slow or halt the disease. Furthermore, understanding the behaviour of aberrant neuronal activity may potentially shed new light on the mechanisms of memory processes in normal conditions.

8. Appendix – MATLAB code

The following relevant MATLAB functions are included that were used for the processing and analysis of single unit mEC recordings from 32 channel silicon probes (see **section 2.4**):

8.1 Pre-processing of LFP data

```
function [data_array,TS,Fs,ref_array] =
rewrite_csc_nlx(p,save_loc,ref_av,ref_chan,ref_layout,downSampleFreq,bandPassLims,template_path)
```

```
% rewrite_csc_nlx(p,sav_loc)

% Writes CSC directory into .dat file
```

Outputs:

data_array: array with all CSCs(uVolts) in the order [Time1Channel1, Time1Channel2, .. Time1ChannelN, Time2Channel1, ...]
TSs: row vector of timestamps (sec)
Fs: sampling Frequency (Hz) ** assumes TSs abd Fs are the same for all channels in folder
ref_array: cell array of shank averages used as reference channels

Saves data array as .dat binary data file
Saves template .prm, .prb and . bat files to run klustaKwik

Inputs:

p: file path of directory containing the CSC that you wish to import eg C:\Offline data\KlustaKwik\2015-06-19_15-54-24_314_open_field
save_loc: path of folder to save data into eg 'C:\Offline data\KlustaKwik' Note: output creates folder within this path containing data and files for running klusta
ref_av: 1 = reference to common average (below), 0 = no reference (ie to ground)
ref_chan: vector of channels to be used as average reference (0 = none/exclude, 1 = shank1 , 2 = shank2 etc)
eg ref_chan = [0;1;1;1;1;1;1;1;1;1;1;1;1;1;1;1;2;2;2;2;2;2;2;2;2;2;2;2;2;2;2;2] produces average of shank1 from chan2-16 and average of shank2 from 17-32.
leave empty for all channels on each shank of cambridge probe.
ref_layout: vector of reference shank for each electrode, eg. ref_layout=[2,2,2,2,2,2,2,2,2,2,2,2,2,2,2,2,1,1,1,1,1,1,1,1,1,1,1,1,1,1,1,1]
references electrodes 1:16 from ref_chan(2)(i.e. average of shank 2) and electrodes 17:32 from ref_chan(1).
leave empty for oposite channels on cambridge probe.
downSampleFreq: down sample frequency (in Hz), leave empty if no downsample
bandPassLims: bandpass limits (in Hz), leave empty if no filter
template_path: Folder containing template .prb, .prm and .bat files for running klusta

Defaults

```
if nargin < 2
    save_loc = p;
end

if nargin < 3
```

```
    ref_av = 1;
end

if nargin < 4
    ref_chan(1:16) = 1;
    ref_chan(17:32) = 2;
end

if isempty(ref_chan)
    ref_chan(1:16) = 1;
    ref_chan(17:32) = 2;
end

if nargin < 5
    ref_layout(1:16) = 2;
    ref_layout(17:32) = 1;
end

if isempty(ref_layout)
    ref_layout(1:16) = 2;
    ref_layout(17:32) = 1;
end

if nargin < 6
    downSampleFreq = [];
end

if nargin < 7
   bandPassLims = [];
end

if nargin < 8
   template_path = 'Z:\Methods\TomR\klusta template files\cambridge probe new';
end
```

File params

```
path_parts = strsplit(p,'\');
folder_name = path_parts{end};

mkdir(save_loc,folder_name)
save_loc = strcat(save_loc,'\',folder_name);

save_name = 'WideBandData';
```

Params

```
number_shank = max(ref_chan);
mode ='all';
```

Make an array with all the filenames in it

```
switch p(end)
    case '\'
    otherwise
        p(end+1) = '\';
end

data_dir = dir([p '*.ncs']);


filename = cell(length(data_dir),1);
for i = 1:length(data_dir)
    filename{i} = [p data_dir(i).name];
end

% use sort_nat to arrange filenames in appropriate order
filename = sort_nat(filename);
```

For channel mapping data

%sort_ind = [12,21,6,27,11,22,4,29,9,24,2,31,7,26,1,32,5,28,3,30,8,25,10,23,15,18,16,17,13,20,14,19]; for i = 1:length(filename) s = sort_ind(i); fname{i} = filename{s}; end filename = fname;

Fet TS and Fs info from 1st file

```
[CSCs,TS,Fs,~]  = load_csc_local(filename{1},mode);

if ~isempty(downSampleFreq)
      [~,TS,Fs]    = resample_eeg(CSCs,TS,Fs,downSampleFreq);
end

% preallocate
data_array   = zeros((length(TS))*length(data_dir),1,'int16');
ref_array = cell((number_shank +1),1); % number of shanks + 0 (for excluding channels)
for i = 1:length(ref_array)
ref_array{i} = zeros (length(TS),1,'int16');
end

h_wait = waitbar(0,'Loading/filtering/downsampling CSCs - please wait...');
info = cell(length(data_dir),1);
```

Load in data

```
for i=1:length(data_dir)
   waitbar(i/size(data_dir,1))
   [CSCs,TS,Fs,info{i}]  = load_csc_local(filename{i},mode);
   if ~isempty(bandPassLims)
      [b,a]   = butter(2,[bandPassLims(1)/(Fs/2) bandPassLims(2)/(Fs/2)]); % make butterworth filter
      CSCs = filtfilt(b,a,CSCs); % filter the data
   end
   if ~isempty(downSampleFreq)
      [CSCs,TS,Fs]    = resample_eeg(CSCs,TS,Fs,downSampleFreq);
   end

   %put csc into data array in correct place
   data_array(i:length(data_dir):end,1) = int16(CSCs);

   %put csc into correct ref array if required
   for j  = 0:number_shank
   if ref_chan(i) == j;
   ref_array{j+1} = ref_array{j+1}+int16(CSCs);
   else
   end
   end

 end
close(h_wait)

%divide ref array by number of channels to get average
for i = 0:number_shank
ref_array{i+1} = ref_array{i+1}./(sum(ref_chan == i ));
end
% get rid of unwanted channels (marked 0)
ref_array = ref_array(2:end,1);
```

Reference individual channels

```
if ref_av == 1;

for i=1:length(data_dir);

   data_array(i:length(data_dir):end,1) = data_array(i:length(data_dir):end,1)- ref_array{ref_layout(i)};

end
end
```

Write data file

```
fname = strcat(save_loc,'\',save_name,'.dat');
fid = fopen(fname, 'w');
fwrite(fid, data_array, 'int16');
fclose(fid);
```

Write info file

```
[tracking.tsV,tracking.X, tracking.Y, tracking.A] = Nlx2MatVT(strcat(p,'\VT1.nvt'), [1 1 1 1 0 0], 0, 1);
tracking.tsV=tracking.tsV/1e6;
tracking.screen_x = 138;
tracking.camera_resolution_x = 720;
tracking.camera_resolution_y = 576;

Ts_start = TS(1);
save(strcat(save_loc,'\info.mat'),'info','Ts_start','Fs','tracking','p');
```

Write klusta related files from templates

```
copyfile(template_path,save_loc);

% copyfile(strcat(template_path,'\probe.prb'),save_loc);
% copyfile(strcat(template_path,'\params.prm'),save_loc);
% copyfile(strcat(template_path,'\cluster.bat'),save_loc);
```

```
end
function [samples,ts0,Fs,info] = load_csc_local(filename,mode)
```

```
% load_csc imports Neuralynx *.ncs files into Matlab
```

examples:

```
[csc,ts,Fs] = load_csc('csc4.Ncs','all');
[csc,ts,Fs,info] = load_csc('E:\LA04-03\CSC4.Ncs','ts',[4500e6 6500e6]);
```

outputs:

```
samples: row vector of samples (uVolts)
ts0: row vector of timestamps (sec)
Fs: sampling Frequency (Hz)
info: cell array with header information
```

inputs:

```
filename: string of input file name, may include path
mode : string argument indicating mode of csc to use
       'all' : load all
       'ts' : load timestamp range (ts in par)
       'ind' : load index range (indices in par)
       'info': load only header info
par (only for modes 'ts', and 'ind'):
       with ts: pair of timestamps [start_ts end_ts]
       with end: pair of indices [start_ind end_ind]
```

```
%%%(c) U Bartsch, Bristol, 2009

% Set the field selection for reading CSC files.
fieldSelection(1) = 1; % Timestamps
fieldSelection(2) = 1; % Channel number
fieldSelection(3) = 1; % Sample Frequency
fieldSelection(4) = 1; % Number of valid samples
fieldSelection(5) = 1; % Samples (EEG data)
%return header
extractHeader = 1;

switch mode
   case 'all'
```

```
        extractMode = 1; % Extract all data
        [ts,channumber,sampFreq,numvalsamp,samp,Header] =...
                Nlx2MatCSC(filename,fieldSelection,extractHeader,extractMode);
    case 'ind'
        if ~exist('par','var')
            error ('Please add index range as input variable, eg: load_eeg(filename,mode,[index_start index_stop])!')
        end
        extractMode = 2; %index range
        [ts,channumber,sampFreq,numvalsamp,samp,Header] =...
                Nlx2MatCSC(filename,fieldSelection,extractHeader,extractMode,par./512);
    case 'ts'
        if ~exist('par','var')
            error ('Please add timestamp range as input variable, eg: load_eeg(filename,mode,[ts_start ts_stop])!')
        end
        extractMode = 4; % ts range
        [ts,channumber,sampFreq,numvalsamp,samp,Header] =...
                Nlx2MatCSC(filename,fieldSelection,extractHeader,extractMode,par);
    case 'info'
        extractMode = 1;
        fieldSelection(1) = 0; % Timestamps
        fieldSelection(2) = 1; % Channel number
        fieldSelection(3) = 1; % Sample Frequency
        fieldSelection(4) = 1; % Number of valid samples
        fieldSelection(5) = 0; % Samples (EEG data)
        extractHeader = 1;
        [channumber,sampFreq,numvalsamp,Header] =...
                Nlx2MatCSC(filename,fieldSelection,extractHeader,extractMode,par);
        ts0=[]; samples=[];
        Fs = sampFreq(1,1);
        info.reclen=length(numvalsamp)*512 /Fs/60;
        info.header=Header;


        return
    otherwise
        error('Unknown option to load_csc!')


end

 info.numvalsamp=numvalsamp;
 info.header=Header;
 info.chno=channumber;

% Transform the 2-D samples array to an 1-D array
samples=reshape(samp,512*size(samp,2),1);

%Get sampling frequency
Fs = sampFreq(1,1);

% create timestamps for every 512 sample buffer
ts00=[0:1/Fs:511*1/Fs]*1e6;
ts0=zeros(length(ts),512);
for i=1:length(ts00)
    ts0(1:length(ts),i)=ts+ts00(i);
end
ts0=reshape(ts0',512*size(samp,2),1)./1e6;

k = strfind(Header,'-ADBitVolts');
for i=1:length(k);
    if ~isempty(k{i})
        k0(i)=k{i};
    end
end
scale=  eval(Header{find(k0)}(13:end));
samples = samples*scale*1e6;
```

```
end

function [re_csc,re_cts,reFs]=resample_eeg(csc,cts,cFs,reFs)
% resample_eeg changes the the sampling rate of a csc trace and generates
% new timestamps
% Example [re_csc,re_cts,reFs]=resample_eeg(csc,cts,cFs,reFs)
% inputs: csc = csc samples vector as loaded with load_eeg
%         cts = originals timestamps vector
%         cFs = origianl sampling frequency
%         reFs = desired sampling frequency (> 1 Hz!)
```

```
%re_csc= [resample(csc,reFs,cFs)]';

n=round(cFs/reFs);
reFs=(cFs/n);

re_cts=downsample(cts,n);
re_csc=downsample(csc,n);
end
```

Published with MATLAB® R2016a

8.2 Analysis of basic unit properties

```
function clus = unit_properties_tr(clus)
```

```
% describe the basic properties of the single units contained within a
% structure clus, derived from Klustakwik and import_cluster_data.m
%
% INPUTS:
%   clus    = struct containg time stamp info
%
% OUTPUTS:
%   clus    = input structure with cell_props field added
%
```

Some parameters

```
%%%%%%%%%%%%%%%%%%%%%%%%%%%%%%%%%%%%%%%%%%%%%%%%%%%%%%%%%%%
%%%%%%%%%%%%%%%%
```

Fast or slow

```
pause on
```

Min and max ISI for ISI histogram plot

```
maxLogISI = 3;
nBins = 60;
minLogISI = -3;
```

Figure parameters

```
close all
fsize = 12;                         % font size
scrsz = get(0,'ScreenSize');
h_cell_prop_fig = figure('OuterPosition', [scrsz(3)*0.5, scrsz(4)*0.05, scrsz(3)*0.5, scrsz(4)*0.95]);
set(0,'DefaulttextInterpreter','none')
prec = '%.2f';
%%%%%%%%%%%%%%%%%%%%%%%%%%%%%%%%%%%%%%%%%%%%%%%%%%%%%%%%%%%
%%%%%%%%%%%%%%%%

% number of cells in clus
numCells = length(clus);
```

Loop through each cell and calculate basic properties

```
for i = 1:numCells
```

```
    clf(h_cell_prop_fig)

    ind = clus(i).max_chan;                      % find index for max amplitude channel from clus
    Fs = clus(i).Fs;                            % sample frequency
```

Extract the average waveform

```
    %bigWV = mean(clus(i).waveforms_raw(ind,:,:),3); % mean waveform
    bigWV = clus(i).waveforms_raw_mean(ind,:);

    % make a time axis (in samples)
```

```
    t = 1:length(bigWV);
    tt = 1:0.1:length(bigWV);

    % upsample bigWV
    bigWV = spline(t,bigWV,tt);

    % set baseline to zero
    bigWV = bigWV-bigWV(1);
```

Calculate peak to trough width

```
    [peak,peak_ind] = max(bigWV);
    [trough,trough_ind] = min(bigWV);

    peakTroughWidth = abs(tt(peak_ind)-tt(trough_ind));             % peak-to-trough width in samples
    peakTroughTs = (([tt(peak_ind),tt(trough_ind)])/Fs)*1e3;        % time stamps for the peak and trough (for plotting)
    clus(i).cell_props.peakTroughWidth = (peakTroughWidth/Fs)*1e3;  % peak-to-trough width in ms (put into
clus.cell_props

    tt = (tt/Fs)*1e3;                                   % upsampled time axis in ms
```

Determine mean spike frequency for cell mean spike freq

```
    clus(i).cell_props.spikeFreq = length(clus(i).tstamp{1})/(clus(i).tstamp{1}(end)-clus(i).tstamp{1}(1));
```

ISI histogram

```
    [clus(i).cell_props.HistISI.H, clus(i).cell_props.HistISI.bins] = HistISI_JB(clus(i).tstamp{1},'nBins',nBins);
```

Plotting

```
    figure(h_cell_prop_fig)
    h(1) = subplot('Position',[0.1,0.75,0.8,0.2]);
    h(2) = subplot('Position',[0.1,0.1,0.8,0.55]);
```

Plot the spike waveform

```
    plot(h(1),tt,bigWV,'k','LineWidth',3);                                  % waveform
    hold(h(1));
    plot(h(1),[peakTroughTs(2),peakTroughTs(2)],[peak,trough],'r--','LineWidth',2); % ref line for peak to trough
    plot(h(1),peakTroughTs,[peak,peak],'g--','LineWidth',2);
    ylabel(h(1),'\muV','FontSize',fsize,'Interpreter','tex');
    xlabel(h(1),'Time (ms)','FontSize',fsize);
```

Plot the ISI histogram

```
    plot(h(2),clus(i).cell_props.HistISI.bins,clus(i).cell_props.HistISI.H,'LineWidth',2);
    set(gca, 'XScale', 'log', 'XLim', [10^minLogISI 10^maxLogISI],'FontSize',fsize);
    % labels
    xlabel('ISI (s)','FontSize',fsize);
    ylabel('count','FontSize',fsize);
    set(gca, 'YTick', max(clus(i).cell_props.HistISI.H));
    % add some text
    text(3,max(clus(i).cell_props.HistISI.H)*.8,...
        {['cell ID: ' clus(i).name],...
        ['Mean Freq = ' num2str(clus(i).cell_props.spikeFreq,prec) ' Hz'],...
        ['Peak-to-trough width = ' num2str(clus(i).cell_props.peakTroughWidth,prec) ' ms']},...
        'FontSize',fsize);
    pause
end
```

Published with MATLAB® R2016a

8.3 Analysis of theta modulation

```
function [clus,tmi,mod_freq,theta_z] = thetaModulation_tr(clus)

%  Function to calculate the theta modulation index for each cell based on the fast fourier transform of the spike time autocorrellogram.

% If the theta index is >= 5 then the cell is consisdered to be theta modulated.

t_win = 1;
tmi = nan(length(clus),2);
mod_freq = nan(length(clus),2);

    % Cycle through individual cells
for c = 1:numel(clus)
for s = 1:length(clus(c).tstamp)
 multiWaitbar( 'session' , 'Value', s/length(clus(c).tstamp));
 multiWaitbar( 'cell', 'Value', c/length(clus));

  if ~isempty(clus(c).tstamp{s})

      clus(c).info{s}.average_firing_rate = length(clus(c).tstamp{s})./(clus(c).tstamp{s}(end)-clus(c).tstamp{s}(1));

      spikes = clus(c).tstamp{s} *1000 ;

      [tmi(c,s),mod_freq(c,s), hist,bin] = tmi_tr(spikes);

clus(c).theta{s}.tmi = tmi(c,s);
% clus(c).theta{s}.bin = bin;
% clus(c).theta{s}.hist = hist;
% clus(c).theta{s}.pow = pow;
% clus(c).theta{s}.f = f;
clus(c).theta{s}.mod_freq = mod_freq(c,s);
clus(c).theta{s}.hist = hist;
clus(c).theta{s}.bin = bin;

if ~isnan(mod_freq(c,s));
```

Extract running speed info and get theta modulation index for each time bin

```
[pos] = runningspeed_TR(clus(c).info{s}.tracking,t_win);

pos.ts = pos.ts*1000;
speed_mod_freq = nan(length(pos.ts)-1,1);

 for t = 1:length(pos.ts)-1
     spike_ind =  spikes < pos.ts(t+1) & spikes> pos.ts(t);
     if sum(spike_ind) > 5;
    [~,speed_mod_freq(t)] = tmi_tr(spikes(spike_ind)); %tmi>5 = nan
     else
     end
 end
 % get rid of nans and only carry on if enough values
nan_ind = ~isnan(speed_mod_freq);
if sum(nan_ind)>3;
speed_mod_freq = speed_mod_freq(nan_ind);
speed = pos.speed(2:end);
speed = speed(nan_ind);

 [r,p] = corr(speed',speed_mod_freq,'rows','pairwise','type','Pearson');
 theta_z(c,s) = fisherz(r);
clus(c).theta{s}.speed_mod_freq = speed_mod_freq;
clus(c).theta{s}.speed = speed;
clus(c).theta{s}.speed_r = r;
clus(c).theta{s}.speed_z = theta_z(c,s);
clus(c).theta{s}.speed_p = p;

speedBins = [1:30];
for i = 2:length(speedBins)
    % find all time bins where speed is within range of this speed bin
    ind = speed>speedBins(i-1) & speed<=speedBins(i);
```

```
    clus(c).theta{s}.av_speed_mod_freq(i) = sum(speed_mod_freq(ind)/(sum(ind)*t_win));
  end
clus(c).theta{s}.av_speed_mod_freq(clus(c).theta{s}.av_speed_mod_freq == 0) = nan;
else
clus(c).theta{s}.speed_mod_freq = [];
clus(c).theta{s}.speed = [];
clus(c).theta{s}.speed_r = [];
clus(c).theta{s}.speed_z = [];
clus(c).theta{s}.speed_p = [];
clus(c).theta{s}.av_speed_mod_freq = [];
end
```

```
end
    else
        clus(c).theta{s} = [];
  end
end
end
multiWaitbar( 'CloseAll' );
```

```
end

%%%% subfunctions
function [tmi,mod_freq, hist,bin] = tmi_tr(spikes)
```

```
% Adapted from  thetaModulation.m by Jon Witton, May 2013
% Function to calculate the theta modulation index for each cell based on the fast fourier transform of the spike time autocorrellogram.
% If the theta index is >= 5 then the cell is consisdered to be theta modulated.
```

Generate spike time autocorrelation (with 2 ms bins, truncated at 500 ms)

```
        [hist, bin] = CrossCorr(spikes,spikes,2,500);

        % Autocorrelation value in zero lag bin will be massive, as corresponds to perfect correlation (i.e. 1) iterated X times.
        % Rescale autocorrelation function relative to zero lag bin, and reset zero lag to equal with next highest value in autocorr.
        zero = find(bin == 0);                                  % Find index of zero lag bin
        %hist = hist/hist(zero);                                % Divide autocorrelation by zero lag bin to rescale for R
        %hist(zero) =  mean([hist(zero-1) hist(zero+1)]);
        hist(zero) = 0;                                         % Clear value at zero lag and replace with next highest value
        peak = max(hist);                                       % in autocorrelation
        hist(zero) = peak;

        % Mean normalise autocorrelation by subtracting meant tm
        histMean = mean(hist);
        histNorm = hist - histMean;
```

Perform fast Fourier transform on autocorrelation

Taper normalised autocorrelation using a Hamming window.

```
        ham = hamming(length(histNorm),'periodic');
        histT = ham .* histNorm;

        % Perform fast fourier transform
        fs = 1000 / ( bin(2) - bin(1) );                        % Data sampling frequency
        %winLength = length(histT);                             % Window length
        tLength = 2^16;%pow2(nextpow2(winLength));              % Transform length
        dft = fft(histT,tLength);                               % DFT
        f = (0:tLength-1)*(fs/tLength);                         % Frequency range
        pow = dft.*conj(dft)/tLength;                           % Power of the DFT

        % Remove frequency and power values for frequencies above the Nyquist frequency
        f = f(1:floor(tLength/2));
        pow = pow(1:floor(tLength/2));
```

Caculate theta modulation index for cell

Find index of peak power in theta (5-12 Hz) band

```
        thetaIdx = f > 5  &  f <= 12;                           % Index theta band
        theta = pow(thetaIdx);                                  % Isolate theta band power values
        [~,tPeakIdx_theta] = max(theta);                            % Find index of peak theta band power within isoalted theta
band
        tPeakIdx = find(thetaIdx == 1, 1, 'first') - 1 + tPeakIdx_theta;    % Find index of peak theta band power within
broadband spectrum
        mod_freq = f(tPeakIdx);
        % Find mean power for +/- 1 Hz of peak theta power
        oneHz = find(f <= 1,1,'last');                          % Find number of frequency vector indices corresponding to 1
Hz
        thetaMean = mean(pow(tPeakIdx - oneHz:tPeakIdx + oneHz));

        %Find mean broadband (0 - 125 Hz) power
        bbIdx = f >= 0  &  f <= 125;                            % Index 'broadband'
        bb = pow(bbIdx);                                        % Isolate theta band power values
        bbMean = mean(bb);                                          % Find mean 'broadband' power

        % Calculate theta modulation index
        tmi= thetaMean/bbMean;

        if tmi < 5
            %tmi = nan;
            mod_freq = nan;
            %mod_freq_sig = nan;
        end
```

```
 end
```

Published with MATLAB® R2016a

8.4 Speed modulation

```
function [speed_rate,rate_per_tbin,speed_per_tbin,z,z_shf,z_sig,r,r_shf,mod_depth,mod_depth_shf,lz,exp_z_sig,clus] =
speed_firing_final(clus,t_win)
```

```
% speed_firing.m
%
% performs speed cell analysis on time stamps derived from
% import_cluster_data.m
%
% inputs:
%   clus    = struct containg time stamp info
%   headers = struct containing header info
%   t_win   = (optional) time window for speed binning (in seconds)
%
% DEPENDENCIES:
%   runningspeed_TR.m
%   mkShuffledTstamp.m
%   cbrewer.m
%   fisherz.m
```

set up some parameters

```
%%%%%%%%%%%%%%%%%%%%%%%%%%%%%%%%%%%%%%%%%%%%%%%%%%%%%%%%%%%%%%%%%%%%%%%%%%%
%%%%%%%%%%%%%%%%%%%%%%%%%%%%%%
```

Paused or automatic?

```
pause off
```

Speed bin info

```
speedBinSize          = 1;    % in cm/s
minSpeed              = 2;    % in cm/s
maxSpeed              = 30;   % in cm/s
minBinDurPercent        = 0.5; %0.05;  % percent of total recording duration

% default values for time window
if nargin < 2, t_win = 0.04; end % in sec
```

Gaussian smoothing function

```
%-------- CHECK THIS; particularly derivation of alpha---------
% Gaussian for speed and rate histograms
stdevGaus = 0.15;                  % stdev of the gaussian function in s
sigma = stdevGaus/t_win;           % stdev in samples
n = 4*(floor(3*sigma));
alpha = (n-1)/(2*sigma);
w = gausswin(n,alpha);             % construct the gaussian
w = w/sum(w);                      % normalize the gaussian

% Gaussian for speed tuning curves
stdevGaus = 0.5;                   % stdev of the gaussian function in cm/s
sigma = stdevGaus/speedBinSize;    % stdev in samples
n = 1+(2*(floor(3*sigma)));
alpha = (n-1)/(2*sigma);
wS = gausswin(n,alpha);            % construct the gaussian
wS = wS/sum(wS);                   % normalize the gaussian
%-------------------------------------------------------------
```

shuffling parameters

```
numShf            = 250;    % number of suffles
minTShf           = 30;     % minimum duration of shuffle
binHistSize        = 0.02;              % bins for histogram of shuffled r/z
binsHist          = -.2:binHistSize:.2;   % bins for histogram of shuffled r/z
binHistSizeD       = 0.2;               % bins for histogram of shuffled r/z
binsHistD         = 0:binHistSizeD:4;     % bins for histogram of shuffled r/z
centile           = 95;                % percentile to determine significance
```

Output directory for figures

```
output_dir = '\\isad.isadroot.ex.ac.uk\UOE\User\data\mEC unit speed\';
delete([output_dir '*.*'])
```

Plotting info

```
close all scrsz = get(groot,'ScreenSize'); hFig = figure('OuterPosition', [0,
scrsz(4)*0.2, scrsz(3)*0.5, scrsz(4)*0.8]); fontSize = 12; prec = '%.3f'; grey =
[0.7,0.7,0.7]; set(0,'DefaulttextInterpreter','none')
```

```
%%%%%%%%%%%%%%%%%%%%%%%%%%%%%%%%%%%%%%%%%%%%%%%%%%%%%%%%%%%%%%%
%%%%%%%%%%%%%%%%%
z = zeros(length(clus),length(clus(1).info));
r = zeros(length(clus),length(clus(1).info));
z_sig = nan(length(clus),length(clus(1).info));
exp_z_sig = nan(length(clus),length(clus(1).info));
speed_rate = cell(length(clus(1).info),1);

% wait bar
hwait = waitbar(0,'Calculating speed relationships');


for j = 1:length(clus)

for s = 1:length(clus(j).info)
 if length(clus(j).tstamp{s})<100;
       clus(j).speed_rate{s} = [];
 else
```

Extract running speed info

```
[pos] = runningspeed_TR(clus(j).info{s}.tracking,t_win);
% smooth the speed data with the gaussian function - comment out if not required
pos.speed = conv(pos.speed,w,'same');

% create a series of time bins based on pos.ts with the Ts_start
[~,timeBins] = histcounts(pos.ts,length(pos.ts));

% numTimeBins = length(timeBins);

% define speed bins
speedBins = minSpeed:speedBinSize:maxSpeed;
speedBins = speedBins';
numSpeedBins = length(speedBins);
```

Loop through each cell and define run speed

```
% preallocated matrix for speed rates
%speed_rate{s}              = zeros(numSpeedBins,length(clus));
rate_per_tbin          = zeros(length(pos.ts),length(clus));
speed_per_tbin          = zeros(length(pos.ts),length(clus));
% z = zeros(length(clus),1);
% r = zeros(length(clus),1);
%z_sig = zeros(length(clus),1);
z_shf = zeros(length(clus),numShf);
r_shf = zeros(length(clus),numShf);
%speed modulation depth
```

```
mod_depth      = zeros(length(clus),1);
mod_depth_shf  = zeros(length(clus),numShf);



%    clf(hFig)
```

Determine speed firing rate relationship - calls speedRateRelationship

```
    [speed_rate{s}(:,j),rate_per_tbin(:,j)] = ...
        speedRateRelationship(clus(j).tstamp{s},numSpeedBins,timeBins,speedBins,t_win,pos,minBinDurPercent,wS);
    % smooth the rate_per_tbin data with the gaussian function
    rate_per_tbin(:,j) = conv(rate_per_tbin(:,j),w,'same');
```

Behavioural filtering of data - remove bins where animal isn't moving

```
    [rate_per_tbin(:,j),speed_per_tbin] = behavFiltering(rate_per_tbin(:,j),pos.speed,minSpeed);
```

Calculate the correlation coefficients for this relationship -calls speedCorr

```
    [clus(j).speed_rate{s}.r,...
        clus(j).speed_rate{s}.z,...
        clus(j).speed_rate{s}.p,...
        clus(j).speed_rate{s}.lr,...
        clus(j).speed_rate{s}.lz,...
        clus(j).speed_rate{s}.lp] = ...
        speedCorr(speed_per_tbin',rate_per_tbin(:,j));

    z(j,s) = clus(j).speed_rate{s}.z;
    r(j,s) = clus(j).speed_rate{s}.r;
    lz(j,s) = clus(j).speed_rate{s}.lz;
    lr(j,s) = clus(j).speed_rate{s}.lr;
```

Put the speed-firing rate curves into clus

Speed tuning curve

```
    clus(j).speed_rate{s}.speedBins    = speedBins;
    clus(j).speed_rate{s}.firing_rate  = speed_rate{s}(:,j);
    % rates per bin
    clus(j).speed_rate{s}.speed_per_tbin = speed_per_tbin;
    clus(j).speed_rate{s}.rate_per_tbin  = rate_per_tbin(:,j);
    clus(j).speed_rate{s}.timeBins       = timeBins;
    % modulation depth
    mod_depth(j,s) = max(speed_rate{s}(:,j)) - min(speed_rate{s}(:,j));
    clus(j).speed_rate{s}.mod_depth = mod_depth(j,s);
```

Shuffle the data and perform the same calculations on each

```
    shf_tstamp = mkShuffledTstamp(clus(j).tstamp{s},numShf,minTShf);
```

Determine speed firing rate relationship for shuffled data

preallocate

```
    shf_speed_rate = zeros(numSpeedBins,numShf);
    rate_per_tbin_shf = zeros(length(pos.speed),numShf);
    for n = 1:numShf
        [shf_speed_rate(:,n),rate_per_tbin_shf(:,n)] = ...
            speedRateRelationship(shf_tstamp(:,n),numSpeedBins,timeBins,speedBins,t_win,pos,minBinDurPercent,wS);
        % smooth the rate_per_tbin data with the gaussian function
        rate_per_tbin_shf(:,n) = conv(rate_per_tbin_shf(:,n),w,'same');
```

```
    end
    mod_depth_shf(j,:) = max(shf_speed_rate) - min(shf_speed_rate);
    clus(j).speed_rate{s}.mod_depth_shf = mod_depth_shf(j,:);
```

Behavioural filtering of data - remove bins where animal isn't moving much

```
    [rate_per_tbin_shf,~] = behavFiltering(rate_per_tbin_shf,pos.speed,minSpeed);
```

Calculate the correlation coefficients for shuffled data

```
    [clus(j).speed_rate{s}.shf_r,...
        clus(j).speed_rate{s}.shf_z,...
        clus(j).speed_rate{s}.shf_p,...
        clus(j).speed_rate{s}.shf_lr,...
        clus(j).speed_rate{s}.shf_lz,...
        clus(j).speed_rate{s}.shf_lp] = ...
        speedCorr(pos.speed',rate_per_tbin_shf);
    z_shf(j,:) = clus(j).speed_rate{s}.shf_z;
    r_shf(j,:) = clus(j).speed_rate{s}.shf_r;
```

Centiles of speed score shuffled data set

```
    clus(j).speed_rate{s}.centileHi = prctile(clus(j).speed_rate{s}.shf_z,centile);
    clus(j).speed_rate{s}.centileLo = prctile(clus(j).speed_rate{s}.shf_z,100-centile);
    clus(j).speed_rate{s}.exp_centileHi = prctile(clus(j).speed_rate{s}.shf_lz,centile);
    clus(j).speed_rate{s}.exp_centileLo = prctile(clus(j).speed_rate{s}.shf_lz,100-centile);

    if z(j)> clus(j).speed_rate{s}.centileHi || z(j)< clus(j).speed_rate{s}.centileLo
        z_sig(j,s) = z(j,s);
    else
    end

    if lz(j)> clus(j).speed_rate{s}.exp_centileHi || lz(j)< clus(j).speed_rate{s}.exp_centileLo
        exp_z_sig(j,s) = lz(j,s);
    else
    end

if exp_z_sig(j,s)> z_sig(j,s);
    z_sig(j,s) = nan;
else
    exp_z_sig(j,s) = nan;
end
```

Centiles of speed modulation depth shuffled data set

```
    clus(j).speed_rate{s}.modDcentileHi = prctile(clus(j).speed_rate{s}.mod_depth_shf,centile);
    clus(j).speed_rate{s}.modDcentileLo = prctile(clus(j).speed_rate{s}.mod_depth_shf,100-centile);
```

Put all the analysis parameters into clus speed bin params

```
    clus(j).speed_rate{s}.params{s}.speedBinSize       = speedBinSize;     % in cm/s
    clus(j).speed_rate{s}.params{s}.minSpeed           = minSpeed;         % in cm/s
    clus(j).speed_rate{s}.params{s}.maxSpeed           = maxSpeed;         % in cm/s
    clus(j).speed_rate{s}.params{s}.minBinDurPercent   = minBinDurPercent;  % percent of total recording duration
```

shuffling parameters

```
    clus(j).speed_rate{s}.params{s}.numShf             = numShf;           % number of suffles
    clus(j).speed_rate{s}.params{s}.minTShf            = minTShf;          % minimum duration of shuffle
    clus(j).speed_rate{s}.params{s}.binsHist           = binsHist;         % bins for histogram of shuffled r
    clus(j).speed_rate{s}.params{s}.centile            = centile;          % percentile to determine significance
    clus(j).speed_rate{s}.params{s}.t_win              = t_win;
    waitbar(j/length(clus),hwait)
```

```
    end
 end

end
close(hwait)
```

SUBFUNCTIONS

Speed_rate

```
function [speed_rate,rate_per_tbin] =
speedRateRelationship(time_stamps,numSpeedBins,timeBins,speedBins,t_win,pos,minBinDurPercent,wS)
```

Create spike histogram for time bins

```
[no_spikes,~] = histcounts(time_stamps,timeBins);

rate_per_tbin = no_spikes./t_win;
% smooth this in the main script...
```

Loop through all the speed bins and calculate the average firing rate

```
speed_rate = zeros(numSpeedBins-1,1);
total_dur = time_stamps(end)-time_stamps(1);
for i = 2:numSpeedBins

    % find all time bins where speed is within range of this speed bin
    ind = pos.speed>speedBins(i-1) & pos.speed<=speedBins(i);

    if sum(ind)*t_win < total_dur * (minBinDurPercent/100);
        speed_rate(i) = NaN;
    else
        % calculate the average firing rate for that speed bin (in Hz)
        speed_rate(i) = sum(no_spikes(ind)/(sum(ind)*t_win));
    end

end

% tidy up speed_rate by replacing zeros with NaN
speed_rate(speed_rate == 0) = NaN;

% apply a gaussian filter to the speed curve
y=conv(speed_rate(~isnan(speed_rate)),wS,'same');    % convolve the valid samples with the filer
speed_rate(~isnan(speed_rate)) = y;

end
```

BehavFiltering

```
function [rate_per_tbin,speed_per_tbin] = behavFiltering(rate_per_tbin,speed,minSpeed)

% determine original shape of inputs, for reshaping later
[m,n] = size(rate_per_tbin);

% replace all non-relevant bins with NaN
indS = speed <= minSpeed;
if n>1
    indR = repmat(indS,1,n);
else
    indR = indS;
end
rate_per_tbin(indR) = NaN;
speed_per_tbin = speed;
speed_per_tbin(indS) = NaN;
```

```
end
```

SpeedCorr

```
function [r,z,p,lr,lz,lp] = speedCorr(speedBins,speed_rate)
[r,p] = corr(speedBins,speed_rate,...
    'rows','pairwise',...
    'type','Pearson');
[lr,lp] = corr(log(speedBins),speed_rate,...
    'rows','pairwise',...
    'type','Pearson');
z = fisherz(r);
lz = fisherz(lr);
end
```

```
end
```

Published with MATLAB® R2016a

8.5 Firing maps and grid score

```
function [clus,GridScore,GridScore_sig,spatial_info] = maps_working_final(clus)

t_win = 0.4;
bins = 50;
speed_min = 3;
arena_size = 120; %cm
```

Shuffling parameters

```
numShf            = 250;    % number of suffles
minTShf           = 20;     % minimum duration of shuffle
binHistSize       = 0.02;           % bins for histogram of shuffled data
centile           = 95;             % percentile to determine significance

%smoothing
F = fspecial('gaussian', bins, 1.5);

 multiWaitbar( 'cell', 'Value', 0);
 for j =1:length(clus)
    multiWaitbar( 'cell', 'Value', j/length(clus));


for s = 1:length(clus(j).info)

      if length(clus(j).tstamp{s})>300;
```

```
    multiWaitbar( 'session' , 'Value', s/length(clus(1).info));

   [pos] = runningspeed_TR(clus(j).info{s}.tracking, t_win);

   pos.speed = interp1(pos.ts,pos.speed,clus(j).info{s}.tracking.tsV);
   pos.X = interp1(pos.ts,pos.X(2:end),clus(j).info{s}.tracking.tsV);
   pos.Y = interp1(pos.ts,pos.Y(2:end),clus(j).info{s}.tracking.tsV);
   pos.ts = clus(j).info{s}.tracking.tsV;

  Fs  = 1/(pos.ts(2)-pos.ts(1)) ;
```

Find bins with spikes

```
[~,timeBins] = histcounts(pos.ts,length(pos.ts));
[no_spikes,~] = histcounts(clus(j).tstamp{s},timeBins);
```

Get rid of spikes when animal not moving

```
ind = pos.speed < speed_min;
spikes(ind) = 0 ;
pos.X(ind) = nan;
pos.Y(ind) = nan;

clus(j).map{s}.x_loc = [];
clus(j).map{s}.y_loc = [];

for i = 1: max(no_spikes)
  spikes = no_spikes == i ;
for l = 1:i
clus(j).map{s}.x_loc = [clus(j).map{s}.x_loc,pos.X(spikes)];
clus(j).map{s}.y_loc = [clus(j).map{s}.y_loc,pos.Y(spikes)];
end
end

clus(j).map{s}.pos = pos;
```

2d histcount to find spikes/time spent in each spatial bin

```
screen_size = clus(j).info{s}.tracking.screen_x;
maX = max(clus(j).map{s}.pos.X); maY = max(clus(j).map{s}.pos.Y);
miX = min(clus(j).map{s}.pos.X); miY = min(clus(j).map{s}.pos.Y);
Xedges = linspace(miX,maX,bins);
Yedges =  linspace(miY,maY,bins);

[clus(j).map{s}.time,Xedges,Yedges] = histcounts2(pos.X,pos.Y,Xedges,Yedges);
clus(j).map{s}.OcProb = clus(j).map{s}.time/sum(sum(clus(j).map{s}.time)); %time in sec
clus(j).map{s}.time = clus(j).map{s}.time*(1/Fs); %time in sec

[clus(j).map{s}.count,clus(j).map{s}.Xedges,clus(j).map{s}.Yedges] =
histcounts2(clus(j).map{s}.x_loc,clus(j).map{s}.y_loc,Xedges,Yedges);

clus(j).map{s}.rate_map =  clus(j).map{s}.count./clus(j).map{s}.time;
clus(j).map{s}.rate_map(isnan(clus(j).map{s}.rate_map)) = 0;

clus(j).map{s}.rate_map_smooth = conv2(clus(j).map{s}.rate_map,F,'same');


meanRate = sum(sum(clus(j).map{s}.count))/sum(sum(clus(j).map{s}.time));

scBin = conv2(clus(j).map{s}.OcProb,F,'same').* (clus(j).map{s}.rate_map_smooth/meanRate) .*
log2(clus(j).map{s}.rate_map_smooth/meanRate);

scBin = scBin(~isnan(scBin));
clus(j).map{s}.spatial_info = sum(scBin);
spatial_info(j,s) = clus(j).map{s}.spatial_info;
```

xcorr

```
ang = [0,30,60,90,120,150]; %should be peak at 60 and 120
mask_size = [0.1:0.01:0.5]; %proportion of total field

[clus(j).map{s}.xcorr,clus(j).map{s}.r, clus(j).map{s}.grid_score,clus(j).map{s}.grid_spacing,clus(j).map{s}.g_scores]...
                                        = grid_score(clus(j).map{s}.rate_map_smooth, ang, mask_size, bins,arena_size);

GridScore(j,s) = max(clus(j).map{s}.grid_score);
```

Shuffle the data and perform the same calculations on each

```
shf_tstamp = mkShuffledTstamp(clus(j).tstamp{s},numShf,minTShf);

for sh = 1:numShf
```

```
[shuf_no_spikes,~] = histcounts(shf_tstamp(:,sh),timeBins);

shuf_x_loc = [];
shuf_y_loc = [];
for i = 1: max(shuf_no_spikes)
  shuf_spikes = shuf_no_spikes == i ;
for l = 1:i
shuf_x_loc = [shuf_x_loc,pos.X(shuf_spikes)];
shuf_y_loc = [shuf_y_loc,pos.Y(shuf_spikes)];
end
end
```

2d histcount to find spikes/time spent in each spatial bin

```
[count,clus(j).map{s}.Xedges,clus(j).map{s}.Yedges] = histcounts2(shuf_x_loc,shuf_y_loc,Xedges,Yedges);
shuf_rate_map =  count./clus(j).map{s}.time;
shuf_rate_map(isnan(shuf_rate_map)) = 0;
shuf_rate_map_smooth = conv2(shuf_rate_map,F,'same');
shuf_meanRate = sum(sum(count))/sum(sum(clus(j).map{s}.time));
scBin = conv2(clus(j).map{s}.OcProb,F,'same').* (shuf_rate_map_smooth/shuf_meanRate) .*
log2(shuf_rate_map_smooth/shuf_meanRate);
scBin = scBin(~isnan(scBin));
clus(j).map{s}.shuf.spatial_info(sh) = sum(scBin);
```

Grid score

```
[~,~, clus(j).map{s}.shuf.grid_score(sh),~] = grid_score(shuf_rate_map_smooth, ang, mask_size, bins,arena_size);
```

Percentile

```
clus(j).map{s}.shuf.grid_centile = prctile(clus(j).map{s}.shuf.grid_score,centile);
clus(j).map{s}.shuf.spatial_info_centile = prctile(clus(j).map{s}.shuf.spatial_info,centile);

if clus(j).map{s}.shuf.grid_centile > clus(j).map{s}.grid_score
    GridScore_sig(j,s) = nan;
end
```

```
end
```

```
      else
       clus(j).map{s} = [];
      end

 end
end
multiWaitbar( 'CloseAll' );
end

function [x,varargout] = ZeroToOne(x,varargin)

if nargin < 1,
            error('Incorrect number of parameters (type "help <a href="matlab:help ZeroToOne">ZeroToOne</a>" for
details).');
end

if nargin ~= nargout,
            error('Different numbers of input and output parameters (type "help <a href="matlab:help
ZeroToOne">ZeroToOne</a>" for details).');
end

m = min(x);
M = max(x);
x = (x-m)/(M-m);

for i = 1:nargin-1,
            varargout{i} = (varargin{i}-m)/(M-m);
end
end

function [xcorr,r,grid_score,grid_spacing,g_scores] = grid_score(rate_map, ang, mask_size, bins,arena_size)
```

```
xcorr = cell(length(ang),length(mask_size));
r = zeros(length(ang),length(mask_size));

% 1st xcorr
%xcorr{1} = xcorr2(rate_map);
xcorr{1} = normxcorr2(rate_map,rate_map);
x_size = size(xcorr{1});
```

work out grid score and spacing

```
for g = 1:length(mask_size)
```

```
% crop xcorr to take out centre and increase autocorr by factor mask_size
  c_large = [bins, bins,x_size(1)*mask_size(g)];  % center and radius of circle ([c_row, c_col, r])
  [xx,yy] = ndgrid((1:x_size(1))-c_large(1),(1:x_size(2))-c_large(2));
  mask_large = (xx.^2 + yy.^2)<c_large(3)^2;

  x_crop= zeros(x_size);
  x_crop(mask_large) = xcorr{1}(mask_large);

  c_centre = [bins, bins, x_size(1)*0.06];     % center and radius of circle ([c_row, c_col, r])0.075
 [xx,yy] = ndgrid((1:x_size(1))-c_centre(1),(1:x_size(2))-c_centre(2));
  mask_centre = (xx.^2 + yy.^2)<c_centre(3)^2;

 x_crop(mask_centre) = 0;
```

```
x = x_crop;
```

Rotate and correlate with original xcorr

```
  for i = 2:length(ang)
  xcorr{i,g} = imrotate(x,ang(i),'crop');
  x_crop= zeros(x_size);
  x_crop(mask_large) = xcorr{i,g}(mask_large);
  x_crop(mask_centre) = 0;
  xcorr{i,g} = x_crop;
  r(i,g) = corr2(xcorr{i,g},x);
  end

% diff between 60/120 deg and 30/90/150 deg gives 'gridness'
g_diff = diff(r(:,g));
g_diff(1:2:end) = g(1:2:end)*-1;
g_scores(g) = max(g_diff(2:end));
```

```
end
% size of xcorr with best gridscore gives grid spacing
[grid_score,size_ind] = max(g_scores);
grid_spacing = mask_size(size_ind)*arena_size;
```

```
end
```

Published with MATLAB® R2016a

8.6 Head direction analysis

```
function [clus,meanVecLength,meanVec_sig] = head_direction_firing_final(clus,t_win)
```

```
% %
% performs head direction cell analysis on time stamps derived from
% import_cluster_data.m
%
% inputs:
%   clus    = struct containg time stamp info
%   headers = struct containing header info
%   t_win   = (optional) time window for speed binning (in seconds)
%
% DEPENDENCIES:
%   runningspeed_TR.m
%
% TR 15/03/17
```

Set up some parameters

```
%%%%%%%%%%%%%%%%%%%%%%%%%%%%%%%%%%%%%%%%%%%%%%%%%%%%%%%%%%%
%%%%%%%%%%%%%%%%
```

Bin info

```
minSpeed          = 1;    % in cm/s

bin_size = 3; % in degrees

% default values for time window
if nargin < 3, t_win = 0.04; end % in sec
```

Gaussian smoothing function

```
%-------- CHECK THIS; particularly derivation of alpha---------
% Gaussian for speed and rate histograms
stdevGaus = 0.15;                 % stdev of the gaussian function in s
sigma = stdevGaus/t_win;          % stdev in samples
n = 4*(floor(3*sigma));
alpha = (n-1)/(2*sigma);
w = gausswin(n,alpha);            % construct the gaussian
w = w/sum(w);                     % normalize the gaussian

% Gaussian for head tuning curves
stdevGaus = 14;                   % stdev of the gaussian function in deg
sigma = stdevGaus/bin_size;       % stdev in samples
n = 1+(2*(floor(3*sigma)));
alpha = (n-1)/(2*sigma);
wS = gausswin(n,alpha);           % construct the gaussian
wS = wS/sum(wS);                  % normalize the gaussian
%------------------------------------------------------------
```

Shuffling parameters

```
numShf          = 1;     % number of suffles
minTShf         = 30;    % minimum duration of shuffle
binHistSize     = 0.02;            % bins for histogram of shuffled
binsHist        = -.2:binHistSize:.2;  % bins for histogram of shuffled
binHistSizeD    = 0.2;             % bins for histogram of shuffled
binsHistD       = 0:binHistSizeD:4;    % bins for histogram of shuffled
centile         = 95;              % percentile to determine significance

meanVecLength = nan(length(clus),length(clus(1).info));
meanVec_sig= nan(length(clus),length(clus(1).info));
```

```
%%%%%%%%%%%%%%%%%%%%%%%%%%%%%%%%%%%%%%%%%%%%%%%%%%%%%%%%%%%%%%%%%%
%%%%%%%%%%%%%%%%%%%

  multiWaitbar( 'cell', 'Value', 0);
for j = 1:length(clus) % loop for cells

for s = 1: length(clus(j).info) % loop for recording sessions

% multiWaitbar( 'session' , 'Value', s/length(clus(j).info));
  multiWaitbar( 'cell', 'Value', j/length(clus));
```

Extract running speed info

```
[pos] = runningspeed_TR(clus(j).info{s}.tracking,t_win);
% smooth the data with the gaussian function - comment out if not required
pos.speed = conv(pos.speed,w,'same');
pos.A = conv(pos.A(2:end),w,'same');

% create a series of time bins based on pos.ts with the Ts_start
[~,timeBins] = histcounts(pos.ts,length(pos.ts));
```

Loop through each cell and define run speed

```
% preallocated matrix

rate_per_tbin = zeros(length(pos.ts),length(clus));

    if ~isempty(clus(j).tstamp{s})
```

Create spike histogram for time bins

```
[no_spikes,~] = histcounts(clus(j).tstamp{s},timeBins);

rate_per_tbin(:,j) = no_spikes./t_win;
rate_per_tbin(:,j) = conv(rate_per_tbin(:,j),w,'same');
```

Behavioural filtering of data - remove bins where animal isn't moving much

```
[rate_per_tbin(:,j),~] = behavFiltering(rate_per_tbin(:,j),pos.speed,minSpeed);
```

Rate and position maps

```
[clus(j).head_direction{s}.rate_map,clus(j).head_direction{s}.rate_map_smooth,clus(j).head_direction{s}.angle_bin] =
head_map(pos.A,rate_per_tbin(:,j),bin_size,wS);
clus(j).head_direction{s}.angle_bin = deg2rad(clus(j).head_direction{s}.angle_bin);
clus(j).head_direction{s}.spike_angles = interp1(pos.ts,pos.A,clus(j).tstamp{s});
clus(j).head_direction{s}.pos_angles = pos.A;

clus(j).head_direction{s}.spike_angles = clus(j).head_direction{s}.spike_angles .* pi./180;%convert to radians
[clus(j).head_direction{s}.mean_vec_length] =
circ_r(clus(j).head_direction{s}.angle_bin,clus(j).head_direction{s}.rate_map_smooth);
[clus(j).head_direction{s}.mean_direction,~,~] = circ_mean(clus(j).head_direction{s}.spike_angles);
[clus(j).head_direction{s}.rayleigh_pval, clus(j).head_direction{s}.rayleigh_z] =
circ_rtest(clus(j).head_direction{s}.angle_bin,clus(j).head_direction{s}.rate_map_smooth);

meanVecLength(j,s) = clus(j).head_direction{s}.mean_vec_length;
```

Shuffle the data and perform the same calculations on each

```
shf_tstamp = mkShuffledTstamp(clus(j).tstamp{s},numShf,minTShf);
% preallocate
rate_per_tbin_shf = zeros(length(pos.ts),numShf);
clus(j).head_direction{s}.shuffle.rate_map = zeros(length(clus(j).head_direction{s}.angle_bin),numShf);
```

```
clus(j).head_direction{s}.shuffle.mean_vec_length = zeros(numShf,1);
clus(j).head_direction{s}.shuffle.rayleigh_pval= zeros(numShf,1);
clus(j).head_direction{s}.shuffle.rayleigh_z= zeros(numShf,1);

   for sh = 1:numShf
[no_spikes,~] = histcounts(shf_tstamp(:,sh),timeBins);
rate_per_tbin_shf(:,sh) = no_spikes./t_win;
rate_per_tbin_shf(:,sh) = conv(rate_per_tbin_shf(:,sh),w,'same');
[rate_per_tbin_shf(:,sh),~] = behavFiltering(rate_per_tbin_shf(:,sh),pos.speed,minSpeed);
[clus(j).head_direction{s}.shuffle.rate_map(:,sh),clus(j).head_direction{s}.shuffle.rate_map_smooth(:,sh),clus(j).head_dir
ection{s}.shuffle.angle_bin] = head_map(pos.A,rate_per_tbin_shf(:,sh),bin_size,wS);
clus(j).head_direction{s}.shuffle.angle_bin = deg2rad(clus(j).head_direction{s}.shuffle.angle_bin);
%test
[clus(j).head_direction{s}.shuffle.mean_vec_length(sh)] =
circ_r(clus(j).head_direction{s}.shuffle.angle_bin,clus(j).head_direction{s}.shuffle.rate_map_smooth(:,sh));
[clus(j).head_direction{s}.shuffle.rayleigh_pval(sh), clus(j).head_direction{s}.shuffle.rayleigh_z(sh)] =
circ_rtest(clus(j).head_direction{s}.angle_bin,clus(j).head_direction{s}.shuffle.rate_map_smooth(:,sh));
   end
%99th centiles of shuffled data set
clus(j).head_direction{s}.RayZCent = prctile(clus(j).head_direction{s}.shuffle.rayleigh_z,100-centile);
clus(j).head_direction{s}.MeanVecCent = prctile(clus(j).head_direction{s}.shuffle.mean_vec_length,centile);

 if clus(j).head_direction{s}.mean_vec_length>clus(j).head_direction{s}.MeanVecCent
    meanVec_sig(j,s) = clus(j).head_direction{s}.mean_vec_length;
 end
```

```
   else
    clus(j).head_direction{s} = [];
   end
```

```
end

end
multiWaitbar( 'CloseAll' );
```

```
end
```

Subfunctions

```
function [rate_per_tbin,speed_per_tbin] = behavFiltering(rate_per_tbin,speed,minSpeed)

% determine original shape of inputs, for reshaping later
[m,n] = size(rate_per_tbin);

% replace all non-relevant bins with NaN
indS = speed <= minSpeed;
if n>1
   indR = repmat(indS,1,n);
else
   indR = indS;
end
rate_per_tbin(indR) = NaN;
speed_per_tbin = speed;
speed_per_tbin(indS) = NaN;


end

function [rate_map,rate_map_smooth,angle_bin] = head_map(A,rate_per_tbin,bin_size,wS)


angle_bin = 1:bin_size:360;
angle_bin = angle_bin';

rate_map = NaN(length(angle_bin),1);


for a = 2:length(angle_bin)

   ind = A < angle_bin(a) & A > angle_bin(a-1);

   rate_map(a) = mean(rate_per_tbin(ind));
end

rate_map2 = [rate_map; rate_map;rate_map]; %make copies and interp/smooth - for betwen 360 and 0.
rate_map2 = fillmiss(rate_map2);
```

```
rate_map_smooth = conv(rate_map2,wS,'same');    % convolve the valid samples with the filer

rate_map2 = reshape(rate_map2,length(angle_bin),3);
rate_map_smooth= reshape(rate_map_smooth,length(angle_bin),3);

rate_map = rate_map2(:,2);

rate_map_smooth = rate_map_smooth(:,2);

end
```

Published with MATLAB® R2016a

References

Abásolo D, Hornero R, Espino P, Álvarez D & Poza J (2006). Entropy analysis of the EEG background activity in Alzheimer's disease patients. *Physiol Meas* **27,** 241–253.

Abrahams S, Pickering A, Polkey C. & Morris R. (1997). Spatial memory deficits in patients with unilateral damage to the right hippocampal formation. *Neuropsychologia* **35,** 11–24.

Ahmed OJ & Mehta MR (2012). Running Speed Alters the Frequency of Hippocampal Gamma Oscillations. *J Neurosci*, **32,** 7373-7383.

Aksoy-Aksel A & Manahan-Vaughan D (2013). The temporoammonic input to the hippocampal CA1 region displays distinctly different synaptic plasticity compared to the Schaffer collateral input in vivo: significance for synaptic information processing. *Front Synaptic Neurosci* **5,** 5.

Allen K, Gil M, Resnik E, Toader O, Seeburg P & Monyer H (2014). Impaired Path Integration and Grid Cell Spatial Periodicity in Mice Lacking GluA1-Containing AMPA Receptors. *J Neurosci,* **34,** 6245-6259

Allison SL, Fagan AM, Morris JC & Head D (2016). Spatial Navigation in Preclinical Alzheimer's Disease. *J Alzheimer's Dis* **52,** 77–90.

Alme CB, Miao C, Jezek K, Treves A, Moser EI & Moser M-B (2014). Place cells in the hippocampus: eleven maps for eleven rooms. *Proc Natl Acad Sci U S A* **111,** 18428–18435.

Amaral D & Witter M (1989). The three-dimensional organization of the hippocampal formation: a review of anatomical data. *Neuroscience* **31,** 571–591.

Andersen P (2007). *The hippocampus book*. Oxford University Press.

Ashe KH & Zahs KR (2010). Probing the biology of Alzheimer's disease in mice. *Neuron* **66,** 631–645.

Avoli M, D'Antuono M, Louvel J, Köhling R, Biagini G, Pumain R, D'Arcangelo G & Tancredi V (2002). Network and pharmacological mechanisms leading to epileptiform synchronization in the limbic system in vitro. *Prog Neurobiol* **68,**

167–207.

Avoli M, Panuccio G, Herrington R, D'Antuono M, de Guzman P & Lévesque M (2013). Two different interictal spike patterns anticipate ictal activity in vitro. *Neurobiol Dis* **52,** 168–176.

Baglietto-Vargas D, Moreno-Gonzalez I, Sanchez-Varo R, Jimenez S, Trujillo-Estrada L, Sanchez-Mejias E, Torres M, Romero-Acebal M, Ruano D, Vizuete M, Vitorica J & Gutierrez A (2010). Calretinin interneurons are early targets of extracellular amyloid-beta pathology in PS1/AbetaPP Alzheimer mice hippocampus. *J Alzheimers Dis* **21,** 119–132.

Bailey RM, Howard J, Knight J, Sahara N, Dickson DW & Lewis J (2014). Effects of the C57BL/6 strain background on tauopathy progression in the rTg4510 mouse model. *Mol Neurodegener* **9,** 8.

Bakota L & Brandt R (2016). Tau Biology and Tau-Directed Therapies for Alzheimer's Disease. *Drugs* **76,** 301–313.

Bampton ET., Gray RA & Large CH (1999). Electrophysiological characterisation of the dentate gyrus in five inbred strains of mouse. *Brain Res* **841,** 123–134.

Bang J, Spina S & Miller BL (2015). Frontotemporal dementia. *Lancet* **386,** 1672–1682.

Barbarosie M & Avoli M (1997). CA3-Driven Hippocampal-Entorhinal Loop Controls Rather than Sustains In Vitro Limbic Seizures. *J Neurosci* **17,** 9308–9314.

Barlow JS (1964). Inertial navigation as a basis for animal navigation. *J Theor Biol* **6,** 76–117.

Barnes CA, McNaughton BL, Mizumori SJ, Leonard BW & Lin LH (1990). Comparison of spatial and temporal characteristics of neuronal activity in sequential stages of hippocampal processing. *Prog Brain Res* **83,** 287–300.

Barry C & Bush D (2012). From A to Z: a potential role for grid cells in spatial navigation. *Neural Syst Circuits* **2,** 6.

Barry C, Ginzberg LL, O'Keefe J & Burgess N (2012*a*). Grid cell firing patterns signal environmental novelty by expansion. *Proc Natl Acad Sci* **109,** 17687–17692.

Barry C, Heys JG & Hasselmo ME (2012*b*). Possible role of acetylcholine in regulating spatial novelty effects on theta rhythm and grid cells. *Front Neural Circuits* **6,** 5.

Barry C, Lever C, Hayman R, Hartley T, Burton S, O'Keefe J, Jeffery K & Burgess N (2006). The boundary vector cell model of place cell firing and spatial memory. *Rev Neurosci* **17,** 71–97.

Bartolomei F, Khalil M, Wendling F, Sontheimer A, Regis J, Ranjeva J-P, Guye M & Chauvel P (2005). Entorhinal Cortex Involvement in Human Mesial Temporal Lobe Epilepsy: An Electrophysiologic and Volumetric Study. *Epilepsia* **46,** 677–687.

Beed P, Gundlfinger A, Schneiderbauer S, Song J, Böhm C, Burgalossi A, Brecht M, Vida I & Schmitz D (2013). Inhibitory gradient along the dorsoventral axis in the medial entorhinal cortex. *Neuron* **79,** 1197–1207.

Belluscio MA, Mizuseki K, Schmidt R, Kempter R & Buzsáki G (2012). Cross-frequency phase-phase coupling between θ and γ oscillations in the hippocampus. *J Neurosci* **32,** 423–435.

Le Ber I (2013). Genetics of frontotemporal lobar degeneration: An up-date and diagnosis algorithm. *Rev Neurol (Paris)* **169,** 811–819.

Berényi A, Somogyvári Z, Nagy AJ, Roux L, Long JD, Fujisawa S, Stark E, Leonardo A, Harris TD & Buzsáki G (2014). Large-scale, high-density (up to 512 channels) recording of local circuits in behaving animals. *J Neurophysiol*, **11,** 1132-1149

Berger H (1929). Über das Elektrenkephalogramm des Menschen. *Arch Psychiatr Nervenkr* **87,** 527–570.

Berretta N, Ledonne A, Mango D, Bernardi G & Mercuri NB (2012). Hippocampus versus entorhinal cortex decoupling by an NR2 subunit-specific block of NMDA receptors in a rat in vitro model of temporal lobe epilepsy. *Epilepsia* **53,** e80-4.

Bi G & Poo M (1998). Synaptic Modifications in Cultured Hippocampal Neurons: Dependence on Spike Timing, Synaptic Strength, and Postsynaptic Cell Type. *J Neurosci*, **18,** 10464-10472

Bird TD, Nochlin D, Poorkaj P, Cherrier M, Kaye J, Payami H, Peskind E, Lampe TH, Nemens E, Boyer PJ & Schellenberg GD (1999). A clinical pathological comparison of three families with frontotemporal dementia and identical mutations in the tau gene (P301L). *Brain* **122,** 741–756.

Birks JS (2006). Cholinesterase inhibitors for Alzheimer's disease. In *Cochrane Database of Systematic Reviews*, ed. Birks JS. John Wiley & Sons, Ltd, Chichester, UK.

Bjerknes TL, Moser EI & Moser M-B (2014). Representation of Geometric Borders in the Developing Rat. *Neuron* **82,** 71–78.

Blair HT, Welday AC & Zhang K (2007). Scale-invariant memory representations emerge from moiré interference between grid fields that produce theta oscillations: a computational model. *J Neurosci* **27,** 3211–3229.

Boehlen A, Heinemann U & Erchova I (2010). The Range of Intrinsic Frequencies Represented by Medial Entorhinal Cortex Stellate Cells Extends with Age. *J Neurosci* **30,** 4585–4589.

Bokil H, Andrews P, Kulkarni JE, Mehta S & Mitra PP (2010). Chronux: a platform for analyzing neural signals. *J Neurosci Methods* **192,** 146–151.

Bonnevie T, Dunn B, Fyhn M, Hafting T, Derdikman D, Kubie JL, Roudi Y, Moser EI & Moser M-B (2013). Grid cells require excitatory drive from the hippocampus. *Nat Neurosci* **16,** 309–317.

Booth CA, Ridler T, Murray TK, Ward MA, de Groot E, Goodfellow M, Phillips KG, Randall AD & Brown JT (2016*a*). Electrical and Network Neuronal Properties Are Preferentially Disrupted in Dorsal, But Not Ventral, Medial Entorhinal Cortex in a Mouse Model of Tauopathy. *J Neurosci* **36,** 312–324.

Booth CA, Witton J, Nowacki J, Tsaneva-Atanasova K, Jones MW, Randall AD & Brown JT (2016*b*). Altered Intrinsic Pyramidal Neuron Properties and Pathway-Specific Synaptic Dysfunction Underlie Aberrant Hippocampal Network Function in a Mouse Model of Tauopathy. *J Neurosci* **36,** 350–363.

Braak H et al. (1991). Neuropathological stageing of Alzheimer-related changes. *Acta Neuropathol* **82,** 239–259.

Braak H & Braak E (1995). Staging of alzheimer's disease-related neurofibrillary

changes. *Neurobiol Aging* **16,** 271–278.

Bragin A, Jando G, Nadasdy Z, Hetke J, Wise K & Buzsaki G (1995). Gamma (40-100 Hz) oscillation in the hippocampus of the behaving rat. *J Neurosci*,**15**, 47-60

Brandon MP, Bogaard AR, Libby CP, Connerney MA, Gupta K & Hasselmo ME (2011). Reduction of theta rhythm dissociates grid cell spatial periodicity from directional tuning. *Science* **332,** 595–599.

Brenner RP, Ulrich RF, Spiker DG, Sclabassi RJ, Reynolds CF, Marin RS & Boller F (1986). Computerized EEG spectral analysis in elderly normal, demented and depressed subjects. *Electroencephalogr Clin Neurophysiol* **64,** 483–492.

Brioni JD, Decker MW, Gamboa LP, Izquierdo I & McGaugh JL (1990). Muscimol injections in the medial septum impair spatial learning. *Brain Res* **522,** 227–234.

Brown JT, Chin J, Leiser SC, Pangalos MN & Randall AD (2011). Altered intrinsic neuronal excitability and reduced Na(+) currents in a mouse model of Alzheimer's disease. *Neurobiol Aging* **32,** 2109.e1-e2109.e14.

Brown JT, Teriakidis A & Randall AD (2006). A pharmacological investigation of the role of GLUK5-containing receptors in kainate-driven hippocampal gamma band oscillations. *Neuropharmacology* **50,** 47–56.

Brown MW & Aggleton JP (2001). Recognition memory: What are the roles of the perirhinal cortex and hippocampus? *Nat Rev Neurosci* **2,** 51–61.

Brun VH, Leutgeb S, Wu H-Q, Schwarcz R, Witter MP, Moser EI & Moser M-B (2008*a*). Impaired Spatial Representation in CA1 after Lesion of Direct Input from Entorhinal Cortex. *Neuron* **57,** 290–302.

Brun VH, Otnæss MK, Molden S, Steffenach H-A, Witter MP, Moser M-B & Moser EI (2002). Place Cells and Place Recognition Maintained by Direct Entorhinal-Hippocampal Circuitry. *Science,* **296**, 2243-2246.

Brun VH, Solstad T, Kjelstrup KB, Fyhn M, Witter MP, Moser EI & Moser M-B (2008*b*). Progressive increase in grid scale from dorsal to ventral medial entorhinal cortex. *Hippocampus* **18,** 1200–1212.

Buckmaster CA, Eichenbaum H, Amaral DG, Suzuki WA & Rapp PR (2004). Entorhinal Cortex Lesions Disrupt the Relational Organization of Memory in Monkeys. *J Neurosci*, **24**, 9811-9825

Buckner RL (2004). Memory and Executive Function in Aging and AD. *Neuron* **44,** 195–208.

Buetfering C, Allen K & Monyer H (2014). Parvalbumin interneurons provide grid cell–driven recurrent inhibition in the medial entorhinal cortex. *Nat Neurosci* **17,** 710–718.

Burak Y, Fiete IR, Trappenberg T, Araujo I de & Wiggins C (2009). Accurate Path Integration in Continuous Attractor Network Models of Grid Cells ed. Sporns O. *PLoS Comput Biol* **5,** e1000291.

Burgess N, Barry C & O'Keefe J (2007). An oscillatory interference model of grid cell firing. *Hippocampus* **17,** 801–812.

Burwell R. & Hafeman D. (2003). Positional firing properties of postrhinal cortex neurons. *Neuroscience* **119,** 577–588.

Burwell RD, Shapiro ML, O'Malley MT & Eichenbaum H (1998). Positional firing properties of perirhinal cortex neurons. *Neuroreport* **9,** 3013–3018.

Bush D & Burgess N (2014). A hybrid oscillatory interference/continuous attractor network model of grid cell firing. *J Neurosci* **34,** 5065–5079.

Butler JL, Mendonca PRF, Robinson HPC & Paulsen O (2016). Intrinsic Cornu Ammonis Area 1 Theta-Nested Gamma Oscillations Induced by Optogenetic Theta Frequency Stimulation. *J Neurosci* **36,** 4155–4169.

Buzsáki G (2002). Theta Oscillations in the Hippocampus. *Neuron* **33,** 325–340.

Buzsáki G (2004). Large-scale recording of neuronal ensembles. *Nat Neurosci* **7,** 446–451.

Buzsáki G (2006). *Rhythms of the brain*. Oxford University Press.

Buzsáki G, Anastassiou CA & Koch C (2012). The origin of extracellular fields and currents--EEG, ECoG, LFP and spikes. *Nat Rev Neurosci* **13,** 407–420.

Buzsáki G & Draguhn A (2004). Neuronal oscillations in cortical networks. *Science* **304,** 1926–1929.

Buzsáki G & Moser EI (2013). Memory, navigation and theta rhythm in the hippocampal-entorhinal system. *Nat Neurosci* **16,** 130–138.

Buzsáki G, Stark E, Berényi A, Khodagholy D, Kipke DR, Yoon E & Wise KD (2015). Tools for probing local circuits: high-density silicon probes combined with optogenetics. *Neuron* **86,** 92–105.

Cacucci F, Yi M, Wills TJ, Chapman P & O'Keefe J (2008). Place cell firing correlates with memory deficits and amyloid plaque burden in Tg2576 Alzheimer mouse model. *Proc Natl Acad Sci* **105,** 7863–7868.

de Calignon A, Fox LM, Pitstick R, Carlson GA, Bacskai BJ, Spires-Jones TL & Hyman BT (2010). Caspase activation precedes and leads to tangles. *Nature* **464,** 1201–1204.

de Calignon A, Polydoro M, Suárez-Calvet M, William C, Adamowicz DH, Kopeikina KJ, Pitstick R, Sahara N, Ashe KH, Carlson GA, Spires-Jones TL & Hyman BT (2012). Propagation of tau pathology in a model of early Alzheimer's disease. *Neuron* **73,** 685–697.

Canolty RT, Edwards E, Dalal SS, Soltani M, Nagarajan SS, Kirsch HE, Berger MS, Barbaro NM & Knight RT (2006). High gamma power is phase-locked to theta oscillations in human neocortex. *Science* **313,** 1626–1628.

Canto CB, Wouterlood FG & Witter MP (2008). What does the anatomical organization of the entorhinal cortex tell us? *Neural Plast* **2008,** 381243.

Cardin JA, Carlén M, Meletis K, Knoblich U, Zhang F, Deisseroth K, Tsai L-H & Moore CI (2009). Driving fast-spiking cells induces gamma rhythm and controls sensory responses. *Nature* **459,** 663–667.

Van Cauter T, Poucet B & Save E (2008). Unstable CA1 place cell representation in rats with entorhinal cortex lesions. *Eur J Neurosci* **27,** 1933–1946.

Chadwick MJ, Jolly AEJ, Amos DP, Hassabis D & Spiers HJ (2015). A Goal Direction Signal in the Human Entorhinal/Subicular Region. *Curr Biol* **25,** 87–92.

Chen LL, Lin LH, Green EJ, Barnes CA & McNaughton BL (1994). Head-direction cells in the rat posterior cortex. I. Anatomical distribution and behavioral modulation. *Exp brain Res* **101,** 8–23.

Chen Z, Resnik E, McFarland JM, Sakmann B & Mehta MR (2011). Speed controls the amplitude and timing of the hippocampal gamma rhythm. *PLoS One* **6,** e21408.

Cheng J & Ji D (2013). Rigid firing sequences undermine spatial memory codes in a neurodegenerative mouse model. *Elife* **2,** e00647.

Cho J & Sharp PE (2001). Head direction, place, and movement correlates for cells in the rat retrosplenial cortex. *Behav Neurosci* **115,** 3–25.

Chrobak JJ & Buzsaki G (1998). Gamma Oscillations in the Entorhinal Cortex of the Freely Behaving Rat. *J Neurosci* **18,** 388–398.

Coben LA, Danziger W & Storandt M (1985). A longitudinal EEG study of mild senile dementia of Alzheimer type: changes at 1 year and at 2.5 years. *Electroencephalogr Clin Neurophysiol* **61,** 101–112.

Cohen RM, Rezai-Zadeh K, Weitz TM, Rentsendorj A, Gate D, Spivak I, Bholat Y, Vasilevko V, Glabe CG, Breunig JJ, Rakic P, Davtyan H, Agadjanyan MG, Kepe V, Barrio JR, Bannykh S, Szekely CA, Pechnick RN & Town T (2013). A transgenic Alzheimer rat with plaques, tau pathology, behavioral impairment, oligomeric aβ, and frank neuronal loss. *J Neurosci* **33,** 6245–6256.

Colgin LL, Denninger T, Fyhn M, Hafting T, Bonnevie T, Jensen O, Moser M-B & Moser EI (2009). Frequency of gamma oscillations routes flow of information in the hippocampus. *Nature* **462,** 353–357.

Colgin LL & Moser EI (2010). Gamma Oscillations in the Hippocampus. *Physiology*, **25**,319-329

Collins RC, Tearse RG & Lothman EW (1983). Functional anatomy of limbic seizures: Focal discharges from medial entorhinal cortex in rat. *Brain Res* **280,** 25–40.

Colom L V (2006). Septal networks: relevance to theta rhythm, epilepsy and Alzheimer's disease. *J Neurochem* **96,** 609–623.

Constantinescu AO, O'Reilly JX & Behrens TEJ (2016). Organizing conceptual knowledge in humans with a gridlike code. *Science,* **352,** 1464-1468.

Cook C, Dunmore JH, Murray ME, Scheffel K, Shukoor N, Tong J, Castanedes-

Casey M, Phillips V, Rousseau L, Penuliar MS, Kurti A, Dickson DW, Petrucelli L & Fryer JD (2014). Severe amygdala dysfunction in a MAPT transgenic mouse model of frontotemporal dementia. *Neurobiol Aging* **35,** 1769–1777.

Couey JJ, Witoelar A, Zhang S-J, Zheng K, Ye J, Dunn B, Czajkowski R, Moser M-B, Moser EI, Roudi Y & Witter MP (2013). Recurrent inhibitory circuitry as a mechanism for grid formation. *Nat Neurosci* **16,** 318–324.

Coyle J, Price D & DeLong M (1983). Alzheimer's disease: a disorder of cortical cholinergic innervation. *Science*, **219,** 1184-1190.

Crimins JL, Rocher AB & Luebke JI (2012). Electrophysiological changes precede morphological changes to frontal cortical pyramidal neurons in the rTg4510 mouse model of progressive tauopathy. *Acta Neuropathol* **124,** 777–795.

Cummings JL, Morstorf T & Zhong K (2014). Alzheimer's disease drug-development pipeline: few candidates, frequent failures. *Alzheimers Res Ther* **6,** 37.

Cunningham MO, Davies CH, Buhl EH, Kopell N & Whittington MA (2003). Gamma Oscillations Induced by Kainate Receptor Activation in the Entorhinal Cortex In Vitro. *J Neurosci* **23,** 9761–9769.

Cunningham MO, Halliday DM, Davies CH, Traub RD, Buhl EH & Whittington MA (2004). Coexistence of gamma and high-frequency oscillations in rat medial entorhinal cortex in vitro. *J Physiol* **559,** 347–353.

Cunningham MO, Hunt J, Middleton S, LeBeau FEN, Gillies MJ, Gillies MG, Davies CH, Maycox PR, Whittington MA & Racca C (2006). Region-specific reduction in entorhinal gamma oscillations and parvalbumin-immunoreactive neurons in animal models of psychiatric illness. *J Neurosci* **26,** 2767–2776.

Czigler B, Csikós D, Hidasi Z, Anna Gaál Z, Csibri É, Kiss É, Salacz P & Molnár M (2008). Quantitative EEG in early Alzheimer's disease patients — Power spectrum and complexity features. *Int J Psychophysiol* **68,** 75–80.

D'Antuono M, Köhling R, Ricalzone S, Gotman J, Biagini G & Avoli M (2010). Antiepileptic drugs abolish ictal but not interictal epileptiform discharges in

vitro. *Epilepsia* **51,** 423–431.

Darwin C (1873). Origin of Certain Instincts. *Nature* **7,** 417–418.

Dascalov D (1969). EEG findings in Alzheimer's disease. *Electroencephalogr Clin Neurophysiol* **27,** 447.

Davies P & Maloney AJF (1976). Selective loss of central cholinergic neurons in alzheimer's disease. *Lancet*; DOI: 10.1016/S0140-6736(76)91936-X.

Deller T, Martineq2 A, Nitsch R & Frotscherl M (1996). A Novel Entorhinal Projection to the Rat Dentate Gyrus: Direct Innervation of Proximal Dendrites and Cell Bodies of Granule Cells and GABAergic Neurons. *J Neurosci* **16,** 3322–3333.

Deng W, Aimone JB & Gage FH (2010). New neurons and new memories: how does adult hippocampal neurogenesis affect learning and memory? *Nat Rev Neurosci* **11,** 339–350.

Deshmukh SS & Knierim JJ (2011). Representation of non-spatial and spatial information in the lateral entorhinal cortex. *Front Behav Neurosci* **5,** 69.

Devenney E, Hornberger M, Irish M, Mioshi E, Burrell J, Tan R, Kiernan MC & Hodges JR (2014). Frontotemporal Dementia Associated With the *C9ORF72* Mutation. *JAMA Neurol* **71,** 331.

Dhillon A & Jones RS. (2000). Laminar differences in recurrent excitatory transmission in the rat entorhinal cortex in vitro. *Neuroscience* **99,** 413–422.

Dodson PD, Pastoll H & Nolan MF (2011). Dorsal-ventral organization of theta-like activity intrinsic to entorhinal stellate neurons is mediated by differences in stochastic current fluctuations. *J Physiol* **589,** 2993–3008.

Doeller CF, Barry C & Burgess N (2010). Evidence for grid cells in a human memory network. *Nature* **463,** 657–661.

Domnisoru C, Kinkhabwala AA & Tank DW (2013). Membrane potential dynamics of grid cells. *Nature* **495,** 199–204.

Doody RS (2003). Current treatments for Alzheimer's disease: cholinesterase inhibitors. *J Clin Psychiatry* **64 Suppl 9,** 11–17.

Dragoi G, Buzsáki G, Buzsaki G, Lipa P, O'Keefe J, Sun LD, Kato A, Carr CA,

Johnston D, Wilson MA & Tonegawa S (2006). Temporal encoding of place sequences by hippocampal cell assemblies. *Neuron* **50,** 145–157.

Driver JE, Racca C, Cunningham MO, Towers SK, Davies CH, Whittington MA & LeBeau FEN (2007). Impairment of hippocampal gamma-frequency oscillations in vitro in mice overexpressing human amyloid precursor protein (APP). *Eur J Neurosci* **26,** 1280–1288.

Du F, Eid T, Lothman E, Kohler C & Schwarcz R (1995). Preferential neuronal loss in layer III of the medial entorhinal cortex in rat models of temporal lobe epilepsy. *J Neurosci* **15,** 6301–6313.

Du F, Whetsell WO, Abou-Khalil B, Blumenkopf B, Lothman EW & Schwarcz R (1993). Preferential neuronal loss in layer III of the entorhinal cortex in patients with temporal lobe epilepsy. *Epilepsy Res* **16,** 223–233.

Dudchenko PA (2004). An overview of the tasks used to test working memory in rodents. *Neurosci Biobehav Rev* **28,** 699–709.

Duffy AM, Morales-Corraliza J, Bermudez-Hernandez KM, Schaner MJ, Magagna-Poveda A, Mathews PM & Scharfman HE (2015). Entorhinal cortical defects in Tg2576 mice are present as early as 2-4 months of age. *Neurobiol Aging* **36,** 134–148.

Dumanchin C, Camuzat A, Campion D, Verpillat P, Hannequin D, Dubois B, Saugier-Veber P, Martin C, Penet C, Charbonnier F, Agid Y, Frebourg T & Brice A (1998). Segregation of a missense mutation in the microtubule-associated protein tau gene with familial frontotemporal dementia and parkinsonism. *Hum Mol Genet* **7,** 1825–1829.

Dunkin JJ, Leuchter AF, Newton TF & Cook IA (1994). Reduced EEG coherence in dementia: State or trait marker? *Biol Psychiatry* **35,** 870–879.

Ego-Stengel V & Wilson MA (2009). Disruption of ripple-associated hippocampal activity during rest impairs spatial learning in the rat. *Hippocampus* **20,** 1-10

Elder GA, Gama Sosa MA & De Gasperi R (2010). Transgenic mouse models of Alzheimer's disease. *Mt Sinai J Med* **77,** 69–81.

Engel AK, Fries P & Singer W (2001). Dynamic predictions: Oscillations and synchrony in top–down processing. *Nat Rev Neurosci* **2,** 704–716.

Etienne AS & Jeffery KJ (2004). Path integration in mammals. *Hippocampus* **14,** 180–192.

Fanselow MS & Dong H-W (2010). Are the dorsal and ventral hippocampus functionally distinct structures? *Neuron* **65,** 7–19.

Fell J, Klaver P, Lehnertz K, Grunwald T, Schaller C, Elger CE & Fernández G (2001). Human memory formation is accompanied by rhinal-hippocampal coupling and decoupling. *Nat Neurosci* **4,** 1259–1264.

Ferri CP, Prince M, Brayne C, Brodaty H, Fratiglioni L, Ganguli M, Hall K, Hasegawa K, Hendrie H, Huang Y, Jorm A, Mathers C, Menezes PR, Rimmer E & Scazufca M (2005). Global prevalence of dementia: a Delphi consensus study. *Lancet* **366,** 2112–2117.

Fisahn A, Pike FG, Buhl EH & Paulsen O (1998). Cholinergic induction of network oscillations at 40 Hz in the hippocampus in vitro. *Nature* **394,** 186–189.

Forsyth LH, Witton J, Brown JT, Randall AD, Jones MW, Forsyth LH, Witton J, Brown JT, Randall AD & Jones MW (2012). In Vitro and In Vivo Recording of Local Field Potential Oscillations in Mouse Hippocampus. In *Current Protocols in Mouse Biology*, pp. 273–294. John Wiley & Sons, Inc., Hoboken, NJ, USA.

Francis PT, Palmer AM, Snape M & Wilcock GK (1999). The cholinergic hypothesis of Alzheimer's disease: a review of progress. *J Neurol Neurosurg Psychiatry* **66,** 137–147.

Frank LM, Brown EN & Wilson M (2000). Trajectory Encoding in the Hippocampus and Entorhinal Cortex. *Neuron* **27,** 169–178.

French JA, Williamson PD, Thadani VM, Darcey TM, Mattson RH, Spencer SS & Spencer DD (1993). Characteristics of medial temporal lobe epilepsy: I. Results of history and physical examination. *Ann Neurol* **34,** 774–780.

Fried I, MacDonald KA & Wilson CL (1997). Single Neuron Activity in Human Hippocampus and Amygdala during Recognition of Faces and Objects. *Neuron* **18,** 753–765.

Fries P (2005). A mechanism for cognitive dynamics: neuronal communication through neuronal coherence. *Trends Cogn Sci* **9,** 474–480.

Fu H, Rodriguez GA, Herman M, Emrani S, Nahmani E, Barrett G, Figueroa HY, Goldberg E, Hussaini SA & Duff KE (2017). Tau Pathology Induces Excitatory Neuron Loss, Grid Cell Dysfunction, and Spatial Memory Deficits Reminiscent of Early Alzheimer's Disease. *Neuron* **93,** 533–541.e5.

Fuchs EC, Neitz A, Pinna R, Melzer S, Caputi A & Monyer H (2015). Local and Distant Input Controlling Excitation in Layer II of the Medial Entorhinal Cortex. *Neuron* **89,** 194–208.

Fuhrmann F, Justus D, Sosulina L, Kaneko H, Beutel T, Friedrichs D, Schoch S, Schwarz MK, Fuhrmann M & Remy S (2015). Locomotion, Theta Oscillations, and the Speed-Correlated Firing of Hippocampal Neurons Are Controlled by a Medial Septal Glutamatergic Circuit. *Neuron* **86,** 1253–1264.

Fuhs MC & Touretzky DS (2006). A Spin Glass Model of Path Integration in Rat Medial Entorhinal Cortex. *J Neurosci*. **26**,4266-4276

Fyhn M, Hafting T, Witter MP, Moser EI & Moser M-B (2008). Grid cells in mice. *Hippocampus* **18,** 1230–1238.

Fyhn M, Molden S, Witter MP, Moser EI & Moser M-B (2004). Spatial representation in the entorhinal cortex. *Science* **305,** 1258–1264.

Games D et al. (1995). Alzheimer-type neuropathology in transgenic mice overexpressing V717F β-amyloid precursor protein. *Nature* **373,** 523–527.

García-Cabrero AM, Guerrero-López R, Giráldez BG, Llorens-Martín M, Avila J, Serratosa JM & Sánchez MP (2013). Hyperexcitability and epileptic seizures in a model of frontotemporal dementia. *Neurobiol Dis* **58,** 200–208.

Garden DLF, Dodson PD, O'Donnell C, White MD & Nolan MF (2008). Tuning of synaptic integration in the medial entorhinal cortex to the organization of grid cell firing fields. *Neuron* **60,** 875–889.

Giacobini E & Gold G (2013). Alzheimer disease therapy—moving from amyloid-β to tau. *Nat Rev Neurol* **9,** 677–686.

Giocomo LM & Hasselmo ME (2008). Time constants of h current in layer II stellate cells differ along the dorsal to ventral axis of medial entorhinal cortex. *J Neurosci* **28,** 9414–9425.

Giocomo LM & Hasselmo ME (2009). Knock-out of HCN1 subunit flattens dorsal-

ventral frequency gradient of medial entorhinal neurons in adult mice. *J Neurosci* **29,** 7625–7630.

Giocomo LM, Hussaini SA, Zheng F, Kandel ER, Moser M-B & Moser EI (2011*a*). Grid Cells Use HCN1 Channels for Spatial Scaling. *Cell* **147,** 1159–1170.

Giocomo LM, Stensola T, Bonnevie T, Van Cauter T, Moser M-B & Moser EI (2014). Topography of head direction cells in medial entorhinal cortex. *Curr Biol* **24,** 252–262.

Giocomo LM, Zilli EA, Fransén E & Hasselmo ME (2007). Temporal frequency of subthreshold oscillations scales with entorhinal grid cell field spacing. *Science* **315,** 1719–1722.

Giocomo LMM, Moser M-B & Moser EII (2011*b*). Computational models of grid cells. *Neuron* **71,** 589–603.

Girardeau G, Benchenane K, Wiener SI, Buzsáki G & Zugaro MB (2009). Selective suppression of hippocampal ripples impairs spatial memory. *Nat Neurosci* **12,** 1222–1223.

Gnatkovsky V, Librizzi L, Trombin F & de Curtis M (2008). Fast activity at seizure onset is mediated by inhibitory circuits in the entorhinal cortex in vitro. *Ann Neurol* **64,** 674–686.

Gomez-Isla T, Price JL, McKeel Jr. DW, Morris JC, Growdon JH & Hyman BT (1996). Profound Loss of Layer II Entorhinal Cortex Neurons Occurs in Very Mild Alzheimer''s Disease. *J Neurosci* **16,** 4491–4500.

Gonzalez-Sulser A, Parthier D, Candela A, McClure C, Pastoll H, Garden D, Sürmeli G & Nolan MF (2014). GABAergic Projections from the Medial Septum Selectively Inhibit Interneurons in the Medial Entorhinal Cortex. *J Neurosci*. **34**, 16739-16745

Gonzalez-Sulser A, Wang J, Motamedi GK, Avoli M, Vicini S & Dzakpasu R (2011). The 4-aminopyridine in vitro epilepsy model analyzed with a perforated multi-electrode array. *Neuropharmacology* **60,** 1142–1153.

Goodridge JP, Dudchenko PA, Worboys KA, Golob EJ & Taube JS (1998). Cue control and head direction cells. *Behav Neurosci* **112,** 749–761.

Götz J, Ittner A & Ittner LM (2012). Tau-targeted treatment strategies in

Alzheimer's disease. *Br J Pharmacol* **165,** 1246–1259.

Götz J & Ittner LM (2008). Animal models of Alzheimer's disease and frontotemporal dementia. *Nat Rev Neurosci* **9,** 532–544.

Gray CM, Maldonado PE, Wilson M & McNaughton B (1995). Tetrodes markedly improve the reliability and yield of multiple single-unit isolation from multi-unit recordings in cat striate cortex. *J Neurosci Methods* **63,** 43–54.

Gulyás-Kovács A, Dóczi J, Tarnawa I, Détári L, Banczerowski-Pelyhe I & Világi I (2002). Comparison of spontaneous and evoked epileptiform activity in three in vitro epilepsy models. *Brain Res* **945,** 174–180.

Hafting T, Fyhn M, Bonnevie T, Moser M-B & Moser EI (2008). Hippocampus-independent phase precession in entorhinal grid cells. *Nature* **453,** 1248–1252.

Hafting T, Fyhn M, Molden S, Moser M-BB & Moser EI (2005). Microstructure of a spatial map in the entorhinal cortex. *Nature* **436,** 801–806.

Hájos N, Pálhalmi J, Mann EO, Németh B, Paulsen O & Freund TF (2004). Spike Timing of Distinct Types of GABAergic Interneuron during Hippocampal Gamma Oscillations In Vitro. *J Neurosci*. **35,** 203-225.

Hakami T, Jones NC, Tolmacheva EA, Gaudias J, Chaumont J, Salzberg M, O'Brien TJ & Pinault D (2009). NMDA Receptor Hypofunction Leads to Generalized and Persistent Aberrant γ Oscillations Independent of Hyperlocomotion and the State of Consciousness ed. Hashimoto K. *PLoS One* **4,** e6755.

Hales JB, Schlesiger MI, Leutgeb JK, Squire LR, Leutgeb S & Clark RE (2014). Medial Entorhinal Cortex Lesions Only Partially Disrupt Hippocampal Place Cells and Hippocampus-Dependent Place Memory. *Cell Rep* **9,** 893–901.

Hall AM & Roberson ED (2012). Mouse models of Alzheimer's disease. *Brain Res Bull* **88,** 3–12.

Hanger DP, Anderton BH & Noble W (2009). Tau phosphorylation: the therapeutic challenge for neurodegenerative disease. *Trends Mol Med* **15,** 112–119.

Hangya B, Borhegyi Z, Szilágyi N, Freund TF & Varga V (2009). GABAergic

Neurons of the Medial Septum Lead the Hippocampal Network during Theta Activity. *J Neurosci*. **29**, 8094-8102

Harada CN, Natelson Love MC & Triebel KL (2013). Normal cognitive aging. *Clin Geriatr Med* **29,** 737–752.

Hargreaves EL, Rao G, Lee I & Knierim JJ (2005). Major Dissociation Between Medial and Lateral Entorhinal Input to Dorsal Hippocampus. *Science*, **308**, 1792-4.

Harris JA, Koyama A, Maeda S, Ho K, Devidze N, Dubal DB, Yu G-Q, Masliah E & Mucke L (2012). Human P301L-mutant tau expression in mouse entorhinal-hippocampal network causes tau aggregation and presynaptic pathology but no cognitive deficits. *PLoS One* **7,** e45881.

Harris KD, Csicsvari J, Hirase H, Dragoi G & Buzsáki G (2003). Organization of cell assemblies in the hippocampus. *Nature* **424,** 552–556.

Hartley T & Lever C (2014). Know Your Limits: The Role of Boundaries in the Development of Spatial Representation. *Neuron* **82,** 1–3.

Hasselmo ME (2005). What is the function of hippocampal theta rhythm?—Linking behavioral data to phasic properties of field potential and unit recording data. *Hippocampus* **15,** 936–949.

Hasselmo ME, Giocomo LM & Zilli EA (2007). Grid cell firing may arise from interference of theta frequency membrane potential oscillations in single neurons. *Hippocampus* **17,** 1252–1271.

Hebb DO (1949). *The organization of behavior : a neuropsychological theory*. L. Erlbaum Associates.

Heys JG & Hasselmo ME (2012). Neuromodulation of I(h) in layer II medial entorhinal cortex stellate cells: a voltage-clamp study. *J Neurosci* **32,** 9066–9072.

Hinman JR, Brandon MP, Climer JR, Chapman GW & Hasselmo ME (2016). Multiple Running Speed Signals in Medial Entorhinal Cortex. *Neuron* **91,** 666–679.

Holcomb L, Gordon MN, McGowan E, Yu X, Benkovic S, Jantzen P, Wright K, Saad I, Mueller R, Morgan D, Sanders S, Zehr C, O'Campo K, Hardy J,

Prada C-M, Eckman C, Younkin S, Hsiao K & Duff K (1998). Accelerated Alzheimer-type phenotype in transgenic mice carrying both mutant amyloid precursor protein and presenilin 1 transgenes. *Nat Med* **4,** 97–100.

Holmes BB & Diamond MI (2014). Prion-like properties of Tau protein: the importance of extracellular Tau as a therapeutic target. *J Biol Chem* **289,** 19855–19861.

Hoover BR, Reed MN, Su J, Penrod RD, Kotilinek LA, Grant MK, Pitstick R, Carlson GA, Lanier LM, Yuan L-L, Ashe KH & Liao D (2010). Tau Mislocalization to Dendritic Spines Mediates Synaptic Dysfunction Independently of Neurodegeneration. *Neuron* **68,** 1067–1081.

Horner AJ, Bisby JA, Zotow E, Bush D & Burgess N (2016). Grid-like Processing of Imagined Navigation. *Curr Biol* **26,** 842–847.

Hort J, Laczó J, Vyhnálek M, Bojar M, Bures J & Vlcek K (2007). Spatial navigation deficit in amnestic mild cognitive impairment. *Proc Natl Acad Sci U S A* **104,** 4042–4047.

Hsiao K, Chapman P, Nilsen S, Eckman C, Harigaya Y, Younkin S, Yang F & Cole G (1996). Correlative Memory Deficits, A beta Elevation, and Amyloid Plaques in Transgenic Mice. *Science* **274,** 99–102.

Hubel DH (1957). Tungsten Microelectrode for Recording from Single Units. *Science* **125**, 549-50.

Hughes JR, Shanmugham S, Wetzel LC, Bellur S & Hughes CA (1989). The relationship between EEG changes and cognitive functions in dementia: a study in a VA population. *Clin Electroencephalogr* **20,** 77–85.

Hussaini SA, Kempadoo KA, Thuault SJ, Siegelbaum SA & Kandel ER (2011). Increased size and stability of CA1 and CA3 place fields in HCN1 knockout mice. *Neuron* **72,** 643–653.

Hutton M et al. (1998). Association of missense and 5|[prime]|-splice-site mutations in tau with the inherited dementia FTDP-17. *Nature* **393,** 702–705.

Huxter J, Burgess N & O'Keefe J (2003). Independent rate and temporal coding in hippocampal pyramidal cells. *Nature* **425,** 828–832.

Hyman JM, Zilli EA, Paley AM & Hasselmo ME (2005). Medial prefrontal cortex

cells show dynamic modulation with the hippocampal theta rhythm dependent on behavior. *Hippocampus* **15,** 739–749.

Igarashi KM, Lu L, Colgin LL, Moser M-B & Moser EI (2014). Coordination of entorhinal–hippocampal ensemble activity during associative learning. *Nature* **510,** 143–147.

Jackson JS, Witton J, Johnson JD, Ahmed Z, Ward M, Randall AD, Hutton ML, Isaac JT, O?Neill MJ & Ashby MC (2017). Altered Synapse Stability in the Early Stages of Tauopathy. *Cell Rep* **18,** 3063–3068.

Jacobs J et al. (2016). *Direct Electrical Stimulation of the Human Entorhinal Region and Hippocampus Impairs Memory*. Neuron, **92**, 983-990

Jacobs J, Weidemann CT, Miller JF, Solway A, Burke JF, Wei X-X, Suthana N, Sperling MR, Sharan AD, Fried I & Kahana MJ (2013). Direct recordings of grid-like neuronal activity in human spatial navigation. *Nat Neurosci* **16,** 1188–1190.

Jacobson TK, Howe MD, Schmidt B, Hinman JR, Escabí MA & Markus EJ (2013). Hippocampal theta, gamma, and theta-gamma coupling: effects of aging, environmental change, and cholinergic activation. *J Neurophysiol*. **109**, 1852-1865

Jadhav SP, Kemere C, German PW & Frank LM (2012). Awake Hippocampal Sharp-Wave Ripples Support Spatial Memory. *Science* **336**, 1454-1458.

Jankowski MM, Islam MN, Wright NF, Vann SD, Erichsen JT, Aggleton JP & O'Mara SM (2014). Nucleus reuniens of the thalamus contains head direction cells. *Elife*; DOI: 10.7554/eLife.03075.

Jeewajee A, Barry C, O'Keefe J & Burgess N (2008*a*). Grid cells and theta as oscillatory interference: electrophysiological data from freely moving rats. *Hippocampus* **18,** 1175–1185.

Jeewajee A, Lever C, Burton S, O'Keefe J & Burgess N (2008*b*). Environmental novelty is signaled by reduction of the hippocampal theta frequency. *Hippocampus* **18,** 340–348.

Jensen O & Colgin LL (2007). Cross-frequency coupling between neuronal oscillations. *Trends Cogn Sci* **11,** 267–269.

Jensen O & Lisman JE (1998). An Oscillatory Short-Term Memory Buffer Model Can Account for Data on the Sternberg Task. *J Neurosci*. **18**,10688-10699

Jeong J (2004). EEG dynamics in patients with Alzheimer's disease. *Clin Neurophysiol* **115,** 1490–1505.

Jinno S, Klausberger T, Marton LF, Dalezios Y, Roberts JDB, Fuentealba P, Bushong EA, Henze D, Buzsáki G & Somogyi P (2007). Neuronal diversity in GABAergic long-range projections from the hippocampus. *J Neurosci* **27,** 8790–8804.

Jog M., Connolly C., Kubota Y, Iyengar D., Garrido L, Harlan R & Graybiel A. (2002). Tetrode technology: advances in implantable hardware, neuroimaging, and data analysis techniques. *J Neurosci Methods* **117,** 141–152.

Jones MW, Wilson MA, Tsien J, Tonegawa S & Wilson M (2005). Theta Rhythms Coordinate Hippocampal–Prefrontal Interactions in a Spatial Memory Task ed. Morris R. *PLoS Biol* **3,** e402.

Jones RS & Heinemann U (1988). Synaptic and intrinsic responses of medical entorhinal cortical cells in normal and magnesium-free medium in vitro. *J Neurophysiol*. **59**, 1476-96.

Jul P, Volbracht C, de Jong IEM, Helboe L, Elvang AB & Pedersen JT (2015). Hyperactivity with Agitative-Like Behavior in a Mouse Tauopathy Model ed. Sahara N. *J Alzheimer's Dis* **49,** 783–795.

Jung M, Wiener S & McNaughton B (1994). Comparison of spatial firing characteristics of units in dorsal and ventral hippocampus of the rat. *J Neurosci*. **14**, 7347-7356

Justus D, Dalügge D, Bothe S, Fuhrmann F, Hannes C, Kaneko H, Friedrichs D, Sosulina L, Schwarz I, Elliott DA, Schoch S, Bradke F, Schwarz MK & Remy S (2016). Glutamatergic synaptic integration of locomotion speed via septoentorhinal projections. *Nat Neurosci* **20,** 16–19.

Kadir SN, Goodman DFM & Harris KD (2014). High-dimensional cluster analysis with the masked EM algorithm. *Neural Comput* **26,** 2379–2394.

Karlsson MP & Frank LM (2009). Awake replay of remote experiences in the

hippocampus. *Nat Neurosci* **12,** 913–918.

Kemere C, Carr MF, Karlsson MP & Frank LM (2013). Rapid and continuous modulation of hippocampal network state during exploration of new places. *PLoS One* **8,** e73114.

Kerr KM, Agster KL, Furtak SC & Burwell RD (2007). Functional neuroanatomy of the parahippocampal region: The lateral and medial entorhinal areas. *Hippocampus* **17,** 697–708.

Khan UA, Liu L, Provenzano FA, Berman DE, Profaci CP, Sloan R, Mayeux R, Duff KE & Small SA (2014). Molecular drivers and cortical spread of lateral entorhinal cortex dysfunction in preclinical Alzheimer's disease. *Nat Neurosci* **17,** 304–311.

Kitamura T, Pignatelli M, Suh J, Kohara K, Yoshiki A, Abe K & Tonegawa S (2014). Island cells control temporal association memory. *Science* **343,** 896–901.

Klein AS, Donoso JR, Kempter R, Schmitz D & Beed P (2016). Early Cortical Changes in Gamma Oscillations in Alzheimer's Disease. *Front Syst Neurosci* **10,** 83.

Klimesch W (1999). EEG alpha and theta oscillations reflect cognitive and memory performance: a review and analysis. *Brain Res Rev* **29,** 169–195.

Kloosterman F, van Haeften T & Lopes da Silva FH (2004). Two reentrant pathways in the hippocampal-entorhinal system. *Hippocampus* **14,** 1026–1039.

Kobayashi M, Wen X & Buckmaster PS (2003). Reduced Inhibition and Increased Output of Layer II Neurons in the Medial Entorhinal Cortex in a Model of Temporal Lobe Epilepsy. *J Neurosci* **23,** 8471–8479.

Kocsis B (2012). Differential Role of NR2A and NR2B Subunits in N-Methyl-D-Aspartate Receptor Antagonist-Induced Aberrant Cortical Gamma Oscillations. *Biol Psychiatry* **71,** 987–995.

Koenig J, Linder AN, Leutgeb JK & Leutgeb S (2011). The Spatial Periodicity of Grid Cells Is Not Sustained During Reduced Theta Oscillations. *Science* **332**, 592-595.

Kohling R, Vreugdenhil M, Bracci E & Jefferys JGR (2000). Ictal Epileptiform Activity Is Facilitated by Hippocampal GABAA Receptor-Mediated Oscillations. *J Neurosci* **20,** 6820–6829.

Kondo H & Zaborszky L (2016). Topographic organization of the basal forebrain projections to the perirhinal, postrhinal, and entorhinal cortex in rats. *J Comp Neurol*, **524**, 2503-15.

Kopeikina KJ, Polydoro M, Tai H-C, Yaeger E, Carlson GA, Pitstick R, Hyman BT & Spires-Jones TL (2013). Synaptic alterations in the rTg4510 mouse model of tauopathy. *J Comp Neurol* **521,** 1334–1353.

Kowalski JW, Gawel M, Pfeffer A & Barcikowska M (2001). The diagnostic value of EEG in Alzheimer disease: correlation with the severity of mental impairment. *J Clin Neurophysiol* **18,** 570–575.

Kropff E, Carmichael JE, Moser M-B & Moser EI (2015). Speed cells in the medial entorhinal cortex. *Nature* **523**, 419-424

Kuchibhotla K V, Wegmann S, Kopeikina KJ, Hawkes J, Rudinskiy N, Andermann ML, Spires-Jones TL, Bacskai BJ & Hyman BT (2014). Neurofibrillary tangle-bearing neurons are functionally integrated in cortical circuits in vivo. *Proc Natl Acad Sci U S A* **111,** 510–514.

Kunz L, Schröder TN, Lee H, Montag C, Lachmann B, Sariyska R, Reuter M, Stirnberg R, Stöcker T, Messing-Floeter PC, Fell J, Doeller CF & Axmacher N (2015). Reduced grid-cell–like representations in adults at genetic risk for Alzheimer's disease. *Science, **350**, 430-3* .

Laczó J, Andel R, Vlček K, Macoška V, Vyhnálek M, Tolar M, Bojar M & Hort J (2011). Spatial navigation and APOE in amnestic mild cognitive impairment. *Neurodegener Dis* **8,** 169–177.

Langston RF, Ainge JA, Couey JJ, Canto CB, Bjerknes TL, Witter MP, Moser EI & Moser M-B (2010). Development of the Spatial Representation System in the Rat. *Science* **328**,1576-80

Lee AK, Wilson MA, Amaral DG, Beck PD, Laubach M, Chapin JK, Kim J, Biggs SJ, Srinivasan MA & Nicolelis MA (2002). Memory of sequential experience in the hippocampus during slow wave sleep. *Neuron* **36,** 1183–1194.

Lee MG, Chrobak JJ, Sik A, Wiley RG & Buzsáki G (1994). Hippocampal theta activity following selective lesion of the septal cholinergic systeM. *Neuroscience* **62,** 1033–1047.

Leonard B, Amaral D, Squire L & Zola-Morgan S (1995). Transient memory impairment in monkeys with bilateral lesions of the entorhinal cortex. *J Neurosci*. **15**, 5637-5659

Leung LS & Yu H-W (1998). Theta-Frequency Resonance in Hippocampal CA1 Neurons In Vitro Demonstrated by Sinusoidal Current Injection. *J Neurophysiol*. **79**, 592-6.

Leutgeb S, Leutgeb JK, Barnes CA, Moser EI, McNaughton BL & Moser M-B (2005*a*). Independent Codes for Spatial and Episodic Memory in Hippocampal Neuronal Ensembles. *Science* **309**, 619-23.

Leutgeb S, Leutgeb JK, Moser M-B & Moser EI (2005*b*). Place cells, spatial maps and the population code for memory. *Curr Opin Neurobiol* **15,** 738–746.

Leutgeb S, Ragozzino K. & Mizumori SJ. (2000). Convergence of head direction and place information in the CA1 region of hippocampus. *Neuroscience* **100,** 11–19.

Lever C, Burton S, Jeewajee A, O'Keefe J & Burgess N (2009). Boundary vector cells in the subiculum of the hippocampal formation. *J Neurosci* **29,** 9771–9777.

Lévesque M, Herrington R, Hamidi S & Avoli M (2016). Interneurons spark seizure-like activity in the entorhinal cortex. *Neurobiol Dis* **87,** 91–101.

Levisohn LF & Isacson O (1991). Excitotoxic lesions of the rat entorhinal cortex. Effects of selective neuronal damage on acquisition and retention of a non-spatial reference memory task. *Brain Res* **564,** 230–244.

Lisman J (2005). The theta/gamma discrete phase code occuring during the hippocampal phase precession may be a more general brain coding scheme. *Hippocampus* **15,** 913–922.

Lisman J & Idiart M (1995). Storage of 7 +/- 2 short-term memories in oscillatory subcycles. *Science (80-)* **267,** 1512–1515.

Lithfous S, Dufour A & Després O (2013). Spatial navigation in normal aging and

the prodromal stage of Alzheimer's disease: Insights from imaging and behavioral studies. *Ageing Res Rev* **12,** 201–213.

Liu L, Drouet V, Wu JW, Witter MP, Small SA, Clelland C & Duff K (2012). Trans-synaptic spread of tau pathology in vivo. *PLoS One* **7,** e31302.

Losi G, Cammarota M, Chiavegato A, Gomez-Gonzalo M & Carmignoto G (2010). A new experimental model of focal seizures in the entorhinal cortex. *Epilepsia* **51,** 1493–1502.

Lu X & Bilkey DK (2009). The velocity-related firing property of hippocampal place cells is dependent on self-movement. *Hippocampus* **20,** NA-NA.

Lu Y, Zhong C, Wang L, Wei P, He W, Huang K, Zhang Y, Zhan Y, Feng G & Wang L (2016). Optogenetic dissection of ictal propagation in the hippocampal–entorhinal cortex structures. *Nat Commun* **7,** 10962.

Mangialasche F, Solomon A, Winblad B, Mecocci P & Kivipelto M (2010). Alzheimer's disease: clinical trials and drug development. *Lancet Neurol* **9,** 702–716.

Marson AG, Kadir ZA, Hutton JL & Chadwick DW (1997). The New Antiepileptic Drugs: A Systematic Review of Their Efficacy and Tolerability. *Epilepsia* **38,** 859–880.

Masters CL, Bateman R, Blennow K, Rowe CC, Sperling RA & Cummings JL (2015). Alzheimer's disease. *Nat Rev Dis Prim* **1,** 15056.

Maurer AP, VanRhoads SR, Sutherland GR, Lipa P & McNaughton BL (2005). Self-motion and the origin of differential spatial scaling along the septo-temporal axis of the hippocampus. *Hippocampus* **15,** 841–852.

McDougal RA, Morse TM, Carnevale T, Marenco L, Wang R, Migliore M, Miller PL, Shepherd GM & Hines ML (2017). Twenty years of ModelDB and beyond: building essential modeling tools for the future of neuroscience. *J Comput Neurosci* **42,** 1–10.

McFarland WL, Teitelbaum H & Hedges EK (1975). Relationship between hippocampal theta activity and running speed in the rat. *J Comp Physiol Psychol* **88,** 324–328.

McGowan E, Eriksen J & Hutton M (2006). A decade of modeling Alzheimer's

disease in transgenic mice. *Trends Genet* **22,** 281–289.

McNally JM, McCarley RW, McKenna JT, Yanagawa Y & Brown RE (2011). Complex receptor mediation of acute ketamine application on in vitro gamma oscillations in mouse prefrontal cortex: modeling gamma band oscillation abnormalities in schizophrenia. *Neuroscience* **199,** 51–63.

McNaughton BL, Barnes CA, Gerrard JL, Gothard K, Jung MW, Knierim JJ, Kudrimoti H, Qin Y, Skaggs WE, Suster M & Weaver KL (1996). Deciphering the hippocampal polyglot: the hippocampus as a path integration system. *J Exp Biol*. **199**: 173-185;

McNaughton BL, Barnes CA, Meltzer J & Sutherland RJ (1989). Hippocampal granule cells are necessary for normal spatial learning but not for spatially-selective pyramidal cell discharge. *Exp brain Res* **76,** 485–496.

McNaughton BL, Barnes CA & O'Keefe J (1983*a*). The contributions of position, direction, and velocity to single unit activity in the hippocampus of freely-moving rats. *Exp Brain Res* **52,** 41–49.

McNaughton BL, Battaglia FP, Jensen O, Moser EI & Moser M-BB (2006). Path integration and the neural basis of the "cognitive map". *Nat Rev Neurosci* **7,** 663–678.

McNaughton BL, O'Keefe J & Barnes CA (1983*b*). The stereotrode: A new technique for simultaneous isolation of several single units in the central nervous system from multiple unit records. *J Neurosci Methods* **8,** 391–397.

Melzer S, Michael M, Caputi A, Eliava M, Fuchs EC, Whittington MA & Monyer H (2012). Long-Range–Projecting GABAergic Neurons Modulate Inhibition in Hippocampus and Entorhinal Cortex. *Science* **335,** 1506-1510

Miettinen M, Koivisto E, Riekkinen P & Miettinen R (1996). Coexistence of parvalbumin and GABA in nonpyramidal neurons of the rat entorhinal cortex. *Brain Res* **706,** 113–122.

Minkeviciene R, Rheims S, Dobszay MB, Zilberter M, Hartikainen J, Fulop L, Penke B, Zilberter Y, Harkany T, Pitkanen A & Tanila H (2009). Amyloid -Induced Neuronal Hyperexcitability Triggers Progressive Epilepsy. *J Neurosci* **29,** 3453–3462.

Mirra SS, Murrell JR, Gearing M, Spillantini MG, Goedert M, Crowther RA, Levey AI, Jones R, Green J, Shoffner JM, Wainer BH, Schmidt ML, Trojanowski JQ & Ghetti B (1999). Tau Pathology in a Family with Dementia and a P301L Mutation in Tau. *J Neuropathol Exp Neurol* **58,** 335–345.

Mitchell S, Rawlins J, Steward O & Olton D (1982). Medial septal area lesions disrupt theta rhythm and cholinergic staining in medial entorhinal cortex and produce impaired radial arm maze behavior in rats. *J Neurosci*. **2,** 292-302.

Mitchell SJ & Ranck JB (1980). Generation of theta rhythm in medial entorhinal cortex of freely moving rats. *Brain Res* **189,** 49–66.

Mitra P & Bokil H (2008). *Observed brain dynamics*. Oxford University Press.

Mittelstaedt M-L & Mittelstaedt H (1980). Homing by path integration in a mammal. *Naturwissenschaften* **67,** 566–567.

Mokrisova I, Laczo J, Andel R, Gazova I, Vyhnalek M, Nedelska Z, Levcik D, Cerman J, Vlcek K & Hort J (2016). Real-space path integration is impaired in Alzheimer's disease and mild cognitive impairment. *Behav Brain Res* **307,** 150–158.

Monacelli AM, Cushman LA, Kavcic V & Duffy CJ (2003). Spatial disorientation in Alzheimer's disease: the remembrance of things passed. *Neurology* **61,** 1491–1497.

Montgomery SM & Buzsáki G (2007). Gamma oscillations dynamically couple hippocampal CA3 and CA1 regions during memory task performance. *Proc Natl Acad Sci U S A* **104,** 14495–14500.

Moser EI, Kropff E & Moser M-B (2008). Place cells, grid cells, and the brain's spatial representation system. *Annu Rev Neurosci* **31,** 69–89.

Moser EI, Roudi Y, Witter MP, Kentros C, Bonhoeffer T & Moser M-B (2014). Grid cells and cortical representation. *Nat Rev Neurosci* **15,** 466–481.

Muessig L, Hauser J, Wills TJ & Cacucci F (2015). A Developmental Switch in Place Cell Accuracy Coincides with Grid Cell Maturation. *Neuron* **86,** 1167–1173.

Muller R & Kubie J (1987). The effects of changes in the environment on the spatial firing of hippocampal complex-spike cells. *J Neurosci*. **7**, 1951-1968

Naber PA, Lopes da Silva FH & Witter MP (2001). Reciprocal connections between the entorhinal cortex and hippocampal fields CA1 and the subiculum are in register with the projections from CA1 to the subiculum. *Hippocampus* **11,** 99–104.

Nagao T, Alonso A & Avoli M (1996). Epileptiform activity induced by pilocarpine in the rat hippocampal-entorhinal slice preparation. *Neuroscience* **72,** 399–408.

Navratilova Z, Giocomo LM, Fellous J-M, Hasselmo ME & McNaughton BL (2012). Phase precession and variable spatial scaling in a periodic attractor map model of medial entorhinal grid cells with realistic after-spike dynamics. *Hippocampus* **22,** 772–789.

Newman EL, Climer JR & Hasselmo ME (2014). Grid cell spatial tuning reduced following systemic muscarinic receptor blockade. *Hippocampus* **24,** 643–655.

Newman EL, Gillet SN, Climer JR & Hasselmo ME (2013). Cholinergic blockade reduces theta-gamma phase amplitude coupling and speed modulation of theta frequency consistent with behavioral effects on encoding. *J Neurosci* **33,** 19635–19646.

Niedermeyer E & Lopes da Silva FH (2005). *Electroencephalography : basic principles, clinical applications, and related fields*.

O'Brien JT & Thomas A (2015). Vascular dementia. *Lancet* **386,** 1698–1706.

O'Brien RJ & Wong PC (2011). Amyloid precursor protein processing and Alzheimer's disease. *Annu Rev Neurosci* **34,** 185–204.

O'Keefe J (1976). Place units in the hippocampus of the freely moving rat. *Exp Neurol* **51,** 78–109.

O'Keefe J & Burgess N (1996). Geometric determinants of the place fields of hippocampal neurons. *Nature* **381,** 425–428.

O'Keefe J & Burgess N (2005). Dual phase and rate coding in hippocampal place cells: theoretical significance and relationship to entorhinal grid cells. *Hippocampus* **15,** 853–866.

O'Keefe J & Conway DH (1978). Hippocampal place units in the freely moving

rat: Why they fire where they fire. *Exp Brain Res* **31,** 573–590.

O'Keefe J & Dostrovsky J (1971). The hippocampus as a spatial map. Preliminary evidence from unit activity in the freely-moving rat. *Brain Res* **34,** 171–175.

O'Keefe J & Nadel L (1978). *The hippocampus as a cognitive map*. Clarendon Press.

O'Keefe J & Recce ML (1993). Phase relationship between hippocampal place units and the EEG theta rhythm. *Hippocampus* **3,** 317–330.

Oke OO, Magony A, Anver H, Ward PD, Jiruska P, Jefferys JGR & Vreugdenhil M (2010). High-frequency gamma oscillations coexist with low-frequency gamma oscillations in the rat visual cortex *in vitro*. *Eur J Neurosci* **31,** 1435–1445.

Okun M, Lak A, Carandini M & Harris KD (2016). Long Term Recordings with Immobile Silicon Probes in the Mouse Cortex ed. Chacron MJ. *PLoS One* **11,** e0151180.

Onslow ACE, Bogacz R & Jones MW (2011). Quantifying phase-amplitude coupling in neuronal network oscillations. *Prog Biophys Mol Biol* **105,** 49–57.

Ormond J & McNaughton BL (2015). Place field expansion after focal MEC inactivations is consistent with loss of Fourier components and path integrator gain reduction. *Proc Natl Acad Sci U S A* **112,** 4116–4121.

Ozmen L, Albientz A, Czech C & Jacobsen H (2009). Expression of transgenic APP mRNA is the key determinant for beta-amyloid deposition in PS2APP transgenic mice. *Neurodegener Dis* **6,** 29–36.

Palop JJ, Chin J, Roberson ED, Wang J, Thwin MT, Bien-Ly N, Yoo J, Ho KO, Yu G-Q, Kreitzer A, Finkbeiner S, Noebels JL & Mucke L (2007). Aberrant excitatory neuronal activity and compensatory remodeling of inhibitory hippocampal circuits in mouse models of Alzheimer's disease. *Neuron* **55,** 697–711.

Parron C & Save E (2004). Evidence for entorhinal and parietal cortices involvement in path integration in the rat. *Exp Brain Res* **159,** 349–359.

Pastoll H, Ramsden HL & Nolan MF (2012). Intrinsic electrophysiological properties of entorhinal cortex stellate cells and their contribution to grid cell

firing fields. *Front Neural Circuits* **6,** 17.

Pastoll H, Solanka L, van Rossum MCW & Nolan MF (2013*a*). Feedback inhibition enables θ-nested γ oscillations and grid firing fields. *Neuron* **77,** 141–154.

Pastoll H, Solanka L, van Rossum MCW & Nolan MF (2013*b*). Feedback Inhibition Enables Theta-Nested Gamma Oscillations and Grid Firing Fields. *Neuron* **77,** 141–154.

Paxinos G & Franklin KBJ (2001). *Paxinos and Franklin's the Mouse Brain in Stereotaxic Coordinates, Second Edition*.

Perry EK, Gibson PH, Blessed G, Perry RH & Tomlinson BE (1977). Neurotransmitter enzyme abnormalities in senile dementia: Choline acetyltransferase and glutamic acid decarboxylase activities in necropsy brain tissue. *J Neurol Sci* **34,** 247–265.

Phillips KG, Cotel MC, McCarthy AP, Edgar DM, Tricklebank M, O'Neill MJ, Jones MW & Wafford KA (2012). Differential effects of NMDA antagonists on high frequency and gamma EEG oscillations in a neurodevelopmental model of schizophrenia. *Neuropharmacology* **62,** 1359–1370.

Pinault D (2008). N-Methyl d-Aspartate Receptor Antagonists Ketamine and MK-801 Induce Wake-Related Aberrant γ Oscillations in the Rat Neocortex. *Biol Psychiatry* **63,** 730–735.

Prince M (2015). World Alzheimer Report 2015: the global impact of dementia: an analysis of prevalence, incidence, cost and trends.

Prince M, Albanese E, Guerchet M & Prina M (2014). World Alzheimer Report 2014: Dementia and risk reduction: An analysis of protective and modifiable risk factors. *London Alzheimer Dis*.

Quirk G, Muller R, Kubie J & Ranck J (1992). The positional firing properties of medial entorhinal neurons: description and comparison with hippocampal place cells. *J Neurosci*. **12**, 1945-63.

Quiroga RQ, Reddy L, Kreiman G, Koch C & Fried I (2005). Invariant visual representation by single neurons in the human brain. *Nature* **435,** 1102–1107.

Radde R, Bolmont T, Kaeser SA, Coomaraswamy J, Lindau D, Stoltze L, Calhoun ME, Jäggi F, Wolburg H, Gengler S, Haass C, Ghetti B, Czech C, Hölscher C, Mathews PM & Jucker M (2006). Abeta42-driven cerebral amyloidosis in transgenic mice reveals early and robust pathology. *EMBO Rep* **7,** 940–946.

Raina P et al. (2008). Effectiveness of Cholinesterase Inhibitors and Memantine for Treating Dementia: Evidence Review for a Clinical Practice Guideline. *Ann Intern Med* **148,** 379.

Ramsden HL et al. (2015). Laminar and Dorsoventral Molecular Organization of the Medial Entorhinal Cortex Revealed by Large-scale Anatomical Analysis of Gene Expression ed. Chechik G. *PLOS Comput Biol* **11,** e1004032.

Ramsden M, Kotilinek L, Forster C, Paulson J, McGowan E, SantaCruz K, Guimaraes A, Yue M, Lewis J, Carlson G, Hutton M & Ashe KH (2005). Age-dependent neurofibrillary tangle formation, neuron loss, and memory impairment in a mouse model of human tauopathy (P301L). *J Neurosci* **25,** 10637–10647.

Ranck J. (1984). Head-direction cells in the deep cell layers of dorsal presubiculum in freely moving rats. In *Society for Neuroscience Abstracts*.

Randall AD, Witton J, Booth C, Hynes-Allen A & Brown JT (2010). The functional neurophysiology of the amyloid precursor protein (APP) processing pathway. *Neuropharmacology* **59,** 243–267.

Ray S, Naumann R, Burgalossi A, Tang Q, Schmidt H & Brecht M (2014). Grid-layout and theta-modulation of layer 2 pyramidal neurons in medial entorhinal cortex. *Science* **343,** 891–896.

Ringman JM & Cummings JL (2006). Current and Emerging Pharmacological Treatment Options for Dementia. *Behav Neurol* **17,** 5–16.

Rocher AB, Crimins JL, Amatrudo JM, Kinson MS, Todd-Brown MA, Lewis J & Luebke JI (2010). Structural and functional changes in tau mutant mice neurons are not linked to the presence of NFTs. *Exp Neurol* **223,** 385–393.

Rossant C, Kadir SN, Goodman DFM, Schulman J, Hunter MLD, Saleem AB, Grosmark A, Belluscio M, Denfield GH, Ecker AS, Tolias AS, Solomon S, Buzsáki G, Carandini M & Harris KD (2016). Spike sorting for large, dense

electrode arrays. *Nat Neurosci* **19,** 634–641.

Ryan LJ (1984). Characterization of cortical spindles in DBA/2 and C57BL/6 inbred mice. *Brain Res Bull* **13,** 549–558.

Santacruz K, Lewis J, Spires T, Paulson J, Kotilinek L, Ingelsson M, Guimaraes A, DeTure M, Ramsden M, McGowan E, Forster C, Yue M, Orne J, Janus C, Mariash A, Kuskowski M, Hyman B, Hutton M & Ashe KH (2005). Tau suppression in a neurodegenerative mouse model improves memory function. *Science* **309,** 476–481.

Sargolini F, Fyhn M, Hafting T, McNaughton BL, Witter MP, Moser M-B & Moser EI (2006). Conjunctive representation of position, direction, and velocity in entorhinal cortex. *Science* **312,** 758–762.

Schindelin J, Arganda-Carreras I, Frise E, Kaynig V, Longair M, Pietzsch T, Preibisch S, Rueden C, Saalfeld S, Schmid B, Tinevez J-Y, White DJ, Hartenstein V, Eliceiri K, Tomancak P & Cardona A (2012). Fiji: an open-source platform for biological-image analysis. *Nat Methods* **9,** 676–682.

Schwarcz R & Witter MP (2002). Memory impairment in temporal lobe epilepsy: the role of entorhinal lesions. *Epilepsy Res* **50,** 161–177.

Scoville WB & Milner B (1957). Loss of recent memory after bilateral hippocampal lesions. *J Neurol Neurosurg Psychiatry* **20,** 11–21.

Sederberg PB, Schulze-Bonhage A, Madsen JR, Bromfield EB, McCarthy DC, Brandt A, Tully MS & Kahana MJ (2006). Hippocampal and Neocortical Gamma Oscillations Predict Memory Formation in Humans. *Cereb Cortex* **17,** 1190–1196.

Selenica M-L, Benner L, Housley SB, Manchec B, Lee DC, Nash KR, Kalin J, Bergman JA, Kozikowski A, Gordon MN & Morgan D (2014). Histone deacetylase 6 inhibition improves memory and reduces total tau levels in a mouse model of tau deposition. *Alzheimers Res Ther* **6,** 12.

Sha SJ, Takada LT, Rankin KP, Yokoyama JS, Rutherford NJ, Fong JC, Khan B, Karydas A, Baker MC, DeJesus-Hernandez M, Pribadi M, Coppola G, Geschwind DH, Rademakers R, Lee SE, Seeley W, Miller BL & Boxer AL (2012). Frontotemporal dementia due to C9ORF72 mutations: clinical and

imaging features. *Neurology* **79,** 1002–1011.

Sharp PE, Tinkelman A & Cho J (2001). Angular velocity and head direction signals recorded from the dorsal tegmental nucleus of gudden in the rat: Implications for path integration in the head direction cell circuit. *Behav Neurosci* **115,** 571–588.

Shinder ME & Taube JS (2011). Active and passive movement are encoded equally by head direction cells in the anterodorsal thalamus. *J Neurophysiol*.

Shipston-Sharman O, Solanka L & Nolan MF (2016). Continuous attractor network models of grid cell firing based on excitatory-inhibitory interactions. *J Physiol* **106**, 788-800..

Shirvalkar PR, Rapp PR & Shapiro ML (2010). Bidirectional changes to hippocampal theta-gamma comodulation predict memory for recent spatial episodes. *Proc Natl Acad Sci U S A* **107,** 7054–7059.

Skaggs WE, Mcnaughton BL, Gothard KM & Markus EJ (1993). An Information-Theoretic Approach to Deciphering the Hippocampal Code. *Neural Inf Process Syst* 1030–1037.

Skaggs WE, McNaughton BL, Wilson MA & Barnes CA (1996). Theta phase precession in hippocampal neuronal populations and the compression of temporal sequences. *Hippocampus* **6,** 149–172.

Sławińska U & Kasicki S (1998). The frequency of rat's hippocampal theta rhythm is related to the speed of locomotion. *Brain Res* **796,** 327–331.

Sohal VS, Zhang F, Yizhar O & Deisseroth K (2009). Parvalbumin neurons and gamma rhythms enhance cortical circuit performance. *Nature* **459,** 698–702.

Solstad T, Boccara CN, Kropff E, Moser M-B & Moser EI (2008). Representation of geometric borders in the entorhinal cortex. *Science* **322,** 1865–1868.

Solstad T, Moser EI & Einevoll GT (2006). From grid cells to place cells: a mathematical model. *Hippocampus* **16,** 1026–1031.

Spencer SS & Spencer DD (1994). Entorhinal-Hippocampal Interactions in Medial Temporal Lobe Epilepsy. *Epilepsia* **35,** 721–727.

Spires TL, Orne JD, SantaCruz K, Pitstick R, Carlson GA, Ashe KH & Hyman BT

(2006). Region-specific dissociation of neuronal loss and neurofibrillary pathology in a mouse model of tauopathy. *Am J Pathol* **168,** 1598–1607.

Stackman RW & Taube JS (1998). Firing properties of rat lateral mammillary single units: head direction, head pitch, and angular head velocity. *J Neurosci* **18,** 9020–9037.

Steffenach H-A, Witter M, Moser M-B & Moser EI (2005). Spatial Memory in the Rat Requires the Dorsolateral Band of the Entorhinal Cortex. *Neuron* **45,** 301–313.

Stelzmann RA, Norman Schnitzlein H & Reed Murtagh F (1995). An english translation of alzheimer's 1907 paper, Uber eine eigenartige erkankung der hirnrinde *Clin Anat* **8,** 429–431.

Stensola H, Stensola T, Solstad T, Frøland K, Moser M-B & Moser EI (2012). The entorhinal grid map is discretized. *Nature* **492,** 72–78.

Stranahan AM & Mattson MP (2010). Selective vulnerability of neurons in layer II of the entorhinal cortex during aging and Alzheimer's disease. *Neural Plast* **2010,** 108190.

Sullivan D, Mizuseki K, Sorgi A & Buzsáki G (2014). Comparison of sleep spindles and theta oscillations in the hippocampus. *J Neurosci* **34,** 662–674.

Sun C, Kitamura T, Yamamoto J, Martin J, Pignatelli M, Kitch LJ, Schnitzer MJ & Tonegawa S (2015). Distinct speed dependence of entorhinal island and ocean cells, including respective grid cells. *Proc Natl Acad Sci* **112,** 201511668.

van Swieten JC & Heutink P (2008). Mutations in progranulin (GRN) within the spectrum of clinical and pathological phenotypes of frontotemporal dementia. *Lancet Neurol* **7,** 965–974.

Takeda Y, Nakamura F, Ito M, Itaichi Y, Hayashi Y & Koyama T (1998). Different Effects of Antiepileptic Drugs on Initiation and Propagation of Ictal Discharges in a Case of Frontal Lobe Epilepsy. *Epilepsia* **39,** 81–81.

Taube J (1995). Head direction cells recorded in the anterior thalamic nuclei of freely moving rats. *J Neurosci*.**15**, 70-86.

Taube J, Muller R & Ranck J (1990*a*). Head-direction cells recorded from the

postsubiculum in freely moving rats. I. Description and quantitative analysis. *J Neurosci*. **10**, 420-35

Taube J, Muller R & Ranck J (1990*b*). Head-direction cells recorded from the postsubiculum in freely moving rats. II. Effects of environmental manipulations. *J Neurosci*. **10**, 436-47.

Taube JS (2007). The Head Direction Signal: Origins and Sensory-Motor Integration. *Annu Rev Neurosci* **30,** 181–207.

Terry A V. & Buccafusco JJ (2003). The Cholinergic Hypothesis of Age and Alzheimer's Disease-Related Cognitive Deficits: Recent Challenges and Their Implications for Novel Drug Development. *J Pharmacol Exp Ther*. **306**, 821-7

Tolman EC (1948). Cognitive maps in rats and men. *Psychol Rev* **55,** 189–208.

Tort ABL, Kramer MA, Thorn C, Gibson DJ, Kubota Y, Graybiel AM & Kopell NJ (2008). Dynamic cross-frequency couplings of local field potential oscillations in rat striatum and hippocampus during performance of a T-maze task. *Proc Natl Acad Sci U S A* **105,** 20517–20522.

Traub RD, Bibbig A, Fisahn A, LeBeau FEN, Whittington MA & Buhl EH (2000). A model of gamma-frequency network oscillations induced in the rat CA3 region by carbachol in vitro. *Eur J Neurosci* **12,** 4093–4106.

Trinh N-H et al. (2003). Efficacy of Cholinesterase Inhibitors in the Treatment of Neuropsychiatric Symptoms and Functional Impairment in Alzheimer Disease. *JAMA* **289,** 210.

Tsao A, Moser M-B & Moser EI (2013). Traces of Experience in the Lateral Entorhinal Cortex. *Curr Biol* **23,** 399–405.

Unal G, Joshi A, Viney TJ, Kis V & Somogyi P (2015). Synaptic Targets of Medial Septal Projections in the Hippocampus and Extrahippocampal Cortices of the Mouse. *J Neurosci*. **35**, 15812-26.

Valerio S & Taube JS (2012). Path integration: how the head direction signal maintains and corrects spatial orientation. *Nat Neurosci* **15,** 1445–1453.

Vandamme TF (2014). Use of rodents as models of human diseases. *J Pharm Bioallied Sci* **6,** 2–9.

Vandecasteele M, Varga V, Berényi A, Papp E, Barthó P, Venance L, Freund TF & Buzsáki G (2014). Optogenetic activation of septal cholinergic neurons suppresses sharp wave ripples and enhances theta oscillations in the hippocampus. *Proc Natl Acad Sci U S A* **111,** 13535–13540.

Vanderwolf C. (1969). Hippocampal electrical activity and voluntary movement in the rat. *Electroencephalogr Clin Neurophysiol* **26,** 407–418.

Varela F, Lachaux J-P, Rodriguez E & Martinerie J (2001). The brainweb: Phase synchronization and large-scale integration. *Nat Rev Neurosci* **2,** 229–239.

Verret L, Mann EO, Hang GB, Barth AMI, Cobos I, Ho K, Devidze N, Masliah E, Kreitzer AC, Mody I, Mucke L & Palop JJ (2012). Inhibitory interneuron deficit links altered network activity and cognitive dysfunction in Alzheimer model. *Cell* **149,** 708–721.

Walker Z, Possin KL, Boeve BF & Aarsland D (2015). Lewy body dementias. *Lancet* **386,** 1683–1697.

Walsh DM & Selkoe DJ (2004). Deciphering the Molecular Basis of Memory Failure in Alzheimer's Disease. *Neuron* **44,** 181–193.

Wang Y & Mandelkow E (2016). Tau in physiology and pathology. *Nat Rev Neurosci* **17,** 5–21.

Wells CE, Amos DP, Jeewajee A, Douchamps V, Rodgers J, O'Keefe J, Burgess N & Lever C (2013). Novelty and anxiolytic drugs dissociate two components of hippocampal theta in behaving rats. *J Neurosci* **33,** 8650–8667.

Wells JA et al. (2015). In vivo imaging of tau pathology using multi-parametric quantitative MRI. *Neuroimage* **111,** 369–378.

Whishaw IQ & Vanderwolf CH (1973). Hippocampal EEG and behavior: Change in amplitude and frequency of RSA (Theta rhythm) associated with spontaneous and learned movement patterns in rats and cats. *Behav Biol* **8,** 461–484.

Whitehouse P, Price D, Struble R, Clark A, Coyle J & Delon M (1982). Alzheimer's disease and senile dementia: loss of neurons in the basal forebrain. *Science, **215**, :1237-9.*

Wills TJ, Barry C & Cacucci F (2012). The abrupt development of adult-like grid

cell firing in the medial entorhinal cortex. *Front Neural Circuits* **6,** 21.

Wills TJ, Cacucci F, Burgess N & O'Keefe J (2010). Development of the hippocampal cognitive map in preweanling rats. *Science* **328,** 1573–1576.

Wilson DIG, Langston RF, Schlesiger MI, Wagner M, Watanabe S & Ainge JA (2013). Lateral entorhinal cortex is critical for novel object-context recognition. *Hippocampus* **23,** 352–366.

Wilson M & McNaughton B (1993). Dynamics of the hippocampal ensemble code for space. *Science **261**, 1055-8*

Wilson M & McNaughton B (1994). Reactivation of hippocampal ensemble memories during sleep. *Science **265**, :676-9.*

Winson J (1978). Loss of hippocampal theta rhythm results in spatial memory deficit in the rat. *Science **201**, 160-3.*

Winter SS, Clark BJ & Taube JS (2015). Disruption of the head direction cell network impairs the parahippocampal grid cell signal. *Science **347**, 870-874*.

Wischik CM, Harrington CR & Storey JMD (2014). Tau-aggregation inhibitor therapy for Alzheimer's disease. *Biochem Pharmacol* **88,** 529–539.

Witter M (2006). Connections of the subiculum of the rat: Topography in relation to columnar and laminar organization. *Behav Brain Res* **174,** 251–264.

Witter MP (2007). The perforant path: projections from the entorhinal cortex to the dentate gyrus. In, pp. 43–61.

Witter MP, Griffioen AW, Jorritsma-Byham B & Krijnen JLM (1988). Entorhinal projections to the hippocampal CA1 region in the rat: An underestimated pathway. *Neurosci Lett* **85,** 193–198.

Witter MP, Groenewegen HJ, Lopes da Silva FH & Lohman AHM (1989). Functional organization of the extrinsic and intrinsic circuitry of the parahippocampal region. *Prog Neurobiol* **33,** 161–253.

Witton J, Staniaszek LE, Bartsch U, Randall AD, Jones MW & Brown JT (2014). Disrupted hippocampal sharp-wave ripple-associated spike dynamics in a transgenic mouse model of dementia. *J Physiol*, **594**, 4615-30

Wong G & Skolnick P (1992). High affinity ligands for "diazepam-insensitive"

benzodiazepine receptors. *Eur J Pharmacol* **225,** 63–68.

Wood ER, Dudchenko PA & Eichenbaum H (1999). The global record of memory in hippocampal neuronal activity. *Nature* **397,** 613–616.

Yamasaki T, Horie S, Muranaka H, Kaseda Y, Mimori Y & Tobimatsu S (2012). Relevance of in vivo Neurophysiological Biomarkers for Mild Cognitive Impairment and Alzheimer's Disease. *J Alzheimer's Dis* **31,** S137–S154.

Yartsev MM & Ulanovsky N (2013). Representation of Three-Dimensional Space in the Hippocampus of Flying Bats. *Science* **340**, 367-372.

Yartsev MM, Witter MP & Ulanovsky N (2011). Grid cells without theta oscillations in the entorhinal cortex of bats. *Nature* **479,** 103–107.

Yoganarasimha D, Rao G & Knierim JJ (2011). Lateral entorhinal neurons are not spatially selective in cue-rich environments. *Hippocampus* **21,** 1363–1374.

Yoon K, Buice MA, Barry C, Hayman R, Burgess N, Fiete IR, Fried I, Moser M, Moser E, Roudi Y & Witter M (2013). Specific evidence of low-dimensional continuous attractor dynamics in grid cells. *Nat Neurosci* **16,** 1077–1084.

Yoshida M, Jochems A & Hasselmo ME (2013). Comparison of properties of medial entorhinal cortex layer II neurons in two anatomical dimensions with and without cholinergic activation. *PLoS One* **8,** e73904.

Young B, Fox G & Eichenbaum H (1994). Correlates of hippocampal complex-spike cell activity in rats performing a nonspatial radial maze task. *J Neurosci*. **14**, 6553-6563

Young BJ, Otto T, Fox GD & Eichenbaum H (1997). Memory Representation within the Parahippocampal Region. *J Neurosci*. **17,** 5183-95.

Zhang S-J, Ye J, Miao C, Tsao A, Cerniauskas I, Ledergerber D, Moser M-B & Moser EI (2013). Optogenetic dissection of entorhinal-hippocampal functional connectivity. *Science* **340,** 1232627.

Zheng C, Bieri KW, Trettel SG & Colgin LL (2015). The relationship between gamma frequency and running speed differs for slow and fast gamma rhythms in freely behaving rats. *Hippocampus* **25,** 924–938.

Ziburkus J, Cressman JR, Barreto E & Schiff SJ (2006). Interneuron and pyramidal cell interplay during in vitro seizure-like events. *J Neurophysiol* **95,** 3948–3954.

Zilli E a. (2012). Models of Grid Cell Spatial Firing Published 2005–2011. *Front Neural Circuits* **6,** 1–17.